Neutral Current π^0 Production Rate Measurement On-Water Using the π^0 Detector in the Near Detector of the T2K Experiment

A Dissertation presented

by

Karin Gilje

to

The Graduate School

in Partial Fulfillment of the

Requirements

for the Degree of

Doctor of Philosophy

in

Physics and Astronomy

Stony Brook University

August 2014

Stony Brook University

The Graduate School

Karin Gilje

We, the dissertation committe for the above candidate for the

Doctor of Philosophy degree, hereby recommend

acceptance of this dissertation

Chang Kee Jung - Dissertation Advisor
Professor, Physics and Astronomy

Matt Dawber - Chairperson of Defense
Associate Professor, Physics and Astronomy

Patrick Meade
Assistant Professor, C.N. Yang Institute for Theoretical Physics

Christopher Mauger
Staff Scientist, Los Alamos National Laboratory

This dissertation is accepted by the Graduate School

Charles Taber
Dean of the Graduate School

Abstract of the Dissertation

Neutral Current π^0 Production Rate Measurement On-Water Using the π^0 Detector in the Near Detector of the T2K Experiment

by

Karin Gilje

Doctor of Philosophy

in

Physics and Astronomy

Stony Brook University

2014

The T2K Experiment is a long-baseline neutrino experiment that stretches 295 km from the east to the west coast of Japan (Tokai-Mura to Kamioka). One of the major goals of the experiment is a measurement of θ_{13} and (if θ_{13} is non-zero) potentially CP violation in the lepton sector. This is performed by searching for ν_e appearance in a ν_μ beam from the Japan Proton Accelerator Research Complex (J-PARC). The far detector, Super Kamiokande (SK), is a water Cherenkov detector. One of the dominant backgrounds for SK in the oscillation measurement is the uncertainty on the cross section of the Neutral Current Single π^0 (NC1π^0) interaction. In order to constrain this background, the π^0 detector (P∅D) was placed in the near detector complex, 280 meters from the beam origin. The P∅D was constructed with a water target that can be filled and drained in order to perform a material subtraction to measure various cross sections on-water. This analysis presents the first on-water NC1π^0 rate measurement with a neutrino beam energy less than 1 GeV. Using the NEUT Monte Carlo, a cut selection was developed in order to accentuate the difference between the signal and background shapes of the reconstructed invariant mass of the π^0 particle. The selected events and a muon decay sideband, used to constrain the shape of the background events, are then simultaneously fit in order to extract an observed number of signal events. The observed data is then compared to Monte Carlo. Using T2K Runs 1-4 (total of 6.13×10^{20} protons on target), a ratio of $0.790 \pm 0.076(\text{stat}) \pm 0.143(\text{sys})$ ($0.850 \pm 0.091(\text{stat}) \pm 0.137(\text{sys})$) is found for the P∅D water-in (water-out) configuration. After calculating the subtracted number of events on-water from the water-in and water-out data, a data to NEUT Monte Carlo ratio of $0.677 \pm 0.261(\text{stat}) \pm 0.462(\text{sys})$ is found for the rate of NC1π^0 interactions on-water.

Dedication Page

To my husband,
Joshua

Table of Contents

1 Introduction **1**
1.1 Basic Particles . . . 1
1.2 A Brief History Of Neutrinos . . . 3
1.3 Neutrino Oscillation . . . 13
1.4 The Neutral Current Single π^0 Interaction . . . 17

2 T2K **19**
2.1 Description of Beam Line . . . 19
2.2 Overview of ND280 Detectors . . . 22
2.2.1 INGRID . . . 22
2.2.2 ND280 . . . 24
2.3 Super Kamiokande . . . 26

3 P∅D **28**
3.1 Detector Construction . . . 28
3.2 Data Acquisition . . . 35
3.3 Software Process . . . 37
3.4 P∅D Particle Identification . . . 40
3.4.1 Stopping Muon Sample . . . 40
3.4.2 Creating a Map . . . 43
3.4.3 Mapping the PID . . . 47
3.5 Converting Deposited Charge to Energy . . . 50
3.5.1 Creating a Photon Sample . . . 50
3.5.2 Calculating the PEU to MeV Conversion . . . 51
3.5.3 Checking the PEU to MeV Conversion . . . 53
3.6 P∅D Alignment . . . 64
3.6.1 P∅D Layer Resolution . . . 64
3.6.2 Internal Alignment . . . 65
3.6.3 Alignment to the TPC . . . 67
3.6.4 Alignment Survey Measurements . . . 69

4 NC1π^0 Rate Measurement **73**
4.1 Reconstruction of the NC1π^0 . . . 75
4.2 Event Selection . . . 79
4.3 Sideband Selection . . . 88

4.4 Analysis . . . 93
4.4.1 Final Sample Cross Checks . . . 93
4.4.2 Definition of Likelihood . . . 98
4.4.3 Fit Results . . . 113
4.4.4 On-Water Calculation . . . 115
4.5 T2KReWeight . . . 116
4.5.1 Fit Results . . . 120
4.5.2 Comparing Fit Results . . . 126

5 Systematics 128
5.1 Energy Scale . . . 128
5.1.1 Geometry Differences . . . 129
5.1.2 PE Peak Uncertainty . . . 129
5.1.3 Energy Scale . . . 132
5.2 Detector Variations . . . 135
5.3 Mass Uncertainty . . . 137
5.4 Alignment . . . 140
5.5 Fiducial Volume . . . 140
5.5.1 Fiducial Volume Scaling . . . 140
5.5.2 Fiducial Volume Shift . . . 143
5.6 Flux and Event Generator Uncertainties . . . 145
5.7 Reconstruction Uncertainties . . . 151
5.7.1 Track PID Efficiency . . . 151
5.7.2 Continuous Distribution Cuts . . . 151
5.7.3 Muon Decay Systematic . . . 157
5.8 g Factor . . . 158
5.8.1 Statistical g Contribution . . . 158
5.8.2 Systematic g Contribution . . . 158
5.9 Summary of Systematic Errors . . . 160

6 Conclusion 163
6.1 Future Improvements . . . 164

Appendices 167

Appendix A Supporting Plots for Fit Result 167
A.1 Unconstrained g Fit . . . 171

List of Figures

1.1 Standard Model view of basic particles 2
1.2 The decay of the π^0 3
1.3 Beta decay 4
1.4 Neutrino mass and the shape of the β-decay energy spectrum 5
1.5 Direct Observation of ν_τ 7
1.6 Neutrino number and the Z decay width 8
1.7 Asymmetry of atmospheric neutrinos 10
1.8 Rate of atmospheric neutrinos 11
1.9 SNO results 13
1.10 NC1π^0 interaction 18

2.1 The J-PARC accelerator complex 20
2.2 Schematic diagrams of the beam extraction 20
2.3 Affect of the off-axis flux 21
2.4 A diagram of the ND280 Complex 23
2.5 Schematic diagram of the INGRID detector 23
2.6 Diagram of the INGRID Modules 24
2.7 Diagram of the ND280 detectors 25
2.8 A cut away view of the TPC 25
2.9 A diagram of SK 27

3.1 A schematic diagram of the P∅D 29
3.2 A schematic showing a singlet and doublet hit 35
3.3 A schematic of the WLS fiber to MPPC assembly 36
3.4 A diagram of the data collection system 36
3.5 A diagram of the software process 38
3.6 A diagram of the P∅D reconstruction process 39
3.7 Last P∅Dule used in the stopping muon sample 41
3.8 Length of tracks in stopping muon sample 41
3.9 Vertex distribution for the water-in stopping muon sample 42
3.10 Vertex distribution for the water-out stopping muon sample 42
3.11 Angular distribution of the water-in stopping muon sample 43
3.12 Angular distribution of the water-out stopping muon sample 44
3.13 Example of the layer charge PID variable 44
3.14 Example of the layer asymmetry PID variable 45

3.15 Example of the PØDule asymmetry PID variable 46
3.16 Example of the number of empty layers PID variable 46
3.17 Example of the median PID variable 47
3.18 Comparison of deposited charge and true energy of photons with an energy less than 500 MeV. 51
3.19 Comparison of deposited charge and true energy of photons with an energy less than 1 GeV. 52
3.20 Water-in energy bin fits 54
3.21 Water-out energy bin fits 55
3.22 ECal-only energy bin fits 56
3.23 Fitting the charge to energy conversion 57
3.24 The fractional accuracy of the estimated energy 58
3.25 Estimated energy versus true energy 60
3.26 The estimated energy versus the corrected charge deposit 61
3.27 Mono-energetic test results for the water-in configuration 62
3.28 Mono-energetic test results for the water-out configuration 63
3.29 Monte Carlo predicted resolution of a singlet. 65
3.30 Monte Carlo predicted resolution of a doublet. 66
3.31 Measured resolution of a singlet. 66
3.32 Measured resolution of a doublet. 67
3.33 Internal PØD Alignment method testing. 68
3.34 Internal PØD Alignment of the in situ PØD 68
3.35 External PØD to TPC Alignment Monte Carlo test 69
3.36 External PØD to TPC Alignment in situ 70
3.37 Comparison of PØDule Y alignment and survey 71
3.38 Comparison of PØDule X alignment and survey 72

4.1 The NC1π^0 vertex resolution for the water-in configuration 76
4.2 The NC1π^0 vertex resolution for the water-out configuration 77
4.3 Angular resolution of decay photons 78
4.4 Opening angle resolution of decay photons 78
4.5 Fractional momentum resolution of the π^0 79
4.6 The N-1 plot of the fiducial cut 81
4.7 The N-1 plot of the muon decay cut 82
4.8 The N-1 plot of the shower charge cut 82
4.9 The N-1 plot of the PID weight cut 83
4.10 The N-1 plot of the π^0 direction cut 83
4.11 Diagram of overlapping 2D projections of a 3D shower 84
4.12 The N-1 plot of shower separation cut 85
4.13 Cut optimization for the water-in configuration 86
4.14 Cut optimization for the water-out configuration 87
4.15 The muon decay sideband 89
4.16 The charge in shower sideband 89
4.17 The PID weight sideband 90
4.18 The shower separation sideband 90

4.19 Comparison of background with the muon decay sideband 91
4.20 Comparison of background with the charge in shower sideband 92
4.21 Comparison of background with the PID weight sideband 92
4.22 Comparison of background with the shower separation sideband 93
4.23 The invariant mass of the selected events 94
4.24 The efficiency of the NC1π^0 analysis as a function of the momentum of the π^0. 97
4.25 The distribution of the true neutrino energy for the saved Monte Carlo events. 98
4.26 The rate of π^0 candidates observed per POT 99
4.27 The bunch timing of the observed candidates in the water-in configuration . 100
4.28 The bunch timing of the observed candidates in the water-out configuration 101
4.29 The vertex distribution of selected events in the water-in configuration . . . 102
4.30 The vertex distribution of the selected events in the water-out configuration 103
4.31 The vertex distribution of the selected events in the water-in configuration . 104
4.32 The vertex distribution of the selected events in the water-out configuration 105
4.33 The reconstructed π^0 energy for the selected events. 106
4.34 The input PDFs for the PØD water-in configuration 107
4.35 The input PDFs for the PØD water-out configuration 108
4.36 The PØD water-in and water-out configuration simultaneous invariant mass fit.112
4.37 The PØD water-in and water-out configuration simultaneous invariant mass fit with an unconstrained g factor. 114
4.38 Comparison of NEUT Monte Carlo to pre- and post-weighted BANFF values for the PØD water-in configuration 117
4.39 Comparison of NEUT Monte Carlo to pre- and post-weighted BANFF values for the PØD water-out configuration 117
4.40 Comparison of BANFF errors for the PØD water-in configuration 118
4.41 Comparison of BANFF errors for the PØD water-out configuration 118
4.42 Comparison of BANFF errors on the number of observed events for the PØD water-in configuration 119
4.43 Comparison of BANFF errors on the number of observed events for the PØD water-out configuration 119
4.44 Simultaneous invariant mass fits with BANFF PDFs for the PØD water-in configuration 121
4.45 Simultaneous invariant mass fits with BANFF PDFs for the PØD water-out configuration 122
4.46 Simultaneous invariant mass fits with BANFF PDFs for the PØD water-in configuration with an unconstrained g factor 124
4.47 Simultaneous invariant mass fits with BANFF PDFs for the PØD water-out configuration with an unconstrained g factor 125

5.1 Hit charge deposit in candidate showers 129
5.2 Number of hits in XZ and YZ projections for the PØD water-in configuration 130
5.3 Number of hits in XZ and YZ projections for the PØD water-out configuration 130
5.4 Distribution of energy scale throws 132
5.5 The distribution of weighted signal events from energy scale throws 133
5.6 Distribution of energy scale throws for an unconstrained g factor 134

5.7 The distribution of weighted signal events from energy scale throws with an unconstrained g factor . . . 134
5.8 The MIP peak after correction . . . 136
5.9 Throws of possible mass corrections . . . 138
5.10 Data to Monte Carlo ratio after 10,000 throws of mass corrections . . . 138
5.11 Data to Monte Carlo ratio after 10,000 throws of mass corrections with an unconstrained g factor . . . 139
5.12 Event rate at fiducial boundary for the P∅D water-in configuration . . . 141
5.13 Event rate at fiducial boundary for the P∅D water-out configuration . . . 142
5.14 Distance from π^0 to photon conversion. for the P∅D water-in configuration . 143
5.15 Distance from π^0 to photon conversion. for the P∅D water-in configuration . 144
5.16 Input BANFF correlation matrices . . . 146
5.17 Input BANFF errors . . . 146
5.18 The distribution of the number of signal for pre-BANFF throws . . . 149
5.19 The distribution of the number of signal for post-BANFF throws . . . 149
5.20 The distribution of the number of signal for pre-BANFF throws with an unconstrained g factor . . . 150
5.21 The distribution of the number of signal for post-BANFF throws with an unconstrained g factor . . . 150
5.22 Cumulative plots of the continuous cut values for a control sample with the P∅D water-in configuration . . . 152
5.23 Cumulative plots of the continuous cut values for a control sample with the P∅D water-out configuration . . . 153
5.24 Number of muon decay clusters reconstructed from a control sample . . . 153
5.25 Time delay of a muon decay for a control sample in the water-in configuration 155
5.26 Time delay of a muon decay for a control sample in the water-out configuration 156
5.27 The distribution of the throws of the g factor . . . 159
5.28 The weighted signal events due to throws of the g factor . . . 159

A.1 The negative log likelihood curves for the energy scale parameter for both the P∅D water-in and water-out configurations. . . . 168
A.2 The negative log likelihood curves for the number of signal events in the selected region for both the P∅D water-in and water-out configurations. . . . 168
A.3 The negative log likelihood curves for the number of background events in the selected region for both the P∅D water-in and water-out configurations. . . . 169
A.4 The negative log likelihood curves for the number of signal events in the sideband region for both the P∅D water-in and water-out configurations. . . 169
A.5 The negative log likelihood curves for the number of background events in the sideband region for both the P∅D water-in and water-out configurations. . . 170
A.6 The negative log likelihood curves for the number of signal events in the sideband region for both the P∅D water-in and water-out configurations. . . 170
A.7 The negative log likelihood curves for the number of background events in the sideband region for both the P∅D water-in and water-out configurations. . . 171
A.8 The negative log likelihood curves for the energy scale parameter for both the P∅D water-in and water-out configurations. . . . 172

A.9 The negative log likelihood curves for the g factor parameter for both the P∅D water-in and water-out configurations. 172
A.10 The negative log likelihood curves for the number of signal events in the selected region for both the P∅D water-in and water-out configurations. . . . 173
A.11 The negative log likelihood curves for the number of background events in the selected region for both the P∅D water-in and water-out configurations. . . . 173
A.12 The negative log likelihood curves for the number of signal events in the sideband region for both the P∅D water-in and water-out configurations. . . 174
A.13 The negative log likelihood curves for the number of background events in the sideband region for both the P∅D water-in and water-out configurations. . . 174
A.14 The negative log likelihood curves for the number of signal events in the sideband region for both the P∅D water-in and water-out configurations. . . 175
A.15 The negative log likelihood curves for the number of background events in the sideband region for both the P∅D water-in and water-out configurations. . . 175

List of Tables

1.1 Current Measurement of Mixing Matrix Elements 16

3.1 PØD Fiducial Volume Definition 30
3.2 The mass of the components of the PØD 33
3.3 The areal densities of the components of the PØD 33
3.4 The fiducial mass of the PØD 35
3.5 A raw water-in PID confusion matrix 48
3.6 A water-in PID confusion matrix 48
3.7 A raw water-out PID confusion matrix 49
3.8 A water-in PID confusion matrix 49
3.9 Summary of the charge to energy conversion 53
3.10 Summary of the mono-energetic study 61
3.11 PØD resolution 65
3.12 PØD-TPC Survey results 71

4.1 Summary of beam specifications used in the Monte Carlo generation. 74
4.2 Summary of data POT 74
4.3 Summary of NEUT Monte Carlo POT 75
4.4 The vertex position resolution of NC1π^0 events. 75
4.5 PØD fiducial volume. 80
4.6 Summary of the background compositions of the sidebands for the PØD water-in configuration 88
4.7 Summary of the purities of the sidebands for the PØDwater-in configuration 89
4.8 Summary of the background compositions of the sidebands for the PØD water-out configuration 91
4.9 Summary of the purities of the sidebands for the PØD water-out configuration 91
4.10 The number of events passing each cut for the PØD water-in configuration . 94
4.11 The number of events passing each cut for the PØD water-out configuration . 95
4.12 The breakdown of the final sample in the Monte Carlo for the PØD water-in configuration. 95
4.13 The breakdown of the final sample in the Monte Carlo for the PØD water-out configuration. 96
4.14 The breakdown of the muon decay sideband in the Monte Carlo for the PØD water-in configuration. 96

4.15 The breakdown of the muon decay sideband in the Monte Carlo for the PØD water-out configuration. 96
4.16 Summary of high invariant mass events 97
4.17 Summary of efficiency and purity 97
4.18 Summary of the simultaneous fit results 111
4.19 Summary of Monte Carlo predictions 111
4.20 Summary of the signal events observed and data to Monte Carlo ratios . . . 111
4.21 Summary of the simultaneous fit result with unconstrained g factor 113
4.22 Summary of Monte Carlo predictions 113
4.23 Summary of the signal events observed and data to Monte Carlo ratios with an unconstrained g factor 113
4.24 Efficiencies and purities of the selection 115
4.26 Summary of fit results using pre-BANFF adjusted PDFs 120
4.27 Pre-BANFF event expectations 120
4.28 Summary of fit results using post-BANFF adjusted PDFs 120
4.29 Post-BANFF event expectations 121
4.30 Summary of fit results using pre-BANFF adjusted PDFs with an unconstrained g factor 123
4.31 Pre-BANFF event expectations with an unconstrained g factor 123
4.32 Summary of fit results using post-BANFF adjusted PDFs with an unconstrained g factor 123
4.33 Post-BANFF event expectations with an unconstrained g factor 124
4.34 Summary of the water-in and water-out configuration data to Monte Carlo ratios 126
4.35 Summary of the predictions for the number of NC1π^0 on-water vertices. . . . 126
4.36 Summary of the on-water NC1π^0 event rate calculations for the PØD 126
4.37 Summary of the data to Monte Carlo ratios of the rate of NC1π^0 interactions in the PØD 127

5.1 Summary of event loss for low charge deposit cuts for the PØD water-in configuration 131
5.2 Summary of event loss for low charge deposit cuts for the PØD water-out configuration 131
5.3 Summary of systematic error due to energy scale 132
5.4 Summary of systematic error due to energy scale with an unconstrained g factor 133
5.5 Summary of the post-correction data. 135
5.6 Event weighting correction factors based on mass 137
5.7 Summary of the throws of mass corrections 139
5.8 Summary of the throws of mass corrections with an unconstrained g factor . 139
5.9 Summary of the fiducial scaling systematic errors. 140
5.10 Summary of the distance between the π^0 and the photon conversion 144
5.11 Summary of flux uncertainty 147
5.12 Summary of energy bins used for the flux uncertainty 147
5.13 Summary of cross section uncertainties 148
5.14 Summary of energy bins used for the cross section uncertainties 148

5.15 Summary of the widths of the pre- and post-BANFF variations 148
5.16 Summary of the widths of the pre- and post-BANFF variations with an unconstrained g factor 149
5.17 Summary of the systematic error due to continuous cuts for the PØD water-in configuration 154
5.18 Summary of the systematic error due to continuous cuts for the PØD water-out configuration 154
5.19 Summary of the purities in the control sample 155
5.20 Efficiency of finding a muon decay 155
5.21 Summary of the muon decay fit for the PØD water-in configuration 155
5.22 Summary of the muon decay fit for the PØD water-out configuration 156
5.23 Summary of error due to the error on g 158
5.24 Summary of Systematic errors. 161
5.25 Summary of constraints intended for the fit 161
5.26 Summary of systematic errors with an unconstrained g factor 162

List of Abbreviations

AGS	Alternating Gradient Synchrotron
BANFF	Beam And Neutrino Flux task Force
BNL	Brookhaven National Laboratory
CCQE	Charged Current Quasi Elastic
CECal	Central ECal, a SuperP∅Dule
CP	Charge Parity
CTM	Cosmic Trigger Module
CWT	Central Water Target
DONUT	Direct Observation of NU Tau
DSECal	DownStream ECal
ECal	Electromagnetic Calorimeter
FGD	Fine Grained Detector
FPN	Front-end Processing Node
FSI	Final State Interaction
INGRID	Interactive Neutrino GRID
J-PARC	Japan Proton Accelerator Research Complex
LEP	Large Electron Positron Collider
MC	Monte Carlo
MCM	Master Clock Module
MIDAS	Maximum Integrated Data Acquisition System
MIP	Minimum Ionizing Particle
MPPC	Multi-Pixel Photon Counter
MUMON	MUon MONitor
NC1π^0	Neutral Current Single π^0
ND280	The near detector complex at 280 m from the target
ND280	The off-axis near detector at T2K
PDF	Probability Distribution Function
PE	Photo-Electron
PEU	Photo-Electron Unit, a unit of deposited charge
PID	Particle IDentification
PMT	PhotoMultiplier Tube
P∅D	π^0 detector
RMM	Readout Merger Module
SCM	Slave Clock Module
SK	Super Kamiokande

SM	Standard Model
SMRD	Side Muon Range Detector
SSM	Standard Solar Model
T2K	A long-baseline neutrino oscillation experiment
TFB	TripT Front End Board
TPC	Time Projection Chamber
USECal	Upstream ECal, a SuperP∅Dule
USWT	Upstream Water Target
WLS	Wave Length Shifting (fiber)

Acknowledgements

It takes a village to raise a child, or PhD candidate. Over the last six years, many people have had a large influence on my life and on the scientific work I've done. Even before that, many people have helped me become the scientist I am today.

I would like to thank my high school physics teacher, Mr. Askey, for inspiring me to even think of physics as a possible career. I would also like to thank all the physics and math professors I've had at St. Olaf College for giving me the tools to succeed in physics and in becoming a well rounded person. In particular, I wish to acknowledge Dr. Brian Borovsky and Dr. Jason Engbrecht. Both men have encouraged me to pursue my interests. They also pushed me to apply to Stony Brook. I really appreciate the post-graduate opportunities Dr. Engbrecht has provided, allowing me to work with high school women and reinvigorating my enthusiasm for the field. Thank you to Dr. Jill Dietz, my advisor at St. Olaf, for supporting me even when I left math for physics.

At Stony Brook, I have had a wonderful support group of my peers, helping me through some difficult times. I would like to acknowledge the support and love of many people. The soccer guys have helped me stay in shape and keep my stress level down with weekly games. I have also had many running buddies throughout the years, who have provided much needed confidantes: Poppy, Shawn, Sarah T., Jeanine and Adam. I really appreciate the socialization and companionship provided by a weekly game night, even though most of the evenings ended in yelling. I especially want to thank the best friends, and bridesmaids, one could ever want, Sara Callori and Betül Pamuk who, with Vanessa Iiams, made my wedding an event to remember. A big thank you to all the cat sitters I have had over the years while I was away in Japan: Shawn, John, Joshua, Jay, Sara C., Karen, and David.

I wish to thank all the members of T2K for building and running the experiment. I would like to specifically acknowledge Helen O'Keeffe for her friendship and guidance in my analysis.

The people of the NNGroup, both past and present members, have provided me with a lot of support in my research. Thank you to Chang Kee Jung, for supporting me during my PhD. I really appreciate the legacy that Glenn Lopez left for me to work on and improve. Ian Taylor and Clark McGrew were very patient with me while I learned how to code in order to contribute to the experiment. Clark continued to be patient and supportive throughout my analysis. I would also like to thank James Imber for always listening to any new issues I found in my code and for taking care of my husband in Japan. I especially want to acknowledge the support and time that I have received from Jeanine Adam from analysis to sea otters.

Finally, I want to thank my family who have encouraged me and helped me up when I was down. My parents have put forth a phenomenal effort to make sure I was happy and successful all my life. I am so greatful to all of the time and energy they have devoted to me and they have been my ‘mainstay’ and will contine to be so. I am very lucky to still have my grandmother who is always excited to hear what I have been working on even though she doesn’t know what a neutrino is. A final thank you goes to my husband, Joshua, who continues to support me and makes me believe that anything is possible.

Chapter 1

Introduction

The fundamental information needed to follow this dissertation is presented in this chapter. First, the basic building blocks of the universe are described, as well as the particles of interest for this analysis. A brief history of neutrinos and their interactions follows. In less than a century, three neutrinos have been hypothesized and discovered as well as the oscillation between the types of neutrinos. After the history section, neutrino oscillation is described in general terms. The last section in this chapter is devoted to the Neutral Current Single π^0 (NC1π^0) interaction whose measurement is the goal of this analysis.

1.1 Basic Particles

The current view of the construction of matter, called the Standard Model (SM), holds that the universe is constructed with two types of particles, leptons and quarks, divided into three generations. In addition to these particles, there are also four gauge bosons, which are the means of communication between particles and one scalar boson that is the means of communication between particles and a Higgs field. A brief description of these particles is shown in Figure 1.1. The photon, γ, interacts with charged particles to communicate the electromagnetic forces and therefore does not interact with neutrinos or the Z or Higgs bosons. The gluon, g, is the carrier of the strong force and interacts with quarks. The Z and $W^{\pm}$ bosons are the carriers of the weak force and interact with all other particles. The Z boson does not have a charge and, when used, is referred to as Neutral Current. The charged W boson is used in Charged Current events. The Z and $W^{\pm}$ bosons are the only force carriers that interact with neutrinos. In other words, all neutrino interactions must be weak and are therefore rare. The last, and most recently discovered, boson is the Higgs, which is a scalar boson and provides mass for all massive particles. The word massive must be used because in Standard Model physics, neutrinos are massless. However, from various experiments, neutrinos have been found to have small non-zero masses. This breaks the Standard Model, but makes the universe far more interesting.

The quarks combine to construct the common particles of matter, such as protons and neutrons. The proton is composed of two up quarks and a down quark giving an overall charge of +1 and spin $1/2$. The neutron is composed of one up quark and two down quarks, making a neutral particle with a spin of $1/2$. These three quark particles belong to a family

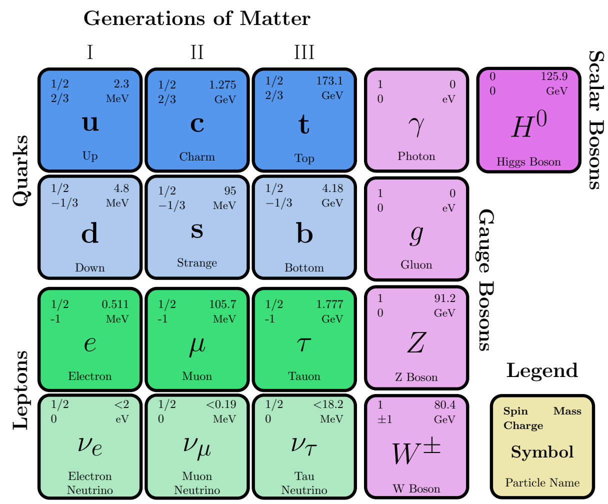

Figure 1.1: The basic particles in the standard model. The descriptions contain the particle name, symbol, mass, spin and charge. The blue boxes describe the quarks, where the green ones describe the leptons. The purple boxes describe the force carriers that are used to communicate between the particles. Values taken from the PDG [1].

called baryons. Another particle of interest for this work is called the π^0 meson, which will commonly be called the π^0. This particle is in the meson family because it is constructed by two quarks. The π^0 has a slightly more complicated construction because it is a superposition of two states. The quark composition is

$$\pi^0 = \frac{u\bar{u} - d\bar{d}}{\sqrt{2}}. \tag{1.1}$$

As the π^0 is a composition of quarks and their antiparticles, it lives for a very short time before annihilation. The mean lifetime is measured to be $(8.52 \pm 0.18) \times 10^{-17}$ seconds [1]. The π^0 decays to two photons $(98.823 \pm 0.034)\%$ of the time [1]. Figure 1.2 shows the lowest order Feynman diagrams of the decay of the π^0 particle. The mass of the π^0 particle has been measured to be 134.9766 ± 0.0006 MeV$/c^2$ [1]. This will be used in the work presented to be a central value of the reconstructed invariant mass peak.

(a) Diagram 1. (b) Diagram 2.

Figure 1.2: Shown are the highest order decays of the π^0 particle. Since the π^0 decays through a chiral anomaly, the decay must be described by a triangle diagram. The black line indicates the original bound state of the π^0 particle. The blue lines represent the quark that annihilates with its antiparticle. The quarks are either up or down quarks. The red lines represent the photons that come out of the decay. Diagram 1 and Diagram 2 are mathematically different, but experimentally indistinguishable. In both diagrams, time propagates to the right.

1.2 A Brief History Of Neutrinos

The creation of the field of particle physics is a relatively recent development. In fact, the idea of a neutrino is less than a century old. Part of the lag behind other areas of physics was the ability to resolve the small scales necessary to investigate the structures of the universe. In 1897, J.J. Thompson discovered the electron [2]. It was the first truly fundamental particle examined in physics. This led to the idea that atoms were not the elemental building blocks in matter, which in turn led to a deeper investigation of the fine structure of the universe.

The discovery of the electron also led scientists to understand more about the β-decay of an atom. A β-decay occurs when a neutron in the nucleus turns into a proton and an electron is emitted. The proton can turn into a neutron and emit a positron as well. Several studies were conducted on the spectrum emitted from an atom during β-decay. The nucleus, before and after the decay, has a specific mass. The mass difference was expected to contribute to the mass of the electron and its kinetic energy, leading to an expected discrete kinetic energy spectrum of the electron. James Chadwick, in 1914, proved beyond any doubt that the spectrum was a continuous function, which violates the conservation of energy and rocked the physics world to its core [2].

It wasn't until 1930 that a possible explanation was put forward. To the "Radioactive Ladies and Gentlemen," Wolfgang Pauli presented "a desperate remedy" to reconcile the continuous β-decay spectrum with the expected discrete distribution. Pauli suggested the existence of "electrically neutral particles … which have spin $1/2$ and obey the exclusion principle." He continued to list some properties of this new particle, eventually named *neutrino* by Enrico Fermi, and summarized that it would account for any of the missing energy in the reaction. Additionally, Pauli expressed regret for theorizing a particle that would be incredibly difficult to detect and it would prove to remain elusive throughout the next several decades [3].

Using the idea of a neutrino and considering the continuous spectrum of the β-decay, Enrico Fermi published his theory of β decay in 1934. Fermi's theory, which includes the concept of neutrinos and particle creation and annihilation, has proven robust over time, see Figure 1.3. He treats the emission of an electron from the nucleus as though it were a photon

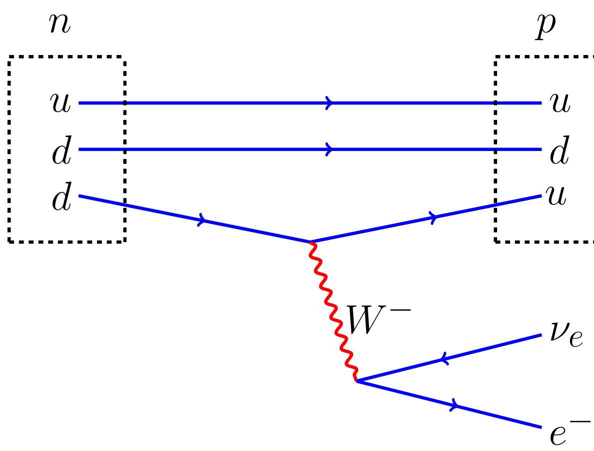

Figure 1.3: This diagram shows a neutron in a nucleus transforming into a proton through β-decay. The nucleus emits a W^- boson, red line, that decays into an electron antineutrino (or a backwards-going electron neutrino) and an electron. The W^- boson was introduced later as a force carrier in this interaction. It was not a part of Fermi's original theory. Time propagates to the right.

escaping the nucleus due to de-excitation. He additionally prepared for the reverse process (electron or positron capture) considering that it "must be associated with the annihilation of an electron and a neutrino." In addition, he made the first prediction of the so-called forbidden β-decays where the decay is highly disfavored due to a vanishing term in the transition operator. Fermi even made the first approximation of a very small neutrino mass, denoted by μ, by predicting the maximum energy of the continuous emission spectrum. He noted that the existence of a massive neutrino would affect the spectrum shape. Given Figure 1.4 he "conclude[d] that the rest mass of the neutrino is either zero, or . . . very small in comparison to the mass of the electron." He compared the contemporary experiments to his theoretical predictions and asserted that the "greatest similarity . . . is given by the theoretical curve for $\mu = 0$" [4].

In 1952, the first indirect evidence of a neutrino was found. George Rodeback and James Allen conducted an electron capture experiment. This experiment studied the transformation of Argon-37 (${}^{18}\mathrm{A}^{37}$) to Chlorine-37 (${}^{17}\mathrm{Cl}^{37}$). This interaction is described as

$$ {}^{18}\mathrm{A}^{37} + e_{\mathrm{K,L}} \rightarrow {}^{17}\mathrm{Cl}^{37} + \nu + Q, \tag{1.2} $$

where $e_{\mathrm{K,L}}$ describes the orbital the electron was taken from,K, and captured to, L, ν is a neutrino and Q is the disintegration energy. The electron is pulled from an orbital shell to combine with a proton, which results in a neutron. An Auger electron is emitted often during this process. An Auger electron is a low energy electron that is ejected from an outer shell when an excited atom returns to the ground state. Essentially, the energy of the de-excitation of the atom is directed to an outer shell electron rather than a photon. This experiment measured the difference in time between the Auger electron and the recoil of the nucleus. They were then able to measure the initial kinetic energy of the atom based on the ejected Auger electron and use the recoil information in order to then look for any

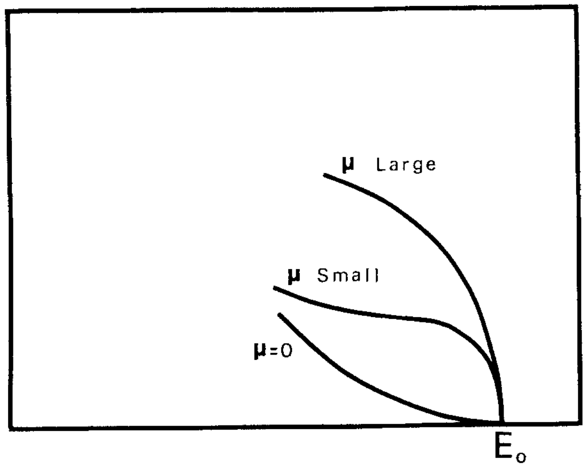

Figure 1.4: The expected shape of the continuous β-decay spectrum predicted by Fermi in 1934. The maximum possible electron kinetic energy is denoted by E_0. Here, the effect of a neutrino mass on the shape is shown for zero, small, and large masses [4].

missing energy that could be attributed to a neutrino. The results were consistent with the hypothesis of single neutrino emission from the nucleus [5].

Finally, a neutrino had been observed. Additional studies were made to try to understand the properties of the neutrino. Was there only one? How many were there? Did an anti-neutrino exist? In 1957, Maurice Goldhaber conducted an experiment to measure the helicity of neutrinos. The experiment used Europium-152m ($^{63}\text{Eu}^{152m}$), a meta-stable element which undergoes β capture with a half life of 9.3 hours. The process relied on the conservation of angular momentum and on the short life time of the excited state of the decay product of $^{63}\text{Eu}^{152m}$. Consider a parent particle, A, with spin zero and a decay product, B, with spin zero that has an excited state, $B^\star$, with a spin of one. The direction of the spin of the neutrino can be deduced from this information by examining the polarization of the outgoing photon. The excited state, $B^\star$, has three possible spin projections $(+1, 0, -1)$ which imply the projection of the spin of the neutrino. The photon carries the spin away from $B^\star$ as it enters its ground state, B. For example, assuming the electron has a spin projection of $+1/2$ and the excited state of the nucleus has a spin projection of $+1$,

$$\begin{aligned} A(J=0) + e^-(J=+1/2) &\to B^\star(J=+1) + \nu_e(J=-1/2) \\ &\to B(J=0) + \gamma(J=+1) + \nu_e(J=-1/2). \end{aligned} \tag{1.3}$$

If the neutrino is assumed to be emitted in the +Z direction and the photon is then emitted in the opposite direction, both the neutrino and photon will have a negative helicity. Likewise, the inverse of Equation 1.3 shows that when the photon has positive helicity, the neutrino will as well. Samarium-152 ($^{62}\text{Sm}^{152}$) is the decay product of $^{63}\text{Eu}^{152m}$ and has a mean half-life of $3 \pm 1 \times 10^{-14}$ seconds. The short lifetime of the excited state of $^{62}\text{Sm}^{152}$ is necessary to prevent the dissipation of the momentum into the recoil of the nucleus. In other words, Goldhaber and his team want to insure that the majority of the momentum leaves with the photon. They discovered that the light emitted from the decay was mostly circularly polarized, giving the light ray an effective negative helicity. Thus, they concluded that the neutrino was left-handed. They also suggested that a similar study could be performed on a nucleus that β-decays to study the helicity of the anti-neutrino [6].

The first direct detection of the neutrino was published in 1959. F. Reines and C. Cowan Jr. spearheaded an experiment at the Savannah River Plant that not only verified the existence of the free antineutrino, $\bar{\nu}$, but also provided an initial measurement of the neutrino cross section. They placed a 1400 liter liquid scintillator detector in a number of places, with a variety of shielding, around the plant. The scintillator was doped with a cadmium compound which captured free neutrons which resulted in a photon signature. They searched for the interaction

$$\bar{\nu} + p^{+} \rightarrow \beta^{+} + n^{0} \tag{1.4}$$

where an antineutrino would interact with a proton, p^{+}, to turn it into a neutron, n^{0}, and release a positron. The antineutrinos were provided by the nearby reactor. The positron annihilates very quickly and the resulting light is captured. After some time, the cadmium doped scintillator absorbs the free neutron and emits light. By studying these delayed coincidences, they measured a cross section of $(11 \pm 2.6) \times 10^{-44} \mathrm{cm}^2/\bar{\nu}$ [7].

At the Brookhaven National Laboratory (BNL) Alternating Gradient Synchrotron (AGS), G. Danby et al. constructed an experiment with two main goals. The first goal was to see if the neutrino in an event with a muon was the same type of neutrino as one with an electron ($\nu_\mu = \nu_e$). The second goal was to calculate the respective cross sections on nucleons to compare with the theoretical calculations of Lee and Yang. At the time of the experiment, physicists had started to accept the idea of different types of neutrinos. The team bombarded a Beryllium target with protons to create charged pions that would then decay to neutrinos and muons. In this neutrino beam, they placed a shielded spark chamber and began to count the created muons and electrons. If the flavor was not conserved, they would expect to see the same number of muons and electrons from the neutrino interactions. However, they found 34 muons and only 6 electrons. They concluded that having at least two flavors was "the most probable explanation" [8].

A third lepton, the tau lepton (τ), was discovered in 1975. Given this discovery, was likely that this new lepton also corresponded to a new neutrino. It took 26 years before the first direct evidence was found in 2000. The DONUT (Direct Observation of NU Tau) experiment looked directly for charged current ν_τ interactions with only one outgoing lepton, a tau lepton. They bombarded a tungsten target with protons to generate their neutrinos from charmed meson decays. They expected $5 \pm 1\%$ of the neutrinos to be ν_τ. The neutrinos were detected with an emulsion target that contained layers of steel and plastic. After a six month exposure, the DONUT group was able to tag four events as ν_τ with a background of 0.34 events. Figure 1.5 shows an event display of one such event typified by the evidence of a kinked track [9].

With each neutrino flavor discovery, an effort was made to calculate how many more flavors existed. At the Large Electron Positron Collider (LEP), several experiments made an effort to unfold the number of flavors of the neutrino. They investigated this question by examining the width of the Z boson resonance, a weak force carrier. The total decay width

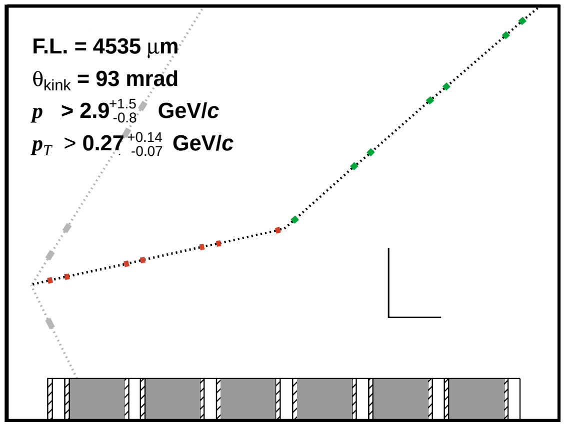

Figure 1.5: The diagram at the bottom shows the construction of the emulsion detector which has layers of steel (shaded), the emulsion sheets (hashed) and plastic (clear). The perpendicular lines provide a position scale of 1.0 by 1.0 mm. The ν_τ is incident from the left hand side. The red line represents the τ particle and the green line is an electron after the τ decay [9].

of the Z is split into multiple pieces. At this point, three leptons had been discovered: the electron (e), the muon (μ), and the tau lepton (τ). Each of those has a contribution to the Z decay width, denoted, for example, by Γ_e for electrons. For this experiment, the leptonic decay widths are assumed to be the same, called Γ_ℓ. However, there is a known difference due to the large mass of the tau lepton (a -0.23% difference, δ_τ). Additionally, there is a hadronic contribution that is denoted Γ_{had} which is the sum of the quark contributions. Finally there is an invisible width that is from the decays to neutrinos and therefore is not seen. This can be defined as the sum over all neutrino flavor width contributions, $\Gamma_{\text{inv}} = N_\nu \Gamma_\nu$, where N_ν is the number of neutrino flavors. In summary,

$$\Gamma_Z \approx 3\Gamma_\ell + \Gamma_{\text{had}} + \Gamma_{\text{inv}}. \tag{1.5}$$

Furthermore, they determined that the "hadronic pole cross-section" can be defined as

$$\sigma^0_{\text{had}} = \frac{12\pi}{m_Z^2} \frac{\Gamma_e \Gamma_{\text{had}}}{\Gamma_Z^2}. \tag{1.6}$$

Using this information, the LEP experiments were able to consider the ratio of the invisible width to the leptonic width, expressed as

$$R^0_{\text{inv}} = \frac{\Gamma_{\text{inv}}}{\Gamma_\ell} = N_\nu \left(\frac{\Gamma_{\text{inv}}}{\Gamma_\ell}\right)_{\text{SM}} = \left(\frac{12\pi R^0_\ell}{\sigma^0_{\text{had}} m_Z^2}\right)^{1/2} - R^0_\ell - (3 + \delta_\tau) \tag{1.7}$$

where $R^0_\ell = \Gamma_{\text{had}}/\Gamma_\ell$ and $(\Gamma_{\text{inv}}/\Gamma_\ell)_{\text{SM}}$ refers to the standard model prediction. The LEP groups then measured the absolute hadronic cross section around the mass of the Z boson, seen in Figure 1.6. They found $N_\nu = 2.9840 \pm 0.0082$ to be the fitted number of neutrinos.

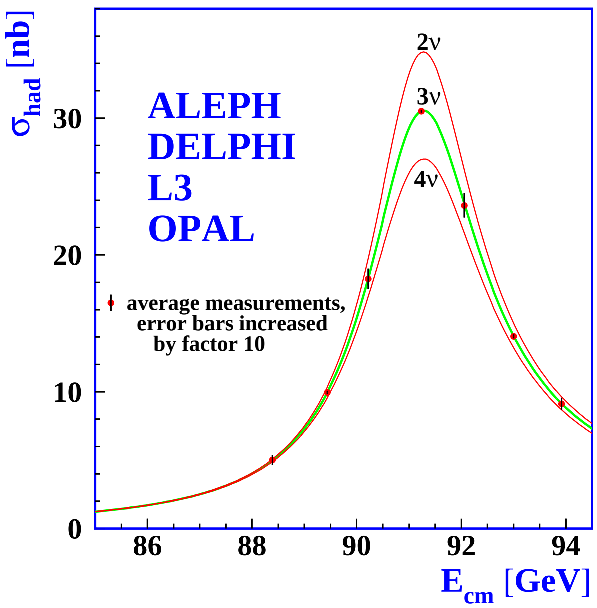

Figure 1.6: The y-axis is the measured hadronic cross section in nanobarns. The x-axis is the energy of the center of mass around the Z boson mass, 91.2 GeV. The red and green curves represent the theoretical prediction for integer number of neutrino flavors. The data points are the combined measurement from the four LEP detectors [10].

This coincides well with the idea of three generations of matter and the knowledge that three charged leptons had been discovered [10].

Around the same time as the Cowen-Reines experiment, Ray Davis began an experiment at BNL to see if there was a difference between neutrinos and antineutrinos in their interactions with a nucleus. Using a large tank of carbon tetrachloride, he attempted to use anti-neutrinos in an interaction that was known for neutrinos. Specifically, he compared the neutrino induces β-decay of Chlorine to Argon,

$$\mathrm{Cl}^{37} + \nu \rightarrow \mathrm{Ar}^{37} + e^- \tag{1.8}$$

versus

$$\mathrm{Cl}^{37} + \bar{\nu} \rightarrow \mathrm{Ar}^{37} + e^-. \tag{1.9}$$

This experiment placed detectors in a variety of locations. Davis was able to set upper limits on this interactions and on the solar neutrino flux. However, this experiment's lasting effect seems to be reflected as a proof of concept for the future ground breaking experiment at the Homestake mine [11].

Nearly a decade after the original experiment, Davis constructed a few small 500 liter tanks to test the ability to measure the solar neutrino flux. He planned to use the inverse β-decay reaction shown in Equation 1.8. He filled the tanks with a cleaning solution containing Cl^{37}. Then after a period of time elapsed, he purged and counted the Ar^{37} created. For this initial measurement Davis worked in conjunction with John Bahcall to study the internal structure of the sun. From the rate of events observed by Davis, Bahcall concluded that the "central temperature of the sun is less than 20 million degrees." Bahcall points out that this measurement is the only way to glimpse the sun's interior mechanisms since photon cross sections are so large and their mean free path is "less than 10^{-10} of the radius of the star" and are therefore inaccessible [12][13].

An upgrade to the experiment yielded very curious results. In 1968, Davis and Bahcall published the first of a series of papers attempting to rectify the discrepancies between theory and experiment. Davis's experimental setup included a 390,000 liter tank placed into the Homestake mine. His new setup was 400 times the size of the previous one and was placed underground to reduce the cosmic ray background. Davis found a neutrino capture rate of $\sum \phi\sigma \leq 0.3 \times 10^{-35} {}^{s^{-1}}/_{\mathrm{Cl}^{37}}$ compared to the predicted background of $(2.0 \pm 1.2) \times 10^{-35} {}^{s^{-1}}/_{\mathrm{Cl}^{37}}$ [14][15]. There was an immediate flurry of papers discussing solar models to try to understand this discrepancy. This problem wasn't solved until much later with the suggestion of neutrino oscillation.

There were many theories created to explain the solar neutrino problem, but other evidence continued to disprove these theories. In February 1987, there was a supernova that was detected by both the Kamiokande II and the IMB (Irvine-Michigan-Brookhaven) water Cherenkov experiments as an increase in the number of neutrino interactions. In fact, Kamiokande II recorded the neutrino event burst approximately 18 hours before the "first optical sighting." One of the first important claims based on the supernova data was that the lifetimes of ν_e and $\bar{\nu}_e$ were too long to use "neutrino decay as an explanation of the solar-neutrino puzzle" [16]. Again, several theories had to return to the drawing board.

Then, in 1998, Super-Kamiokande, SK, released results of a curious observation which revolutionized neutrino physics. SK made a study of the number of neutrinos coming from the atmosphere. These neutrinos are naturally occurring from cosmic rays scattering in the upper atmosphere. Since neutrinos easily travel through matter, one would expect the same ν_μ to ν_e ratio from any direction. The SK collaboration examined neutrinos that travelled 15 km (downward) and those that travelled 13,000 km (upward) through the charged current interactions in the detector. These interactions are typically expressed as

$$\nu + N \rightarrow \ell + X \tag{1.10}$$

where N is the initial nucleus and X is the final state nucleus. They found that in the whole detector the ratio of data to Monte Carlo (MC) is

$$R = \frac{({}^{\nu_\mu}/_{\nu_e})_{\text{data}}}{({}^{\nu_\mu}/_{\nu_e})_{\text{MC}}} = \begin{cases} 0.63 \pm 0.03(\text{stat}) \pm 0.05(\text{sys}), \text{if } E_\nu \text{ is sub-GeV} \\ 0.65 \pm 0.05(\text{stat}) \pm 0.08(\text{sys}), \text{if } E_\nu \text{ is multi-GeV} \end{cases} . \tag{1.11}$$

Somehow, muon neutrinos were being lost. They also studied the asymmetry between the upward going events (U) and the downward going events (D), defined as

$$A = \frac{U - D}{U + D}, \tag{1.12}$$

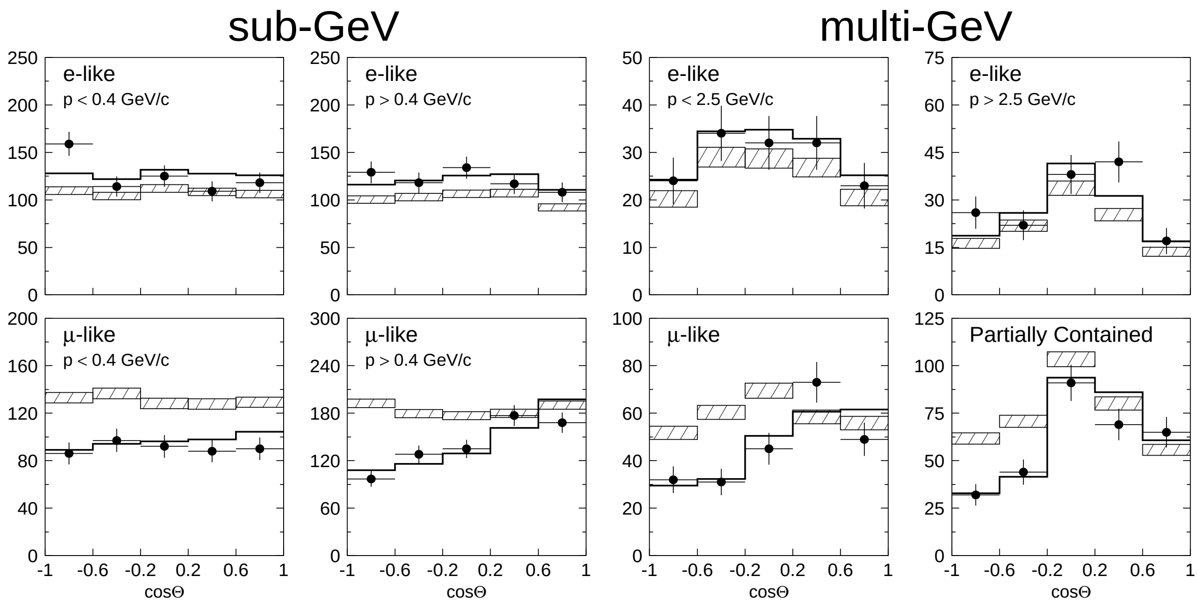

Figure 1.7: This series of plots show the interaction rate dependence on the angle and energy. The top row describes the e-like sample while the bottom row describes the μ-like sample. The x-axis is the zenith angle with $\cos\theta = 1$ coming from above and $\cos\theta = -1$ coming from below. The y-axis is the rate of events. The hashed box is the non-oscillation prediction of the rate and the line is the prediction given a best fit for ν_μ to ν_τ oscillations [17].

and found that although the ν_e flux was roughly constant, there were serious discrepancies in the ν_μ flux, see Figure 1.7. It should be noted that SK cannot resolve the interaction

$$\nu_\tau + N \to \tau + X \tag{1.13}$$

because the lifetime of the tau lepton is very short and the decay products can be easily confused with other signal. So the conclusion was that these muon neutrinos may have oscillated to ν_τ or a hypothesized sterile neutrino ν_X. Since the ν_e flux is unchanged, they concluded that the oscillation between ν_μ and ν_e is disfavored. The two flavor oscillation model, described in Section 1.3, was applied to fit the ν_μ spectrum of the length over the neutrino energy L/E_ν, to make the first measurement of the atmospheric oscillation parameters, shown in Figure 1.8. Since this deficit is many sigma off of the null oscillation hypothesis, this is evidence of neutrino oscillation [17]. Additionally, the shape of the deficit can be used to calculate a mathematical description of the oscillation, explained further in Section 1.3.

In the early 2000s that the Sudbury Neutrino Observatory (SNO) definitively proved that solar neutrinos oscillate. The detector consists of a giant tank of heavy water which allows it to study much lower energy interactions, specifically neutral current (NC) and elastic scattering (ES). Heavy water typically has targets of deuterium, d, rather than a proton or a neutron. SNO examined three interactions modes:

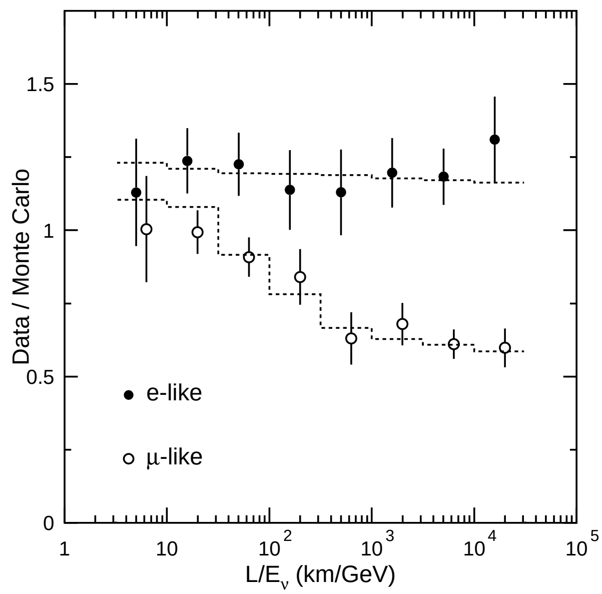

Figure 1.8: The x-axis is the length over neutrino energy metric. The y-axis is the ratio of the measured rate of events to the predicted non-oscillated rate. The filled circles represent the events that are considered to be from ν_e interactions and the empty circles represent the ν_μ interactions. The dashed lines represent a set of suggested oscillation parameters considering a two flavor oscillation between ν_μ and ν_e [17].

$$\begin{aligned} \text{CC: } & \nu_e + d \rightarrow p + p + e^-, \\ \text{NC: } & \nu_\ell + d \rightarrow p + n + \nu_\ell, \\ \text{and ES: } & \nu_\ell + e^- \rightarrow \nu_\ell + e^-. \end{aligned} \tag{1.14}$$

The CC interaction is only sensitive to ν_e, similar to the experiments performed by Davis. The SNO experiment found a ν_e flux of

$$\phi_{\mathrm{CC}\nu_e} = 1.76^{+0.06}_{-0.05}(\mathrm{stat}) \pm 0.09(\mathrm{sys}) \times 10^6 \mathrm{cm}^{-2}\mathrm{s}^{-1}. \tag{1.15}$$

The elastic scattering mode is less sensitive to ν_μ and ν_τ since is is a scatter of an electron. The measured flux is

$$\phi_{\mathrm{ES}} = 2.39^{+0.24}_{-0.23}(\mathrm{stat}) \pm 0.12(\mathrm{sys}) \times 10^6 \mathrm{cm}^{-2}\mathrm{s}^{-1}. \tag{1.16}$$

The NC mode is equally sensitive to all three neutrino types with an overall measured flux of

$$\phi_{\mathrm{NC}} = 5.09^{+0.44}_{-0.43}(\mathrm{stat})^{+0.46}_{-0.43}(\mathrm{sys}) \times 10^6 \mathrm{cm}^{-2}\mathrm{s}^{-1}. \tag{1.17}$$

Finally the solar neutrino problem was resolved. The different flux calculations (ϕ_{NC}, $\phi_{\mathrm{CC}\nu_e}$, and ϕ_{ES}) should be the same if the solar neutrinos don't oscillate. In fact the standard solar model predicts a flux of $\phi_{\mathrm{SSM}} = 5.05^{+1.01}_{-0.81} \times 10^6 \mathrm{cm}^{-2}\mathrm{s}^{-1}$ which agrees quite well with ϕ_{NC}. The results from SNO were also important to unfold the parameters that describe solar neutrino oscillation. SNO split the measured solar flux into an electron flavor part and a muon/tauon flavor part, measured to be

$$\begin{aligned} \phi_e &= 1.76 \pm 0.05(\mathrm{stat}) \pm 0.09(\mathrm{sys}) \\ \phi_{\mu\tau} &= 3.41 \pm 0.45(\mathrm{stat})^{+0.48}_{-0.45}(\mathrm{sys}). \end{aligned} \tag{1.18}$$

This measurement is shown as a global fit of the three interaction rates in Figure 1.9. These results indicated a second mass splitting, one that is at least an order of magnitude smaller than that found for atmospheric neutrinos, indicating an additional layer of complexity to the structure of the neutrinos [18][19].

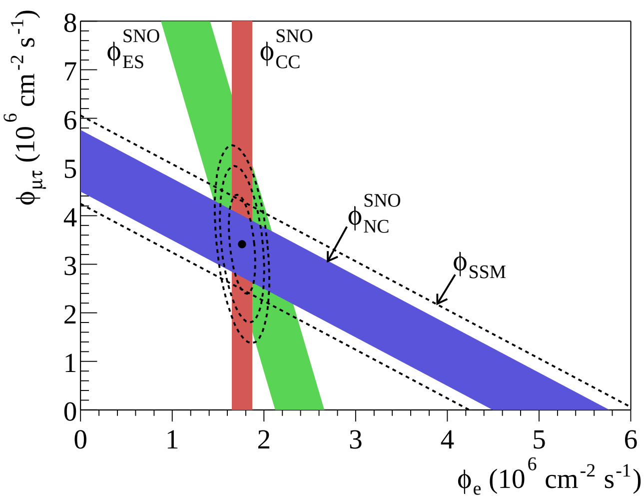

Figure 1.9: This figure displays how the three measurements (ES, CC, and NC) can be used to calculate the ν_e flux and the ν_μ and ν_τ combined flux. The x-axis represents the ν_e flux and the y-axis shows the ν_μ and ν_τ combined flux. The dashed lines show the flux prediction of the standard solar model. The dashed ellipses represent the errors on the global fit (black dot) of the three measurements [19].

1.3 Neutrino Oscillation

The oscillation between the flavors of e, μ and τ type neutrinos leads to a small neutrino mass because the mass eigenstates are superpositions of the flavor eigenstates, in other words, not one-to-one. As a neutrino travels, it falls into a mass state. The neutrino can only be observed by looking at the weak interactions that are associated with a flavor state. The mass eigenstate of a neutrino that is traveling through a vacuum can be represented by a standing wave,

$$|\nu_i(t)\rangle = e^{-i(E_i t - \vec{p_i}\cdot\vec{x})}\,|\nu_i(0)\rangle\,, \tag{1.19}$$

where E_i, $\vec{p_i}$, and m_i refer to the energy, momentum and mass of the ith type of neutrino and $\vec{x}$ refers to the length traveled and t refers to the time elapsed. The i types of neutrino refer to the mass eigenstates, of which there are assumed to be three (ν_1, ν_2, and ν_3), although theories exist that predict far more. Any possible additional mass eigenstates are discounted for this explanation because their theorized cross sections are considered to be negligibly small. The relationship between the energy, momentum and mass of any particle is

$$E_i = \sqrt{p_i^2 + m_i^2} = p_i\sqrt{1 + \frac{m_i^2}{p_i^2}}. \tag{1.20}$$

Using a Maclaurin series, this relationship can be rearranged. Since $p_i^2 >> m_i^2$, the series is truncated to first order,

$$E_i \approx p_i(1 + \frac{1}{2}\frac{m_i^2}{p_i^2}) = p_i + \frac{m_i^2}{2p_i} \tag{1.21}$$

The momentum, p_i, can be set to the total energy E since the mass of the neutrino is negligibly small. This gives

$$E_i \approx E + \frac{m_i^2}{2E}. \tag{1.22}$$

Returning to Equation 1.19, E_i can be replaced with Equation 1.22 and p_i with E. In addition, x refers to the oscillation length, or the baseline, L. The neutrino is assumed to be traveling at approximately the speed of light, so $t = L/c$ or $t = L$ in natural units. The neutrino wave equation can be rewritten as

$$\begin{aligned} |\nu_i(t)\rangle &= e^{-i(E_i t - \vec{p_i}\cdot\vec{x})}\,|\nu_i(0)\rangle \\ &= e^{-i((E+\frac{m_i^2}{2E})L - EL)}\,|\nu_i(0)\rangle \\ &= e^{-i\frac{m_i^2 L}{2E}}\,|\nu_i(0)\rangle\,. \end{aligned} \tag{1.23}$$

The relationship between the flavor eigenstates, α, and the mass eigenstates, i, are described by a unitary matrix, U,

$$\begin{aligned} |\nu_\alpha\rangle &= \sum_i U^\star_{\alpha i}\,|\nu_i\rangle \\ &\text{and} \\ |\nu_i\rangle &= \sum_\alpha U_{\alpha i}\,|\nu_\alpha\rangle\,, \end{aligned} \tag{1.24}$$

where $U^\star_{\alpha i}$ is the α element of the ith column of the Hermitian conjugate, $U^\dagger$, of U. A matrix is unitary when $UU^\dagger = U^\dagger U = \mathbf{1}$, the identity matrix. The Hermitian conjugate is the complex conjugate transpose of a matrix. Convention dictates that U describes the transformation of the flavor states into the mass states in order to make incorporating the neutrino masses into the Yukawa coupling easier. Switching the convention has no effect on the final probabilities of oscillation. The probability (P) of oscillating from one flavor, α, to another, β, over a given distance, L, or time, t, is calculated by

$$P_{\alpha\to\beta} = |\,\langle\nu_\beta\,|\,\nu_\alpha(t)\rangle\,|^2. \tag{1.25}$$

The probability in Equation 1.25 can be rewritten using bra and ket operator identities and the wave equation in Equation 1.19 to be

$$P_{\alpha\to\beta} = |\sum_i U^\star_{\alpha i} U_{\beta i} e^{-i\frac{m_i^2 L}{2E}}\,|^2. \tag{1.26}$$

This probability equation holds for any number of flavor states and mass eigenstates. Given the properties of complex numbers, the probability can be cast into a general form depending on the real and imaginary parts of the elements of the U. Setting $\Delta m_{ij}^2 = m_i^2 - m_j^2$, the general form of the probability is

$$\begin{aligned} P_{\alpha\to\beta} = \delta_{\alpha\beta} - 4\sum_{i}^{n-1}\sum_{j=i+1}^{n} Re(U_{\alpha i}^{\star}U_{\beta i}U_{\alpha j}U_{\beta j}^{\star})\sin^2\frac{\Delta m_{ij}^2 L}{4E} \\ +2\sum_{i}^{n-1}\sum_{j=i+1}^{n} Im(U_{\alpha i}^{\star}U_{\beta i}U_{\alpha j}U_{\beta j}^{\star})\sin\frac{\Delta m_{ij}^2 L}{2E} \end{aligned} \tag{1.27}$$

Given a two neutrino oscillation mixing case, let the mixing be defined in the unitary matrix U where the flavor states ν_α and ν_β are related to the mass eigenstates ν_1 and ν_2. One choice for this unitary matrix is to use a mixing angle, θ,

$$U = \begin{bmatrix} \cos\theta & \sin\theta \\ -\sin\theta & \cos\theta \end{bmatrix}. \tag{1.28}$$

Assume two neutrino flavors (α and β) and two neutrino masses (1 and 2). The probability of oscillation from the α flavor to the β flavor is

$$P_{\alpha\to\beta} = \sin^2(2\theta)\sin^2(\frac{\Delta m_{12}^2 L}{4E}). \tag{1.29}$$

It is possible for a neutrino to remain the same flavor or oscillate back to the original flavor. This is essentially the inverse probability of Equation 1.29 that can be written as

$$P_{\alpha\to\alpha} = 1 - \sin^2(2\theta)\sin^2(\frac{\Delta m_{12}^2 L}{4E}) \tag{1.30}$$

Although this two flavor model appeared to work for a few years, there are two distinct mass splittings, one from SK in 1998 and one from SNO in 2002 [17][19]. This meant that the neutrino oscillation should be a three flavor model, which adds another layer of complexity. The two flavor model mixing matrix is relatively easy to understand, but the three flavor mixing matrix requires a bit more unfolding. The three flavor mixing matrix depends on four (or maybe six) angles. The first three are the mixing angles between the mass states, θ_{12}, θ_{13}, and θ_{23}. There is a Charge Parity (CP) violating phase as well, called δ_{CP}. The mixing matrix becomes

$$U = \begin{bmatrix} c_{12}c_{13} & s_{12}c_{13} & s_{13}e^{-i\delta} \\ -s_{12}c_{23} - c_{12}s_{23}s_{13}e^{i\delta} & c_{12}c_{23} - s_{12}s_{23}s_{13}e^{i\delta} & s_{23}c_{13} \\ s_{12}s_{23} - c_{12}c_{23}s_{13}e^{i\delta} & -c_{12}s_{23} - s_{12}c_{23}s_{13}e^{i\delta} & c_{23}c_{13} \end{bmatrix}, \tag{1.31}$$

where $c_{ij} = \cos\theta_{ij}$ and $s_{ij} = \sin\theta_{ij}$ [1]. The last two angles of interest are called the Majorana angles and only contribute if neutrinos are Majorana particles. A Majorana particle is a particle that is also its own antiparticle. At this point, it is unknown if the neutrino is Majorana. However, if the neutrino is Majorana, for three mass eigenstates, two additional CP violating phases, α_{21} and α_{31}, are added to Equation 1.31. If there exist more than three

Table 1.1: The current measurements of the mixing angles and mass splittings used in the three flavor mixing matrix. The left column expresses the name of the value calculated, the right lists the value. There are three mixing angles and two mass splittings [1].

$\sin^2 2\theta_{12}$	0.857 ± 0.024
Δm^2_{21}	$(7.50 \pm 0.20) \times 10^{-5}\text{eV}^2$
$\sin^2 2\theta_{23}$	> 0.95
Δm^2_{32}	$0.00232^{+0.00012}_{-0.00008}\text{eV}^2$
$\sin^2 2\theta_{13}$	0.095 ± 0.010

mass eigenstates, say n, there will be $n-1$ Majorana phases. Specifically, U is multiplied by an additional matrix

$$\begin{bmatrix} 1 & 0 & 0 \\ 0 & e^{i\frac{\alpha_{21}}{2}} & 0 \\ 0 & 0 & e^{i\frac{\alpha_{31}}{2}} \end{bmatrix}. \tag{1.32}$$

However, this becomes a simple phase shift and does not effect the probability of oscillation calculation.

The physics community has contributed a significant amount of resources and effort into measuring the components of the three flavor mixing matrix. Table 1.1 lists the current estimates of the important values, although some pieces are still missing. The CP Violating phase, δ_{CP} is not listed on the table. Until recently, it was unknown if the parameter could even be measured. However, given the large non-zero value for θ_{13}, it is possible that a precision measurement can and will be made in the next ten years. The sign of Δm^2_{32} is unknown. The mass eigenstate, ν_3, is either the largest or smallest neutrino mass. If ν_3 is the heaviest, the neutrino eigenstates are in what is called the normal hierarchy. If instead ν_3 is the lightest, the eigenstates are in an inverted hierarchy. Lastly, the octant for θ_{23} is not known. Most of the time, maximal mixing is assumed, $\theta_{23} = 45°$, but it is probable that the true value is either greater or less than 45°.

Of interest is the oscillation from a ν_μ to a ν_e because it provides a window into both θ_{13} and δ_{CP}. The formula, truncated to leading order, for the probability of the oscillation is

$$\begin{aligned} P(\nu_\mu \to \nu_e) \sim & \sin^2\theta_{23}\sin^2 2\theta_{13}\sin^2\frac{\Delta m^2_{31}L}{4E} \\ & - \frac{\sin 2\theta_{12}\sin 2\theta_{23}}{2\sin\theta_{13}}\sin\frac{\Delta m^2_{21}L}{4E}\sin^2 2\theta_{13}\sin^2\frac{\Delta m^2_{31}L}{4E}\sin\delta_{\text{CP}} \\ & + (\text{CP even term, matter effect term, solar term})[20]. \end{aligned} \tag{1.33}$$

The matter effect refers to a term that is a perturbation on the neutrino oscillation, which was modeled as being in a vacuum. The solar term is a term that has a primary dependence on θ_{12}. As is shown in Equation 1.33, the ability to measure δ_{CP} relies on having a non-zero θ_{13}. Precision measurements have been done at reactor experiments that study the disappearance of electron antineutrinos. The probability for electron antineutrino survival is

$$P(\bar{\nu}_e \rightarrow \bar{\nu}_e) \sim 1 - \sin^2 2\theta_{13} \sin^2 \frac{\Delta m^2_{31} L}{4E_\nu} - \cos^4 \theta_{13} \sin^2 2\theta_{12} \sin^2 \frac{\Delta m^2_{21} L}{4E_\nu} [21]. \quad (1.34)$$

These reactor measurements do not depend on δ_{CP} and the values of θ_{13} can be used from these experiments to constrain the possible values of δ_{CP}.

1.4 The Neutral Current Single π^0 Interaction

The T2K Experiment, explained in further chapters, seeks to make a ν_e appearance measurement from a ν_μ beam. The second largest background of the charged current quasi-elastic (CCQE) interactions that are used to measure the appearance is due to neutral current events, specifically the neutral current single π^0 (NC1π^0) interaction. The most recently published result shows that 1.0 events out of the predicted 4.3 background events are from neutral current processes. One of the biggest problems with the NC1π^0 background is that the cross section, and its associated errors, are not well known. There has been one previous on-water measurement done by the K2K Collaboration. K2K, the predecessor of T2K, was a long baseline experiment that ran from KEK, a research lab in Tsukuba, Japan, to SK. They presented the ratio of the NC1π^0 cross section to the charged current ν_μ cross section which is

$$\frac{\sigma_{\mathrm{NC}1\pi^0}}{\sigma_{CC\nu_\mu}} = 0.064 \pm 0.001(\mathrm{stat}) \pm 0.007(\mathrm{sys}). \quad (1.35)$$

This measurement was done in a wide band neutrino beam, so the incoming neutrinos had a wide range of energies. The model used to make the Monte Carlo predicted this ratio at 0.065, showing excellent agreement. This work presents a rate measurement in a narrow-peaked off-axis neutrino energy beam, which will be explained further in later chapters. Additionally, the K2K measurement utilized a higher energy (1 - 1.5 GeV) neutrino spectrum than that used for this measurement [22].

In experimentation, it is very difficult to separate the different modes of NC1π^0 interactions. Only the final state particles are measured. The requirements placed on the analysis are: no outgoing leptons, one π^0 particle, no other mesons, and any number of baryons (specifically if the nucleon has some recoil). These requirements all refer to particles exiting the entire nucleus, not just the initial interaction since it is possible to have a cascade of interactions inside the nucleus before the output particles can be seen by a detector. As such, the measurement is a combination of several interaction modes. One such mode is delta resonance, shown in Figure 1.10. In this interaction, a neutrino interacts with a nucleon through a Z boson. The nucleon is then in an excited state, called either Δ^+ or Δ^0 depending on if the nucleon is a proton or a neutron. However, examining the final state interaction (FSI) also allows for coherent π^0 creation and other nuclear effects.

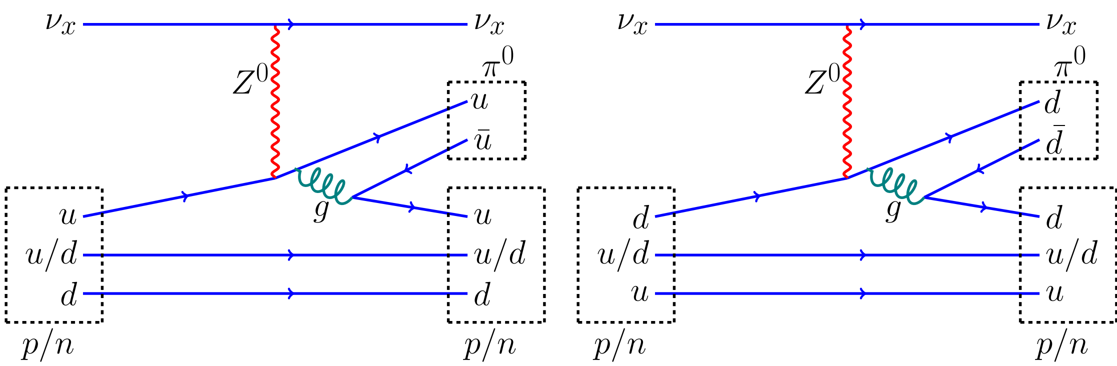

(a) Diagram 1. (b) Diagram 2.

Figure 1.10: NC1π^0 production through a delta resonance. A neutrino of any flavor interacts with a nucleon through a Z boson. The excited nucleus then radiates energy in the form of a gluon which creates a quark-antiquark pair. Diagram 1 shows the result of an $u\bar{u}$ quark pair created by the gluon. Diagram 2 displays a $d\bar{d}$ quark pair.

Chapter 2

T2K

T2K is a long-baseline neutrino experiment. A ν_μ beam is created at the Japan Proton Accelerator Research Complex (J-PARC) and is directed 2.5° off-axis towards the far detector, Super-Kamiokande (SK). Additionally, there are two near detectors, an on-axis detector, the interactive neutrino GRID (INGRID), and an off-axis detector (ND280) that are used to constrain the beam flux and make cross section measurements to constrain the errors on measurements made at SK.

T2K has several physics goals, ranging from understanding neutrino oscillations to measuring neutrino interactions on various targets. The two main oscillation analyses are the electron neutrino appearance and muon neutrino disappearance. Electron neutrino appearance at SK allows a measurement of the mixing angle θ_{13} and the CP violating phase factor, δ_{CP}, see Equation 1.33. The muon neutrino disappearance looks towards a precision measurement of θ_{23}. In order to better understand both measurements, several cross section measurements were undertaken to further ascertain the effect of the backgrounds. The NC1π^0 interaction rate measurement is one such cross section.

2.1 Description of Beam Line

The J-PARC beam line was constructed between 2004 and 2009. As a relatively new facility, it has been constantly upgraded every year to improve the proton beam power. Figure 2.1 shows the design of the J-PARC laboratory. A linear accelerator (LINAC) accelerates hydrogen atoms up to 400 MeV. The electrons are stripped from the atoms and the remaining protons are first injected into a rapid cycling synchrotron (RCS). There the protons are accelerated up to 3 GeV and finally injected into the 30 GeV Main Ring (MR). After accelerating, the protons are directed towards a graphite target in a fast extraction. These protons are monitored by an optical transition radiation (OTR) monitor. There are eight successive beam bunches filled that make up a 5μs spill.

The proton bunches are directed onto a graphite target that is 91.4 cm long (or 1.9 interaction lengths). When the protons hit the graphite hadronic showers occur. The majority of these showers result in pions, π^+, and Kaons, K^+. The π^+ decay to create muon neutrinos $98.98770 \pm 0.00004\%$ of the time [1]. There is a small ν_e contamination that comes from the decay of the resulting muons and from a subdominant Kaon decay. In the end, 93.6% of the

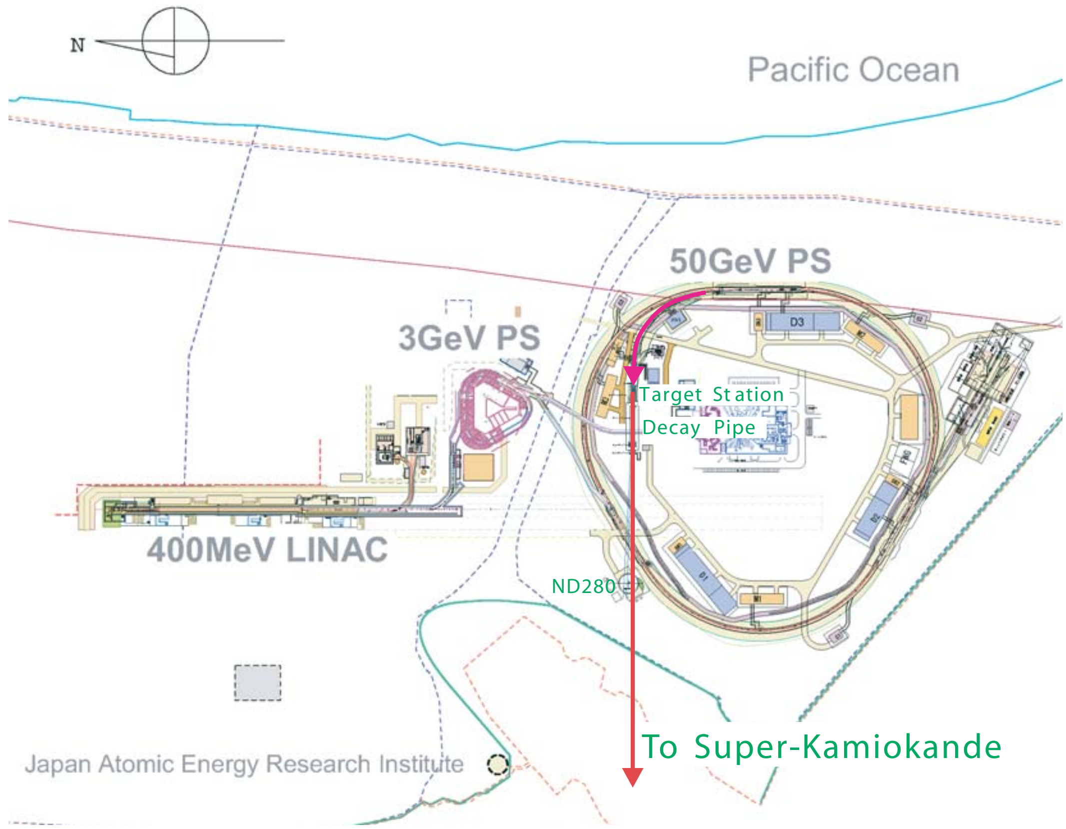

Figure 2.1: A schematic diagram of the J-PARC accelerator complex. This figure details the original design energies from the proposal of the experiment [23].

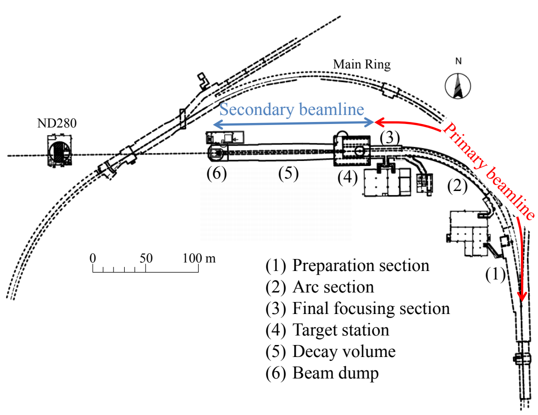

(a) Top view.

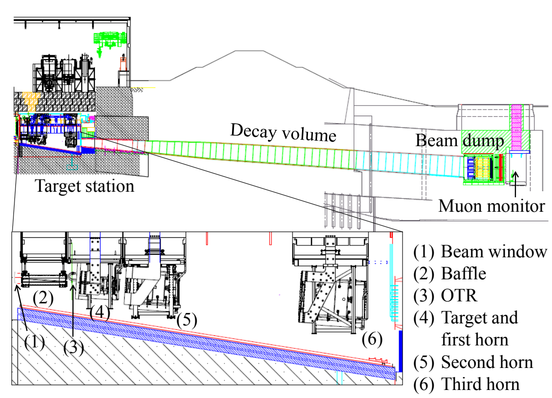

(b) Side view.

Figure 2.2: Schematic diagrams of the top and side views of the beam extraction and target station [24].

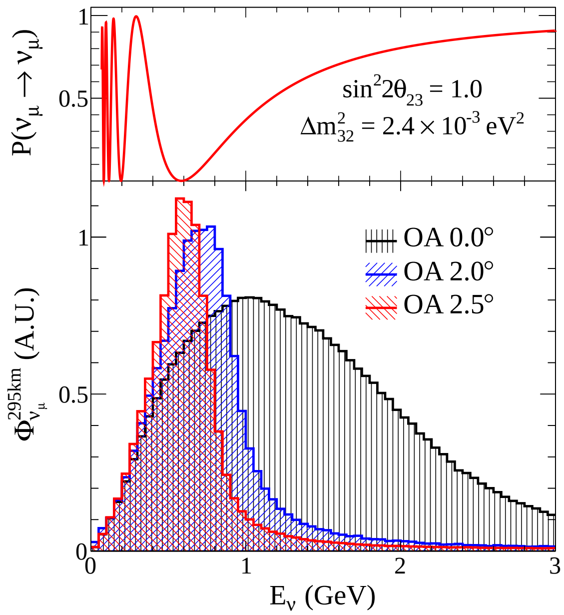

Figure 2.3: The affect of an off-axis angle on the shape of the neutrino flux. The top plot shows the muon neutrino survival probability expected at SK (L = 295km). The bottom plot y-axis is in arbitrary units of flux. The amplitude of the flux shape is not to scale [24].

neutrino flux comes from muon neutrinos, 5.4% from the muon antineutrinos and less than one percent from the electron neutrinos and antineutrinos [24].

The first of three neutrino horns surrounds the graphite target. These horns use a toroidal magnetic field to focus the outgoing charged particles and therefore reveal their decay neutrinos. They operate at 250 kA which creates a 1.7 T field. The horns also have the ability to run at a reversed polarity which will instead focus negatively charge particles and as a result focus an intense antineutrino beam. After the third neutrino horn, there is a large decay volume that allows the pions and kaons to decay into lighter products and neutrinos. At the end of the volume there is a beam dump designed to stop the heavier particles. A muon monitor (MUMON) is also placed at the end of the beam dump to monitor the overall flux and position of the beam. The MUMON found that the beam remained stable in the X and Y coordinates within 1 mrad (design stability) [24].

The beam is designed to be 2.5° off-axis at the near detector ND280 and at the far detector, SK. In Figure 2.3, the muon neutrino disappearance probability is seen at a minimum (with the default assumptions of $\sin^2 2\theta_{23} = 1.0$, $L = 295$ km and $\Delta m^2_{32} = 2.4 \times 10^{-3}$ eV^2) near a neutrino energy of 600 MeV. The off-axis angle was chosen to be 2.5° because the neutrino flux is sharply peaked near 600 MeV. There is a balancing act between gaining a sharper peak and losing flux the larger the off-axis angle is. The amplitudes of the flux is arbitrary in the figure, in fact the amplitude decreases quite dramatically as the beam moves away.

The π^+, the most common result of the protons interacting with the graphite target, decays into a muon and a muon neutrino. The four momenta, $p_\pi = p_\mu + p_\nu$, can be rearranged to

$$E_\nu = \frac{m_\pi^2 - m_\mu^2}{2(E_\pi - |\vec{p_\pi}|\cos\theta_\nu)}, \tag{2.1}$$

where θ_ν is the angle between the incoming π^+ and the outgoing ν_μ. If the angle, θ_ν was zero, then there would be no upper bound on E_ν and one would end up with a very wide band neutrino beam. The beam would only be limited by the energies of the pions produced. If, however, an off-axis angle was introduced, then there would be an inflection point in the equation. The maximum possible neutrino energy would depend on the minimum of $E_\pi - |\vec{p_\pi}|\cos\theta_\nu$. This leads to

$$E_\nu^{\mathrm{max}} = \frac{m_\pi^2 - m_\mu^2}{2E_\pi^{\mathrm{m}}\sin^2\theta_\nu}, \tag{2.2}$$

where E_π^{m} refers to the inflection point. When the pion energy is above the inflection point, the function slowly changes, allowing for a wide range of pion energies creating a very small range of neutrino energy. By building a detector off-axis of a neutrino beam, it can receive a narrow beam of energy which reduces the uncertainties of the energy of the incoming neutrinos.

2.2 Overview of ND280 Detectors

There are two detectors in the near detector hall that was constructed 280 m from the graphite target. The first detector is an on-axis detector called INGRID (Interactive Neutrino GRID). The primary purpose of this detector is to monitor the beam stability and flux. The second detector is an off-axis detector that is installed inside the UA1 magnet (from the UA1 experiment at CERN). The primary purpose of this detector is to monitor the off-axis flux and to measure cross sections in the ν_μ beam that will be used to constrain the analysis results at SK. Figure 2.4 shows both near detectors in situ, with the UA1 magnet open. The beam is directed toward the central modules of INGRID on the lower levels.

2.2.1 INGRID

INGRID is designed to monitor the beam center within 0.4 mrad. Figure 2.5 shows the detector from the view of an incoming neutrino. The x and y position of the beam is measured to within 10 cm. Additionally there are two detectors that are not positioned into the cross that are used to measure the axial symmetry of the beam. Figure 2.6 shows an exploded view of the typical INGRID module. Layers of scintillator bars are sandwiched between a high-Z material, iron. To give an idea of the size of the individual modules, the iron plates measure 124 cm by 124 cm. The high-Z material provides a very dense target for the neutrinos and increases the rate of observed events. The scintillator bars contain wave length shifting (WLS) fibers that collect the light that occurs from a particle passing through the detector and directs towards a Hamamatsu Multi-Pixel Photon Counter (MPPC). Lastly, there is a proton module that resides between the vertical and horizontal modules at the

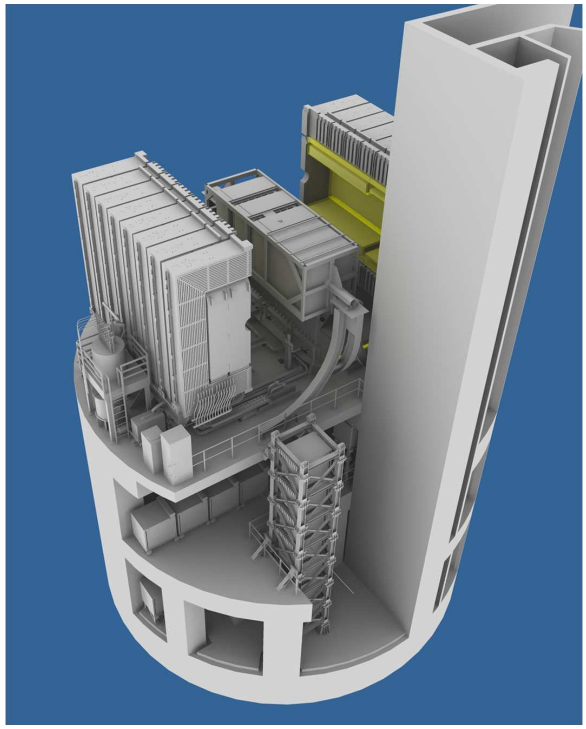

Figure 2.4: A diagram of the near detector hall with the outer walls removed. The whole set of detectors resides just beneath the surface of the earth. The top level depicts the ND280 off-axis detector with the UA1 magnet in the open position. The second level shows the horizontal axis of the INGRID detector crossed by a series of vertical modules in front. The beam is aimed toward the central modules of INGRID [25].

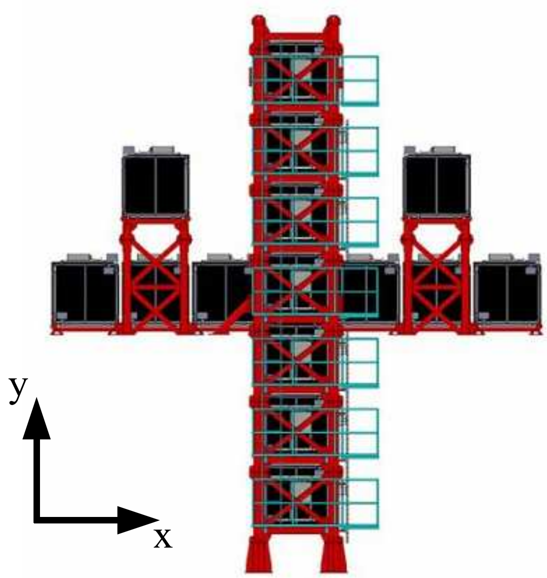

Figure 2.5: A diagram of INGRID oriented so the beam is into the page at the intersection of the vertical and horizontal modules [25].

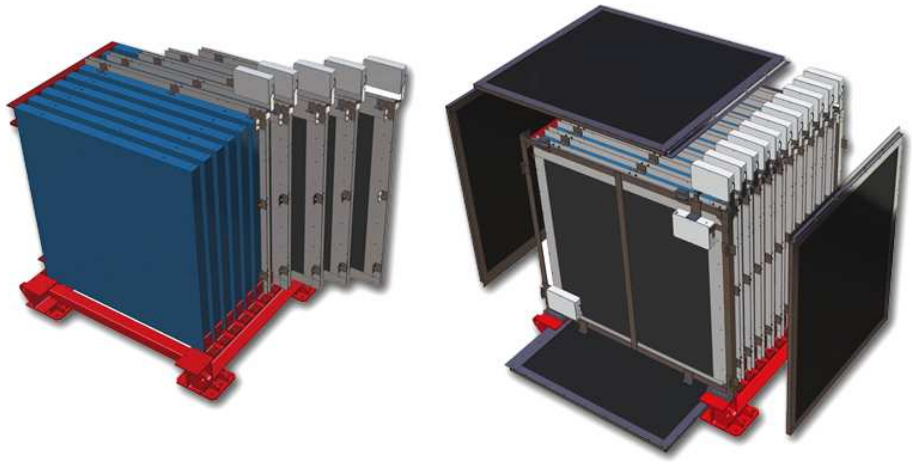

Figure 2.6: A diagram of an INGRID module in an exploded view. The left diagrams shows the layers of scintillator interleaved with iron sheets. The right diagram shows the additional veto layers that surround the module [25].

cross. This module is a finer grained scintillator module with no high-z material to measure the quasi-elastic current in the beam [25].

2.2.2 ND280

Figure 2.7 shows the off-axis near detector, ND280. Surrounding the entire detector is the UA1 magnet yoke from the UA1/NOMAD experiment at CERN. The magnet is run at 0.2 T. Physics data is taken with the magnet in the closed position and on. Occasionally the magnet is turned off in order to take cosmic data for alignment. When necessary, the magnet is opened to provide access to the different subdetectors for upgrades and repairs [25].

Scintillator modules have been inserted into the air gaps between the flux return yokes. They comprise the Side Muon Range Detector or SMRD. The SMRD triggers on cosmic rays that can enter the detector and aid in providing a veto when a beam analysis is undertaken. Additionally, they can measure high angle muons and their momentum as they exit the detector [25].

Inside the magnet, there is a π^0 detector (P∅D), three time projection chambers (TPCs), two fine grained detectors (FGDs) and a selection of electromagnetic calorimeters (ECals). The P∅D will be explained in more detail in the next chapter as it is the primary detector for this analysis.

Figure 2.8 shows a diagram of the general construction of the TPC. A TPC contains of a volume of an argon-based drift gas. An electric field is applied to the gas volume so that when a charged particle passes through the gas and ionizes, emitting electrons which will drift away from the cathode onto a readout plane. The readout planes are called micromegas planes and have a 7 mm by 9.8 mm anode segmentation. This micropattern anode combines for a total of 9 m^2 active readout surface between the three volumes. This is the first application

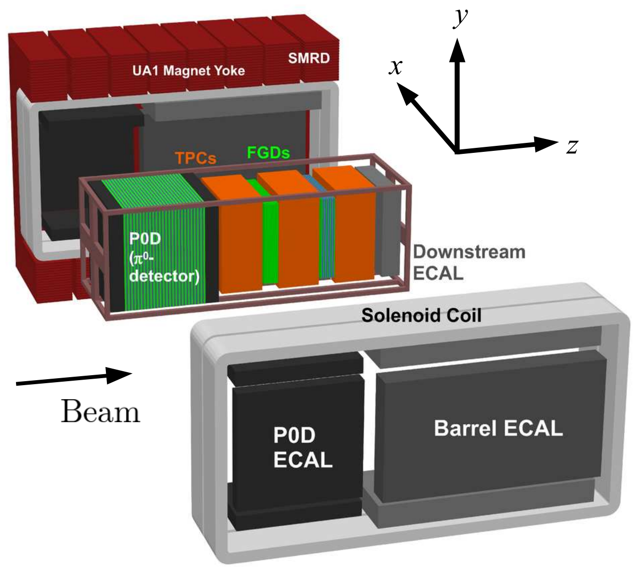

Figure 2.7: An exploded view of the ND280 off-axis subdetectors [25].

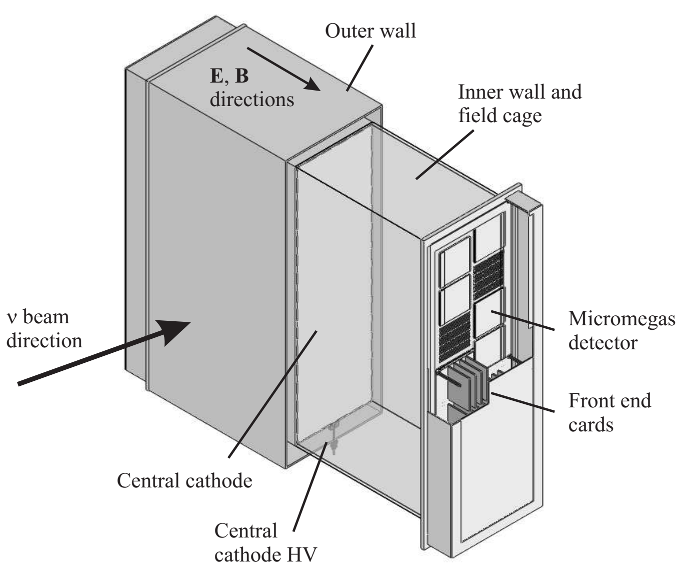

Figure 2.8: An cut away view of the TPC [25].

of this design. The TPC has a high precision three dimensional reconstruction and is used to measure the momenta and charge of the particles recorded in the detector. The TPC can also distinguish between different charged particles by examining the ionization deposit [25].

There are two FGDs sandwiched between the three TPCs. The FGDs have extruded scintillator bars that measure 9.61 mm by 9.61 mm by 1864.3 mm. Inside the bars are WLS fibers that direct the scintillation light to an MPPC readout. The detector layers are constructed to have a alternating layers of bars in the x direction and a layer of bars in the y direction (beam direction is z). The first FGD has 30 scintillator layers as a fully active target volume. The second FGD has a total of 14 layers that are separated into 7 xy modules. Between the xy modules are layers of water that are 2.5 cm thick. The FGD group implemented these water layers to provide a water target for neutrinos [25].

The final collection of detectors are the ECals. The ECals are also scintillator detectors, but the scintillator is layered with lead, a high Z material. The extruded scintillator bars that form the layers have a cross section of 4 cm by 1 cm, four times larger than the FGD. The ECals are arranged to encompass nearly the entire inner magnet detectors, with the exception of the upstream end of the P∅D. There are three different types of ECals based on their positions in the magnet. After the last TPC, there is a downstream ECal (DSECal). This ECal has 34 layers that amount to 10.6 radiation lengths. The TPC and FGD region along with the DSECal are surrounded on the x and y sides by a Barrel ECal. The Barrel ECals have 31 layers or 9.7 radiation lengths. They can be used as a veto for incoming cosmic rays into the TPC and FGD. The P∅D is surrounded by another set of ECals, called the P∅D ECal. These modules are slightly smaller and contain merely six active layers with a thicker lead layer for a radiation length of 3.6 [25].

2.3 Super Kamiokande

Super-Kamikande (SK) is a large water Cherenkov detector located 295 km away from J-PARC near the Japan Sea. A version of the detector has been in operation since the early 1980s, with an update to Super-Kamiokande in 1996, and has devoted a portion of its livetime to the T2K experiment as its far detector. It is placed in a former mine, 1000m underground, in order to use the earth as sheilding from cosmic rays. SK is a large cylinder that has a diameter of 39m and and height of 41m. There is an inner detector that has 11,129 50cm diameter Photomultiplier Tubes (PMTs). The outer detector has 1,885 20cm diameter PMTs, which are used as a veto to ensure that interactions start in the inner detector. The inner and outer detectors are separated by light tight shielding [25].

Cherenkov light occurs when a particle travels faster than the speed of light through a medium. The minimum limit of the particle's speed to create Cherenkov light is $v = c/n$ where c is the speed of light and n is the index of refraction. As a particle travels, a cone of Cherenkov light is created. High momentum electrons undergo bremsstrahlung emmision and the resulting photons then pair produce to create a collection of high momentum electrons that travel in generally the same direction. This collection of particles creates a fuzzy ring signature that is the result of many rings overlapping. As a muon travels through the detector, it does not break and radiate other particles, so a very sharp ring is created. For the ν_e appearance measurement, a selection of one e-like ring is performed. It is possible for

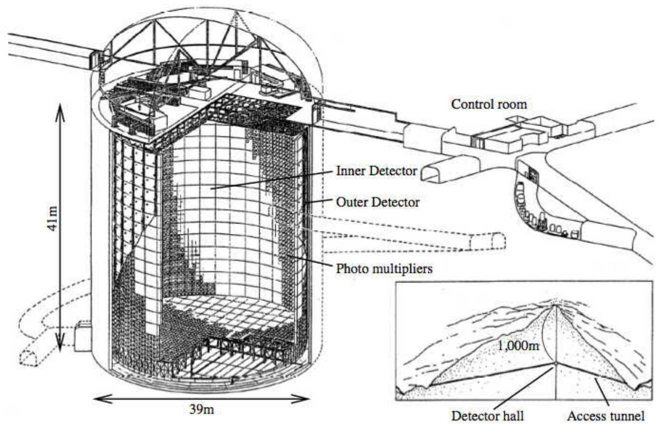

Figure 2.9: A cut away diagram of SK in the Mozumi mine at Kamioka, Japan [25].

a π^0 to appear as an e-like ring in SK, which is how the NC1π^0 interaction sneaks into the background. There are two ways the π^0 particle can decay to form a single observable ring. The first is a symmetric decay where the π^0 decays perpendicular to the direction of motion. If the particle is boosted enough, the angle between the decay photons will be small in the lab frame. This small angle can cause the resulting indistinct ring shapes, corresponding to each photon, to overlap and appear as a single fuzzy e-like ring. The second decay is an asymmetric decay. If the π^0 decays with one photon continuing in the direction of motion, and the other traveling opposite of the direction of motion, the photon traveling backwards may not have enough energy in the lab frame to create a cone of Cherenkov light and be above the detector's energy threshold. Only the photon, now indistinguishable from the electron, travelling in the forward direction will be recorded in this case. As such, knowledge of the NC1π^0 cross section is important in order to reduce the error on the background prediction.

Chapter 3

P∅D

The P∅D detector is the primary detector used in this analysis. As such, this chapter will present a more detailed description of the materials and construction of the P∅D. Along with the construction, an explaination of the data aquisition process will be provided. Following that, a detailed description of the P∅D software process, with a focus placed on the reconstruction PID algorithms, is given. Lasty a study of the internal alignment of the P∅D and the P∅D to TPC external alignment will be shown.

3.1 Detector Construction

Figure 3.1 shows the construction of the P∅D detector. The detector consists of four modules called SuperP∅Dules, two ECals and two water targets. The upstream ECal is referred to as a USECal and the downstream ECal is called the central ECal (CECal) since a DSECal exists as a separate detector. Likewise there is an upstream water target (USWT) and central water target (CWT). The active target for all SuperP∅Dules is broken down into smaller pieces called P∅Dules. The P∅Dules consist of two scintillator layers, one layer for the x direction and one for the y. There are 126 X bars and 134 Y triangular bars in each P∅Dule. In the ECals, the P∅Dules are separated by lead plates. In the Water Targets, the P∅Dules are separated by a layer of brass as well as a layer of water. This water can be drained and refilled to give analyzers access to a mass subtraction to find on-water cross sections.

To have a rigorous definition of the fiducial mass, the fiducial volume needed to be established. The detector was optimized for the fiducial volume to be within 25cm from the edge of the active area for electron or photon based analyses. In practice this definition was inaccurate because it was relative to the ideal volume defined by particular P∅Dules. The position of the P∅Dules change when alignment parameters are applied, altering the fiducial volume. Keeping this in mind, the fiducial volume within the water targets was fixed with an X length of 1600 mm, a Y length of 1740 mm, and a Z length of 1705 mm centered around the active center of the P∅D, see Table 3.1. The edges of the volume are approximately 25 cm from the edge of the active X and Y area and the Z boundary goes from halfway through the first P∅Dule in the USWT to halfway through the last P∅Dule in the CWT.

With the fiducial volume defined, a program to calculate the Monte Carlo geometry fidu-

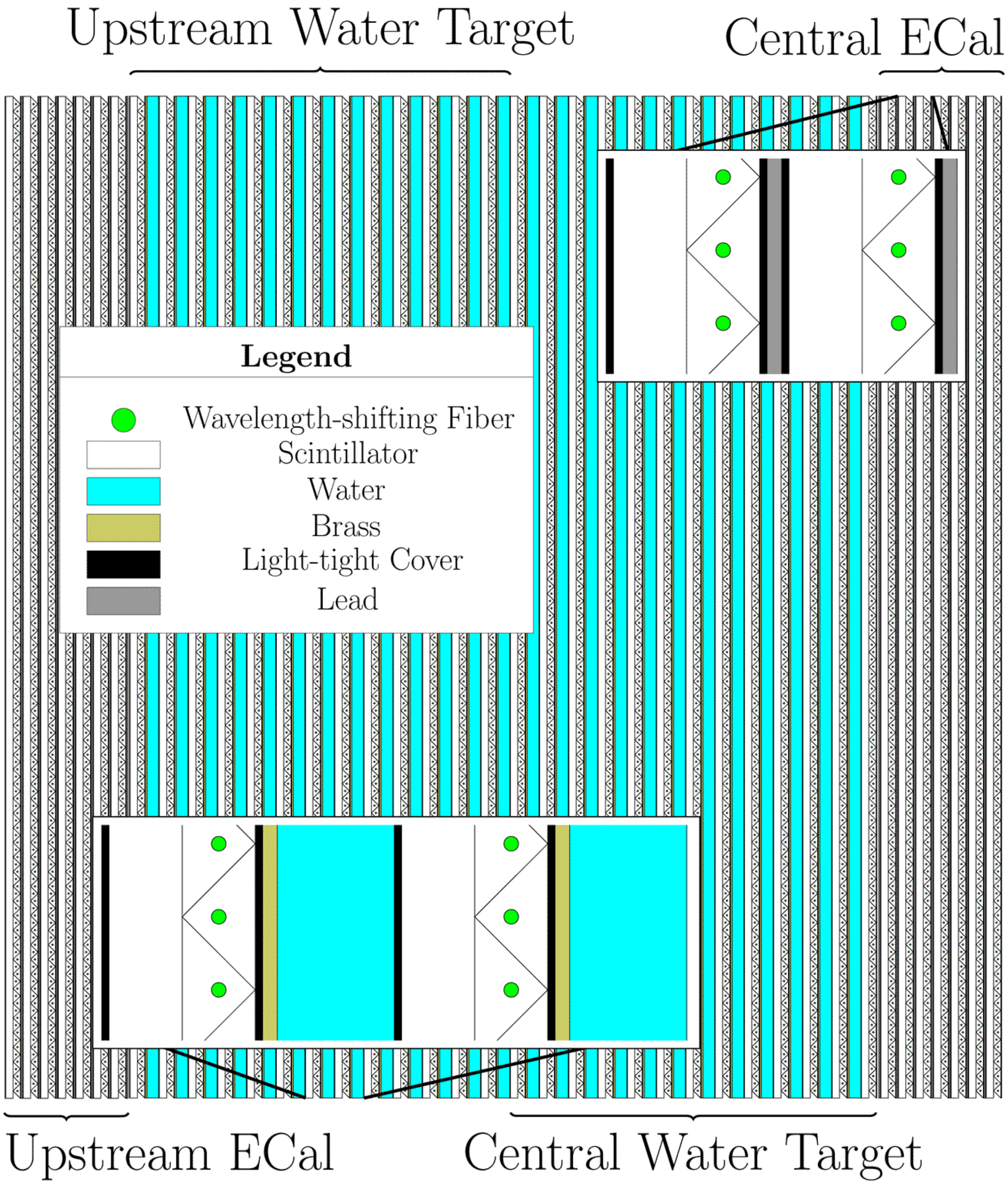

Figure 3.1: A schematic diagram of the PØD [26].

Table 3.1: Definition of the P∅D fiducial volume. The second column shows the center position for all three dimensions in global coordinates. The third column shows the half-widths of the box. The last two columns give the minimum and maximum positions in the Monte Carlo geometry.

Coordinate	Center (mm)	Half-Width (mm)	Minimum (mm)	Maximum (mm)
X	-36	800	-836	764
Y	-1	870	-871	869
Z	-2116	852.5	-2969	-1264

cial mass was constructed. Given a particular volume in the P∅D, a Monte Carlo integration to determine the average density and the statistical error of that density was done. In order to get a mass, the volume was multiplied by the average density. The summary of Monte Carlo fiducial masses follows in Table 3.2. The calculation of the mass is based off of measurements that were taken by various people during construction. There are four pieces in the water target area: brass, P∅Dule, upstream target cover, and water.

Brass Radiator Mass

The brass radiator mass was determined using the measured thickness and the standard density. At Stony Brook University in August 2011, the thickness of the remnant pieces of brass were measured to be 1.28 ± 0.03 mm. The thickness variation measured falls within the manufacturer specification. The brass has not been assayed to determine the density of the brass used, so the standard value for brass was taken, 8.50 ± 0.15 g/cm^3. Given this information, the calculated mass for a single brass radiator layer is 30.29 ± 0.89 kg for the fiducial volume defined in Table 3.1.

P∅Dule Mass

The P∅Dule mass is calculated from the components: two light tight covers, two scintillator planes, 260 wave-length shifting (WLS) fibers and three layers of epoxy. The two light tight covers (also called skins) are made from extruded polystyrene. The thickness was measured at Stony Brook University by Clark McGrew, 1.375 ± 0.125 mm, and the density was found from a range of acceptable values online, 1.05 ± 0.02 g/cm^3. The scintillator planes in the P∅Dule consist of one X layer and one Y layer. During construction, each plank was weighed and measured. From this information, the mass was scaled to the fiducial volume and the X layer was calculated to be 47.94 ± 0.06 kg and the Y layer was 48.06 ± 0.05 kg. In addition to the quoted plank mass uncertainties, there is an additional 0.17% systematic due to the calibration of the scales used to weigh the planks. This systematic is correlated across all planks and adds an additional 4.1 kg uncertainty to the total P∅D fiducial mass. The three layers of epoxy fill the area between the skins and scintillator. During construction batches of either 1.8 kg or 2.0 kg of epoxy were mixed for use in each of the three layers, giving us an upper limit on the epoxy in the P∅D. The amount of epoxy mixed for each P∅Dule was carefully recorded during construction. The design thickness was used to estimate the thickness of each layer of epoxy, 0.25 ± 0.0375 mm, with a 15% error. The design thickness corresponds to a total epoxy layer mass of 1.6 kg, which is reasonable given the amount mixed. This decision was made in order to reduce the dependence on a limited number of P∅Dule thickness measurements. The density is given as 1.36 ± 0.2 g/cm^3, based on the invoice that came with the ordered epoxy. The mass of a single layer of epoxy inside the fiducial volume is calculated to be 0.95 ± 0.20 kg. There are 126 X fibers and 134 Y fibers in a P∅Dule. The number of fibers in the fiducial area are approximately 89 for the X fibers and 110 for the Y fibers. The design specification for the fibers gives a diameter of 0.6 ± 0.1 mm and a density of 1.05 ± 0.01 g/cm^3. The fibers cross the fiducial volume completely, giving us a 0.10 ± 0.02 kg per P∅Dule or 2.5 ± 0.6 kg for the entire fiducial volume. Assuming correlated (density correlations only) errors for each of the components, the total mass of a single P∅Dule is 106.98 ± 0.96 kg (106.98 ± 0.73 kg).

Water Target Cover

There is one upstream target cover. This cover is located at the downstream edge of the USWT. It exists to provide support for the last set of water bags in the USWT. The cover is made from extruded HDPE with a density of 0.94 ± 0.01 g/cm^3. The thickness, 0.25 ± 0.02 inch, was reported by the company that provided the material. The mass of the target cover contributes 16.62 ± 1.34 kg to the total fiducial mass.

Water Target Mass

Inside the water targets, there is a small contribution of mass from dead (non-water) material. Additionally, there is the fiducial mass due to the water itself. Kevin Connolly, a T2K collaborator, calculated the water fiducial mass to be 1902 ± 16 kg. A layer mass was extracted from this measurement by a simple division.

For Run 1, the dead material consists of a central support, two water bags, two pressure sensor assemblies, two level sensor assemblies, and four fill/drain pipes. For Run 2, the dead material consists of a central support, two water bags, four sensor assemblies, and four fill/drain pipes. Only the sensor assemblies differ between the two runs.

The central strut, made from HDPE, has a 28.0 ± 0.2 mm by 18 ± 0.5 mm cross section where the uncertainty is determined by the machining tolerance. Since the strut was manufactured on a computer controlled mill, the masses are assumed to be correlated between layers. It contributes 0.824 ± 0.025 kg per water dead material layer.

The fill/drain pipes are made from PVC (1/2 inch CTS CPVC 4120 pipe). This pipe, according to standard specification, has an inner diameter of 0.469 ± 0.001 in and an outer diameter of 0.625 ± 0.003 in. However, spot check measurements of spare pipes indicate a slightly wider range in the diameters. Due to the uncertainty of the material, the cross section is assumed to be 86 ± 17 mm^2, the spec value, with an error that covers the measured values. Assuming a typical density of PVC (1.38 ± 0.0276 g/cm^3), the mass of a single pipe is 0.21 ± 0.04 kg.

The bag material is HDPE (density of 0.94 ± 0.01 g/cm^3) and the thickness, given by design spec, is 6.0 ± 0.6 mil. In addition to the fiducial area (in X and Y, 1600 mm by 1740 mm) of the bags, an added correction for bag overlap in the middle of the water target was made. There was a measured 200 ± 20 mm overlap. The bags added a mass of 0.90 ± 0.09 kg per layer.

In the sensor assemblies for Run 1 and Run 2, 1/2 inch Schedule 40 PVC was used. Although the pipes remained the same, the sensors changed from Run 1 to Run 2. During Run 1, the sensor was positioned outside of the fiducial volume. Each layer has two bags, and each bag has a primary sensor pipe and a secondary sensor pipe made from this material. Given that the pipes have an inner diameter of 0.607 ± 0.001 in and an outer diameter of 0.840 ± 0.001 in. Again, the pipes were measured to a different cross section so a value of 171 ± 30 mm^2 was used which corresponds to the specification for the pipe with an error that covers the measured value. The mass of a single pipe inside the fiducial volume is 0.410 ± 0.072 kg. The primary sensor pipe also has a readout cable running through it. The cable is approximated to have similar dimensions as the Run 2 readout cable, but with added uncertainty. Thus, the cable is assigned a linear density of 0.7 ± 0.3 oz/ft. Therefore, the mass of one cable is 0.11 ± 0.05 kg.

For the Run 2 sensor assemblies, the sensor (Global Water WL400) was attached to the bottom of a length of PVC. The total length of the PVC pipe plus the sensor was recorded for each pipe installed by Rob Johnson. There are two lengths in each bag for a high sensor and a low sensor. The average of the recorded measurements is used for the length and the standard deviation is used as the length error. The long pipe assembly is 210.4 ± 0.4 cm long and the short pipe assembly is 209.6 ± 0.2 cm long. The specifications for the Global Water WL400 sensor indicate that the sensor is 5.5 ± 0.1 inches long with an error assigned to the last significant figure. The sensor plus the housing weighs 12 ± 1.8 oz where there is a 15% error assigned to the mass due to the uncertainty on the distribution of mass within the sensor. The fiducial volume definition and the length of the sensor pipe assembly (which is measured from the top of the header) is used to calculate how much of the sensor is in the fiducial volume. For the long sensor assembly, $43.5 \pm 3.7\%$ of the sensor is in the fiducial volume or 0.15 ± 0.03 kg. For the short sensor assembly, $49.2 \pm 0.3\%$ of the sensor is in the fiducial volume or 0.17 ± 0.03 kg. The length of the sensor pipe (1/2 inch Schedule 40 PVC) and the readout cable for the long assembly is 1678 ± 5 mm (the length of the assembly minus the lengths of the sensor and the distance from the top of the pipe to the top of the fiducial volume). For the short assembly, the length is 1670 ± 4 mm. In the specification of the cable, the linear density is 0.7 ± 0.1 oz/ft where the error is assigned to the last significant figure. For the long assembly, the mass of the pipe is 0.40 ± 0.07 kg and of the cable is 0.11 ± 0.02 kg. For the short assembly, the mass of the pipe is 0.39 ± 0.07 kg and of the cable is 0.11 ± 0.02 kg.

For Run 1, using correlated (density correlated) errors, the mass per layer of the dead material is 4.42 ± 0.36 kg (4.42 ± 0.11 kg). For Run 2, using correlated (density correlated) errors, the mass per layer of the dead material is 5.20 ± 0.29 kg (5.20 ± 0.07 kg).

For the water out measurement, represented in Table 3.2, there should be no water in the fiducial volume, only the dead material will contribute. The water sensor pipes are not modeled in the Monte Carlo geometry.

Table 3.2: The mass (m) of the components of the PØD from the as-built (AB) measurements for Run 1 and Run 2 and the Monte Carlo geometries, Production 1 (P1) through Production 5 (P5). All errors are assumed to be fully correlated.

	AB (Run 1) (kg)	AB (Run 2) (kg)	P1 (kg)	P2 (kg)	P4 (kg)	P5 (kg)
Brass	30.29 ± 0.89	30.29 ± 0.89	36.9	36.9	36.9	30.2
PØDule	106.98 ± 0.96	106.98 ± 0.96	108.1	109.9	109.9	107.0
WT Cover	16.62 ± 1.34	16.62 ± 1.34	16.6	16.6	16.6	16.6
Water	76.08 ± 0.64	76.08 ± 0.64	77.1	77.1	77.1	77.1
Dead Material	4.42 ± 0.36	5.20 ± 0.29	0.8	0.8	0.8	0.8
Lead Layer	131.24 ± 2.86	131.24 ± 2.86	131.4	131.4	131.4	131.4

Table 3.3: The areal densities (ρ_A) of the components of the PØD from the as-built (AB) measurements and the Monte Carlo geometries, Production 1 (P1) through Production 5 (P5). All errors are assumed to be fully correlated.

	AB (Run 1) (g/cm^2)	AB (Run 2) (g/cm^2)	P1 (g/cm^2)	P2 (g/cm^2)	P4 (g/cm^2)	P5 (g/cm^2)
Brass	1.088 ± 0.032	1.088 ± 0.032	1.33	1.33	1.33	1.09
PØDule	3.843 ± 0.034	3.843 ± 0.034	3.88	3.95	3.95	3.84
WT Cover	0.597 ± 0.048	0.597 ± 0.048	0.60	0.60	0.60	0.60
Water	2.733 ± 0.023	2.733 ± 0.023	2.77	2.77	2.77	2.77
Dead Material	0.159 ± 0.013	0.187 ± 0.010	0.03	0.03	0.03	0.03
Lead Layer	4.714 ± 0.103	4.714 ± 0.103	4.72	4.72	4.72	4.72

ECal Radiator Mass

The ECals are not considered part of the fiducial volume defined above. However, for completeness, the mass information for the ECals is provided. The lead radiators are placed between the PØDules of the Upstream and Central ECals. The lead radiators are composed of tiled lead pieces sandwiched by two layers of steel. Clark McGrew recorded the individual lead piece's weights and dimensions as they were inserted into the sandwich. The lead thickness was measured to be 3.45 ± 0.05 mm, which is the average and RMS of the measurements. The lead was weighed using the same scales as were used to measure the planks. Due to the use of this scale, there is an additional 0.17% systematic error on the total lead mass. The same epoxy and method of mixing used to construct the PØDules was used for the two layers of epoxy within the sandwich. The steel used 26 gauge 304 stainless steel. The design spec gives a thickness of 0.45 ± 0.05 mm and a density of 8.03 ± 0.24 g/cm^3. A single lead sandwich mass in the same fiducial XY area defined in Table 3.1 is 131.24 ± 2.86 kg with fully correlated errors (131.24 ± 2.36 kg with density correlated errors).

PØD Mass Summary

Table 3.2 shows the masses of each component going into the fiducial mass calculation. The masses of the PØDules, brass, and lead layers are for single layers. There are 40 PØDules, 25 layers of brass, 25 layers of water, 25 layers of dead material (in the water target volume)and 14 layers of lead in the entire PØD. The Upstream WT cover is listed with its entire contribution to the mass of the PØD. The lead layer is outside of the water fiducial region, so the mass is for a region with the same X and Y dimensions. The table lists the as-built calculations for Run 1 and Run 2 of the mass as well as the mass for each major production of ND280Monte Carlo. Combining the component masses with correlated errors gives a fiducial mass for the PØD of 3559 ± 34 kg for Run 1 without water and 3578 ± 34 kg for Run 2 water-out running. The Run 1 water-in fiducial mass is 5461 ± 38 kg. For Run 2 water-in running, the fiducial mass is 5480 ± 37 kg. Also provided are the areal densities for the components in Table 3.3. These densities are valid for the X coordinate range from -1041 mm to 969 mm and the Y coordinate range from -1023 mm to 930 mm in the global coordinates of the geometry. However, allowances on the applicable area should be made for alignment uncertainties and reconstruction resolution.

The as-built calculation has an additional systematic error that has been approximated to 2 kg. This systematic error comes from the slight angular rotation around the Y axis that is present in the Monte Carlo geometry that was not accounted for in the as-built calculations. The fiducial volume cut in the Z-direction falls between the X and Y layers of scintillator in a PØDule. This boundary was selected due to the behavior of the reconstruction, but can lead to an asymmetric migration of materials across the boundary (in particular the titanium oxide coating on the scintillator). However, a two kilogram uncertainty easily accounts for this migration.

Two methods of combining the uncertainties are considered. In the first, the density of similar components are assumed to be correlated while the volumes remain uncorrelated. For example, the brass radiators could have different thickness, but because they were made from one batch, the density across all radiators will be the same. In addition to the correlated densities, the correlated systematic error of the scales for weighing the planks (0.17% or 4.1 kg) is added. The resulting estimate of the dry (wet) fiducial PØD mass is 3558.86 ± 18.80 (5460.86 ± 24.69 kg) for Run 1 and 3578.30 ± 18.67 kg (5480.39 ± 24.58 kg) for Run 2 and above. The second method considers the masses for each type of material as correlated (e.g. the masses of all PØDules are correlated). The accuracy of the scales used to weigh the planks is handled separately (0.17% or 4.1 kg). This gives an estimate of a dry (wet) fiducial PØD mass of 3558.86 ± 34.23 kg (5460.86 ± 37.78 kg) for Run 1 and 3578.30 ± 33.80 kg (5480.30 ± 37.40 kg). These two error estimates bracket the true systematic error value. The final uncertainty assumes that the component masses are correlated and is presented in Table 3.4.

Table 3.4 contains the mass of the as-built calculations for Run 1 and Run 2+ as well as the mass for the simulated detector in each of the listed software productions. The differences between different versions of the Monte Carlo are due to a continual, more comprehensive understanding of the mass. The ratio of the as-built mass to the Monte Carlo mass is then used as a correction on the number of Monte Carlo events generated.

Table 3.4: The mass of the fiducial volume of the P∅D for the as-built (AB) information and in the Monte Carlo geometries from Production 1 (P1) to Production 5 (P5). All component errors are correlated in the as-built information. The errors on the Monte Carlo masses are purely statistical.

	Water-In (kg)	Water-Out (kg)
AB (Run 1)	5460.86 ± 37.78	3558.86 ± 34.23
AB (Run 2)	5480.30 ± 37.40	3578.30 ± 33.80
P1	5590.09 ± 2.44	3663.67 ± 2.25
P2	5635.00 ± 2.46	3711.11 ± 2.26
P4	5634.21 ± 0.54	3707.32 ± 0.54
P5	5393.22 ± 0.56	3469.14 ± 0.55

3.2 Data Acquisition

The scintillator bars emit light as a charged particle or high energy photon passes through it. Typically either one or two bars are hit due to the geometry of the bars. If one bar is hit, it is called a singlet. A doublet occurs when two bars are hit. Figure 3.2 shows how the particle would traverse a layer to cause singlets and doublets. In the center of the bar, there is a hole that has a WLS fiber running the length of the bar. This fiber collects the scintillation light and directs it onto the MPPC.

Figure 3.3 depicts the connection between the WLS fiber and the MPPC assembly. The fiber is directed by a Ferrule which holds the fiber end in place near the MPPC. The MPPC is a solid-state photosensor with 667 50-micron pixels. The face of the MPPC is 1.3 mm by 1.3 mm [26]. There are 10,400 bars in the P∅D. The electronic output is sent through the signal wires out of the external shell to the TriptT Front End Boards (TFBs).

Figure 3.4 shows the overall scheme of collecting and recording data. After a signal is sent to the TFB, it is temporarily saved to a TripT computer chip in twenty-three cycles. If an external trigger is not sent, the information is dumped and the next batch of data is temporarily stored. There are two possible external triggers, a GPS trigger and a cosmic ray trigger. The GPS trigger is sent to both the near and far detectors by the beam group to indicate the arrival of the neutrino beam. At the near detector the trigger is received by the Master Clock Module (MCM) which in turn triggers the Slave Clock Modules (SCM). Each detector has a SCM that communicates to the Readout Merger Modules (RMMs) which in turn communicate with the TFBs. In the case of the P∅D, there are 6 RMMs and each RMM

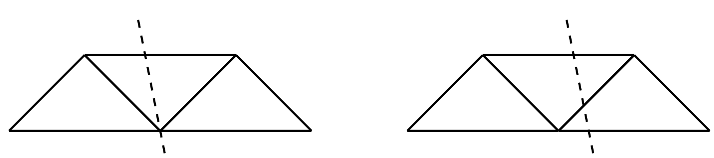

Figure 3.2: A schematic showing a singlet (left) and doublet (right) hit.

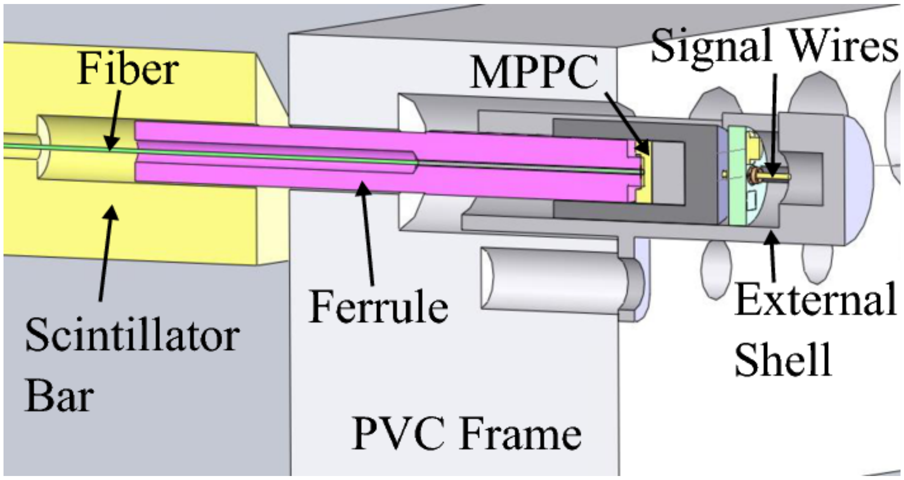

Figure 3.3: A schematic of the WLS fiber to MPPC assembly [26].

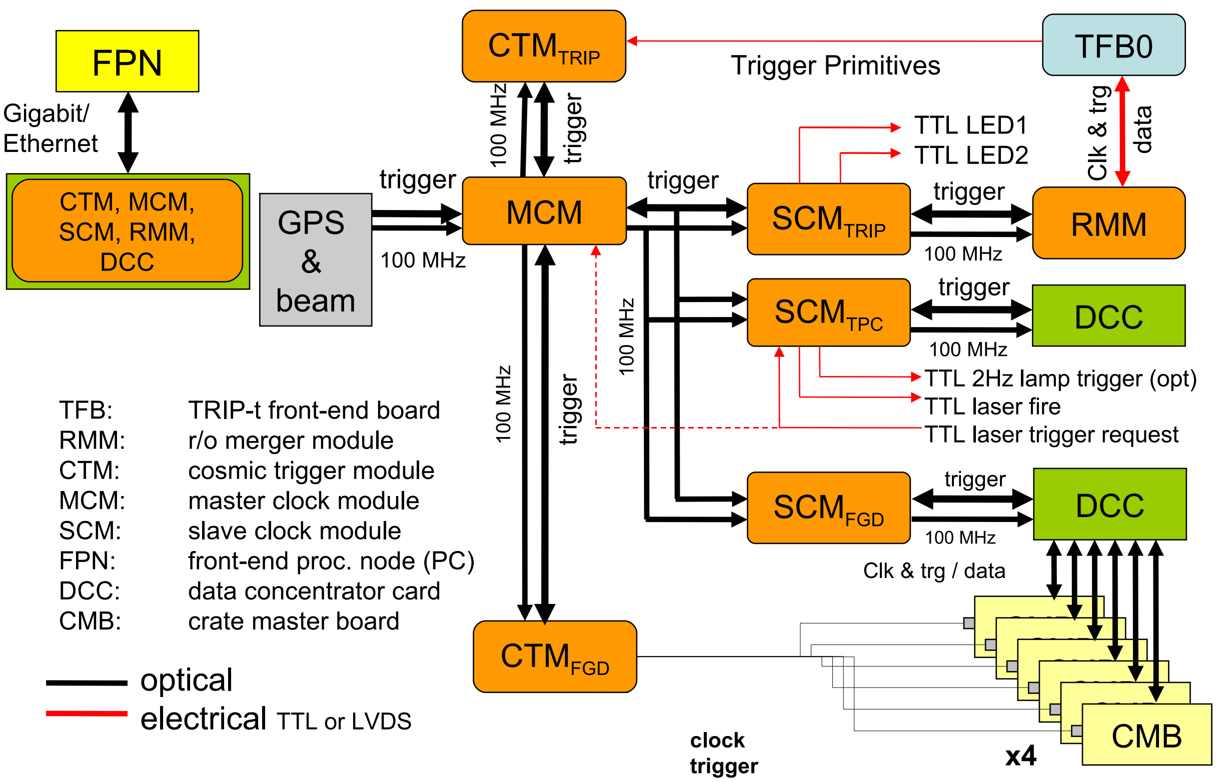

Figure 3.4: A diagram of the data collection system used at the near detector [25].

connects to 29 TFBs. The memory of the TFBs is refreshed to prepare for beam arrival. The beam is sent in eight bunches to the TFBs which are calibrated to have the beam arrival coincide with the fourth time cycle of the TripT chip. The other possible trigger is a cosmic ray trigger. This uses a Cosmic Trigger Module (CTM) to collect trigger primitives from the various TFBs (for the case of the PØD). The trigger primitives contain information on the twenty three buffered cycles. If at the end of the TripT chip's cycle, there appears to be a high number of hits, the CTM assumes a cosmic ray has passed through the detector and sends a request to the MCM to save the data. The MCM, CTM, SCM and RMM signals are then passed through a front end processing node (FPN) that saves the data to external computers. The structure for DAQ communication with the TPC and FGD differ from that used in the PØD and will not be detailed here.

During data taking, cosmic ray running is the default. There are two forms of cosmics, FGD and TripT. In TripT cosmics (which accept triggers from the PØD) any TripT detector can trigger a collection. The TripT detectors are the SMRD, the DSECal, the PØDECal, the Barrel ECal and the PØD. Additionally, there are short calibration runs that can be set up through the DAQ machines. However, any beam trigger supersedes all other triggers to ensure that the beam data is recorded.

3.3 Software Process

The overall software procedure is described in Figure 3.5. There are several steps between Monte Carlo generation and data collection to get to a useful analysis output. The Monte Carlo story begins with the neutrino interaction generators. T2K primarily relies on two generators: GENIE and NEUT. Essentially, they output a list of interactions with the energies and positions of all the particles. This interaction list is passed to nd280mc which places the interactions in the geometrical volume and propagates the particles. The next step is elecSim, which controls the simulation of the electronic noise that is added to the Monte Carlo files as a digitized output. The input data is originally in a maximum integrated data acquisition system (MIDAS) file. The program oaUnpack, extracts the raw data and turns it into digitized hits. This digitized output for both data and Monte Carlo is passed to oaCalib which controls the calibration of all subdetectors. In particular, the photoelectric (PE) peaks and Minimum Ionizing Particle (MIP) peaks are calibrated to specific values in the PØD. This normalizes all MPPC responses. Additionally, any alignment parameters are also applied. The output hits of the calibration are then passed to the reconstruction, oaRecon. The reconstruction files are very large due to the amount of information that is contained in them, so a simplified file is created using oaAnalysis. This simplified file can be accessed using the ROOT program. Most analyses are then run through ROOT macros.

Any PØD analysis relies heavily on the output of the PØD reconstruction. The overview of the reconstruction is shown in Figure 3.6. The input into the reconstruction is the output of the calibration where the data is arranged into hits. These hits represent a single MPPC being fired and the goal of the reconstruction is to map out tracks and showers and calculate the energy and identify particles. The first step in this process is to separate out the 23 cycles of the TripT chip. Each cycle gets reconstructed independently. After separation, the cycles undergo a noise cleaning. The X-Z and Y-Z hits are considered separately and have

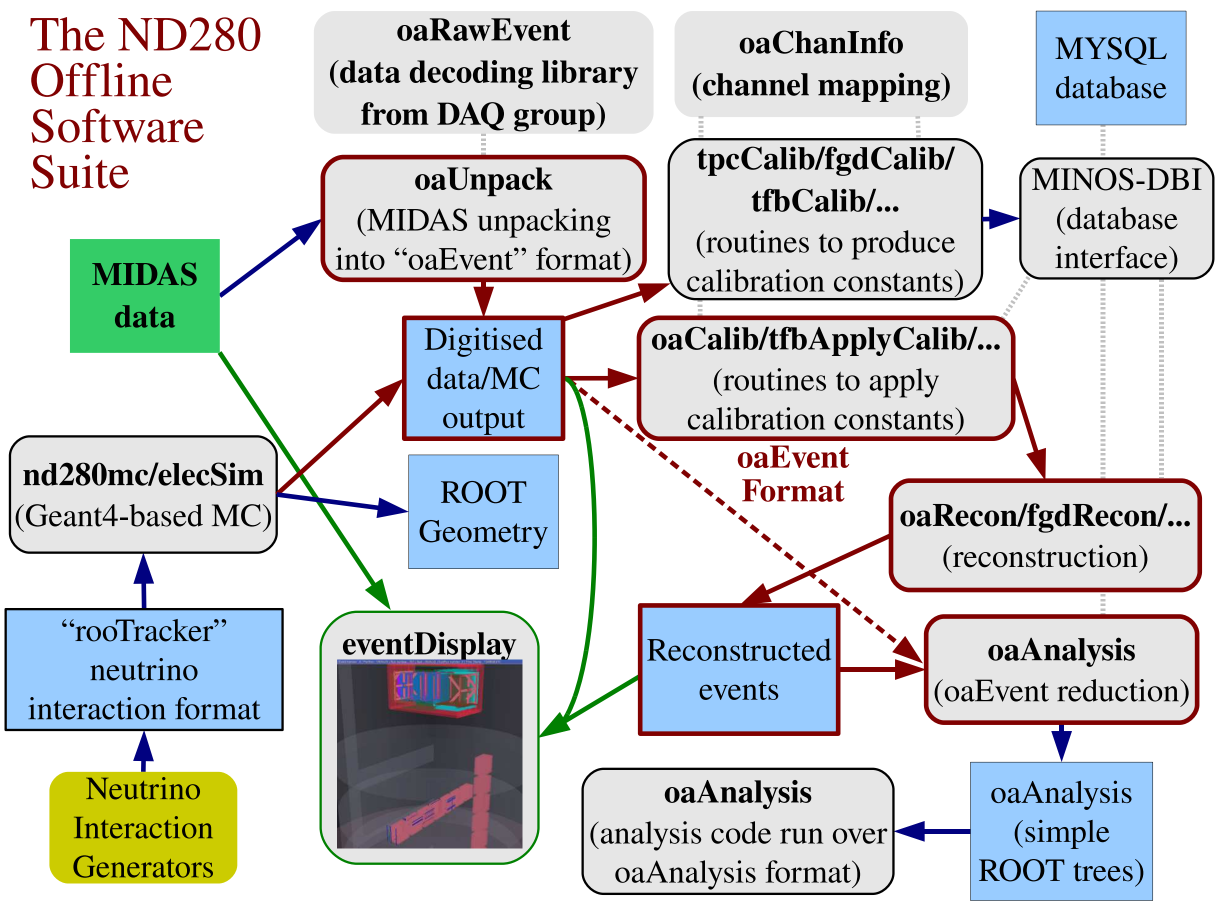

Figure 3.5: A diagram of the general software process [25].

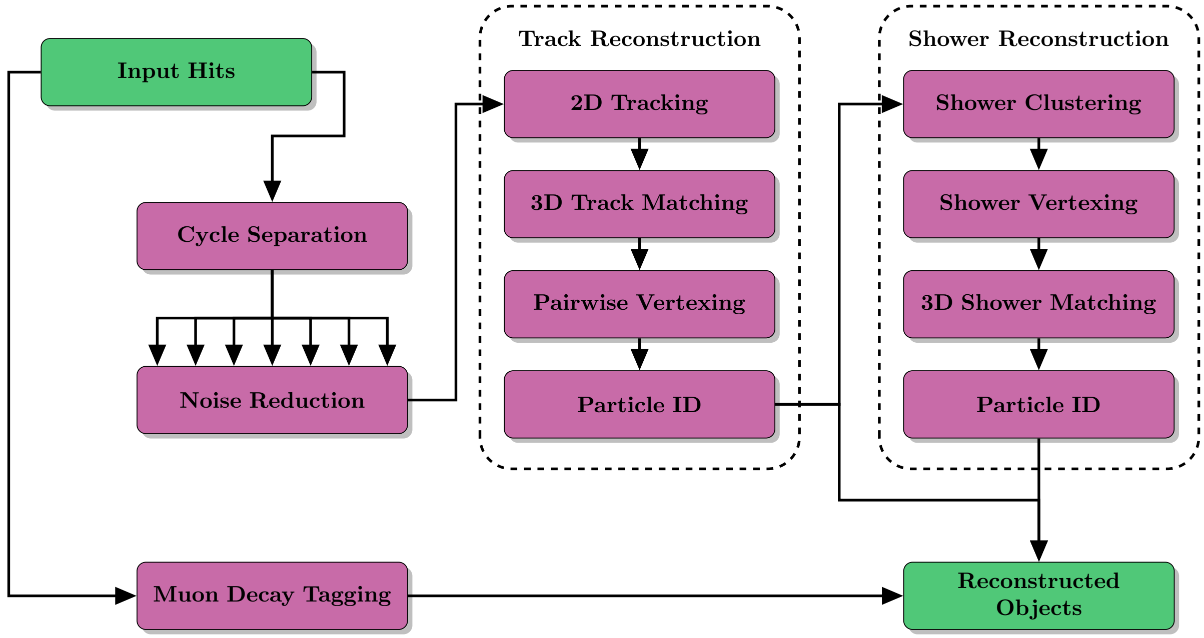

Figure 3.6: A diagram of the PØD reconstruction process.

to pass a few requirements.

- The maximum time difference between compared hits is 30 ns.
- A hit above 15 PEU must have a neighbor within 20 cm.
- A hit above 7 PEU must have a neighbor within 10 cm.
- Any hit is saved if it has a neighbor within 3.5cm (adjacent bar).
- All hits need to be in a 50ns span of time, centered around the median time of the hits.

Additionally, since some MPPCs record hits too frequently, there are around 50 hot channels that are removed from the reconstruction since they can cause events to be mis-reconstructed. The next step in the process is track reconstruction, which is broken down further into smaller steps. First, two dimensional tracks are reconstructed, using a Hough transform to create track seeds. These tracks are then matched between the X-Z and Y-Z planes, allowing tracks to overlap in one dimension if necessary. In the end, all tracks should be matched. With the matched tracks, two options for the three dimensional fit are possible. The parametric fit is reserved for relatively short tracks. The Kalman fit is used for longer tracks and these will be run through a particle identification (PID) process. The three dimensional tracks are used to find a single pairwise vertex. The PID process, further explained in the next section, tags three types of particles based on the Kalman tracks. These are the EM particles (kEM), muons (kLightTrack), and protons (kHeavyTrack). All parametric tracks are labelled kOther and, along with the EM particles, are sent to the shower reconstruction. The protons and muons are sent directly to the output.

The next step for EM-like and short tracks is shower reconstruction. First the hits from the kEM and kOther tracks are clustered, and reconstructed into 2D showers. Then a single vertex is found using the showers and tracks. Finally, the 2D showers are combined into 3D ones. The showers have three to five clusters inside them, which are ellipsoid constructs that describe a portion of the hits in the shower. Additionally, the charges of the showers are shared between overlapping showers to separate the energy of each shower. Finally a PID operation, recently added, is performed. This PID has two choices, kEM or kOther. Any four or five cluster shower is automatically labelled kEM since the parent track of the shower was likely a Kalman fit and has a strong preference for that identification. A log likelihood analysis using PDFs is done for all three clustered showers based on the development and relationship of the clusters of the shower. The results of this PID is then passed to the output.

Lastly, external to the cycle reconstruction, there is a muon decay tagger. This tagger looks for the Michel electrons that result from a muon decay. It looks across multiple cycles so it must be done independent of the rest of the reconstruction. The tagger looks for clusters of overlapping time-delayed hits. It is possible for one muon decay to result in many clusters, as it is mostly used for rejection of events.

3.4 P∅D Particle Identification

After reconstructing a three dimensional track, p∅dRecon offers four possibilities of identification. All 3D tracks are processed with either a parametric fit or a Kalman fit. The first possibility, kOther, is a special category of short tracks that use the parametric fitter. The identification choices available for Kalman tracks are kEM (a photon or electron), kLightTrack (typically muons), or kHeavyTracks (protons). Only kEM and kOther particles are passed on to shower reconstruction, which places an inherent dependence on the efficiency of the track particle identification (PID) on any shower based analysis.

This analysis is done in two parts. First for a selected sample of stopping tracks (which are most likely muons), the PID variables used in the identification are compared and then used to create a Monte Carlo to data mapping. This mapping is then used to calculate the difference in the efficiencies of selecting the correct hypothesis for true Monte Carlo particles.

3.4.1 Stopping Muon Sample

In order to create a mapping between data and Monte Carlo PIDs, an easily extractable sample in data must be used. Stopping muons were tagged as such a sample. A muon particle gun was used to model the incoming muons. A sample of 20,000 muons were created for both the water-in and water-out P∅D configurations and processed through nd280mc, elecSim, oaCalib, P∅DRecon and oaAnalysis. The muons have a linear energy distribution with a gradient of -0.5 MeV goes to zero at 700 MeV. These Monte Carlo muons are shown to roughly agree with the data by studying the track length, see Figure 3.8.

The vertex of the muons in the particle gun was placed at (0.0, 0.0, -345.0) cm in a box that was 200 cm by 200 cm by 2 cm. This is upstream of the P∅D. Figures 3.9 and 3.10

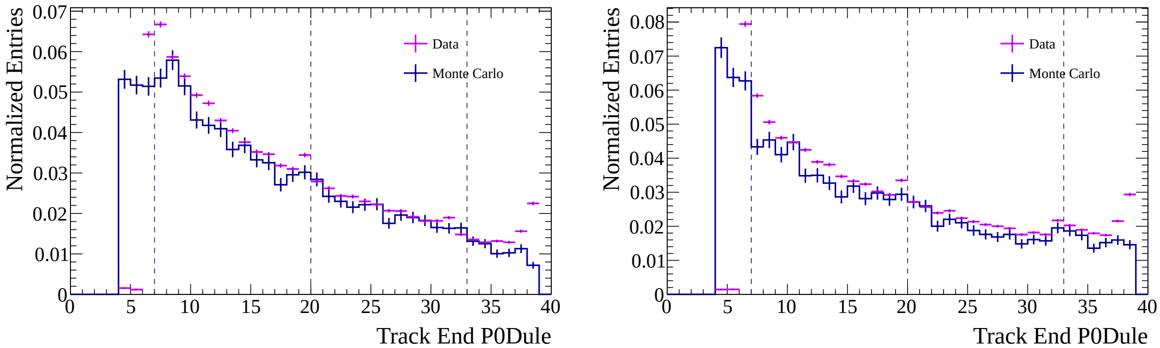

(a) Water-In Configuration (b) Water-Out Configuration

Figure 3.7: The last P∅Dule used in a reconstructed track for muons that enter the front face of the P∅D and do not exit. The dashed lines show the boundaries of the SuperP∅Dules. Note the agreement for mid-range tracks.

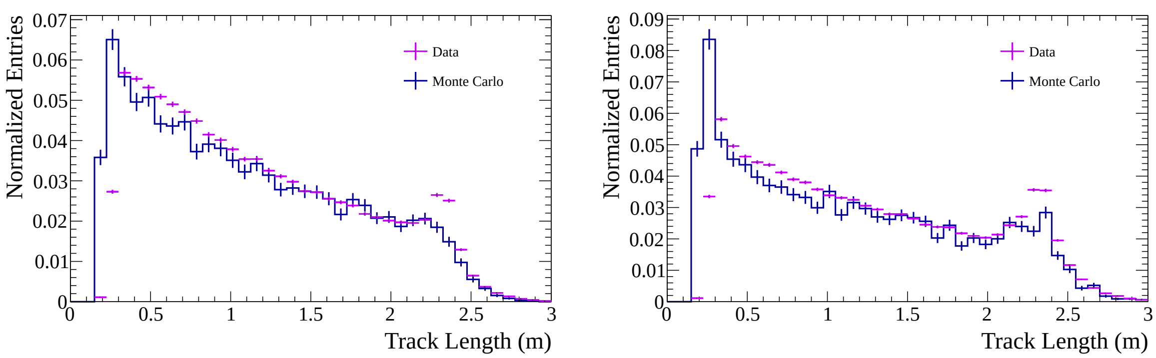

(a) Water-In Configuration (b) Water-Out Configuration

Figure 3.8: The length of the reconstructed tracks for muons that enter the front face of the P∅D and do not exit. Short tracks have historically been difficult to model, but the mid-range tracks have the same shape in data and Monte Carlo.

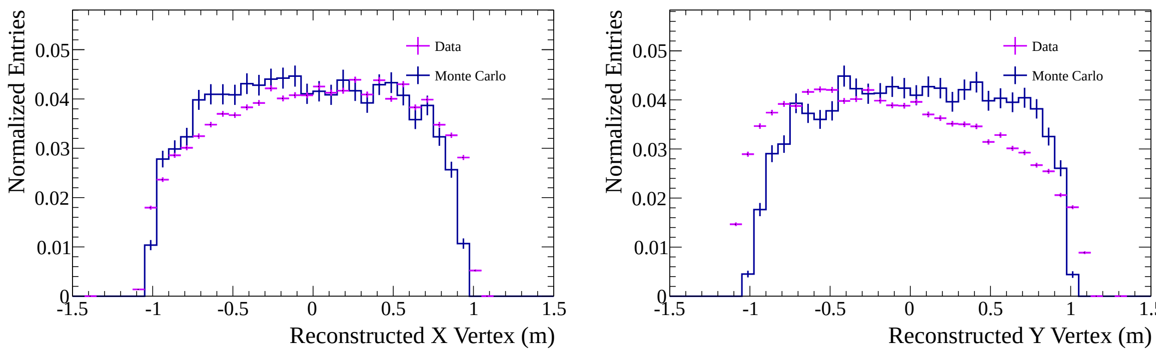

Figure 3.9: For the water-in configuration, the vertex distribution of the stopping muons. Due to the off-axis quality of the neutrino beam, a slight shift in both projections is expected.

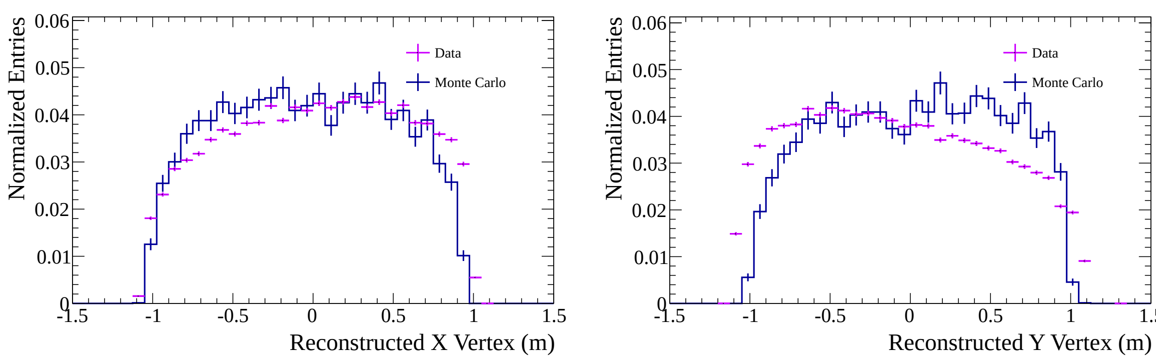

Figure 3.10: For the water-out configuration, the vertex distribution of the stopping muons. Due to the off-axis quality of the neutrino beam, a slight shift in both projections is expected.

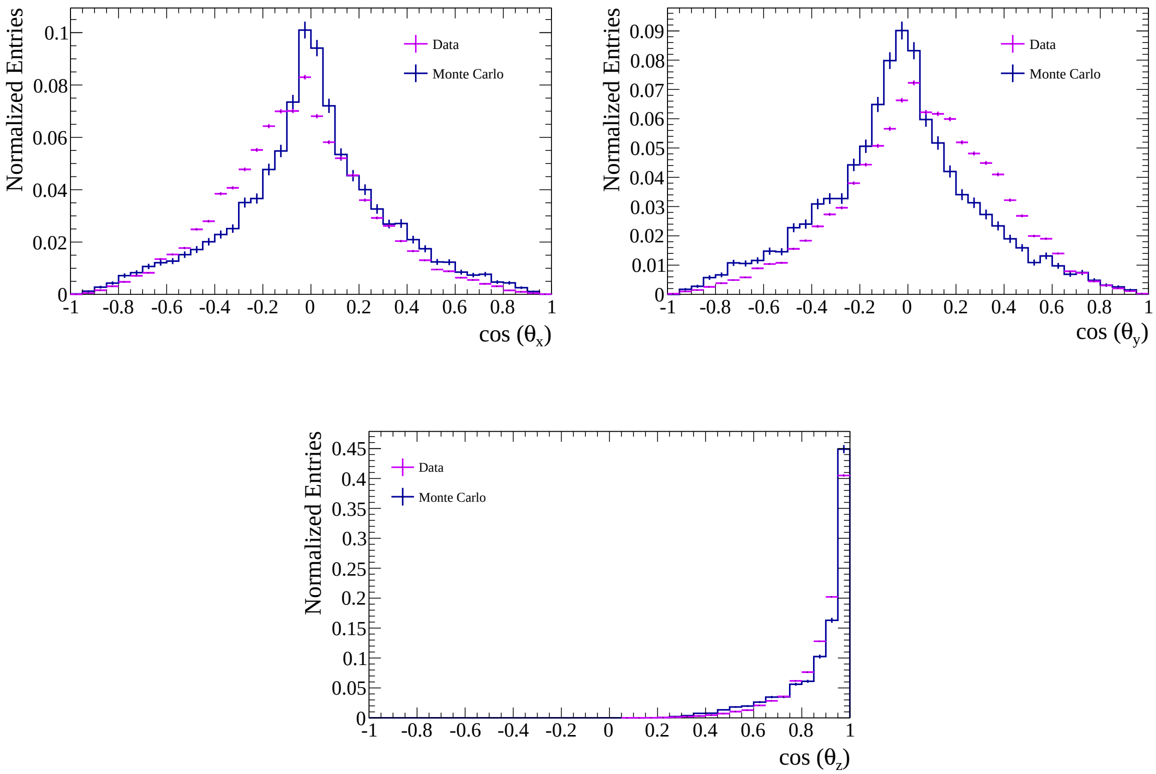

Figure 3.11: For the water-in configuration, the angular distribution of the stopping muons. Due to the off-axis quality of the neutrino beam, a slight shift in x and y is expected.

show that the reconstructed vertex is accurate except for the small offset due to the off-axis nature of the neutrino beam seen in the data.

The muons were directed in a one dimensional beam in the z direction with a radial sigma of 40 degrees. The sigma was hand tuned to match with the data distributions. Figures 3.11 and 3.12 give an idea of the accuracy of this approximation. There is again an offset from the off-axis nature of the neutrino beam in data. However, these distributions show that the particle gun created is a fairly good approximation of the stopping muon sample in the data.

In order to extract this stopping muon sample, the results from TP∅DTrackRecon were examined. One reconstructed vertex with one track fit by a Kalman fitter is required. The track must start in the upstream-most P∅Dule and be contained. A contained object requires that there is no charge in the edge bars or last P∅Dule.

3.4.2 Creating a Map

There are five variables that enter into the Kalman track identification. After a variable for a track is calculated, PDFs are used to make a log likelihood calculation for each identification hypothesis. The three hypotheses are compared and the hypothesis with the largest log likelihood is chosen as the PID.

The first variable is three dimensional. It looks at the relative charge that is deposited

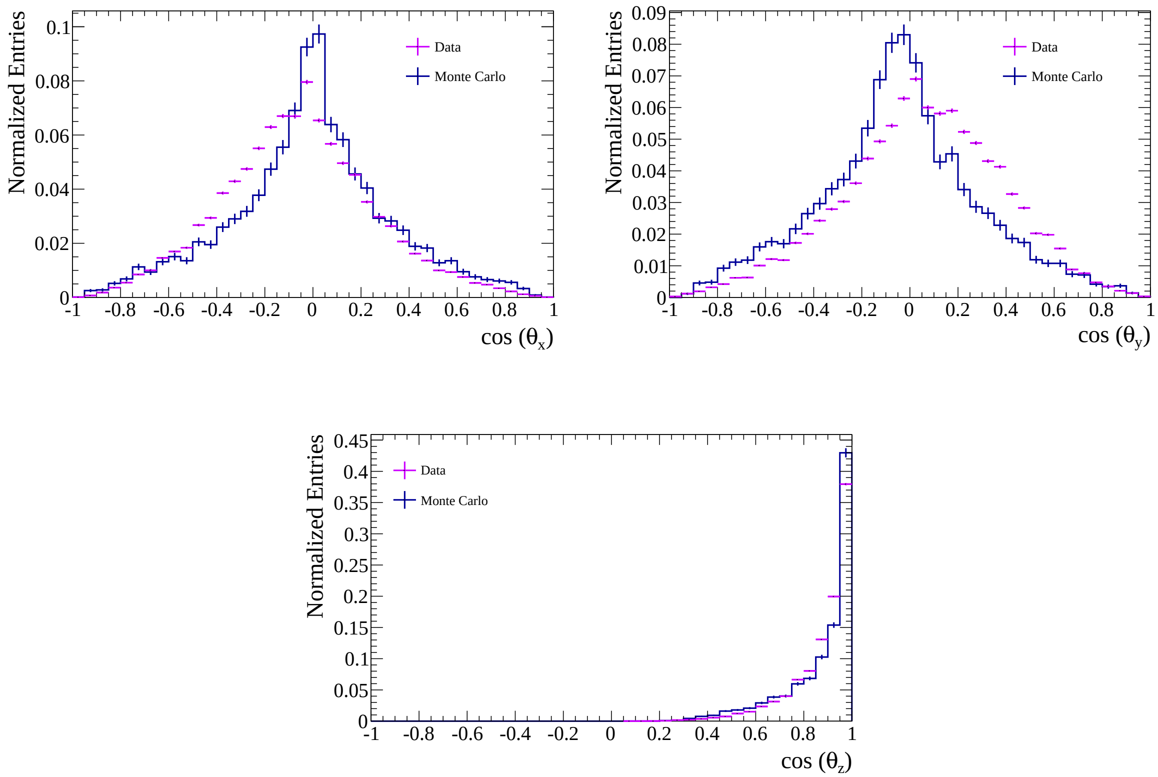

Figure 3.12: For the water-out configuration, the angular distribution of the stopping muons. Due to the off-axis quality of the neutrino beam, a slight shift in x and y is expected.

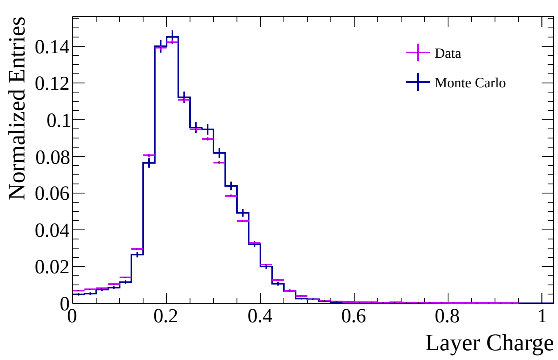

(a) Variable Distribution

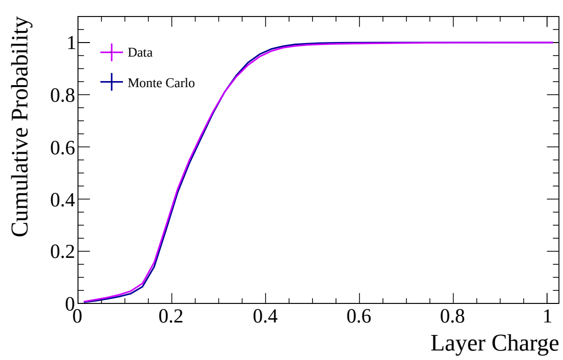

(b) Cumulative Distribution

Figure 3.13: For the water-in configuration, these plots show an example of the distributions of different layer charge ratio variables for the stopping muon sample. This example shows the fractional reconstructed charge in the last layer of the reconstructed track at $\cos\theta_z = (0.9\bar{1}, 1.0)$.

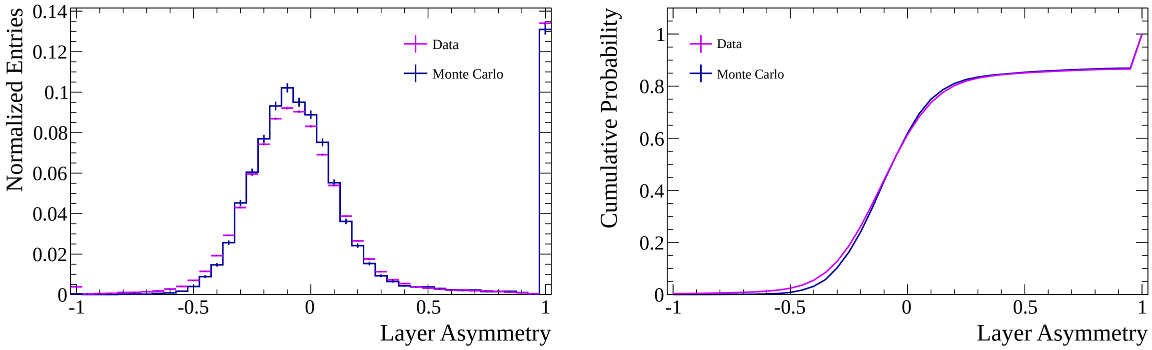

(a) Variable Distribution (b) Cumulative Distribution

Figure 3.14: For the water-in configuration, these plots show an example of the distributions of variables for the stopping muon sample. This example shows the layer asymmetry in the last P∅Dules of the reconstructed track.

in the last five layers of a reconstructed track. For each layer, the angle of the track and the charge deposited as a fraction of the total charge in the last five layers is saved. The angle, defined by the $\cos\theta_z$ is split into nine pieces with all events less than 0.2 reassigned to the $0.2 - 0.2\bar{8}$ bin. This is called the layer charge ratio. An example of the layer charge ratio distribution for a single layer and a single angle bin can be seen in Figure 3.13.

The next variable is the layer asymmetry of the last five P∅Dules. Empty P∅Dules are assigned an asymmetry value of 2.0, all other P∅Dules have asymmetries (A) calculated by

$$A = \frac{Q_X - Q_Y}{Q_X + Q_Y}, \tag{3.1}$$

where Q_X refers to the charge in the X layer and Q_Y refers to the charge in the Y layer. The last four P∅Dules are placed into separate PDFs, all the other P∅Dules used in the tracks have asymmetries used in one PDF. An example of the layer asymmetry distribution for the last P∅Dules of the track can be seen in Figure 3.14.

Next, there is the P∅Dule asymmetry of the five pairs of P∅Dules. If there are two adjacent P∅Dules, the asymmetry is set to 2.0 again. Allowing $Q_i = Q_X + Q_Y$ to be the total charge in the ith P∅Dule, the asymmetry is

$$A = \frac{Q_i - Q_{i+1}}{Q_i + Q_{i+1}} \tag{3.2}$$

The last four pairs of P∅Dules use separate PDFs while all other pairs use the same PDF. An example of the P∅Dule asymmetry in the last pair of P∅Dules in the track can be seen in Figure 3.15.

Another variable counts the integer number of empty layers in a track. This variable also divides the tracks into groups by length for use with the PDFs. There are 5 length categories done by 500 mm sections where anything longer than 2000 mm is grouped together. An

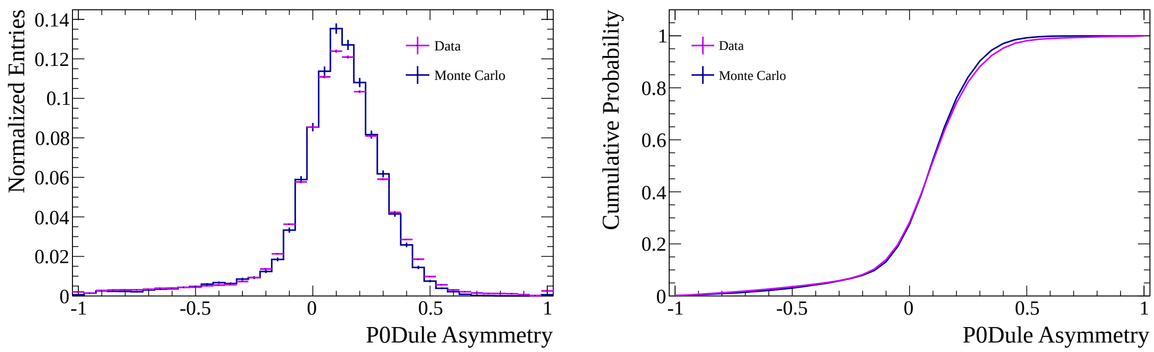

(a) Variable Distribution (b) Cumulative Distribution

Figure 3.15: For the water-in configuration, these plots show an example of the distributions of variables for the stopping muon sample. This example shows the P∅Dule asymmetry in the last pair of P∅Dules of the reconstructed track.

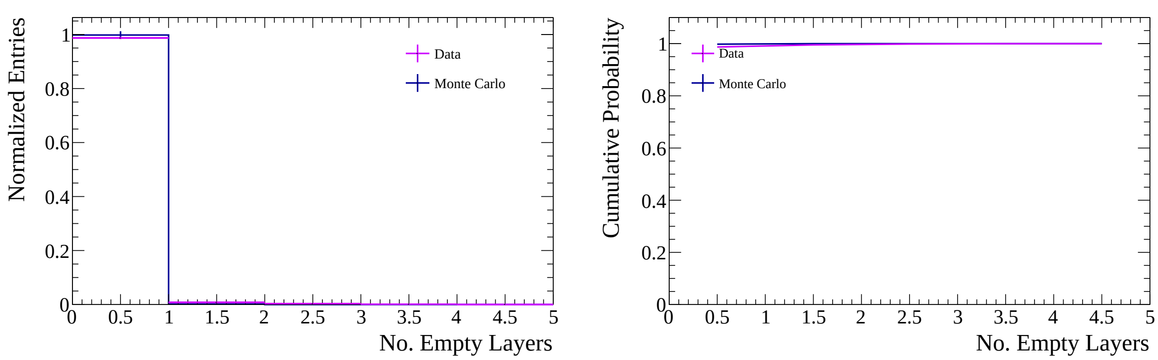

(a) Variable Distribution (b) Cumulative Distribution

Figure 3.16: For the water-in configuration, these plots show an example of the distributions of variables for the stopping muon sample. This example shows the number of empty layers for short (0-500 mm) reconstructed tracks.

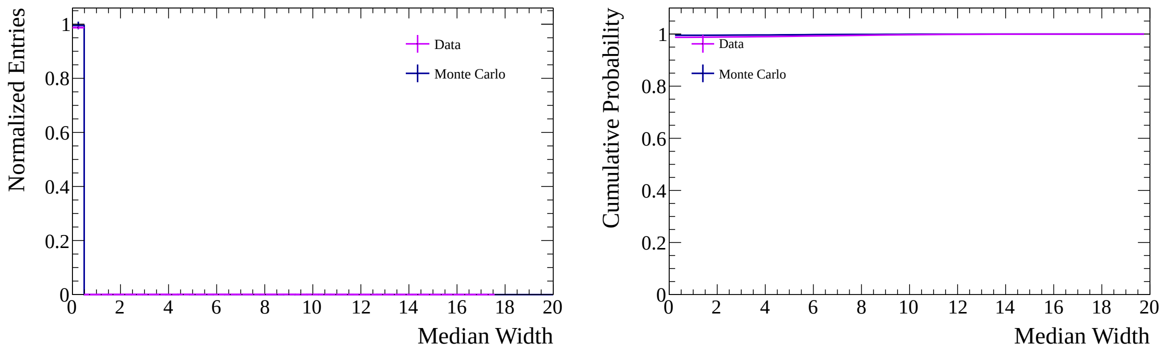

(a) Variable Distribution (b) Cumulative Distribution

Figure 3.17: For the water-in configuration, these plots show an example of the distributions of variables for the stopping muon sample. This example shows the number of empty layers for short (0-500 mm) reconstructed tracks.

example of the distribution of the empty layers for the stopping muon sample is shown in Figure 3.16

The last variable used in the track reconstruction is the median width of the nodes of the track. Essentially this is a measure of how spread out the track is at each node. For muons this width should be small. This variable also uses the length of the track to further differentiate between particles. An example of this distribution of median widths of stopping muons can be seen in Figure 3.17.

With all of the variables accounted for, a mapping from the stopping muon Monte Carlo sample to the stopping muon data sample is created.

3.4.3 Mapping the PID

Using the entire Production 5E Monte Carlo, the default and a mapped version of the PID are compared. Again TP∅DTrackRecon results are examined. A vertex in the fiducial volume is required with at least one three dimensional track. The true particle is determined by requiring most of the true charge deposit to be from one type of particle (EM, Muon or Proton). Next, the PID is calculated using the same PDFs that are found in p∅dRecon. In addition, the variables are recalculated using the mapping created from the stopped muon sample. A variable is mapped by calculating its quantile in the Monte Carlo distribution. That same quantile is found in the data distribution and the variable that matches with it is used to calculate the PID. This mapping is done for each track.

Using the information in Tables 3.5 and 3.7, the difference between the default and mapped PID can be examined. The efficiency and accuracy of the Track PID can be taken from Tables 3.6 and 3.8. There is a clear effort put into correctly identifying the true EM particles. For the P∅D water-in Monte Carlo with statistical Poisson errors, $3.94 \pm 0.02\%$ of the true EM tracks reconstructed with the Kalman method are incorrectly identified using the default PID. With the mapped PID, this reduces to $2.24 \pm 0.01\%$ which gives

Table 3.5: For the water-in configuration, the track-by-track rates of the default and mapped PID. There were 3922930 parametric tracks reconstructed.

	True Muon	True Electron	True Proton
Default PID			
Reconstructed Light Track	1361381	18624	311993
Reconstructed EM	447099	1064310	689316
Reconstructed Heavy Track	370509	25057	535913
Mapped PID			
Reconstructed Light Track	1112131	8876	238387
Reconstructed EM	564760	1083166	778480
Reconstructed Heavy Track	502098	15949	520355
Total True Events	2178989	1107991	1537222

Table 3.6: For the water-in configuration, the track-by-track efficiencies of the default and mapped PID. One can clearly see a directed effort into correctly identifying the EM sample.

	True Muon	True Electron	True Proton
Default PID			
Reconstructed Light Track	62.5%	1.7%	20.3%
Reconstructed EM	20.5%	96.1%	44.8%
Reconstructed Heavy Track	17.0%	2.3%	34.9%
Mapped PID			
Reconstructed Light Track	51.0%	0.08%	15.5%
Reconstructed EM	25.9%	97.8%	50.6%
Reconstructed Heavy Track	23.0%	1.4%	33.8%

Table 3.7: For the water-out configuration, the track-by-track rates of the default and mapped PID. There were 1864414 parametric tracks reconstructed.

	True Muon	True Electron	True Proton
Default PID			
Reconstructed Light Track	403149	8866	102480
Reconstructed EM	253524	496189	371301
Reconstructed Heavy Track	197261	14247	343162
Mapped PID			
Reconstructed Light Track	361716	5129	100355
Reconstructed EM	296773	504353	421055
Reconstructed Heavy Track	195445	9820	295533
Total True Events	853934	519302	816943

Table 3.8: For the water-out configuration, the track-by-track efficiencies of the default and mapped PID. Again there is evidence of a large effort to separate the true EM sample

	True Muon	True Electron	True Proton
Default PID			
Reconstructed Light Track	47.2%	1.7%	12.5%
Reconstructed EM	29.7%	95.5%	45.5%
Reconstructed Heavy Track	23.1%	2.7%	42.0%
Mapped PID			
Reconstructed Light Track	42.4%	1.0%	12.3%
Reconstructed EM	34.8%	97.1%	51.5%
Reconstructed Heavy Track	22.9%	1.9%	36.2%

a $1.70 \pm 0.02\%$ difference in efficiencies. Of all the true EM Kalman tracks in the P∅D water-out Monte Carlo, $4.45 \pm 0.02\%$ are incorrectly identified using the default PID. When using the mapped PID, $2.88 \pm 0.02\%$ are incorrectly identified. This leads to a difference of $1.57 \pm 0.04\%$ for the water-out configuration. However, since the sample used for the map construction is a stopping muon sample, analyses are better served by approximating a PID efficiency by looking at the number of true muons that enter the shower reconstruction. If this definition is used, then there is a $5.40 \pm 0.05\%$ inefficiency difference of muons being misidentified as EM for the water-in configuration and a $5.06 \pm 0.03\%$ inefficiency for the water-out configuration.

3.5 Converting Deposited Charge to Energy

In order to understand the relationship between the reconstructed charge (PEU) and the true energy (MeV), three samples of photons were generated, water-in water target, water-out water target, and ECal. Each sample shows a different charge to energy response. It was previously assumed that the water-in water target had a comparable energy scale to that of the ECal [27]. However, the water-out water target will have a very different energy scale. This conversion is necessary to provide an accurate energy of any reconstructed photons.

3.5.1 Creating a Photon Sample

Using Production 5F (ND280 v10r11p21), 200,000 photons were created in the P∅D water-in configuration and again in the P∅D water-out configuration. An additional 100,000 photons were created in a special ECal geometry. This special geometry remodels the P∅D as 40 ECal layers. The generated particles were uniformly distributed in energy from 1 MeV to 1 GeV. The focus of this study is on photons below 200 MeV, a typical energy of a photon from a decaying π^0. The vertex positions were smeared in a box on the upstream end of the water target, in order to get the best chance of photon conversion in the water target. In addition, the particles were generated isotropically downstream (no upstream going particles) due to reconstruction efficiencies. The simulation process runs events through nd280MC, elecSim, oaCalib, and P∅DRecon.

Next, the events were processed through a selection to extract the cleanest sample of reconstructed photons with their true and reconstructed deposited charge. For the truth information, one vertex containing one particle (a photon) is required. Every event should meet this requirement. At least 90% of the true energy deposit must be in the P∅D, to ensure that the particle is relatively contained inside the P∅D. This is calculated by adding up the energy deposit from the individual true hit segments. The total true energy is accessed by examining the total true particle energy adjusted by the fraction of the true energy that is deposited by the Monte Carlo in the P∅D.

To access the the reconstructed information, every cycle is checked for a result containing TP∅DShowerRecon/TP∅DShowerPID. This requires that the EM particle is reconstructed correctly as a shower. Once a result is found, all vertices and showers are checked, in order to get all possible information from the event. Every particle is checked and the attenuation corrected charge deposit is added together. While the total charge deposit is added, the

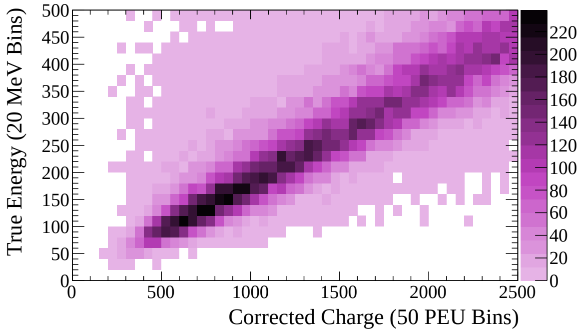

(a) Water-In Configuration.

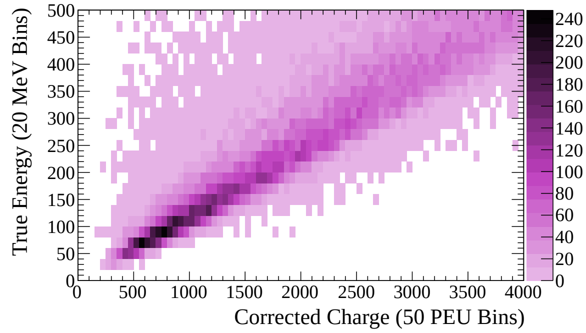

(b) Water-Out Configuration.

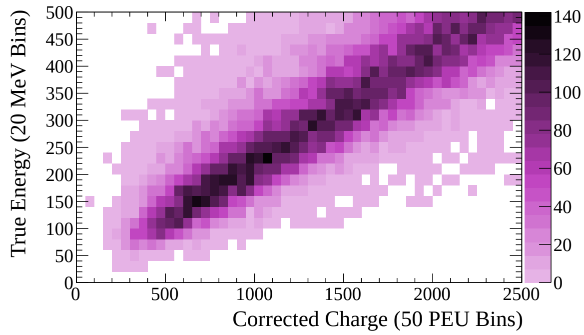

(c) ECal-Only Configuration.

Figure 3.18: The distribution of the relationship between the attenuated corrected charge and the true energy of the photons. The charge is cut off to a region of interest where the true energy is less than 500 MeV. Note that the water-out configuration extends to higher charge region.

largest EM particle is extracted. This particle must have three dimensional information as well as containing 90% of the total charge reconstructed in the event. The charge from the reconstructed particle and the energy deposit from the truth information are studied further. Also considered was the fraction of the attenuated charge in the particle that falls within the water target which allows a division of the reconstructed charge.

3.5.2 Calculating the PEU to MeV Conversion

The true energy against the attenuation corrected reconstructed charge is plotted in Figure 3.18. For the water target samples, all of the charge of the particle is required to be inside the water target to investigate that piece of the PØD. Each bin, 20 MeV wide, of the true energy is projected onto a one dimensional histogram. Using Gaussian fits, the peaks of each projection is found. Although on first glance looking at charge bins makes more sense, since the input is a charge and output should be an energy, there is an inherent dependency on the input distribution of the generated energy. For example, if instead of a

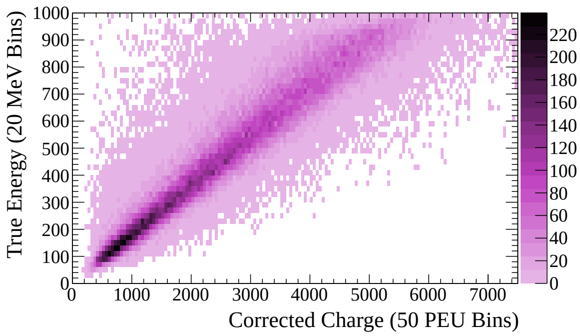

(a) Water-In Configuration.

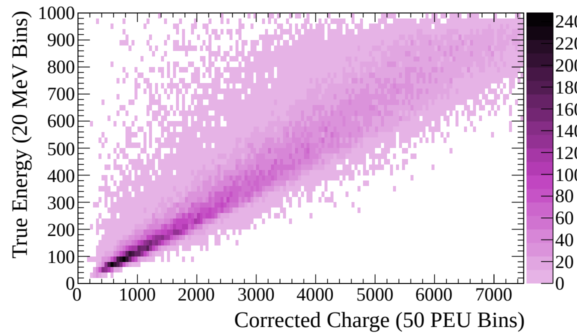

(b) Water-Out Configuration.

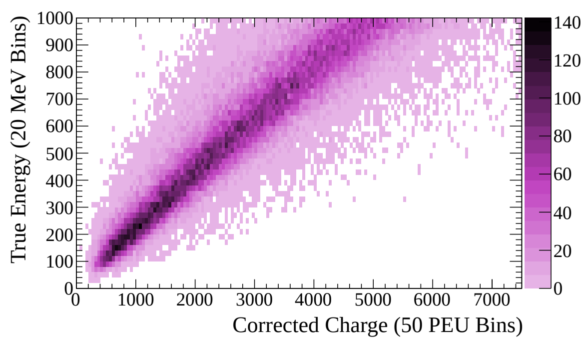

(c) ECal-Only Configuration.

Figure 3.19: The distribution of the relationship between the attenuated corrected charge and the true energy of the photons. The full range of the generated energy and the charge is shown.

Table 3.9: The energy scale values from linear fits of Figure 3.23.

	α_0 (MeV/PEU)	α_1 (MeV)
Water In	0.197 ± 0.019	-14.2 ± 14.1
Water Out	0.121 ± 0.011	-1.3 ± 13.0
ECal	0.262 ± 0.025	-29.6 ± 16.0

uniform true energy particle gun, a gaussian energy distribution was generated, the charge bins would have a drastically different shape. There is additionally some shape variation due to the different efficiencies of the detector at different energies. Due to this difference, the energy bin projections are studied with the individual bins only dealing with monoenergetic detector responses.

For the Gaussian fits, the fit range is restricted to one RMS of the distribution around the mean. The result must have at least one degree of freedom and be relatively narrow ($\sigma < 1000$ PEU). In addition the maximum of the function must be within 50% of the maximum of the histogram. Examples of these fits for photons can be seen in Figures 3.20, 3.21, and 3.22. The means of the Gaussian fits are plotted and fitted with a straight line. The errors shown are calculated by using the RMS divided by the square root of the entries. Since the energy bins were projected, the energy was placed on the x-axis. In addition, in order to get a better handle on the low energy photons used in the NC1π^0 Analysis, the fit was restricted to less than 200 MeV. Finally, the function of energy chosen for the fit was

$$Q = f(E) = \frac{1}{\alpha_0}(E - \alpha_1), \tag{3.3}$$

where α_0 describes a slope and α_1 describes an intercept. This functions was chosen in order to trivially invert the function to a function of charge,

$$E = f^{-1}(Q) = \alpha_0 Q + \alpha_1. \tag{3.4}$$

The fits in Figure 3.23 gives the energy scale parameters for photons and is summarized in Table 3.9.

3.5.3 Checking the PEU to MeV Conversion

For a given water target charge, A, and ECal charge, B, a formula to calculate the total energy needs to be established. The formula considers the sum of the contributions of both parts of the detector,

$$E = \alpha_0 \cdot A + \alpha_1 + \beta_0 \cdot B + \beta_1 \tag{3.5}$$

where α and β describe the water target and ECal charge to energy conversion. There are two types of α, one for the water-in configuration, α^{in}, and one for the water-out configuration α^{out}.

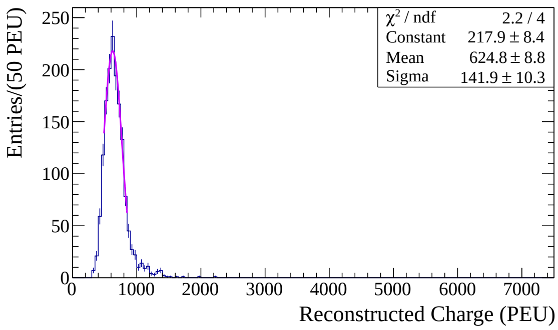

(a) 100 to 120 MeV

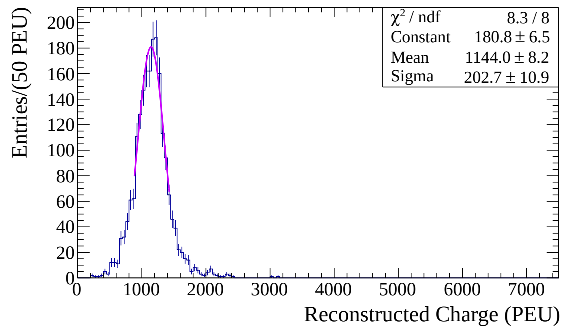

(b) 200 to 220 MeV

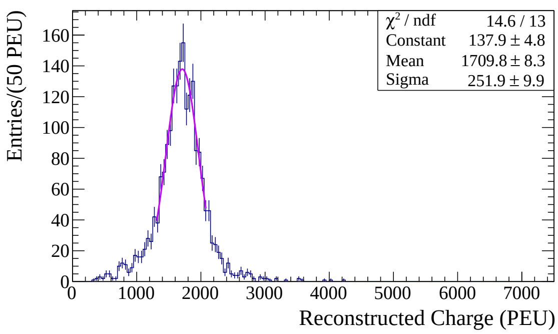

(c) 300 to 320 MeV

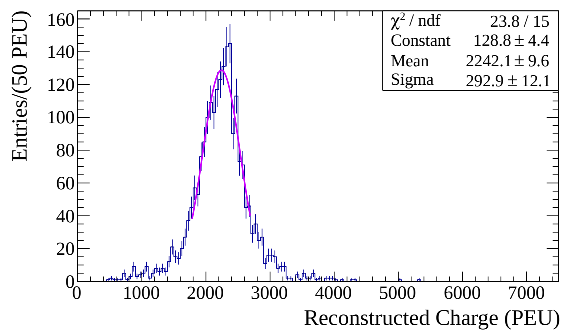

(d) 400 to 420 MeV

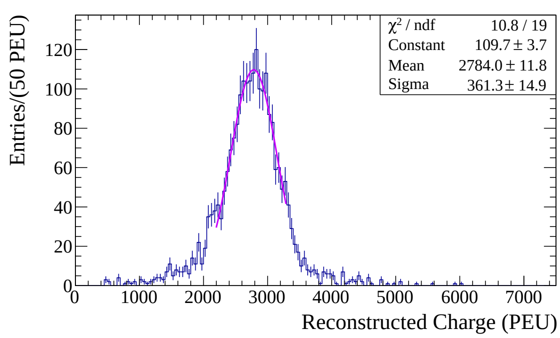

(e) 500 to 520 MeV

Figure 3.20: Examples of the Gaussian fits performed on each energy bin for the water-in water target configuration.

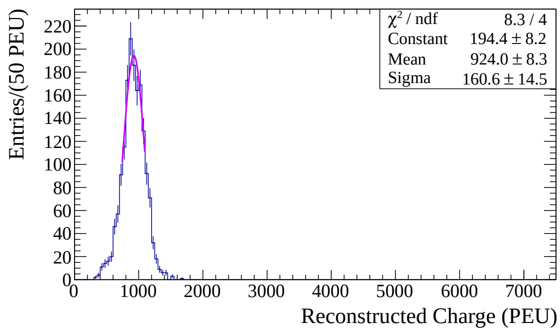

(a) 100 to 120 MeV

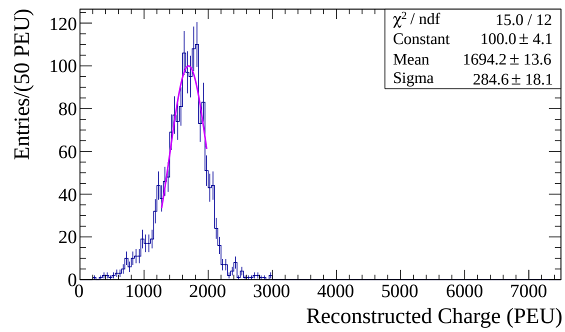

(b) 200 to 220 MeV

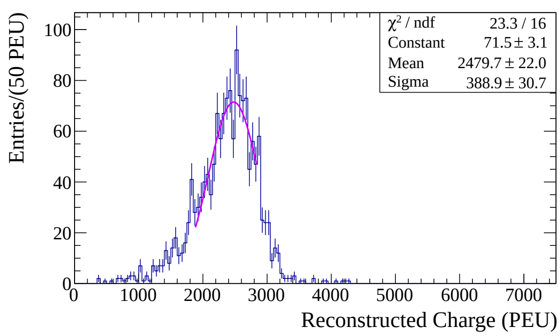

(c) 300 to 320 MeV

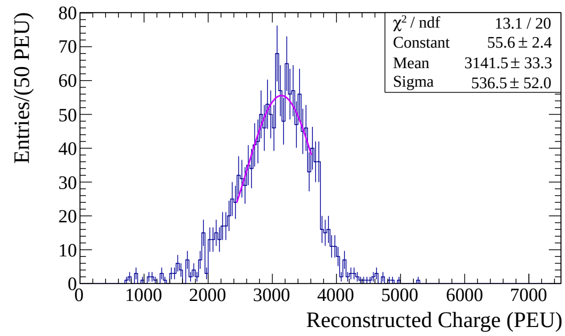

(d) 400 to 420 MeV

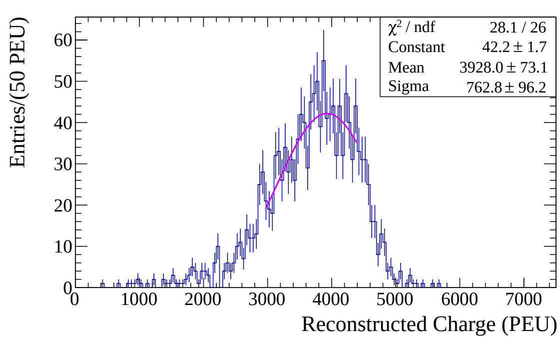

(e) 500 to 520 MeV

Figure 3.21: Examples of the Gaussian fits performed on each energy bin for the water-out water target configuration.

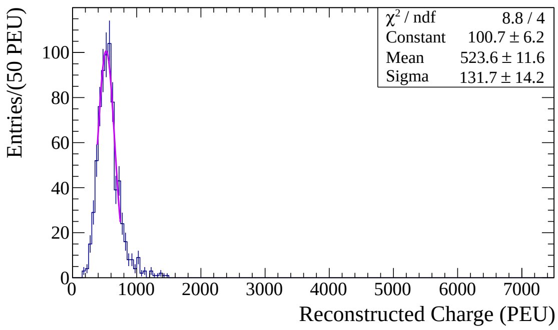

(a) 100 to 120 MeV

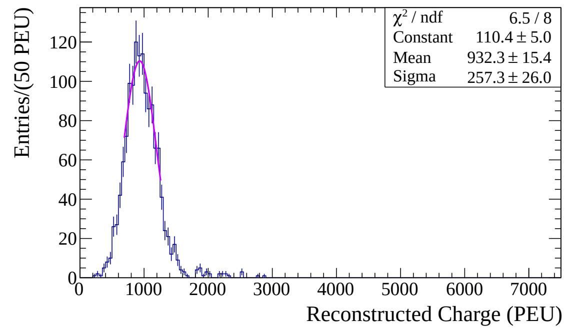

(b) 200 to 220 MeV

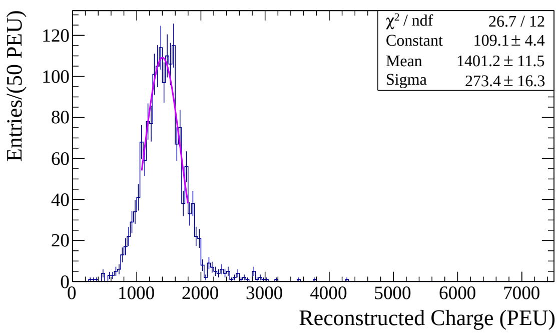

(c) 300 to 320 MeV

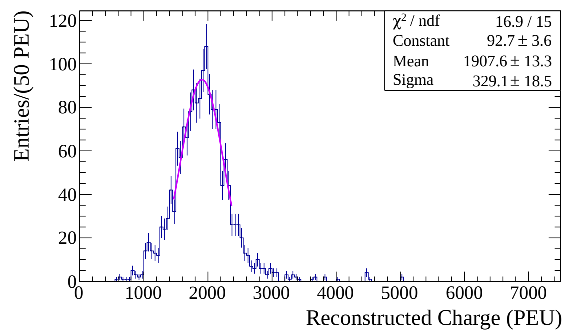

(d) 400 to 420 MeV

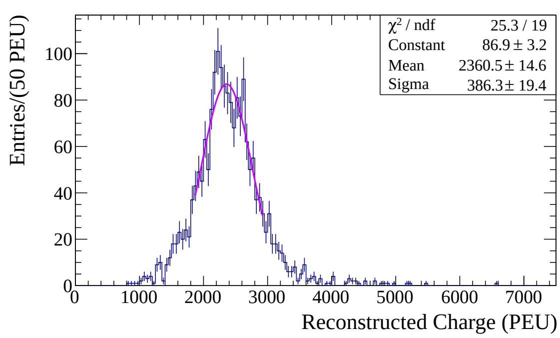

(e) 500 to 520 PEU

Figure 3.22: Examples of the Gaussian fits performed on each energy bin for the ECal-only configuration.

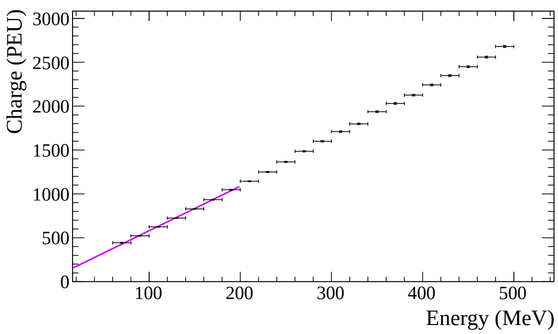

(a) Water-in Configuration

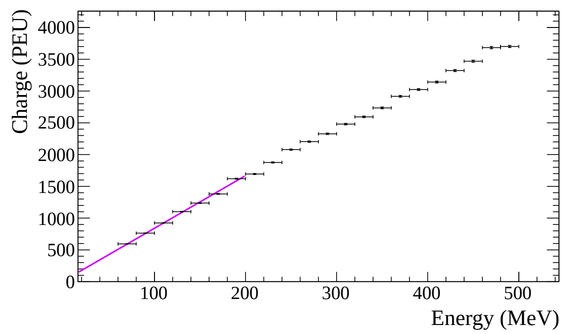

(b) Water-out Configuration

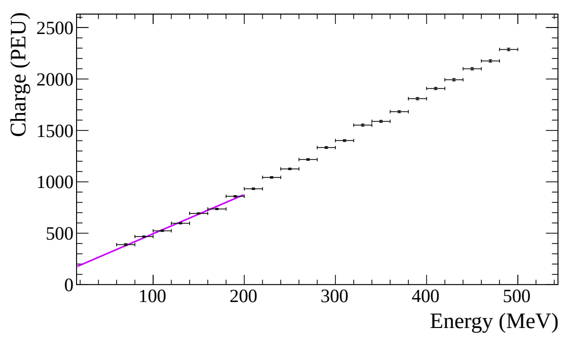

(c) ECal Only Configuration

Figure 3.23: The linear fits of the means from the Gaussian fits of the energy bins of Figure 3.18.

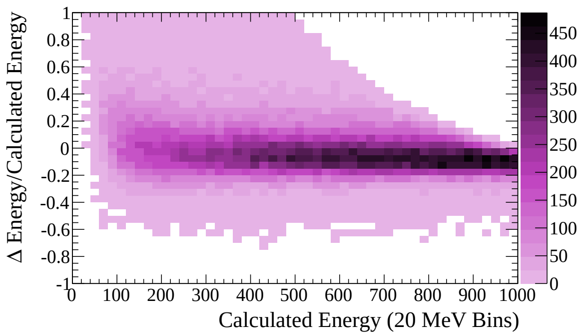

(a) Water-in Configuration.

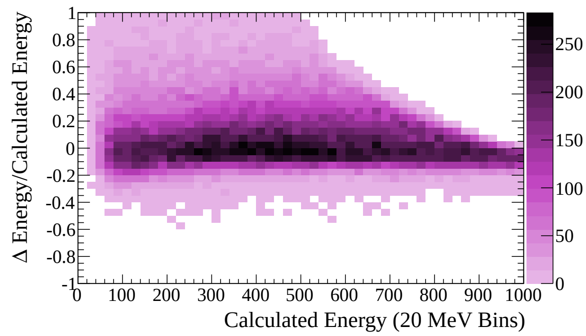

(b) Water-out Configuration.

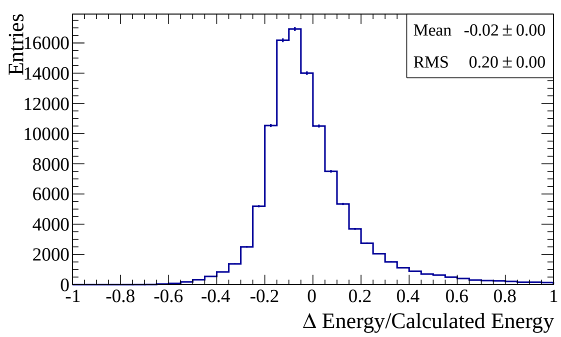

(c) Water-in Configuration.

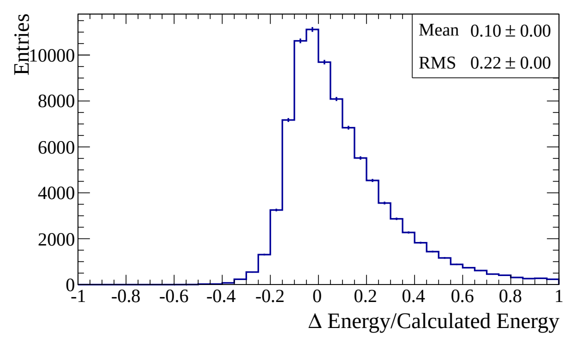

(d) Water-out Configuration.

Figure 3.24: The fractional accuracy of the estimated energy is shown. The two dimensional plots show good consistency throughout the calculated energy scale. There is a long tail due to reconstruction efficiencies present at low energies. The one dimensional plots show an overall mean or peak close to zero as expected, with an RMS of approximately 20%.

Resolution

Using the energy conversion listed in Table 3.9, the accuracy and resolution of the equation above can be examined. Figure 3.24 shows the fractional accuracy of the estimated energy ($(E_{est} - E_{true})/E_{est}$) versus the estimated energy for photons. Ideally, for all estimated energies, all points would be at zero on the Y axis, indicating that the estimated energy is exactly the same as the true energy.

Figures 3.25 show the fractional accuracy of the estimation ($((E_{true} - E_{est}/E_{est}))$, from the Gaussian and median fits respectively, against the true energy for photons. Again this distribution should be flat along the null line of the Y axis. A good consistency over the true energy range and good approximations of the true value is shown. In particular, the low energy values (the range of 50 to 200 MeV) appear to be well predicted, as can be seen in the profile plots.

In Figures 3.26, the accuracy of the true energy is plotted against the corrected charge for photons. These plots, in conjunction with the one dimensional plots in Figure 3.25 can be used to get an idea of the energy resolution. The widths of the one dimensional projections show that the energy resolution is around 20%.

Charge Addition

To check the energy scale response for varied positions in the P∅D, 20,000 monoenergetic events were generated. These events were generated at 200, 300 and 500 MeV for photons. The vertices were generated in a smeared box that starts in the upstream-most layer in the water target and ends at the downstream end in the ECal for both of the water-in and water-out configurations. For these monoenergetic studies, all of the generated charge is required to be in the P∅D, which leads to a loss of statistics in the ECal due to exiting events. The events then go through the same process and selection described in Section 3.5.1. At the end of processing, the estimated energy is calculated for the water target portion of the total energy and the ECal portion of the total energy. The sum of the energy deposit in the ECal and the water target should be the same, no matter what the fraction of the energy is in the water target. For the purpose of display, any event that was only in the water target or only in the ECal was discarded. In addition, the Z-axis is plotted with a log scale to emphasize the shape of the distribution. This allows the topology of the plots to focus on the area of interest, the mixture of charge deposit in the water target and in the ECal. The response to the mono-energetic study is shown in Figures 3.27 and 3.28.

These results of the monoenergetic study are summarized in Tables 3.10. The overall trend of the two dimensional plots shown in Figures 3.27 and 3.28 is linear, showing that this method of adding the charge deposit with individual energy conversions is an acceptable way to estimate the energy. For the P∅D NC1π^0 analysis, the energy conversion calculated here is considered an approximation and a separate energy scale is fit again in the final invariant mass fit.

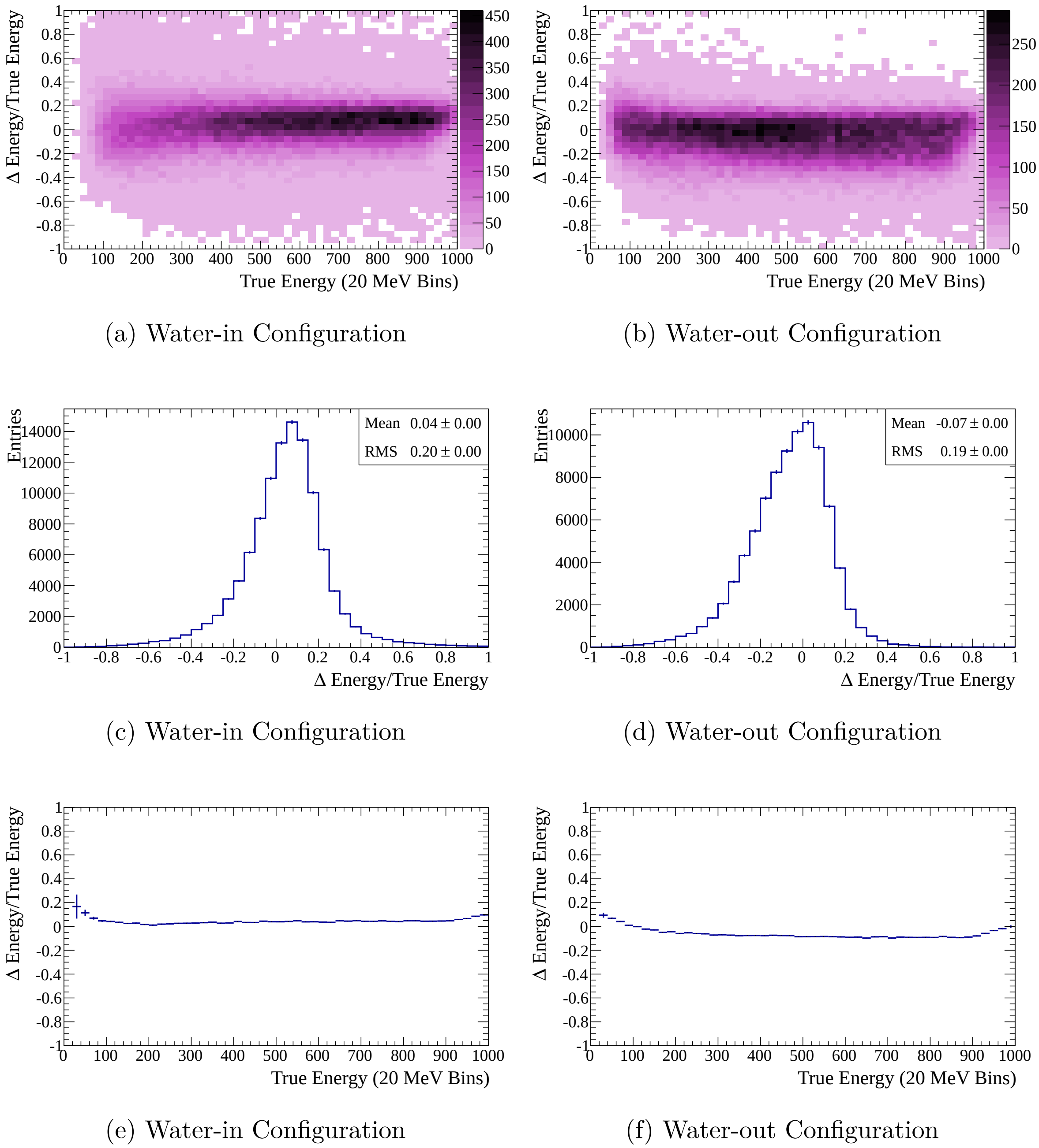

(a) Water-in Configuration

(b) Water-out Configuration

(c) Water-in Configuration

(d) Water-out Configuration

(e) Water-in Configuration

(f) Water-out Configuration

Figure 3.25: The response of the estimation against the true energy. The two dimensional plots show good consistency throughout the true energy scale. The one dimensional plots show an overall mean and peak close to zero as expected, with an RMS of approximately 20%. The profile plots show a slight variation at the low energy region, but energies between 50 and 200 MeV are of most concern to the NC1π^0 analysis which appear to be accurate.

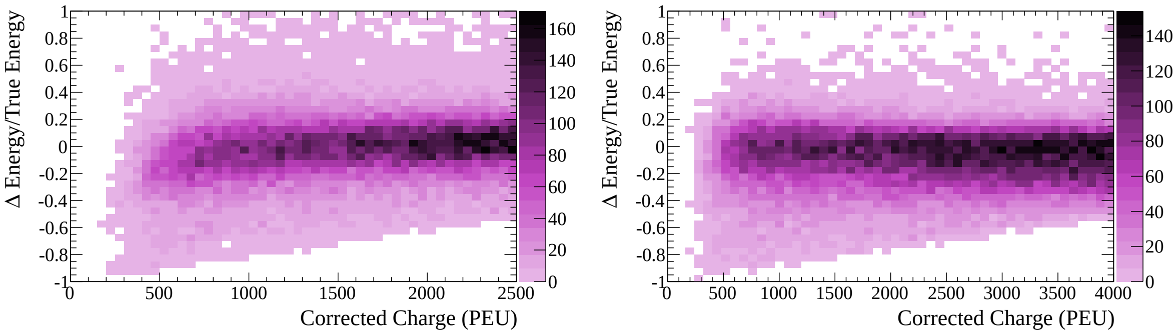

(a) Water-in Configuration (b) Water-out Configuration

Figure 3.26: The response of the estimation against the corrected charge deposit is shown. The two dimensional plots show good consistency throughout the corrected charge deposit scale for the water-out configuration. Some efficiency loss is shown in the water-in configuration. The one dimensional plots are shown in Figure 3.25.

Table 3.10: A summary of the mono-energetic study. The values for the energy and the RMS columns come from the mean and RMS of the one dimensional plots in Figures 3.27 and 3.28. The accuracy column is the reconstructed mean energy divided by the true energy. The resolution column is the RMS of the reconstructed energy divided by the reconstructed energy. The first row for each configuration show the average accuracy and resolution of the individual mono-energetic studies.

	True Energy (MeV)	Energy (MeV)	RMS (MeV)	Accuracy %	Resolution %
Water In				105.5 ± 0.2	19.4 ± 0.1
	200	207.5 ± 0.7	52.0 ± 0.5	103.8 ± 0.4	25.1 ± 0.3
	300	313.8 ± 1.0	62.7 ± 0.7	104.6 ± 0.3	20.0 ± 0.2
	500	540.0 ± 1.7	70.1 ± 1.2	108.0 ± 0.3	13.0 ± 0.2
Water Out				102.7 ± 0.3	18.3 ± 0.2
	200	204.6 ± 0.8	44.1 ± 0.6	102.3 ± 0.4	21.6 ± 0.3
	300	305.4 ± 1.5	60.7 ± 1.1	101.8 ± 0.5	19.9 ± 0.4
	500	520.7 ± 3.2	69.9 ± 2.3	104.1 ± 0.6	13.4 ± 0.4

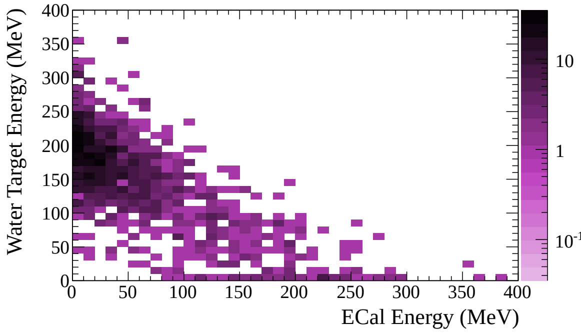

(a) 200 MeV: Sum of Reconstructed Energy

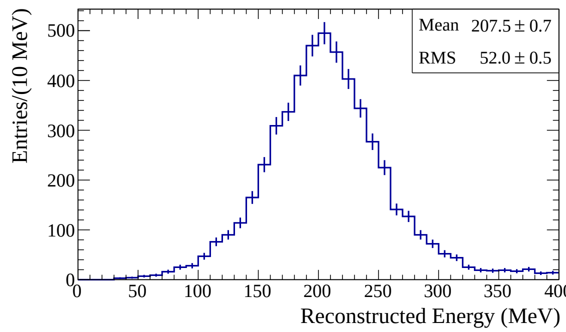

(b) 200 MeV: Total Reconstructed Energy

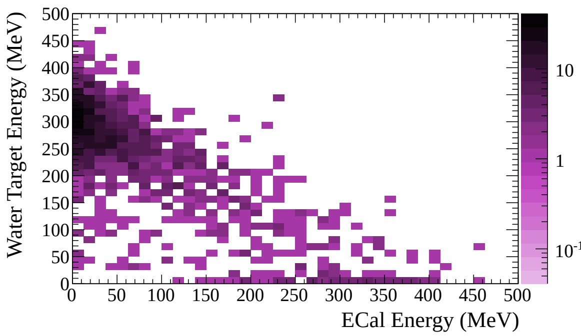

(c) 300 MeV: Sum of Reconstructed Energy

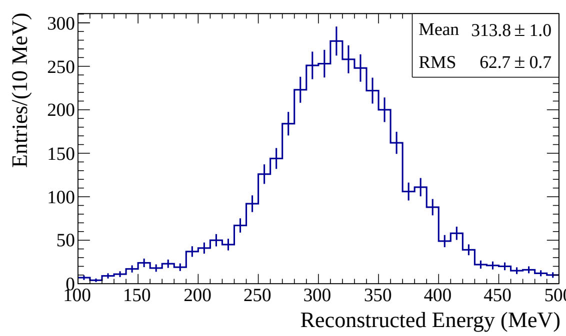

(d) 300 MeV: Total Reconstructed Energy

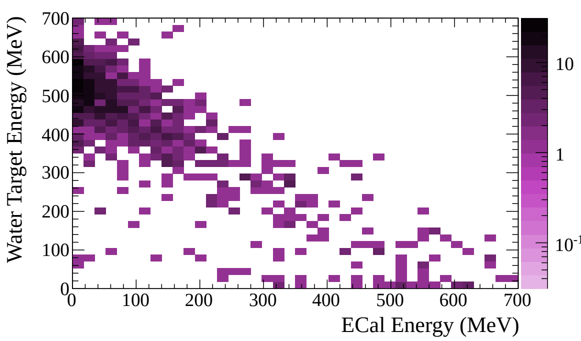

(e) 500 MeV: Sum of Reconstructed Energy

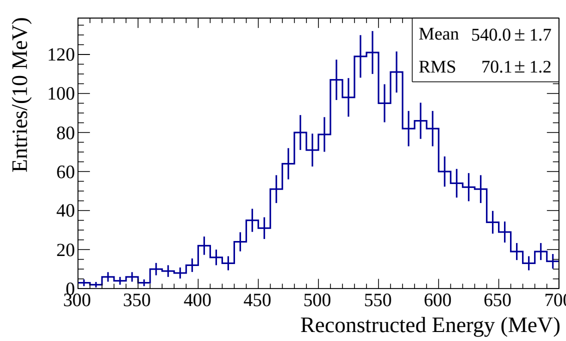

(f) 500 MeV: Total Reconstructed Energy

Figure 3.27: The results of the mono-energetic test of the energy scale for the water-in configuration.

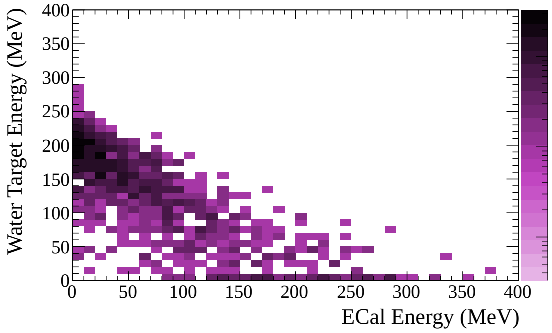

(a) 200 MeV: Sum of Reconstructed Energy

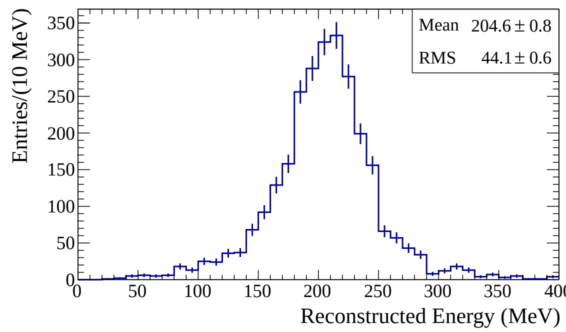

(b) 200 MeV: Total Reconstructed Energy

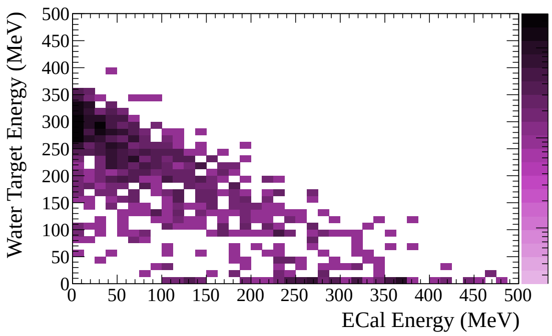

(c) 300 MeV: Sum of Reconstructed Energy

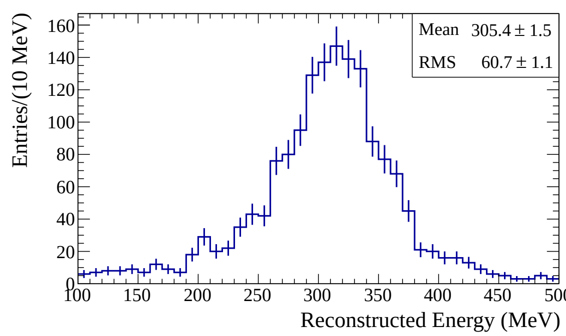

(d) 300 MeV: Total Reconstructed Energy

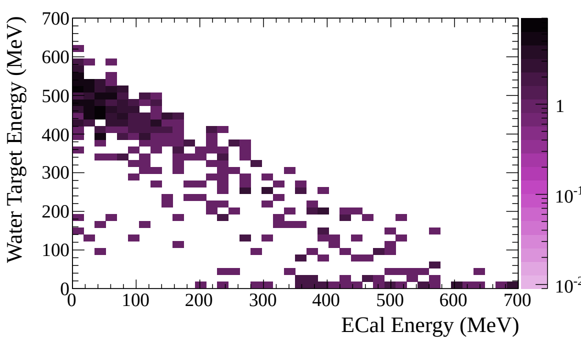

(e) 500 MeV: Sum of Reconstructed Energy

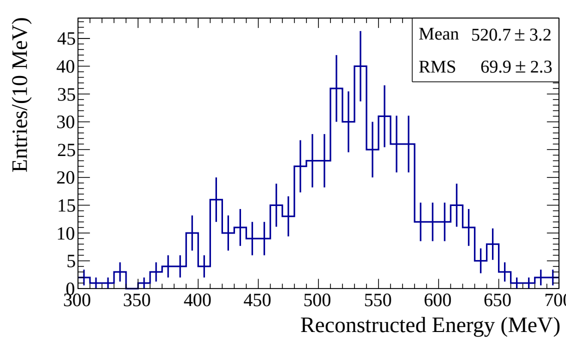

(f) 500 MeV: Total Reconstructed Energy

Figure 3.28: The results of the mono-energetic test of the energy scale for the water-out configuration.

3.6 P∅D Alignment

What follows is a description of the methods and validation for the alignment of the P∅D. First, the hit resolution of the X and Y layers must be determined to give a limit on the alignment precision. The process of finding the hit resolution for both doublet and singlet hits is detailed in Section 3.6.1. After that discussion, the method of alignment, including the process of selecting events for alignment, is explained. As a cross-check on the alignment method, a survey of the external position of the P∅Dules was completed in the fall of 2010. The initial alignment study was completed before the Great East Japan Earthquake and Disaster in 2011. After which it was necessary to do a brief audit which found that no significant displacement of the P∅Dules occurred.

3.6.1 P∅D Layer Resolution

Both the process for finding the single hit resolution and for determining the alignment constants use the same event selection. In order to attain straight tracks through the detector, cosmic ray runs were taken with the UA1 magnet turned off. The first step in the selection process it to loop through each active data-taking time cycle recorded. There must be one and only one 3D matched track in the P∅D, which reduces noise hits from other tracks from interfering with the track of interest. The track must have hits in both the first and last P∅Dule, which provides the longest lever arm for alignment and reduces the uncertainty in the angle of the track. In order to include as many hits as possible, the unused hits from the reconstruction are utilized. The unused hits within one centimeter in the Z direction and four centimeters in the X or Y directions of any hit in the reconstructed track, the unused hit is saved to the track hit selection. The hits from individual bars are clustered together by XZ or YZ layers to form a single charge weighted hit. This single charge-weighted hit is required to come from either a singlet or a doublet. A singlet is a hit or charge deposit in the detector that occurs in only one bar in a layer. A doublet is a charge deposit in two adjacent bars in a layer, the more likely scenario due to bar overlap. Requiring at most two hits per layer prevents any biases due to delta rays coming off the track. Additionally, the resolutions of singlets and doublets are of the most interest. Every layer must have at most one clustered hit which has the benefit of removing delta rays as well as reducing fitting error. At this point, the event is saved and will be used to produce alignment constants and to study the single hit resolution.

Due to the triangular geometry of the scintillator bars, deriving the ideal resolution is difficult. Thus, to find the ideal single hit resolution, a particle gun Monte Carlo was used. Using v8r5p13 of the ND280 Software, one thousand 10GeV muon events were generated along the Z-axis through the P∅D. The Z-axis was chosen because it will give a minimum limit to the resolution of the P∅D since there is a slight angular dependence to the resolution and it coincides with the general beam direction. The sample that was used was constructed with a perfect geometry. The events were run through Monte Carlo particle gun simulation, electronic noise simulation and finally the P∅D reconstruction. A self-made program was used to extract the P∅D reconstruction information used in this study.

The clusters of hits, previously explained, are fit to two two-dimensional lines, one in the XZ projection and one in the YZ projection. The fit result is used to calculate the residual

Table 3.11: The measured resolutions of both layers for data and Monte Carlo. All errors are statistical.

Layer	Data		Monte Carlo	
	Singlet (mm)	Doublet (mm)	Singlet (mm)	Doublet (mm)
X	2.57 ± 0.11	2.46 ± 0.06	2.27 ± 0.03	2.51 ± 0.02
Y	3.13 ± 0.12	2.78 ± 0.06	2.23 ± 0.03	2.43 ± 0.02

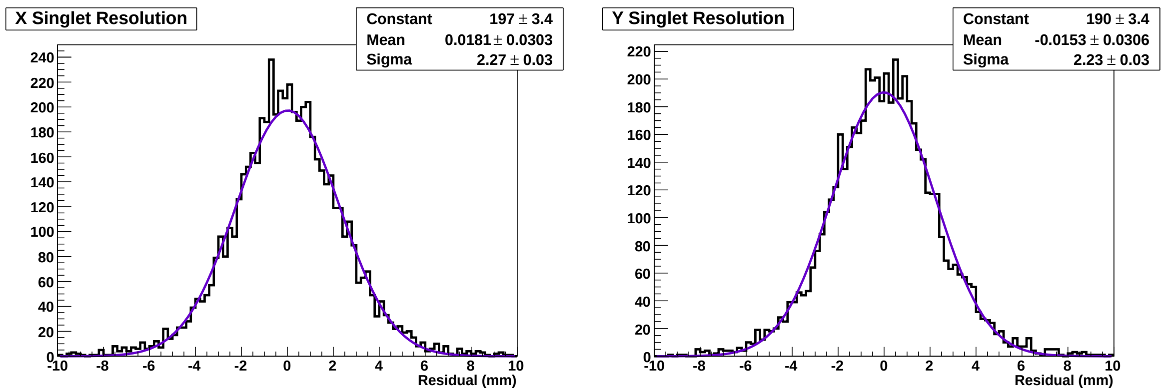

(a) X Layers. (b) Y Layers.

Figure 3.29: The Monte Carlo predicted resolution of a singlet in the P∅D. The errors are purely statistical.

distance to the layer hit. Figures 3.29 and 3.30 show the ideal Monte Carlo singlet and doublet resolutions for the X and Y Layers. These values represent the best resolution it is possible to achieve. For data, the in situ singlet and doublet resolutions are shown in Figures 3.31 and 3.32 for the X and Y layers. The results from this study are summarized in Table 3.11

3.6.2 Internal Alignment

After selecting a 3D track, graphs of the residuals for the hits in each P∅Dule are made. The displacements in X and Y of the P∅Dules are calculated from the mean of the residual distributions. These numbers were saved and uploaded to the database to realign the geometry before reconstruction.

To test the accuracy of this method, a particle gun Monte Carlo was used. One thousand 10GeV muon events were created in the +Z direction and processed with a misaligned geometry. The point of this endeavor was to see if this method could extract the correct constants. Figure 3.33 presents the results. The graph shows the difference between the misalignments programmed into the geometry and the alignment constants that resulted from this alignment process. The fluctuation of the difference is related to the systematic error of the alignment which is 0.5 mm. The standard deviation of the values is 0.10 mm in

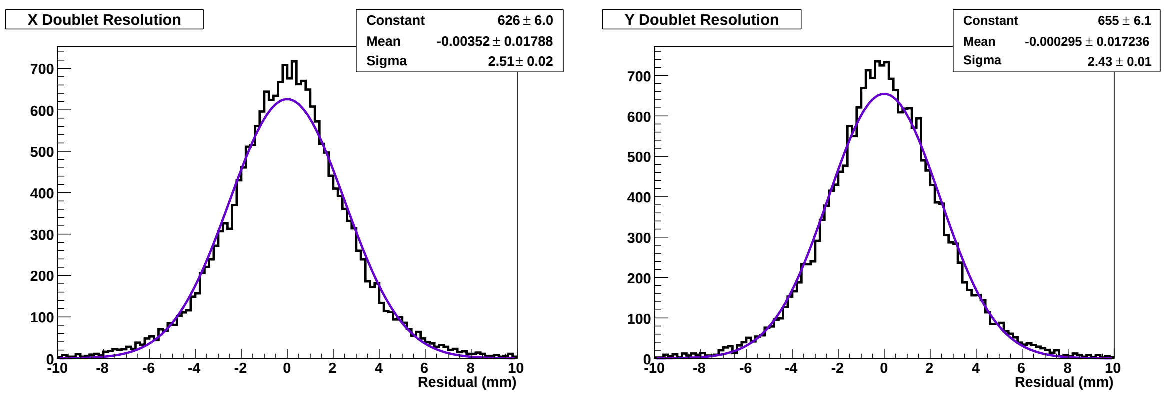

(a) X Layers.

(b) Y Layers.

Figure 3.30: The Monte Carlo predicted resolution of a doublet in the P∅D. The errors are purely statistical.

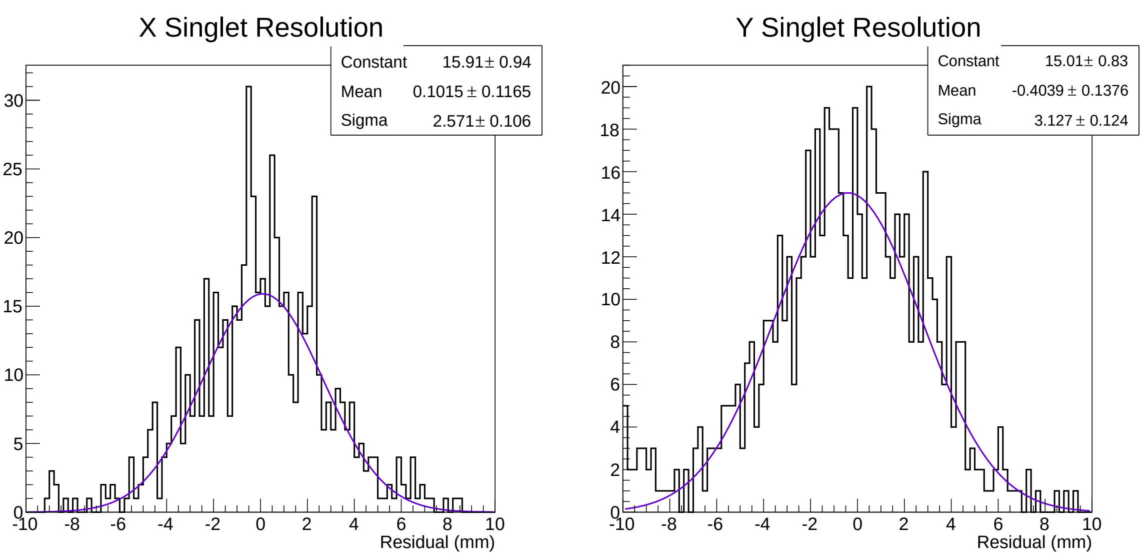

(a) X Layers.

(b) Y Layers.

Figure 3.31: The measured data resolution of a singlet in the P∅D. The errors are purely statistical.

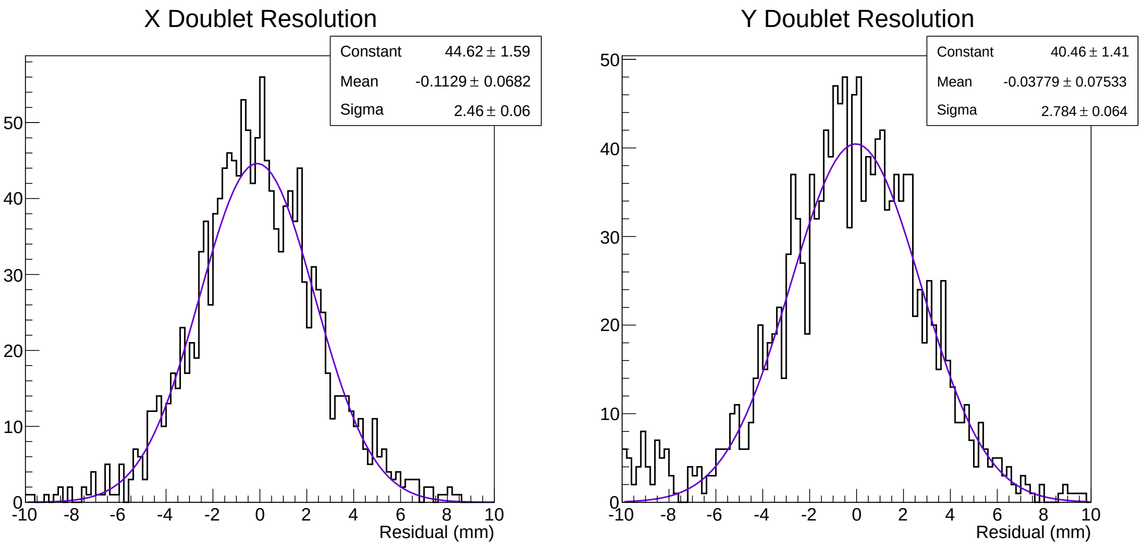

(a) X Layers. (b) Y Layers.

Figure 3.32: The measured data resolution of a doublet in the P∅D. The errors are purely statistical.

X and 0.08 mm in Y.

To find the alignment parameters, Run 4863 Subrun 0 was processed through version v9r7p9 of the ND280 software. For Run 4863, the magnet was turned off and the trigger was set to accept cosmics. Figure 3.34 shows the alignment parameters for the layer by layer alignment. The program found fifty-six useful tracks in this subrun, which is around 30 minutes of data taking. The layer-by-layer variation over the whole P∅D is on order with the resolution of the detector. This means that in situ, the internal P∅D alignment in the geometry is close to the ideal resolution of the detector.

3.6.3 Alignment to the TPC

In order to align the P∅D to TPC1 (the TPC that is adjacent to the upstream end of the P∅D), tracks must be selected that cross the barrier between the two detectors. Several selection criteria are required. One and only one 3D matched track in one time cycle in the P∅D is required to reduce noise hits from other tracks interfering with the track. The track must start before the CECal and go through last P∅Dule which increases the probability of the track having enough momentum to continue into TPC1. The last node of the reconstructed track in the P∅D must contain information both in the X and Y directions. A node is a reconstructed object that describes the position and direction of the hits in the two adjacent layers of the P∅Dule. One and only one object in TPC1 is allowed. The time, position and direction of the last node of the P∅D and the first node of the TPC are saved from these events.

First, is a cut based on the difference in the Z-direction between the last node of the P∅D and the first node of the TPC. Next, the events are cut on the angular difference between the direction of the P∅D node and the TPC node. This is done to prevent any kinks, due to

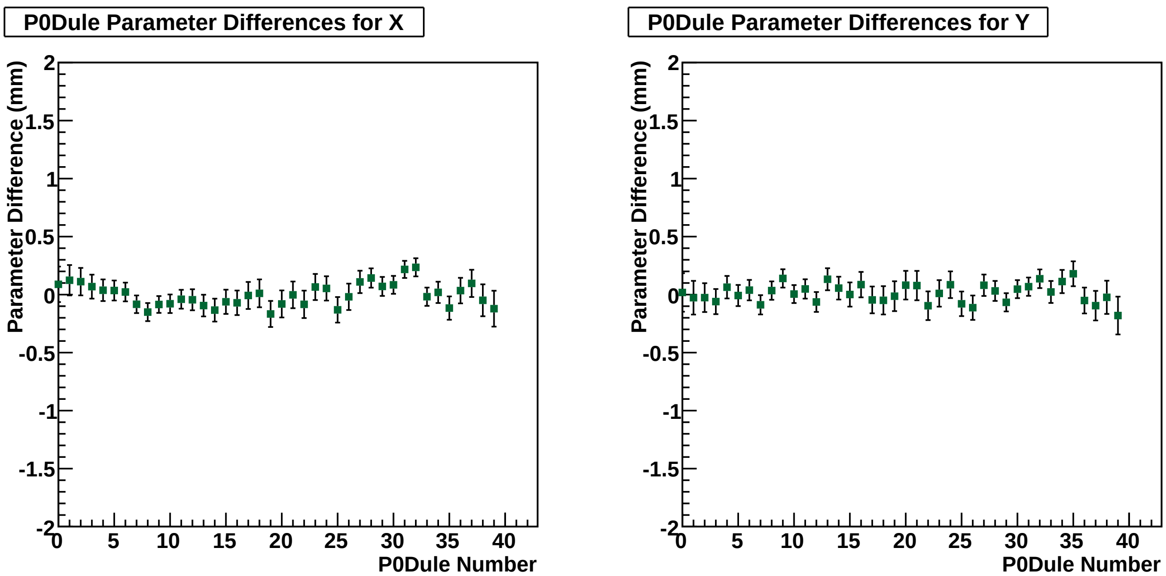

Figure 3.33: The difference between parameters forced on the geometry and the parameters acquired from the full P∅D alignment method.

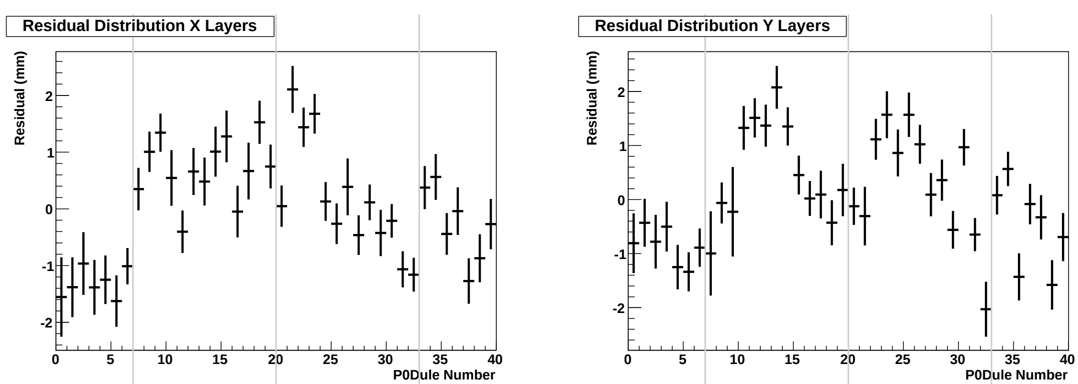

(a) X Layers.

(b) X Layers.

Figure 3.34: Parameters acquired as a result of the P∅D alignment method on Run 4863 Subrun 0. The gray lines mark the divisions of the SuperP∅Dules.

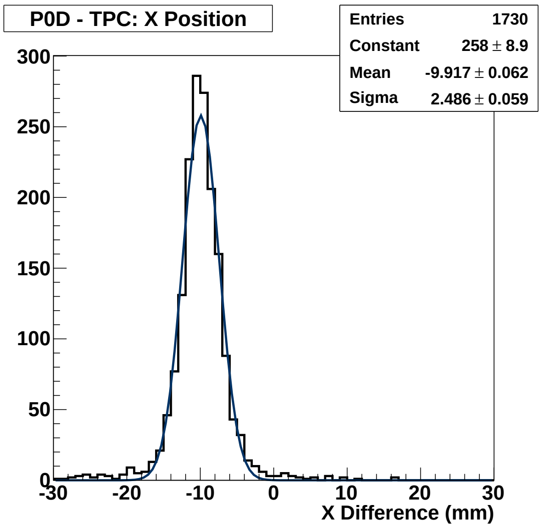

(a) X Direction.

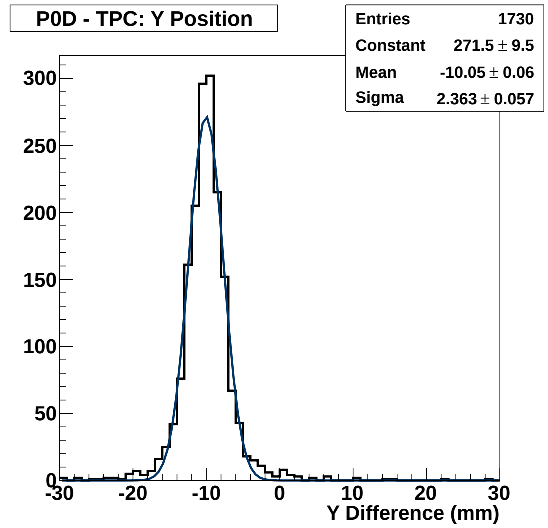

(b) Y Direction.

Figure 3.35: The parameters retrieved from the external alignment process using Monte Carlo particle guns after forcing the PØD to be −10 mm in both the X and Y directions.

possible scattering, that might affect the final result. In order to make the final evaluation, the TPC node is propagated to the same Z position of the PØD node by extrapolating a straight line utilizing the direction associated with the TPC node. The extrapolated TPC position is then subtracted from the PØD position and plotted in histograms. The histograms are then fit to gaussian curves in order to extract the alignment constants.

To test the matching code, twenty five thousand 1GeV muons were produced in the +Z direction using a particle gun monte carlo. At the reconstruction stage, the file was reconstructed three times with three different geometries. These geometries have no misalignment, a −5 mm offset in both X and Y in the PØD, and a −10 mm offset in both X and Y in the PØD. In Figure 3.35, the results from the 10 mm test are shown. The results show that the PØD need to be moved +10.0 mm in the X direction and +9.9 mm in the Y direction to return to the original position. A similar accuracy was present in the other trials. Given the precision of the trials, a systematic error of ±0.5 mm is assigned.

Using 382 tracks from Run 4863 Subrun 0, the in situ external alignment was calculated. Figure 3.36 shows that in the Monte Carlo geometry, the PØD needs to be moved 3.5 ± 0.2(stat) ± 0.5(sys) mm in the -X direction and 13.1 ± 0.3(stat) ± 0.5(sys) mm in the -Y direction. For Production 5 of the near detector software, the active center of the PØD has been moved in the Monte Carlo geometry to the coordinates $(-35.7, -0.7)$.

3.6.4 Alignment Survey Measurements

In the fall of 2010, a survey using a laser level (Stanley 77-154 SP5 FatMax Five Beam Laser Kit by CST/Berger) was conducted. The company that made the level claimed an accuracy of $\frac{1}{4}$ inch at 100 feet. After some on-site testing, the level was assigned a systematic error of 1 mm over six feet. The laser was designed to be self leveling and to have a

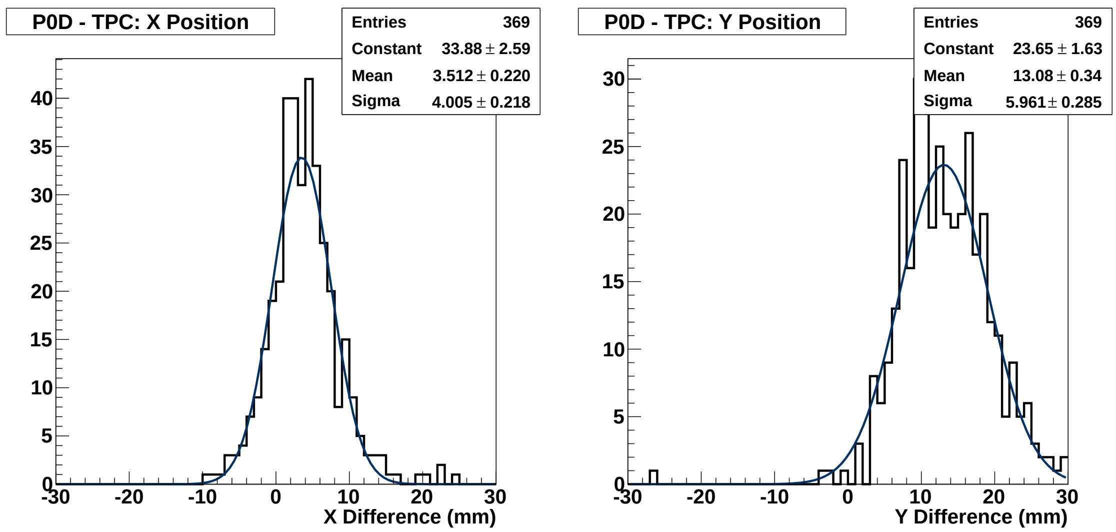

(a) X Direction. (b) Y Direction.

Figure 3.36: Result of TPC-P∅D matching on Run 4863 Subrun 0. This indicates that the P∅D needs to be moved to the north (-X) 3.5 ± 0.2 mm and down (-Y) 13.1 ± 0.3 mm.

beam emitted in five directions. Measurements of the accessible bottom parts of the P∅D along the north and south edges and the accessible north side of the P∅D were taken. For some P∅Dules, an additional measuring tool was used with an assumed 1 mm systematic uncertainty. The measurements made with the ruler had an error of 0.5 mm.

P∅D Bottom Survey

There were two surveys conducted of the bottom of the P∅D. One survey was a comparison to fixed points on the TPCs, the other was a comparison within the P∅D. The global survey was done by sending a laser line down the north side of the detectors and another laser was sent down the south side of the detectors. Using a ruler, fixed points on the outer casings of the P∅D and the TPCs were directly compared. The findings are summarized in Table 3.12. The measurements of the north and south side were done independently and the error on the measurement is 1.1 mm due to the error in the laser and the error in the measurement with a ruler. The surveyed positions were the bottom of the first and last P∅Dules and the aluminum bracket on the bottom of the TPCs. The hope was that a prior professional survey of the TPCs could be extrapolated to the P∅D with these measurements. The north and south side measurements were taken independently and are separately normalized.

A more detailed survey of the bottom of the P∅D is shown in Figure 3.37. In order to conduct this survey, the laser was located at two points: the north-east corner of the P∅D and the south-east corner of the P∅D. Due to the inaccessibility of the part of the bottom of the P∅D, only eighteen P∅Dules on the north side and six P∅Dules on the south side could be measured. The error on these measurements is 1.1 mm. In Figure 3.37, the north side, the south side and the calculated parameters from Figure 3.34 are presented. The three sets are artificially placed so that their averages are zero.

Table 3.12: A P∅D survey taken in reference to the TPC. The Upstream plate of TPC1 was chosen as the reference point. The Upstream(Downstream) measurements are signified by a U(D).

	P∅D		TPC1		TPC2		TPC3	
	U (mm)	D (mm)	U (mm)	D (mm)	U (mm)	D (mm)	U (mm)	D (mm)
North	1	5	0	-2	-3	-3	-4	-4
South	3	3	0	0	-1	-1	-1	-2

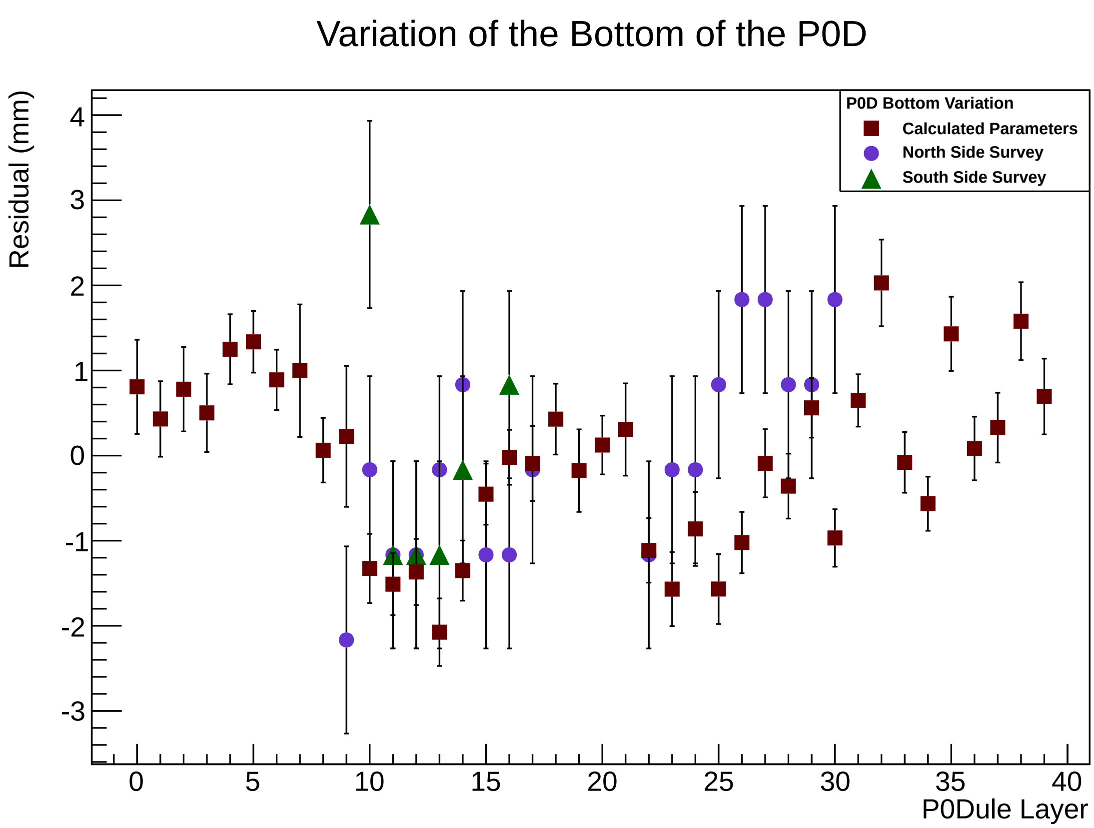

Figure 3.37: Measurements of the variation of the P∅Dules' Y position along the bottom side of the P∅D. The graph includes the north side survey (blue circle), the south side survey (green triangle) and the calculated parameters (red square) from the alignment procedure. The average of each set is artificially fixed at 0mm.

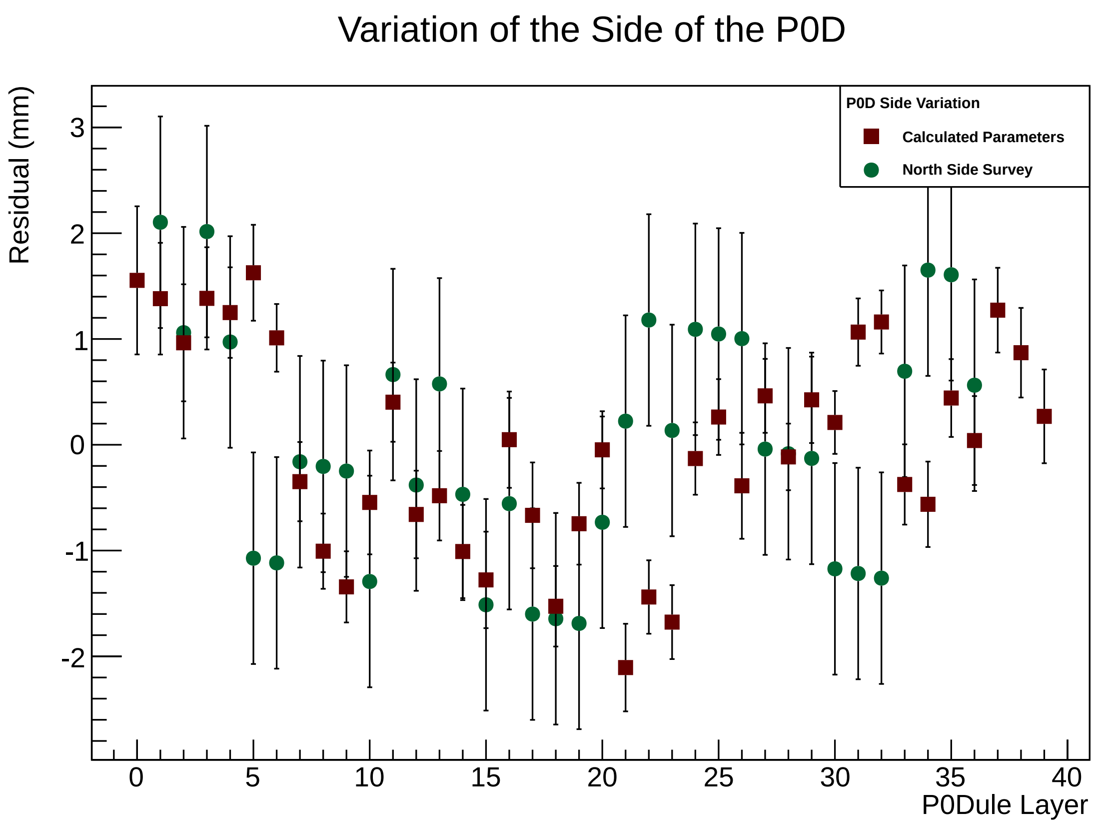

Figure 3.38: Measurements of the variation of the P∅Dules' X position along the north side of the P∅D. The graph includes the survey along the north side (green circle) and the calculated parameters (red square) from the alignment procedure. The average of each set is artificially fixed at 0mm.

P∅D North Side Survey

For this survey, the laser was set up along the north-west corner, arranged so that the beam traveled along the north side of the P∅D. Since there was no way to get a laser line perfectly parallel to the side of the P∅D, this was corrected by subtracting a linear offset determined by the distances. This way, the average position of the side of the P∅D would be zero and the laser line could be artificially adjusted to be parallel to the P∅D. Figure 3.38 is the result of this manipulation. Overlaid on the survey results are the calculated parameters from Figure 3.34.

Chapter 4

NC1π^0 Rate Measurement

For this analysis, the signal is defined by the final state particles. The final state interactions remain uncorrected by the Monte Carlo. One π^0 particle is required to exit the nucleus with no other leptons or mesons. Any number of protons and neutrons are allowed to be present.

The goal of this analysis is three-fold. The first two goals are to find the ratios of data to Monte Carlo of the rate of NC1π^0 events that occur on the P∅D water target for both the P∅D water-in and water-out configurations. The number of events in the P∅D water-in and P∅D water-out configurations are represented as $N_{NC1\pi^0,\text{ Water-In}}$ and $N_{NC1\pi^0,\text{ Water-Out}}$ respectively. These numbers are extracted using an unbinned extended maximum likelihood fit to the reconstructed π^0 invariant mass distribution. The last goal is to find the ratio of data to Monte Carlo of the rate of NC1π^0 events, $N_{NC1\pi^0,\text{ On-Water}}$, that occur on-water from a subtraction of the results of the water-in and water-out measurements.

The general formula for the number of observed events, N_{Obs} can be expressed as

$$N_{\text{Obs}} = \epsilon \cdot \phi \cdot \sigma \cdot t \cdot N_{\text{Target}}, \tag{4.1}$$

where ϵ is the efficiency, ϕ is the flux, σ is the cross section, t is the time exposure, and N_{Target} is the number of target nuclei. The total number of signal events in the water-in configuration can be divided into two parts,

$$N_{\text{Water-In}} = N_{\text{On-Water}} + N_{\text{Not-Water}}, \tag{4.2}$$

where $N_{\text{Not-Water}}$ is the number of single events that occur not on the water in the water-in configuration This number can be related to the water-out configuration measurement, since the target and cross section are the same. Additionally, the flux times the exposure ϕt can simply be expressed as the number of incident neutrinos, N_ν. However, this number is proportional to the number of protons on target (POT). Given this information, the measurement for the number of signal events in the water-out configuration can be related to the number of not-water signal events in the water-in configuration as

$$\sigma_{\text{Not-Water}} N_{\text{Target, Not-Water}} = \frac{N_{\text{Not-Water}}}{\epsilon_{\text{Not-Water}} N_{\nu,\text{ Not-Water}}} = \frac{N_{\text{Water-Out}}}{\epsilon_{\text{Water-Out}} N_{\nu,\text{ Water-Out}}}. \tag{4.3}$$

Table 4.1: Summary of beam specifications used in the Monte Carlo generation.

Beam	Power (kW)	Repetition (s)	POT/Spill (x 10^{13})	Bunch	Duration (ns)
A	50	3.52	3.6617	6	17
B	120	3.2	7.9891	8	19
C	178	2.56	9.463	8	19

Table 4.2: Summary of Run 1 through Run 4 POT used in this analysis. The beam configurations listed reflect the Monte Carlo sample that is used to model the run.

Run	P∅D Water Configuration	Beam Configuration	Run Numbers	POT
1	In	A	4165 - 5115	2.96×10^{19}
2	In	B	6462 - 7663	6.96×10^{19}
2	Out	B	7665 - 7754	3.59×10^{19}
3	Out	B	8360 - 8360	5.65×10^{15}
3	Out	C	8550 - 8753	1.35×10^{20}
4	In	C	8995 - 9413	1.65×10^{20}
4	Out	C	9426 - 9798	1.78×10^{20}

This can be rearranged to

$$N_{\text{Not-Water}} = \frac{\epsilon_{\text{Not-Water}} N_{\nu,\text{ Not-Water}}}{\epsilon_{\text{Water-Out}} N_{\nu,\text{ Water-Out}}} N_{\text{Water-Out}} = \frac{\epsilon_{\text{Not-Water}} \text{POT}_{\text{Not-Water}}}{\epsilon_{\text{Water-Out}} \text{POT}_{\text{Water-Out}}} N_{\text{Water-Out}}. \tag{4.4}$$

The number of POT for not-water is the same as the number of POT for the water-in configuration. Finally, using the efficiencies calculated by the Monte Carlo, the POT delivered for the run period, and the results of the fits, the number of on-water vertices can be determined by

$$N_{NC1\pi^0,\text{ On-Water}} = N_{NC1\pi^0,\text{ Water-In}} - \frac{\epsilon_{\text{Not-Water}} \text{POT}_{\text{Not-Water}}}{\epsilon_{\text{Water-Out}} \text{POT}_{\text{Water-Out}}} N_{NC1\pi^0,\text{ Water-Out}}. \tag{4.5}$$

The final goal is to compare the data collected to the Monte Carlo prediction. To do this a ratio of data to Monte Carlo is examined. The ratio of rates on water is defined as

$$R_{NC1\pi^0,\text{ On-Water}} = \frac{N^{\text{Data}}_{NC1\pi^0,\text{ On-Water}}}{N^{\text{MC}}_{NC1\pi^0,\text{ On-Water}}}. \tag{4.6}$$

This measurement was performed using NEUT Monte Carlo from Production 5E and data collected from Run 1 to Run 4 processed with Production 5G. The measurement is conducted with the intention of inclusion in the 2014 BANFF oscillation analysis.

For the Monte Carlo simulation, there were three different beam configurations used, explained in Table 4.1. Tables 4.2 and 4.3 summarize the POT used in this analysis and

Table 4.3: Summary NEUT Monte Carlo POT used in this analysis.

Run	Monte Carlo Configuration	Beam Configuration	POT
1	2010-02-water	A	9.98×10^{20}
2	2010-11-water	B	1.31×10^{21}
4	2010-11-water	C	4.87×10^{21}
2/3b	2010-11-air	B	1.00×10^{21}
3c	2010-11-air	C	3.01×10^{21}

relates the Run periods to specific beam configurations. It is important to note that the beam A configuration uses 6 bunches per spill where the other configurations use 8 bunches per spill, fundamentally the biggest difference. As such, beam A events are selected under a different pre-selection than those from later periods.

This analysis uses an extended maximum likelihood fit on the invariant mass of the final selected sample selected from 0 to 500 MeV/c^2. This invariant mass window is chosen in order to extend past the π^0 mass peak in order to be able to fit the shape of the background. The selected events also have a fixed angular cut due to detector reconstruction at $\cos\theta_z > 0.5$. Additionally, this angle was chosen as it describes a track that will cross two of the triangular bars in a layer. Tracks or showers that are perpendicular to the beam direction do not contain as much X-Z and Y-Z information to be reconstructed in three dimensions well. Additionally, the reconstruction always reconstructs a vertex upstream of any activity. It is therefore difficult to reconstruct downstream-going particles and resolving their directions and momentum. In order to provide a better constraint on the shape of the background, the μ-decay sideband invariant mass is fitted simultaneously.

This chapter is split into three main sections. The first section describes the reconstruction efficiencies and resolutions. The next section describes the event selection with the following section describing the selection of which cut to use for the sideband in the fit. Then the discussion moves to the construction of the fit and the results.

4.1 Reconstruction of the NC1π^0

There were several reconstruction efficiencies of the NC1π^0 search studied. Of primary concern is the vertex resolution which enters in to the systematic errors discussed in Chapter 5. Figures 4.1 and 4.2 show the vertex resolutions in x, y and z for the water-in and water-

Table 4.4: The vertex position resolution and mean for the saved NC1π^0 events.

	$\langle x \rangle$ (cm)	σ_x (cm)	$\langle y \rangle$ (cm)	σ_y (cm)	$\langle z \rangle$ (cm)	σ_z (cm)
Water In	-0.06	5.52	0.06	6.06	1.67	8.65
Water Out	0.08	6.77	0.20	7.95	1.72	11.21

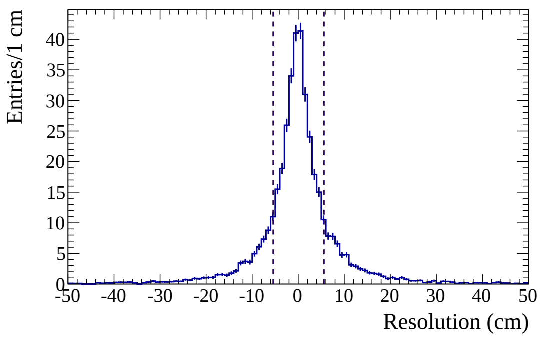

(a) Vertex X Resolution

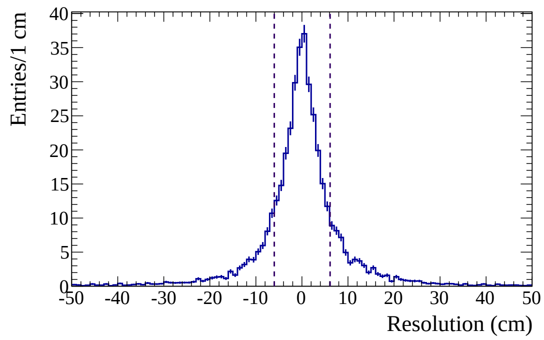

(b) Vertex Y Resolution

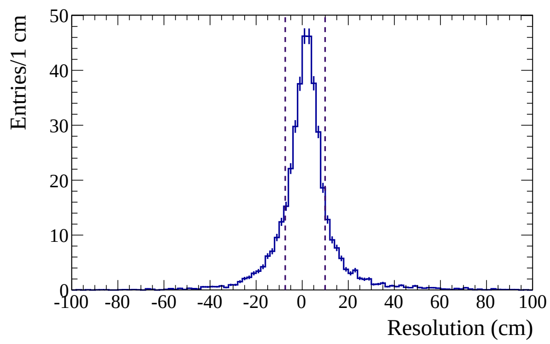

(c) Vertex Z Resolution

Figure 4.1: The NC1π^0 vertex resolution for the water-in configuration. The vertical lines correspond to the 16% and 84% quantiles.

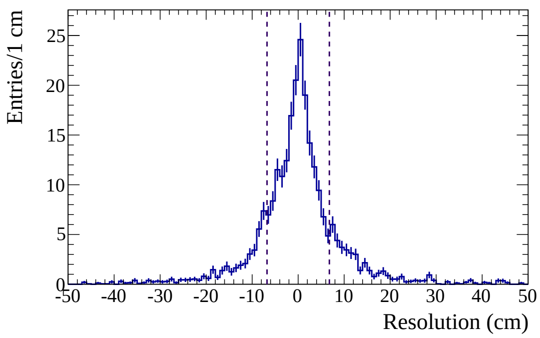

(a) Vertex X Resolution

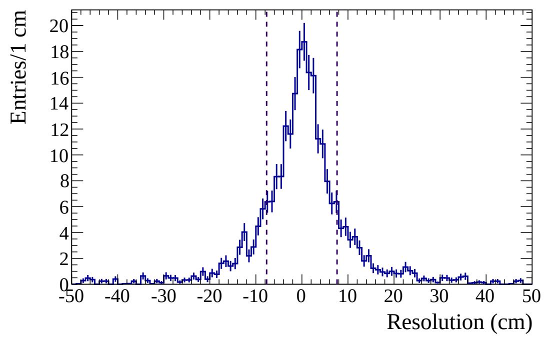

(b) Vertex Y Resolution

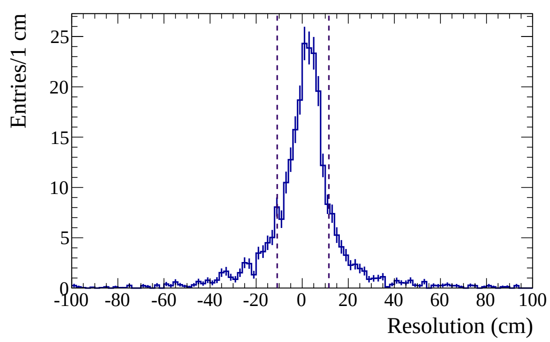

(c) Vertex Z Resolution

Figure 4.2: The NC1π^0 vertex resolution for the water-out configuration. The vertical lines correspond to the 16% and 84% quantiles

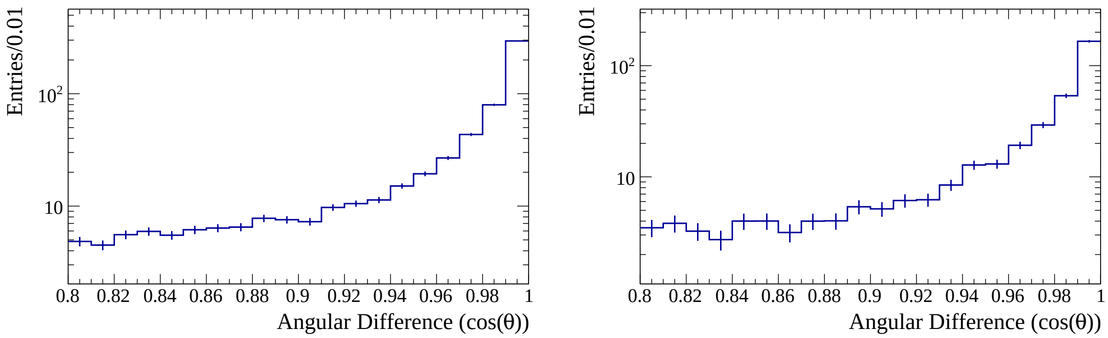

(a) Water-in configuration (b) Water-out configuration

Figure 4.3: The angular difference between the decay photon reconstructed and true directions for selected signal events.

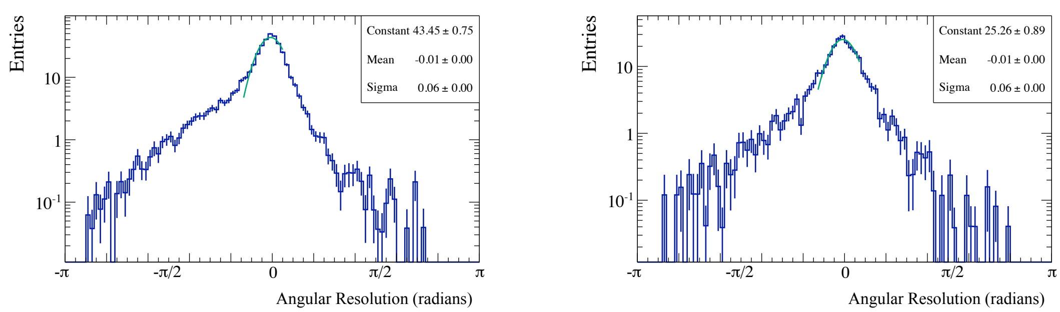

(a) Water-in configuration (b) Water-out configuration

Figure 4.4: The NC1π^0 opening angle angle resolution fit to a Gaussian curve.

out configurations of the P∅D respectively. The plots are from Monte Carlo studies looking at the true NC1π^0 events that pass all selection cuts. Due to the non-Gaussian nature of the distributions, resolutions were found by taking half the distance from the 16% and 84% quantiles which is equivalent to the probability contained in 1σ of a Gaussian distribution. They are summarized in Table 4.4.

In addition to the vertex resolution, the NC1π^0 photon reconstruction was examined. In Figure 4.3, there is sharp peak at $\cos\theta = 1$, θ is the angular difference between the true and reconstructed angle. This shows that the decay photons are well reconstructed, thus the opening angle is also well reconstructed. Figure 4.4 shows the resolution of the reconstructed opening angle in radians. For the P∅D water-in configuration, a Gaussian fit gives a mean of -0.008 ± 0.001 radians and a sigma of 0.062 ± 0.001 radians. For P∅D water-out, the fit gives a mean of -0.008 ± 0.002 radians and a sigma of 0.064 ± 0.003 radians.

The momentum resolution of the π^0 was studied as well. In Figure 4.5, the distribution of the fractional momentum resolution (the difference of the reconstructed and true momenta

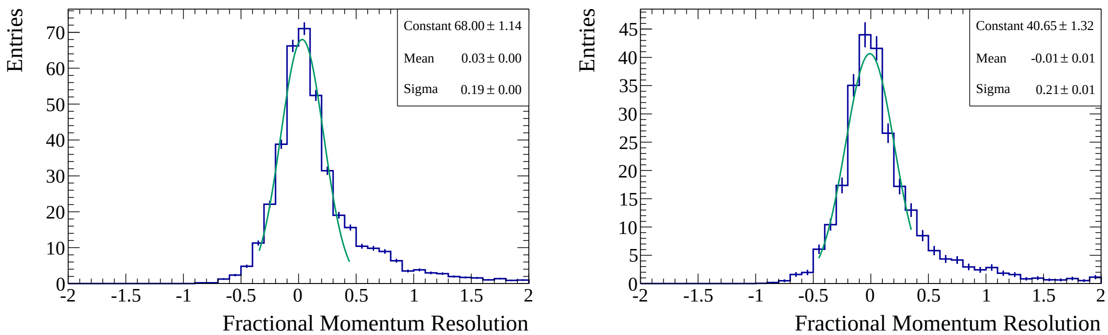

(a) Water-in configuration

(b) Water-out configuration

Figure 4.5: The NC1π^0 fractional momentum resolution is shown fit to a Gaussian distribution here for selected signal events.

divided by the true momentum) was fit to a Gaussian. The mean of the Gaussian is $-3.2 \pm 0.3\%$ with a sigma of $18.7 \pm 0.3\%$ for the water-in P∅D. For the P∅D water-out configuration, the mean is $-0.8 \pm 0.6\%$ with a sigma of $21.1 \pm 0.6\%$. The means of these fits are considered sufficiently close to zero for the energy reconstruction to be considered accurate. The sigmas of the fits can be considered as the resolution of the energy.

4.2 Event Selection

The signature of interest is two reconstructed electromagnetic-like objects that are assumed to be the resulting photons of a π^0 decay after an NC1π^0 interaction. A cut selection was developed in order to emphasize the shape difference between the signal invariant mass and the background invariant mass. Motivation for each cut is described below, followed by a discussion of how the optimization of the cuts is performed.

This analysis uses the output from the package oaAnalysis and only the reconstruction information from p∅dRecon. A description of p∅dRecon is presented in Section 3.3. For this analysis, the output of the cycle reconstruction is used, an event is therefore defined as a cycle with a reconstructed vertex. Events are split into seven categories: NC1π^0, other neutral current, charged current with one π^0, other charged current, events with external vertices, events with multiple interactions and noise. Colors listed in parentheses correspond to Figures 4.6 to 4.12. There are four categories representing physical interactions of interest in the P∅D.

- NC1π^0 (Light Violet)- Signal events. The final state of this interaction contains one exiting π^0, any number of exiting baryons and no other exiting particles.

- NC Other (Yellow Green)- This background contains all other neutral current events defined by no exiting charged leptons.

- CC1π^0 (Pink)- These events contain a single exiting muon and a single exiting pion.

Table 4.5: Definition of the P∅D fiducial volume. Column 2 shows the center position for all three dimensions in global coordinates. Column 3 shows the half-widths of the box. Columns 3 and 4 give the minimum and maximum positions.

Coordinate	Center (mm)	Half-Width (mm)	Minimum (mm)	Maximum (mm)
X	-36	800	-836	764
Y	-1	870	-871	869
Z	-2116	852.5	-2969	-1264

- CC Other (Green)- All other events with a charged lepton exiting the nucleus.

In addition to these physics categories, there are categories based on the topologies of the events. Since this is a P∅D only analysis, events that originate in the P∅D are examined, thus any external events are placed in the background sample. The cleanest set of reconstruction results is desired, so a single true vertex in each cycle of p∅dRecon is required. Lastly, the Production 5 Monte Carlo has implemented a more accurate estimation of the noise that will be present in the data. The noise is defined as any event that has reconstructed P∅D information, but no true vertex, or the true vertex is not found. A true vertex may not be saved if it occurs far outside the detector or if it doesn't have any daughter trajectories that leave an energy deposit in the P∅D. Plots are examined that display a cut variable's distribution for events passing all cuts with the cut of interest not applied. These are called N-1 plots. For cleaner and clearer plots, the N-1 plots are produced with a single other category (Blue) that contains the external vertices, the noise, and the multi-vertex events.

There are eight selection cuts implemented: preselection, fiducial volume, P∅D containment, muon decay, charge in shower, PID, π^0 direction and shower separation. Three of the cuts are considered optimizable due to semi-continuous natures: charge in shower, shower separation, and PID weight. Several optimization methods were considered, the one chosen is explained after the cuts are described. First, a flat tree is constructed that saves all events with P∅D activity. In the flat tree, all the cut variables are calculated for each event as well as any auxiliary information we consider necessary.

The first cut is a preselection cut. A single 3D vertex in the P∅D is required. For Run 1, each beam spill contained six bunches. At the start of Run 2, this was increased to eight bunches per spill. For the rest of the running period, the beam has been sent in eight bunches. For the event to be a beam event, the vertex must occur within the spill window, which corresponds to cycles 4 to 9(11) for Run 1(2-4) of the detector readout.

The next cut is that the 3D vertex is in the fiducial volume, shown in Figure 4.6. This cut is necessary to have fewer reconstruction failures, less energy leakage and better vertex resolution. The fiducial volume is defined in Table 4.5, originally considered as $\sim$ 25 cm from the edge of the active volume. This volume is described and motivated in Section 3.1.

In addition to the fiducial volume cut, a containment cut was constructed. In order to accurately reconstruct the charge deposited from the event in the detector, we require that it does not leave the P∅D. In p∅dRecon, exiting particles are treated differently from

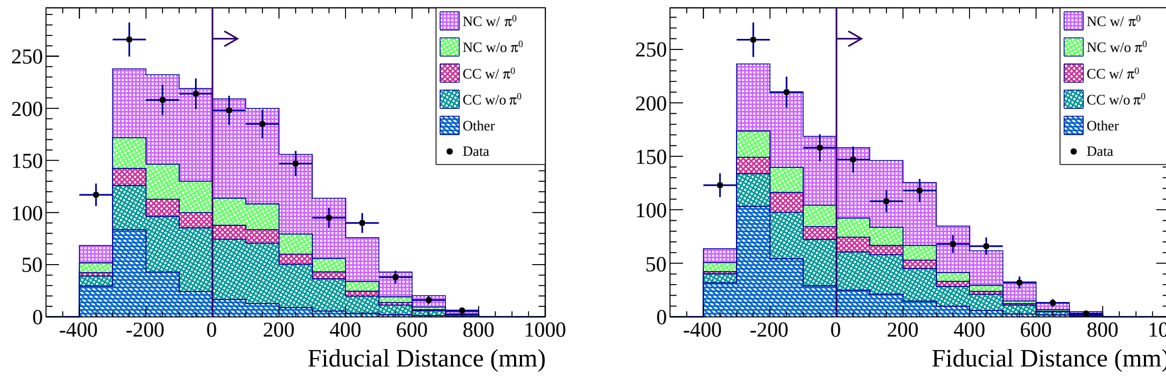

(a) Water-in configuration.

(b) Water-out configuration

Figure 4.6: The N-1 plots of the fiducial volume cut, area normalized to emphasize any shape differences. The fiducial volume parameter is calculated as the minimum distance between the vertex and a fiducial boundary. Positive values indicate that the vertex is inside the fiducial volume. The cut value is set at 0 mm.

contained particles with respect to reconstruction and particle identification. The particle identification present in Production 5 is not as well understood for exiting particles. The same exiting definition as the reconstruction is used. Any particle that has a hit in the last layer of the P∅D or in the outer two bars of any layer that is above a 2 PEU threshold is considered as exiting.

In order to remove charged current ν_μ events, a muon decay cut is employed, shown in Figure 4.7. For this selection, each cycle during and after the main event was examined for a muon decay cluster. The original algorithm to find these decay clusters was developed by Phoc Trung Le [28]. If a muon decay cluster is found in or after the time of the vertex of interest, the event is discarded.

In order to compensate for reconstruction of separate delta rays or any other reconstruction inefficiencies, a cut was constructed on the fraction of event charge in the two decay gamma candidates. In order to do this, we loop through every particle (both reconstructed tracks and showers) reconstructed in the event, which is then the total event charge $Q_{tot} = \sum Q_{shower} + \sum Q_{track}$. The decay photon candidates are considered to be up to two reconstructed showers with the greatest amount of deposited charge in the event $Q_{\gamma\gamma} = \sum_1^2 Q_{shower}$. The N-1 cut distribution for the shower charge, $Q_{\gamma\gamma}/Q_{tot}$, is shown in Figure 4.8.

Until this point, only the information on whether a particle was reconstructed as a shower is necessary. At the shower reconstruction stage of p∅dRecon, after the tracks have been removed, there are two possible particle identifications, kEM (photons and electrons) and kOther (not EM particles). The parameter of interest for cutting on this particle identification is the difference of the log likelihoods of the EM and Other shower PIDs. The distribution of this parameter is shown in Figure 4.9.

The π^0 direction cut is based on detector performance. In general, due to the P∅D

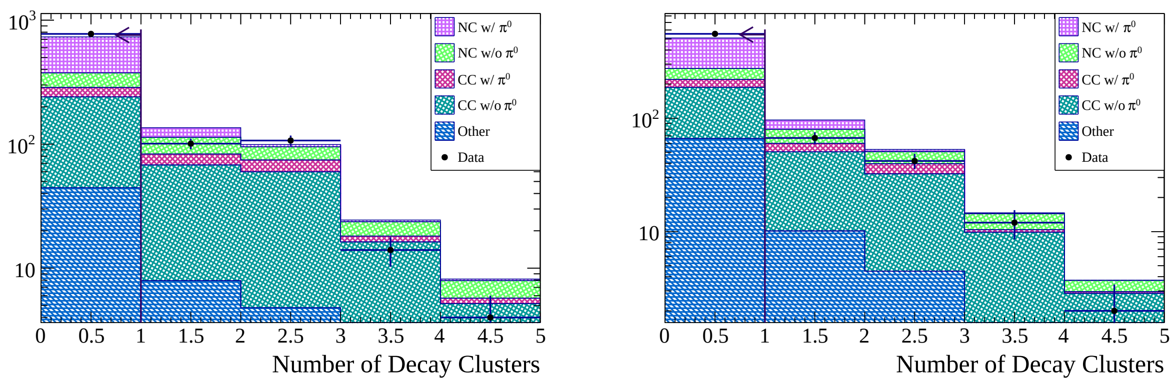

(a) Water-in configuration.

(b) Water-out configuration

Figure 4.7: The N-1 plots of the muon decay cut, area normalized to emphasize any shape differences.

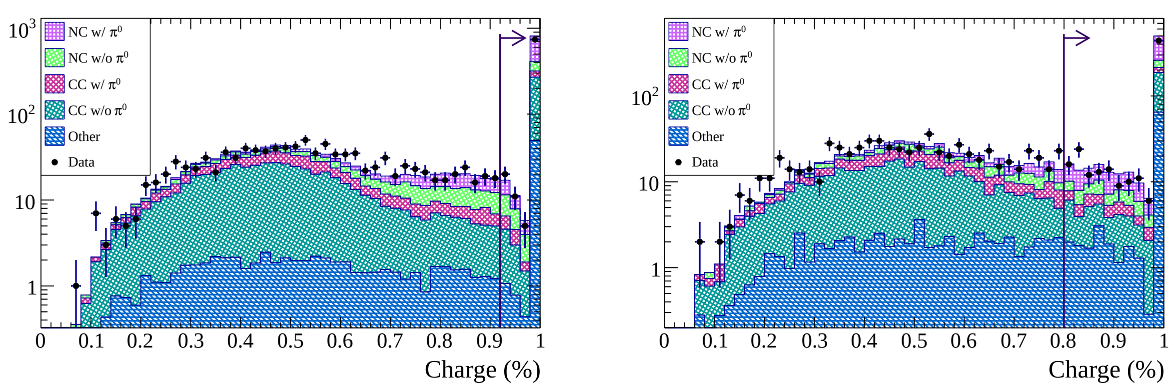

(a) Water-in configuration.

(b) Water-out configuration

Figure 4.8: The N-1 plots of the event shower charge distribution cut, area normalized to emphasize any shape differences. To pass this cut 92% of the charge must be EM-like for the PØD water-in configuration. For the PØD water-out configuration, the cut is placed at 80%.

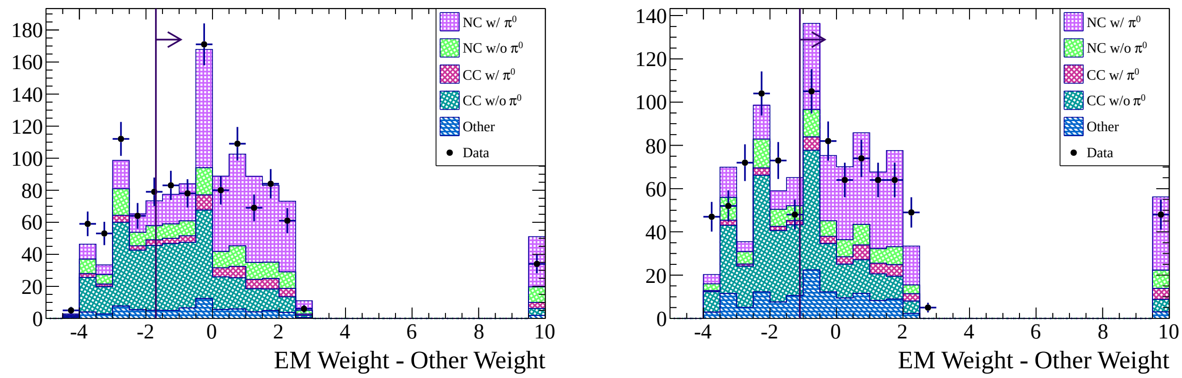

(a) Water-in configuration.

(b) Water-out configuration

Figure 4.9: The N-1 plots of the PID weight cut, area normalized to emphasize any shape differences. The events that fall in the last bin are a special case from the reconstruction that will always be labelled as EM particles. The cut value is set at -1.7 for the P∅D water-in configuration and -1.1 for the P∅D water-out configuration.

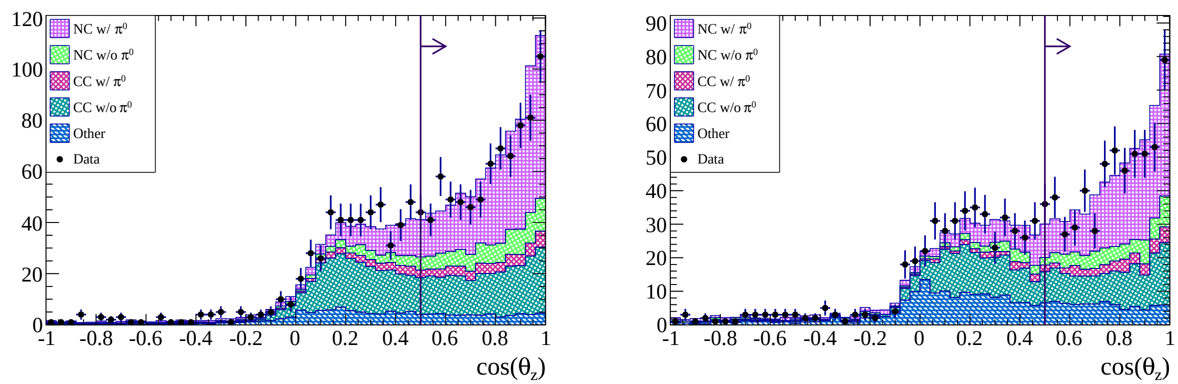

(a) Water-in configuration.

(b) Water-out configuration

Figure 4.10: The N-1 plots of the π^0 direction cut, area normalized to emphasize any shape differences. The cut value is set at $\cos\theta > 0.5$.

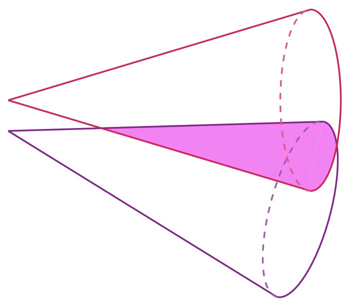

(a) Sample X-Z projection

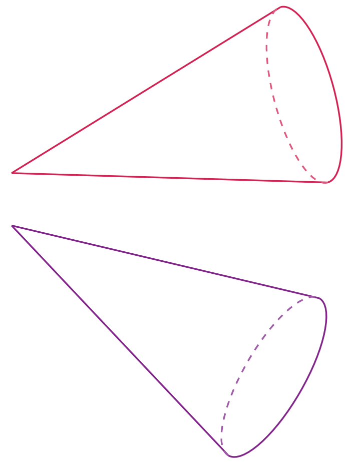

(b) Sample Y-Z projection

Figure 4.11: In Subfigure 4.11a, the two dimensional projections of the 3D showers overlap. The hit distances calculated in that projection will be at most the size of one or two bars. However, the showers are completely separated in 3D, which is apparent in the Y-Z projection shown in Subfigure 4.11b.

geometry, the reconstruction perfoms well up to 75° from the z axis. As such, we fixed the direction of the π^0 to be less than 60° from the z axis or $\cos\theta_z > 0.5$, as shown in Figure 4.10.

Part of the ability to reconstruct two complete decay photons depends on the separation between the two reconstructed objects. In order to get the cleanest reconstruction result, a cut on the separation of the decay photon candidates is imposed. This cut is calculated by finding the distance between the two closest hits of the photon showers, ignoring hits with less than 2 PEU, in the X-Z and Y-Z dimensions. Since it is possible to reconstruct two separate three dimensional objects when the two dimensional projections overlap, the maximum of the X-Z and Y-Z distances is taken as the cut variable, see Figure 4.11. The distribution for this variable is shown in Figure 4.12.

At this point, there are three tunable cuts: charge in shower, shower separation, and particle identification weight. An optimization had to be performed for both water-in and water-out configurations using a sample that has already passed all other cuts. The final goal of the optimization was to assure that there would be two distinct invariant mass distributions, one for the signal and one for the background, which can then be fit. The figure of merit chosen was $\pi^2 \cdot \epsilon$, where π is the purity and ϵ is the efficiency, in order to have an optimization parameter that emphasizes the shape differences in the invariant mass. The optimization method was focused on optimizing the π^0 mass peak window, 90 MeV to 170 MeV. In addition, π^0 particles with a momentum larger than 200 MeV comprise the ν_e appearance background in Super-K that are of the most interest.

A histogram with three axes, one for each of the optimizable cuts, was constructed. For the PID weight difference, based on the initial distribution of the tuning histograms, a range of possible cuts from -4.0 to 4.0 at 0.1 intervals was studied. For the shower separation cut, cuts from 0 to 150 mm at 10 mm intervals were studied. Note that the width of a bar is

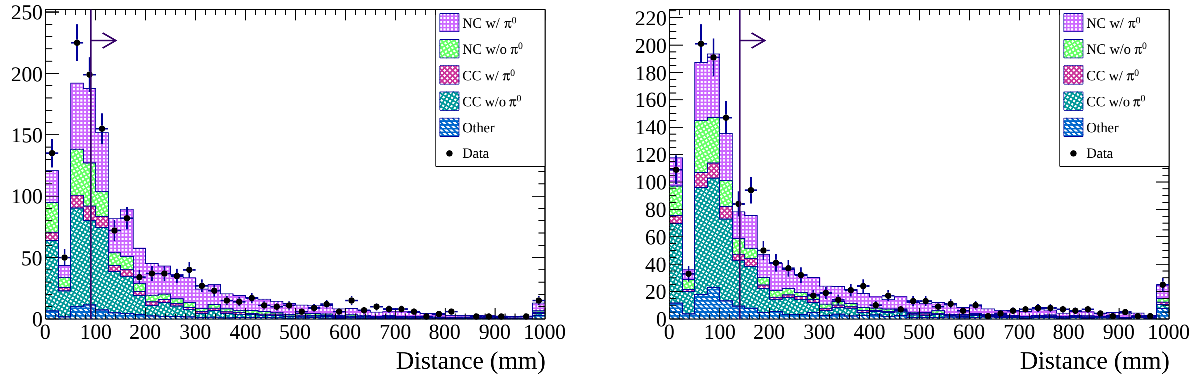

(a) Water-in configuration. (b) Water-out configuration

Figure 4.12: The N-1 plots of the shower separation cut, area normalized to emphasize any shape differences. The cut value is set at 90 mm for the P∅D water-in configuration and 140 mm for the P∅D water-out configuration.

approximately 16 mm, so the step size was small enough to see each bar interval. Lastly, the shower charge cut values encompassed the entire possible range, 0.0 to 1.0 at 0.01 intervals. Using a subsample of the Monte Carlo events that pass all but these three cuts the figure of merit (the efficiency times the square of the purity) is calculated for each bin. The bin position of the maximum value was then used as the optimized cut values.

There is a dependence on the energy scale within this optimization. The energy scale did undergo a reevaluation to improve the energy conversion at low energies. It was decided to preserve the cuts as optimized before looking at the data. The optimization method is highly sensitive to statistical fluctuations. To show that the previous optimized cuts are still applicable, the two dimensional projections at the cut values of the three dimensional figure of merit histogram are shown in Figures 4.13 and 4.14. The cut values fall on the maximum plateaus of the two dimensional projections and are therefore held as still applicable.

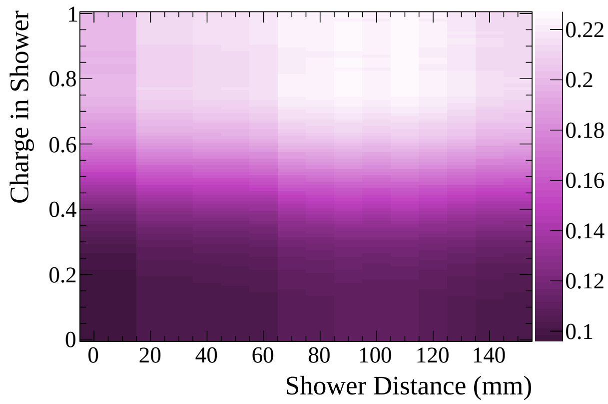

(a) Two dimensional comparison of the charge in shower and shower separation cuts with the particle identification cut fixed at -1.7.

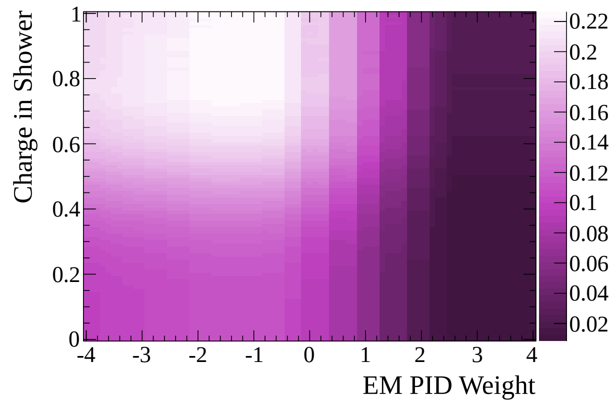

(b) Two dimensional comparison of the charge in shower and particle identification cuts with the shower separation cut fixed at 90 mm.

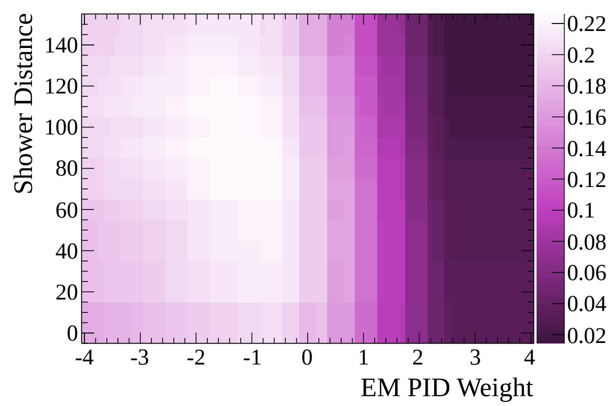

(c) Two dimensional comparison of the shower separation and particle identification cuts with the percent of charge in showers fixed at 92%.

Figure 4.13: The chosen significance, $\pi^2 \cdot \epsilon$, distributions over the ranges for the cut values for the water-in configuration. Each plot shows the 2D projection of the 3D optimization space at a fixed optimized cut. These plots show the figure of merit calculated from the revamped PEU to MeV energy conversion.

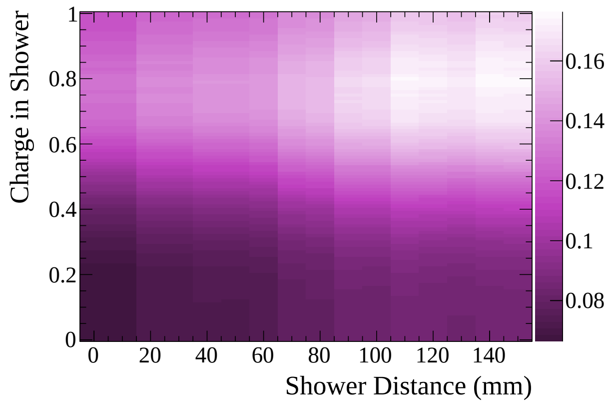

(a) Two dimensional comparison of the charge in shower and shower separation cuts with the particle identification cut fixed at -1.1.

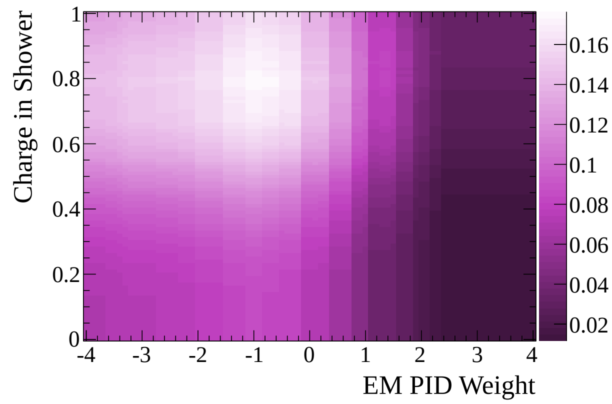

(b) Two dimensional comparison of the charge in shower and particle identification cuts with the shower separation cut fixed at 140 mm.

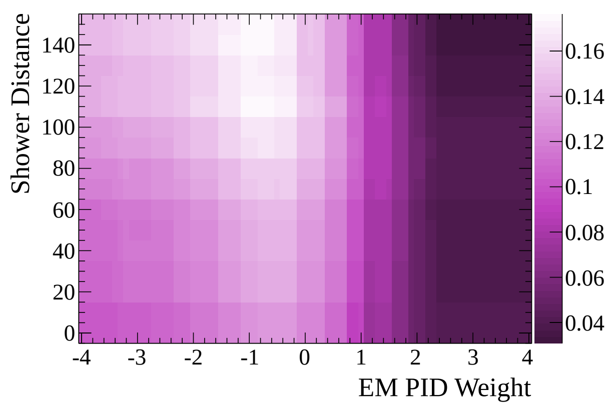

(c) Two dimensional comparison of the shower separation and particle identification cuts with the percent of charge in showers fixed at 80%.

Figure 4.14: The chosen significance, $\pi^2 \cdot \epsilon$, distributions over the ranges for the cut values for the water-out configuration. Each plot shows the 2D projection of the 3D optimization space at a fixed optimized cut. These plots show the figure of merit calculated from the revamped PEU to MeV energy conversion.

4.3 Sideband Selection

There are several possibilities for a sideband selection. In order to pick the best sideband to use in simultaneous fit to constrain the backgrounds in the various possibilities are compared. In the end, the muon decay sideband was chosen for use in the simultaneous fit because it has relatively low purity and a similar background composition to that in the selected events. There are eight cuts and eight possible $N-1$ sidebands. Three of the cuts are discarded, Preselection, Fiducial Volume and Containment, due to the lack of information present in the sideband and the unknown nature of the data to Monte Carlo comparisons. The π^0 direction cut is based on reconstruction efficiencies so its sideband is also not well understood. The remaining possible sidebands are compared in three ways. First, the shape of the sidebands between data and Monte Carlo is compared. Without a reasonable shape match, these sidebands will not be useful to constrain the shape of the background. Figures 4.15 through 4.18 show the area normalized comparisons of the data to the Monte Carlo.

The second item to check is to compare the content of the sideband background and the selected region background. Tables 4.6 and 4.8 show the composition of the background. The composition of the muon decay sideband most closely matches with the content of the background of the selected region. Tables 4.7 and 4.9 list the purities of the different sidebands. It is best to focus on a low signal purity sideband in order to remove the interaction intended for measurement. The goal of the sideband is to effectively constrain the cross section of the background. As such, the sidebands comparing the PID weight, the reconstructed direction of the π^0, and the shower separation, may not be ideal samples. Although the charge in shower sideband has a relatively low purity, the content of this sideband is heavily influenced by the CC1π^0 channel.

The third item of interest is to compare the shapes of the sideband background and the selected region background. Figures 4.19 through 4.22 show the area normalized Monte Carlo predictions of the backgrounds in the selected region and the sideband regions. Visually, the muon decay sideband, Figure 4.19, most closely matches the shape of the selected region background. In addition, the muon decay sideband is composed of the same types of interactions as the selected region background. As such, the muon decay sideband is used to constrain the selected region background in this analysis.

Table 4.6: For the P∅D water-in configuration, the summary of the composition of the background of the sidebands for events with a reconstructed invariant mass less than 500 MeV. For comparison, the first row contains the composition of the selected events. All numbers are in terms of the percent of the total background.

Sideband	NC Other (%)	CCπ^0 (%)	CC Other (%)	External (%)	Multiple (%)	Noise (%)
Selected	23.9 ± 0.2	12.1 ± 0.1	52.1 ± 0.2	8.6 ± 0.1	3.3 ± 0.0	0.0 ± 0.0
Muon Decay	24.8 ± 0.2	13.3 ± 0.1	56.1 ± 0.3	3.1 ± 0.0	2.7 ± 0.0	0.0 ± 0.0
Shower Charge	16.0 ± 0.1	20.2 ± 0.1	56.6 ± 0.2	3.3 ± 0.0	3.9 ± 0.0	0.0 ± 0.0
PID Weight	19.1 ± 0.2	5.6 ± 0.1	65.4 ± 0.3	7.5 ± 0.1	2.3 ± 0.0	0.0 ± 0.0
Nearest Shower	26.6 ± 0.2	7.8 ± 0.1	58.3 ± 0.3	5.4 ± 0.1	1.9 ± 0.0	0.0 ± 0.0

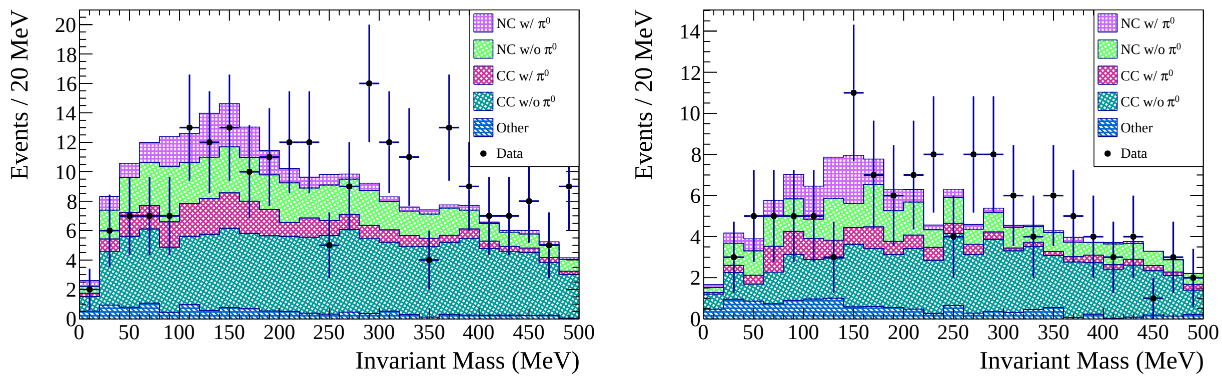

(a) Water-in configuration.

(b) Water-out configuration

Figure 4.15: The comparison between the area normalized muon decay sideband data and Monte Carlo.

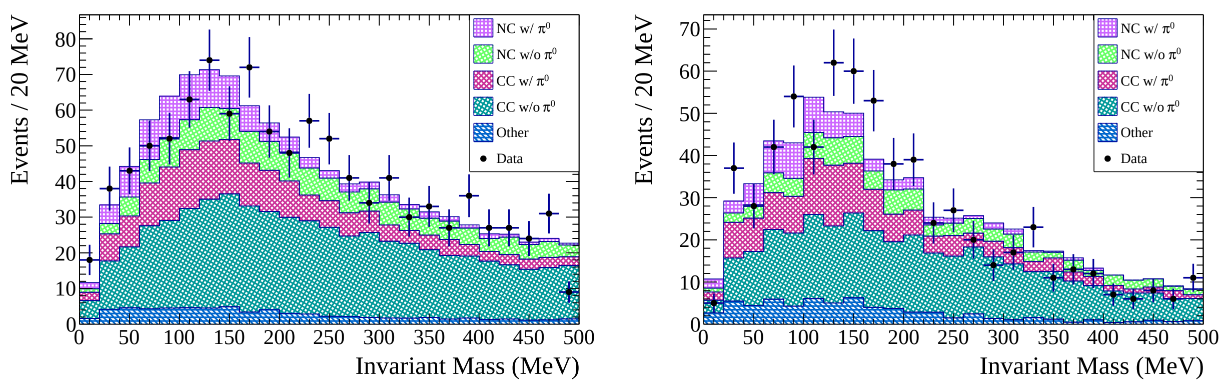

(a) Water-in configuration.

(b) Water-out configuration

Figure 4.16: The comparison between the area normalized charge in shower sideband data and Monte Carlo.

Table 4.7: For the PØD water-in configuration, the summary of the purities in the sideband selections for a reconstructed invariant mass less than 500 MeV. For comparison, the selected event purity is listed in the first column. All numbers are in percent.

Selected	Muon Decay (%)	Shower Charge (%)	PID Weight (%)	Nearest Shower (%)
48.7 ± 0.2	10.1 ± 0.1	10.4 ± 0.1	19.0 ± 0.2	26.7 ± 0.2

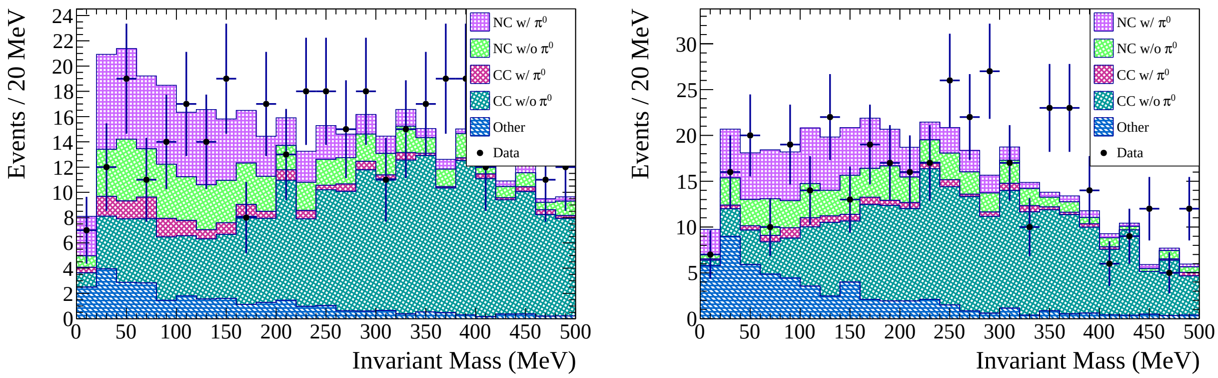

(a) Water-in configuration.　　(b) Water-out configuration

Figure 4.17: The comparison between the area normalized PID weight sideband data and Monte Carlo.

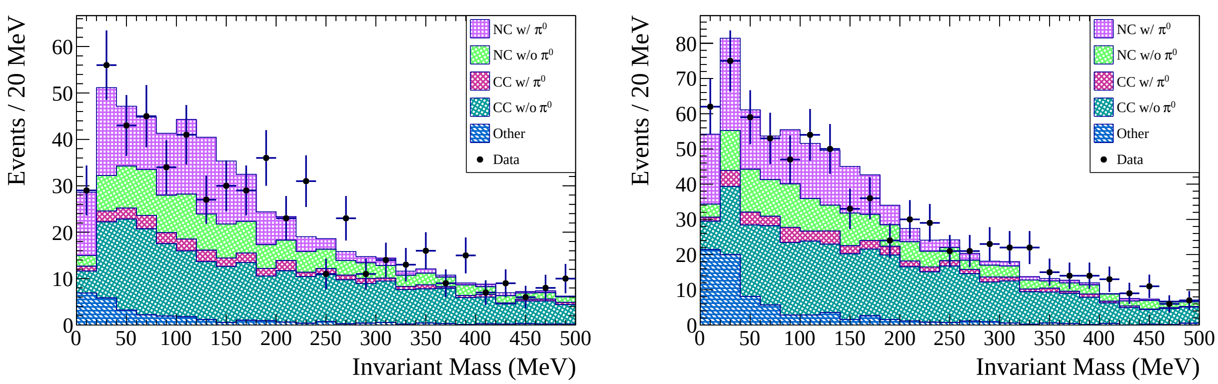

(a) Water-in configuration.　　(b) Water-out configuration

Figure 4.18: The comparison between the area normalized shower separation sideband data and Monte Carlo.

Table 4.8: For the P∅D water-out configuration, the summary of the composition of the background of the sidebands for events with a reconstructed invariant mass less than 500 MeV. For comparison, the first row contains the composition of the selected events. All numbers are in terms of the percent of the total background.

Sideband	NC Other (%)	$CC\pi^0$ (%)	CC Other (%)	External (%)	Multiple (%)	Noise (%)
Selected	20.0 ± 0.3	11.8 ± 0.2	44.1 ± 0.4	20.8 ± 0.3	3.3 ± 0.1	0.0 ± 0.0
Muon Decay	24.1 ± 0.4	11.6 ± 0.2	53.5 ± 0.6	7.3 ± 0.2	3.6 ± 0.1	0.0 ± 0.0
Shower Charge	13.6 ± 0.2	22.4 ± 0.2	52.7 ± 0.3	6.2 ± 0.1	5.1 ± 0.1	0.0 ± 0.0
PID Weight	16.5 ± 0.3	3.8 ± 0.1	62.3 ± 0.4	15.0 ± 0.2	2.3 ± 0.0	0.0 ± 0.0
Nearest Shower	22.5 ± 0.2	7.4 ± 0.1	56.6 ± 0.3	11.3 ± 0.1	2.2 ± 0.0	0.0 ± 0.0

Table 4.9: For the P∅D water-out configuration, the summary of the purities in the sideband selections for a reconstructed invariant mass less than 500 MeV. For comparison, the selected event purity is listed in the first column. All numbers are in percent.

Selected	Muon Decay (%)	Shower Charge (%)	PID Weight (%)	Nearest Shower (%)
46.1 ± 0.3	11.2 ± 0.2	9.5 ± 0.1	17.3 ± 0.2	22.7 ± 0.2

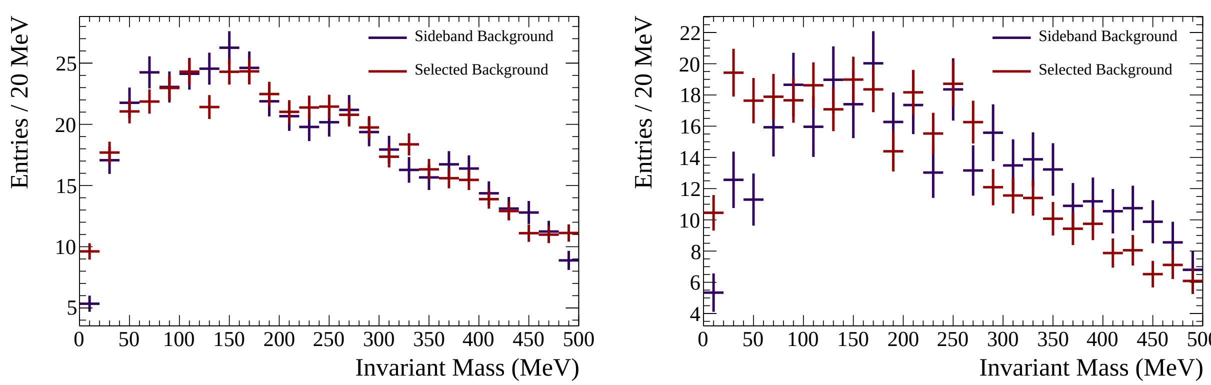

(a) Water-in configuration.

(b) Water-out configuration

Figure 4.19: The comparison between the area normalized selected region predicted background and the muon decay sideband predicted background.

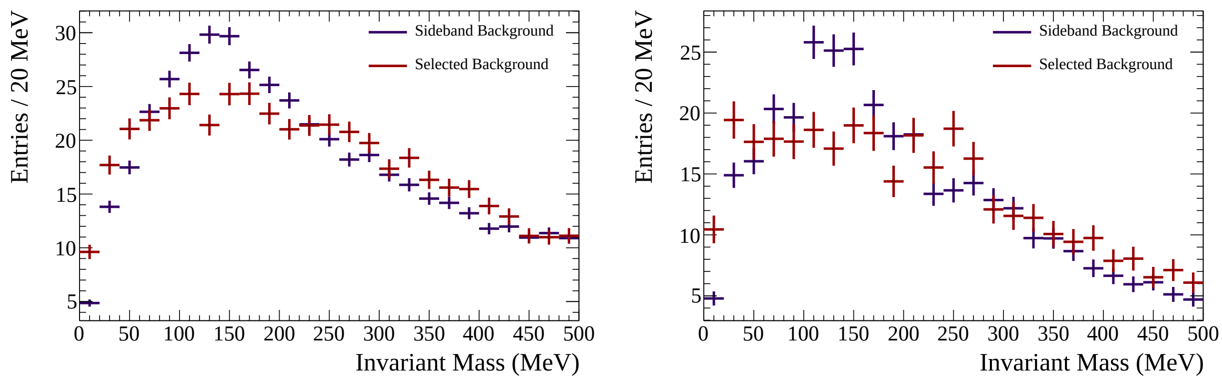

(a) Water-in configuration.

(b) Water-out configuration

Figure 4.20: The comparison between the area normalized selected region predicted background and the charge in shower sideband predicted background.

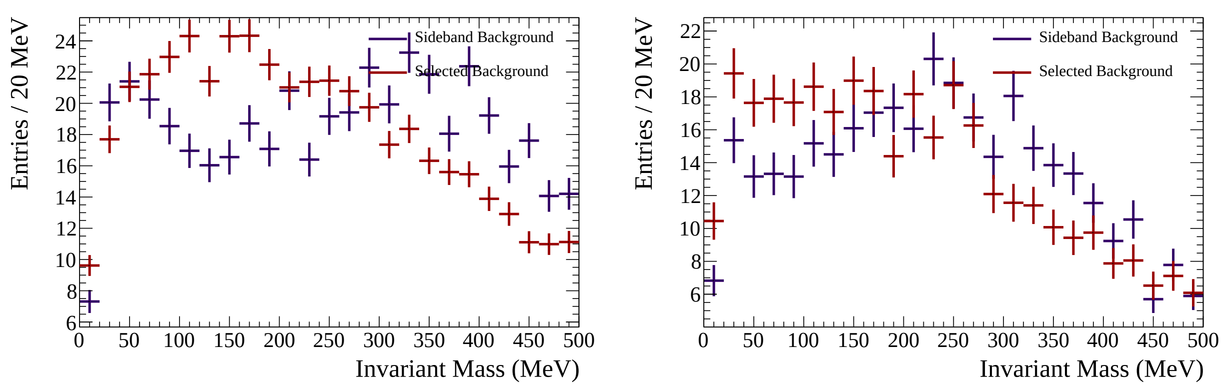

(a) Water-in configuration.

(b) Water-out configuration

Figure 4.21: The comparison between the area normalized selected region predicted background and the PID weight sideband predicted background.

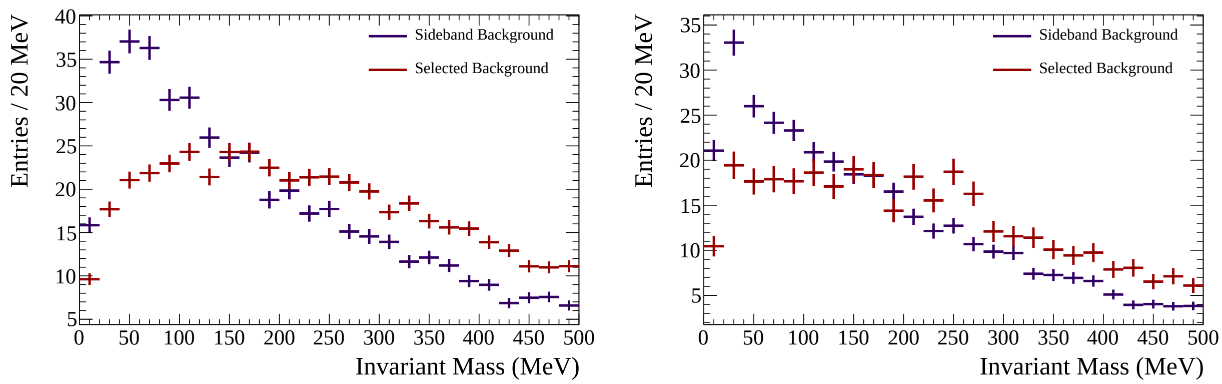

(a) Water-in configuration. (b) Water-out configuration

Figure 4.22: The comparison between the area normalized selected region predicted background and the shower separation sideband predicted background.

4.4 Analysis

The event signature of the search is that of two photons, the π^0 decay signature. In order to examine those photons, the invariant mass, $M_{\gamma\gamma}$ is reconstructed using

$$M_{\gamma\gamma} = \sqrt{2E_{\gamma_1}E_{\gamma_2}(1-\cos\theta_{\gamma\gamma})}, \tag{4.7}$$

where E_{γ_i} is the energy of the ith photon and $\theta_{\gamma\gamma}$ is the angle between the decay photons. The invariant mass of the two photons would ideally match the mass of the π^0 particle, 135.0 MeV. The equation depends on the reconstructed energy of the two decay photon candidates and their opening angle. Hence the invariant mass peak will be smeared due to reconstruction inefficiencies. Figure 4.23 shows the area normalized result of the selection.

4.4.1 Final Sample Cross Checks

Tables 4.10 and 4.11 summarize the effect of each cut on the final sample of NC1π^0 candidate events. The tables contain the number of data events passing each cut as well as the number of simulated events and the number of simulated signal events that make it into the final sample. There is a discrepancy in the efficiency of the fiducial volume cut that is due to sand muons not being modeled in the default NEUT Monte Carlo.

Tables 4.12 and 4.13 show the breakdown of the signal and background present in the final Monte Carlo sample. Tables 4.14 and 4.15 show the breakdown of the signal and background present in the final Monte Carlo muon decay sideband sample. Table 4.16 describes the composition of the events that are used in the analysis that have a reconstructed invariant mass above 500 MeV. All event numbers in Tables 4.10 through 4.16 have been reweighted by the P∅D fiducial mass difference between data and Monte Carlo, the relative data and Monte Carlo POT, and by the flux, using version 11b 3.2 released by the beam group.

There are two efficiencies quoted in Table 4.17. The first, ϵ_{ff}, is introduced as an absolute efficiency of the final selected sample compared to the total number of NC1π^0 events

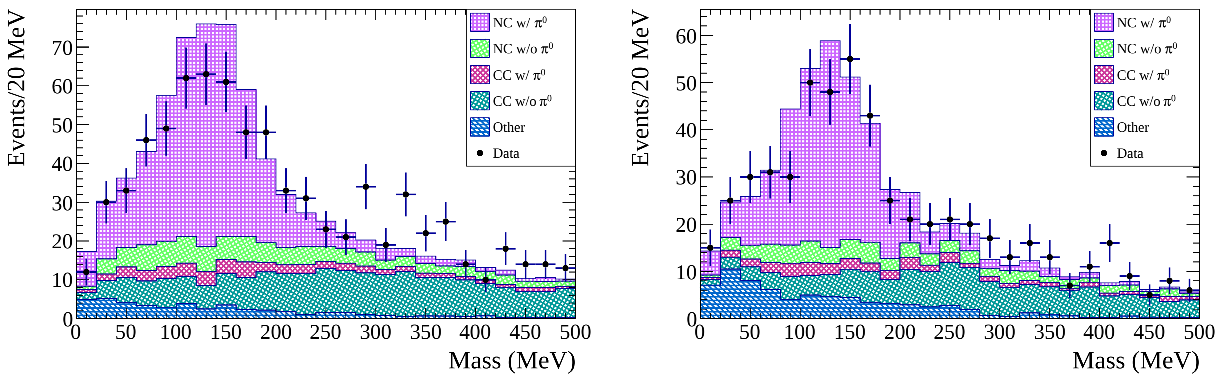

(a) Water-in configuration. (b) Water-out configuration

Figure 4.23: The distribution of the invariant mass of the selected events.

Table 4.10: The number of events passing each cut for the PØD water-in configuration. The first column lists the cut variable names, the second gives the number of events found in the detector. The third and fourth column show the number of events predicted in the Monte Carlo and its relative efficiencies. The last two column show the number of signal events predicted in the Monte Carlo and its relative efficiencies.

Cut	Events	Rel. Eff (%)	Expected	Rel. Eff (%)	Signal	Rel. Eff (%)
Preselection	1255802	N/A	643150.9	N/A	15208.7	N/A
Fiducial	149099	11.9	159698.7	24.8	5857.0	38.5
Contained	121505	81.5	129904.5	81.3	4290.3	73.2
Muon Decay	94043	77.4	93628.7	72.1	3904.2	91.0
Shower Charge	24222	25.8	24065.6	25.7	2915.2	74.7
PID Weight	15138	62.5	15153.5	63.0	1967.4	67.5
π^0 Direction	6325	41.8	6468.1	42.7	1320.0	67.1
Shower Separation	775	12.3	893.0	13.8	434.9	32.9

Table 4.11: The number of events passing each cut for the P∅D water-out configuration. The first column lists the cut variable names, the second gives the number of events found in the detector. The third and fourth column show the number of events predicted in the Monte Carlo and its relative efficiencies. The last two column show the number of signal events predicted in the Monte Carlo and its relative efficiencies.

Cut	Events	Rel. Eff (%)	Expected	Rel. Eff (%)	Signal	Rel. Eff (%)
Preselection	1608938	N/A	793152.1	N/A	16341.7	N/A
Fiducial	158055	9.8	164475.9	20.7	5432.5	33.2
Contained	124235	78.6	127160.1	77.3	3653.3	67.2
Muon Decay	99953	80.5	95570.4	75.2	3329.0	91.1
Shower Charge	30508	30.5	28804.5	30.1	2347.5	70.5
PID Weight	17959	58.9	16902.6	58.7	1495.8	63.7
π^0 Direction	9134	50.9	8046.6	47.6	1000.9	66.9
Shower Separation	555	6.1	629.6	7.8	290.3	29.0

Table 4.12: The breakdown of the final sample in the Monte Carlo for the P∅D water-in configuration.

Data	775		
Monte Carlo Expectation	893.0 ± 6.1		
Signal		434.9 ± 4.3	
Background		458.2 ± 4.4	
Neutral Current			109.5 ± 2.2
Charged Current w/ π^0			55.5 ± 1.5
Charged Current Other			238.8 ± 3.2
External			39.2 ± 1.3
Multiple			15.1 ± 0.8
Noise			0.0 ± -nan

Table 4.13: The breakdown of the final sample in the Monte Carlo for the P∅D water-out configuration.

Data	555		
Monte Carlo Expectation	629.6 ± 8.0		
Signal		290.3 ± 5.4	
Background		339.3 ± 5.9	
Neutral Current			67.8 ± 2.7
Charged Current w/ π^0			40.1 ± 2.0
Charged Current Other			149.7 ± 3.9
External			70.6 ± 2.8
Multiple			11.1 ± 1.1
Noise			0.0 ± -nan

Table 4.14: The breakdown of the muon decay sideband in the Monte Carlo for the P∅D water-in configuration.

Data	227		
Monte Carlo Expectation	330.6 ± 3.8		
Signal		33.2 ± 1.2	
Background		297.3 ± 3.6	
Neutral Current			73.9 ± 1.8
Charged Current w/ π^0			39.4 ± 1.3
Charged Current Other			166.9 ± 2.6
External			9.1 ± 0.6
Multiple			8.0 ± 0.6
Noise			0.0 ± -nan

Table 4.15: The breakdown of the muon decay sideband in the Monte Carlo for the P∅D water-out configuration.

Data	123		
Monte Carlo Expectation	210.4 ± 4.6		
Signal		23.5 ± 1.6	
Background		186.8 ± 4.3	
Neutral Current			45.0 ± 2.2
Charged Current w/ π^0			21.6 ± 1.5
Charged Current Other			99.9 ± 3.2
External			13.6 ± 1.2
Multiple			6.7 ± 0.8
Noise			0.0 ± -nan

Table 4.16: A summary of the events that pass all selection cuts and events that fall in the μ-decay sideband, but have a reconstructed invariant mass greater than 500 MeV for both the P∅D water-in and water-out configurations.

	Water-In		Water-Out	
	Selected	Sideband	Selected	Sideband
Data	138	49	50	25
NC1π^0	6.6 ± 0.1	1.7 ± 0.2	2.5 ± 0.2	0.8 ± 0.4
NC Other	24.6 ± 0.0	18.9 ± 0.0	12.2 ± 0.1	8.7 ± 0.1
CC1π^0	7.3 ± 0.1	4.5 ± 0.1	2.7 ± 0.2	2.9 ± 0.2
CC Other	69.5 ± 0.0	53.9 ± 0.0	27.2 ± 0.1	22.1 ± 0.1
External	1.2 ± 0.2	0.9 ± 0.2	2.6 ± 0.2	0.8 ± 0.4
Multiple Vertices	2.8 ± 0.1	2.3 ± 0.1	1.1 ± 0.3	1.8 ± 0.2
Noise	0.0 ± -nan	0.0 ± -nan	0.0 ± -nan	0.0 ± -nan

Table 4.17: A summary of the efficiencies (ϵ) and purity (π) found for both the water-in and water-out configurations given the event selection described in Section 4.2.

	ϵ_{ff} (%)	ϵ_A (%)	π (%)
Water In	6.01 ± 0.01	12.42 ± 0.04	48.7 ± 0.17
Water Out	4.79 ± 0.02	11.00 ± 0.06	46.1 ± 0.3

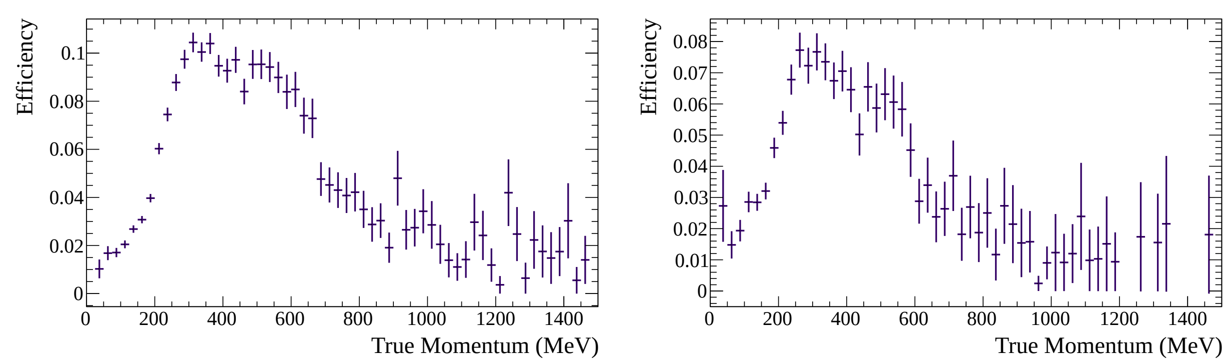

(a) Water-in configuration.

(b) Water-out configuration

Figure 4.24: The efficiency of the NC1π^0 analysis as a function of the momentum of the π^0.

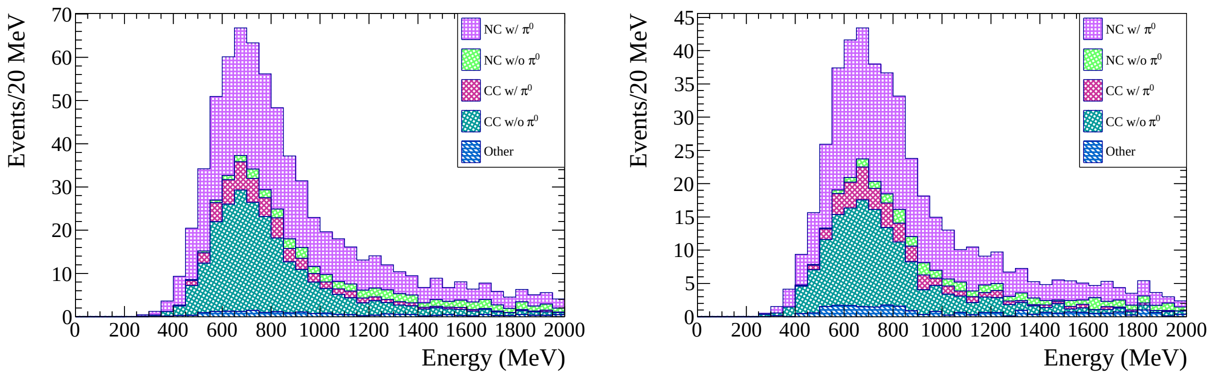

(a) Water-in configuration

(b) Water-out configuration

Figure 4.25: The distribution of the true neutrino energy for the saved Monte Carlo events.

generated in the fiducial volume of the P∅D. There is a difference between the P∅D water-in and water-out configuration efficiencies which can be contributed to the difference in masses between the two configurations. The reduced mass of the P∅D water-out configuration means that photons travel further and are therefore harder to reconstruct. This makes the π^0 harder to reconstruct as well. The second, ϵ_A, is the efficiency of this analysis's topology. It is an efficiency of the final selected sample compared to the sample of events that is preselected, fully contained, with a reconstructed fiducial vertex. The purity quoted is based of the final state of the interaction with one π^0 exiting the nucleus and no other mesons or leptons compared to the total number of saved events. The efficiency as a function of the true momentum of the π^0 is shown in Figure 4.24 and the distribution of the true neutrino energy is shown in Figure 4.25. The low momentum efficiency drop is due to the lower energy photon falling below the reconstruction threshold. The higher end of the momentum also drops as the π^0 is boosted enough to lead to the decay photons overlapping and not resolving separately in the reconstruction.

In the data, 775 events were saved for the water-in configuration and 555 events were saved for the water-out configuration of the P∅D. Figure 4.26 shows the number of π^0 candidate events as a function of POT for each configuration. Figures 4.27 and 4.28 show the timing of the selected events for the separate runs in the detector. The vertex distributions are shown in one dimensional projections in Figures 4.29 and 4.30 and in two dimensional projections in Figures 4.31 and 4.32. Lastly a comparison of the reconstructed energy between data and Monte Carlo is shown in Figure 4.33.

4.4.2 Definition of Likelihood

Using Minuit, the selected region (passing all cuts) and the muon decay sideband region (passing all cuts, but failing the muon decay cut) are fit simultaneously using an unbinned extended maximum likelihood. The shape of each sample is defined by a selection of PDFs. Two PDFs describe the Monte Carlo prediction for the signal and background shape in the selected region, denoted $\rho^{\text{Selected}}_{\text{Sig}}$ and $\rho^{\text{Selected}}_{\text{Bkg}}$. These PDFs are shown in Figures 4.34 and

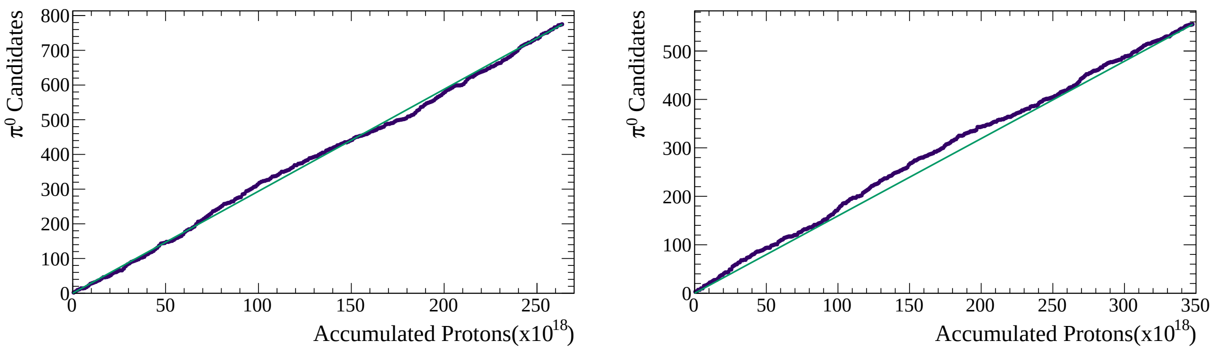

(a) Water-in configuration

(b) Water-out configuration

Figure 4.26: The rate of π^0 candidates observed in the P∅D. The event rate is 2.94 candidates/10^{18} POT for the P∅D water-in configuration and 1.60 candidates/10^{18} POT for the P∅D water-out configuration. A K-S test was performed on each sample. The P∅D water-in configuration has a probability of 0.78 and a maximum distance of 0.03. The P∅D water-out configuration has a probability of 0.35 with a maximum distance of 0.06.

4.35. The other two PDFs describe the prediction for the signal and background shape in the sideband region, denoted $\rho^{\text{Sideband}}_{\text{Sig}}$ and $\rho^{\text{Sideband}}_{\text{Bkg}}$ and are also seen in Figures 4.34 and 4.35.

The overall signature to save is that of two photons in an event. For both the selected and sideband regions, the number of two photon events ($N_{\gamma\gamma}$) is a sum of the true signal events (N_{Sig}) and the background events (N_{Bkg}). There is a fixed relationship between the number of signal events in the signal region and the sideband region. The same holds true for the number of background events. Using the Monte Carlo, that relationship is fixed by $\alpha = N^{\text{Sideband}}_{\text{Sig}}/N^{\text{Selected}}_{\text{Sig}}$ and $\beta = N^{\text{Sideband}}_{\text{Bkg}}/N^{\text{Selected}}_{\text{Bkg}}$ to give

$$N^{\text{Selected}}_{\gamma\gamma} = N^{\text{Selected}}_{\text{Sig}} + N^{\text{Selected}}_{\text{Bkg}} \tag{4.8a}$$
$$N^{\text{Sideband}}_{\gamma\gamma} = N^{\text{Sideband}}_{\text{Sig}} + N^{\text{Sideband}}_{\text{Bkg}} \tag{4.8b}$$
$$= \alpha \cdot N^{\text{Selected}}_{\text{Sig}} + \beta \cdot N^{\text{Selected}}_{\text{Bkg}}. \tag{4.8c}$$

Breaking the likelihood equations down,

$$\mathcal{L}_{\text{Signal}} = \mathcal{L}(N^{\text{Selected}}_{\text{Sig}}, N^{\text{Selected}}_{\text{Bkg}})_{\text{Norm}} \times \mathcal{L}(e, N^{\text{Selected}}_{\text{Sig}}, N^{\text{Selected}}_{\text{Bkg}})_{\text{Shape}} \tag{4.9a}$$
$$\mathcal{L}_{\text{Sideband}} = \mathcal{L}(N^{\text{Sideband}}_{\text{Sig}}, N^{\text{Sideband}}_{\text{Bkg}})_{\text{Norm}} \times \mathcal{L}(e, N^{\text{Sideband}}_{\text{Sig}}, N^{\text{Sideband}}_{\text{Bkg}})_{\text{Shape}} \tag{4.9b}$$
$$\mathcal{L}_{\text{Total}} = \mathcal{L}_{\text{Signal}} \times \mathcal{L}_{\text{Sideband}} \times \mathcal{L}_{\text{Sys}}(N^{\text{Selected}}_{\text{Sig}}, N^{\text{Selected}}_{\text{Bkg}}, N^{\text{Sideband}}_{\text{Sig}}, N^{\text{Sideband}}_{\text{Bkg}}). \tag{4.9c}$$

The total likelihood depends on the number of signal and background in the signal region ($N^{\text{Selected}}_{\text{Sig}}$ and $N^{\text{Selected}}_{\text{Bkg}}$), the number of signal and background in the sideband region ($N^{\text{Sideband}}_{\text{Sig}}$ and $N^{\text{Sideband}}_{\text{Bkg}}$) and the energy scale ($e$) which is common to both samples. In order to simultaneously fit the signal and sideband regions, the likelihoods must be minimized at the same time with the constraint term, Equation 4.9c.

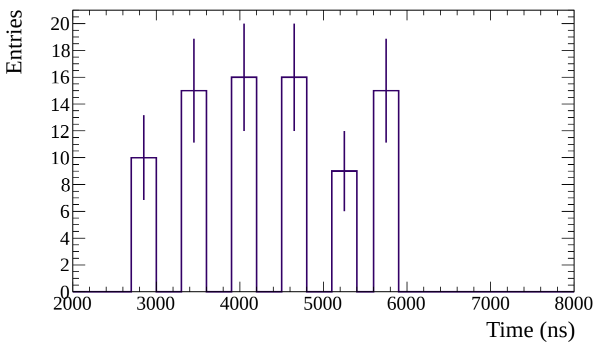

(a) Run 1

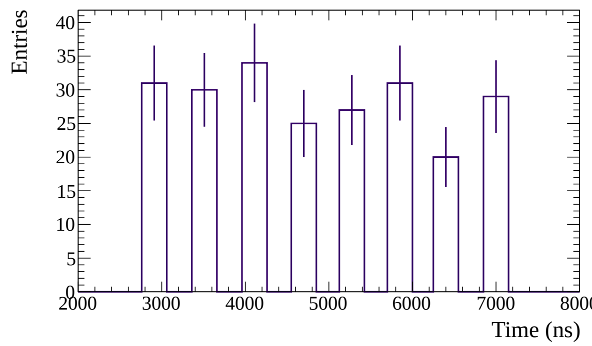

(b) Run 2

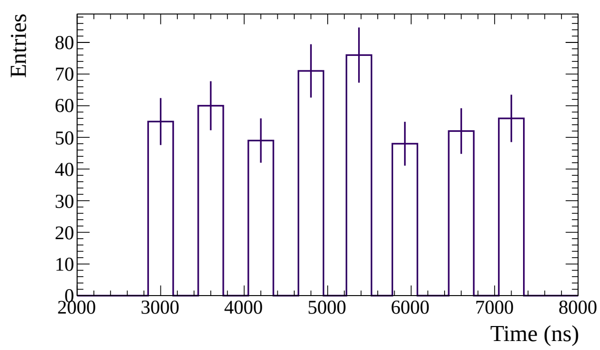

(c) Run 4

Figure 4.27: The bunch timing of the observed candidates in the PØD in the water-in configuration. There were 81 selected events in Run 1, 227 events in Run 2 and 467 events in Run 4.

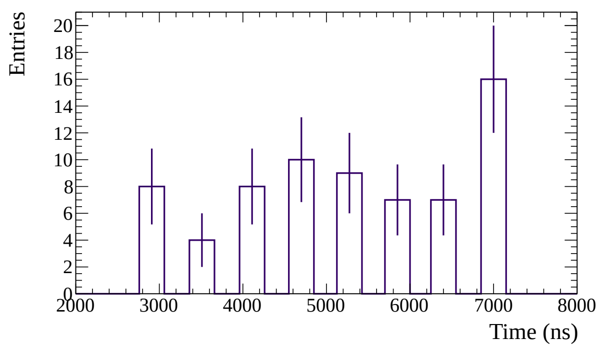

(a) Run 2

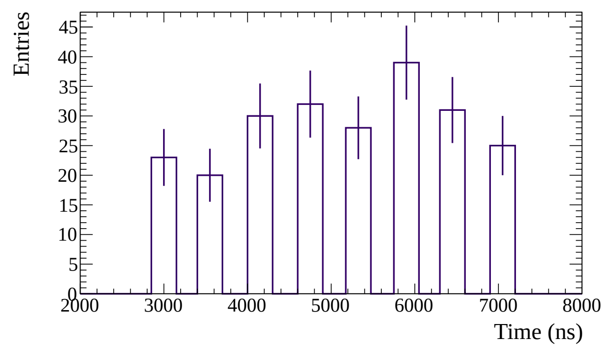

(b) Run 3

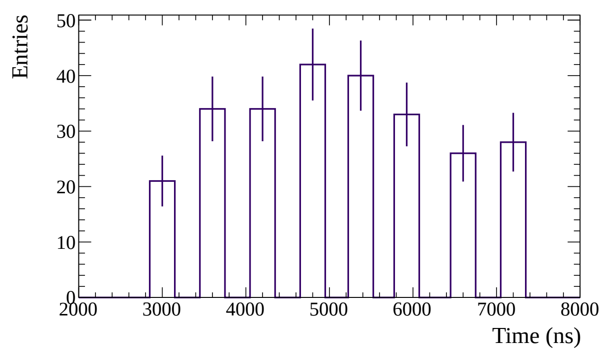

(c) Run 4

Figure 4.28: The bunch timing of the observed candidates in the P∅D in the water-out configuration. There were 69 selected events in Run 2, 228 events for Run 3 and 258 events in Run 4.

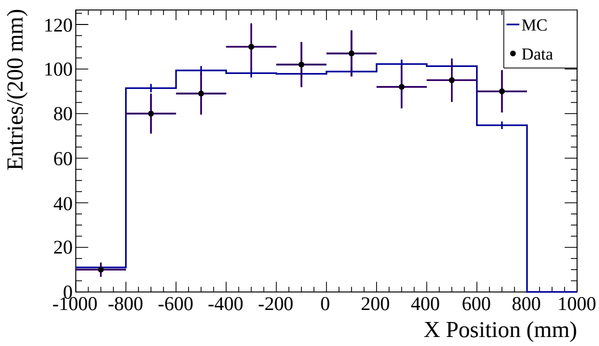

(a) X projection

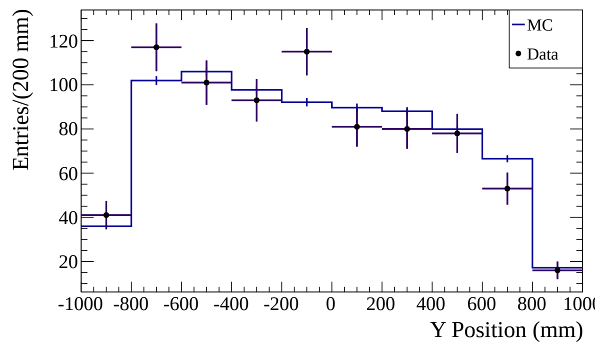

(b) Y projection

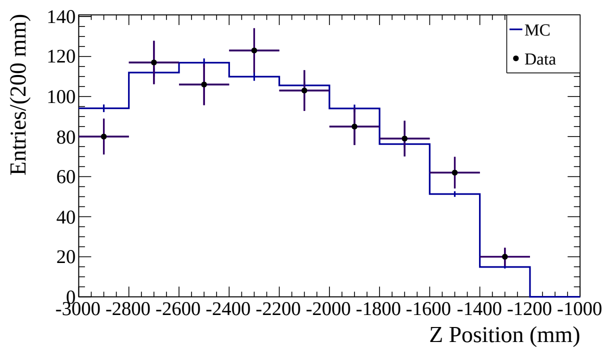

(c) Z projection

Figure 4.29: Comparison of the one-dimensional vertex distributions of candidate events in the P∅D in the water-in configuration. Monte Carlo events are weighted by the mass difference between the Monte Carlo geometry and the as-built measurements, the POT, and the flux.

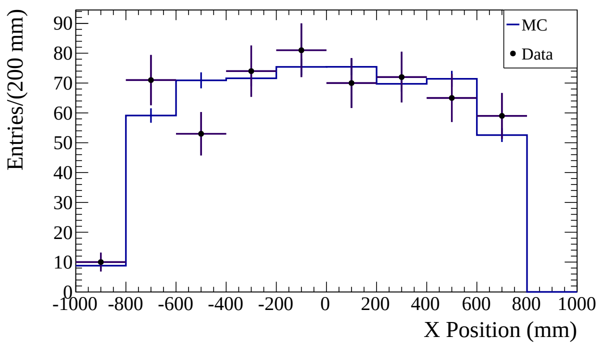

(a) X projection

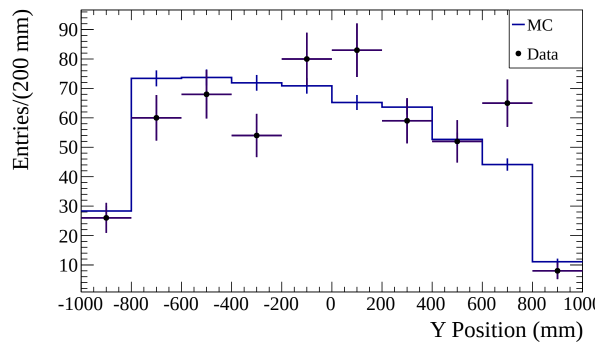

(b) Y projection

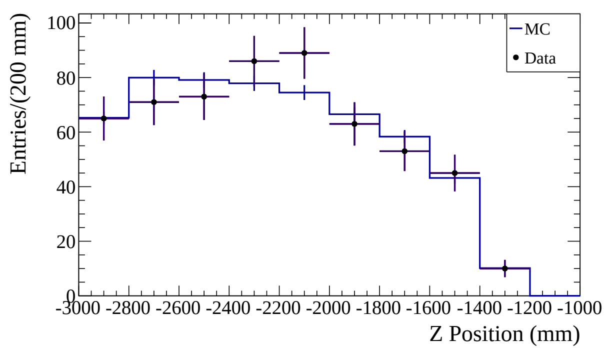

(c) Z projection

Figure 4.30: Comparison of the one-dimensional vertex distributions of candidate events in the P∅D in the water-out configuration. Monte Carlo events are weighted by the mass difference between the Monte Carlo geometry and the as-built measurements, the POT, and the flux.

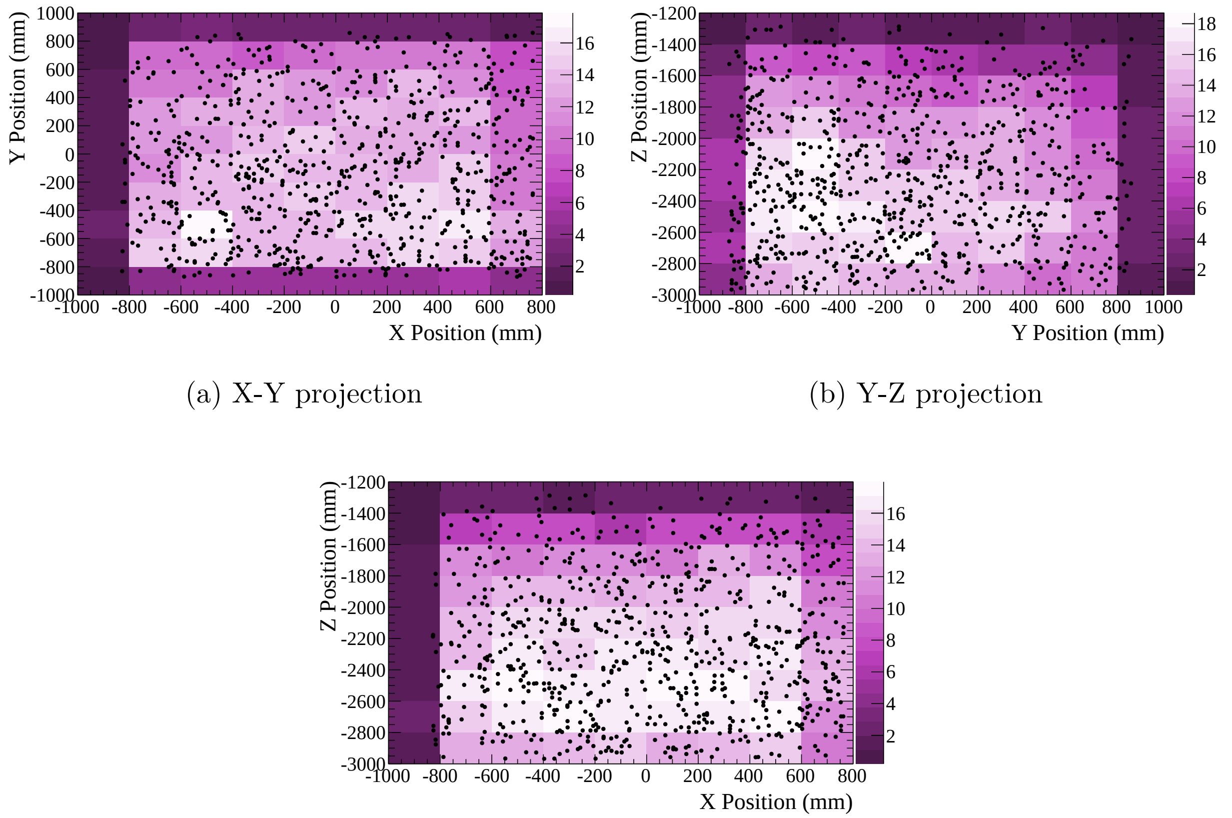

(a) X-Y projection

(b) Y-Z projection

(c) X-Z projection

Figure 4.31: Comparison of the two-dimensional vertex distributions of candidate events in the P∅D in the water-in configuration. Monte Carlo events are weighted by the mass difference between the Monte Carlo geometry and the as-built measurements, the POT, and the flux.

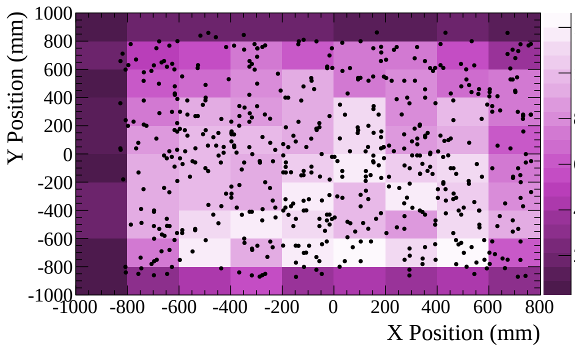

(a) X-Y projection

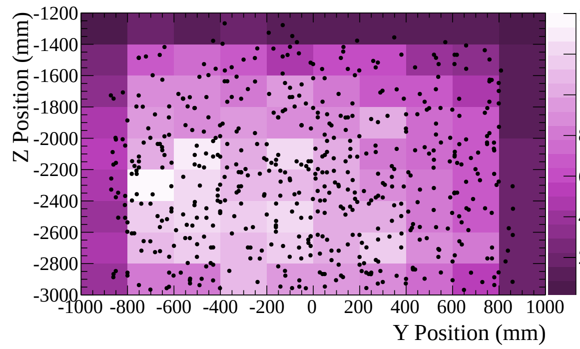

(b) Y-Z projection

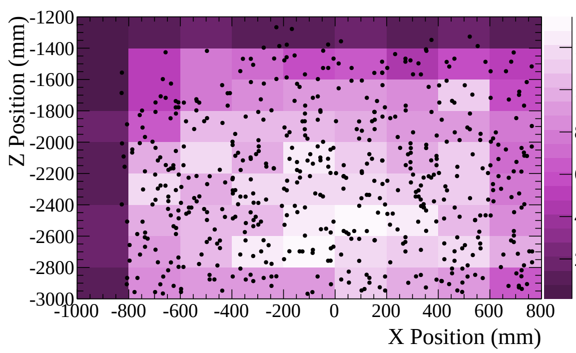

(c) X-Z projection

Figure 4.32: Comparison of the two-dimensional vertex distributions of candidate events in the PØD in the water-out configuration. Monte Carlo events are weighted by the mass difference between the Monte Carlo geometry and the as-built measurements, the POT, and the flux.

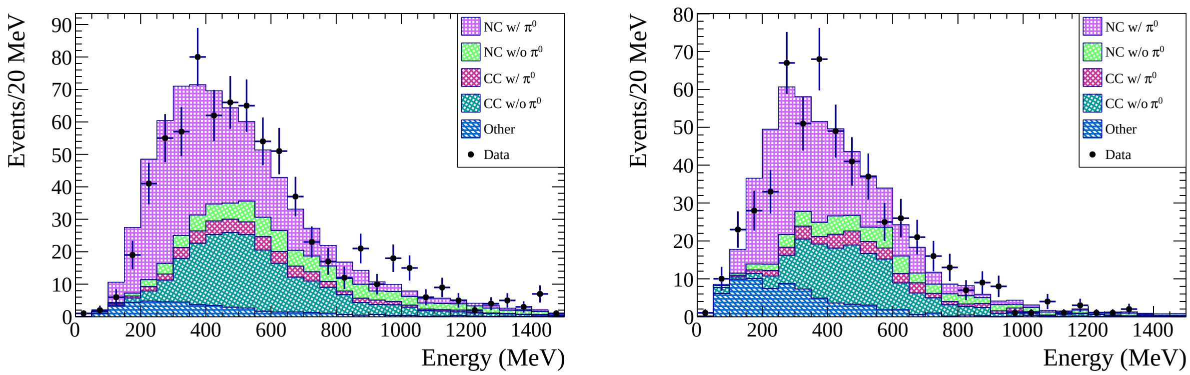

(a) Water-in configuration

(b) Water-out configuration

Figure 4.33: The reconstructed π^0 energy for events passing all selection cuts. The Monte Carlo events are flux, mass and POT weighted, then the overall distribution is area normalized to the data distribution in order to emphasize any shape differences.

The normalization terms for the selected region and the sideband region are defined as Poisson distributions,

$$\mathcal{L}(N_{\text{Sig}}^{\text{Selected}}, N_{\text{Bkg}}^{\text{Selected}})_{\text{Norm}} \sim \frac{(N_{\text{Sig}}^{\text{Selected}} + N_{\text{Bkg}}^{\text{Selected}})^{N_{\text{Obs}}^{\text{Selected}}} e^{-(N_{\text{Sig}}^{\text{Selected}} + N_{\text{Bkg}}^{\text{Selected}})}}{N_{\text{Obs}}^{\text{Selected}}!} \tag{4.10}$$

$$\mathcal{L}(N_{\text{Sig}}^{\text{Sideband}}, N_{\text{Bkg}}^{\text{Sideband}})_{\text{Norm}} \sim \frac{(N_{\text{Sig}}^{\text{Sideband}} + N_{\text{Bkg}}^{\text{Sideband}})^{N_{\text{Obs}}^{\text{Sideband}}} e^{-(N_{\text{Sig}}^{\text{Sideband}} + N_{\text{Bkg}}^{\text{Sideband}})}}{N_{\text{Obs}}^{\text{Sideband}}!}. \tag{4.11}$$

with the number of observed events, N_{Obs}, remaining constant through the fitting procedure.

The likelihood of the shape of the distributions, $\mathcal{L}(e, N_{\text{Sig}}^{\text{Selected}}, N_{\text{Bkg}}^{\text{Selected}})_{\text{Shape}}$ and $\mathcal{L}(e, N_{\text{Sig}}^{\text{Sideband}}, N_{\text{Bkg}}^{\text{Sideband}})_{\text{Shape}}$, are defined by the four non-parametric PDFs shown in Figures 4.34 and 4.35. These PDFs are first normalized to one, then the linear interpolated value at the energy scale shifted invariant mass is pulled as the likelihood from the PDFs. Since the mass of the data events (m_i) is shifted by the energy scale, an addition multiplication of the likelihood by e is needed. The shape likelihood becomes

$$\begin{aligned} \mathcal{L}(e, N_{\text{Sig}}^{\text{Selected}}, N_{\text{Bkg}}^{\text{Selected}})_{\text{Shape}} \sim \prod_i e \cdot \Bigg(& \frac{N_{\text{Sig}}^{\text{Selected}}}{N_{\text{Sig}}^{\text{Selected}} + N_{\text{Bkg}}^{\text{Selected}}} \cdot \rho_{\text{Sig}}^{\text{Selected}}(e \cdot m_i) \\ & + \frac{N_{\text{Bkg}}^{\text{Selected}}}{N_{\text{Sig}}^{\text{Selected}} + N_{\text{Bkg}}^{\text{Selected}}} \cdot \rho_{\text{Bkg}}^{\text{Selected}}(e \cdot m_i) \Bigg) \end{aligned} \tag{4.12}$$

$$\begin{aligned} \mathcal{L}(e, N_{\text{Sig}}^{\text{Sideband}}, N_{\text{Bkg}}^{\text{Sideband}})_{\text{Shape}} \sim \prod_i e \cdot \Bigg(& \frac{N_{\text{Sig}}^{\text{Sideband}}}{N_{\text{Sig}}^{\text{Sideband}} + N_{\text{Bkg}}^{\text{Sideband}}} \cdot \rho_{\text{Sig}}^{\text{Sideband}}(e \cdot m_i) \\ & + \frac{N_{\text{Bkg}}^{\text{Sideband}}}{N_{\text{Sig}}^{\text{Sideband}} + N_{\text{Bkg}}^{\text{Sideband}}} \cdot \rho_{\text{Bkg}}^{\text{Sideband}}(e \cdot m_i) \Bigg). \end{aligned} \tag{4.13}$$

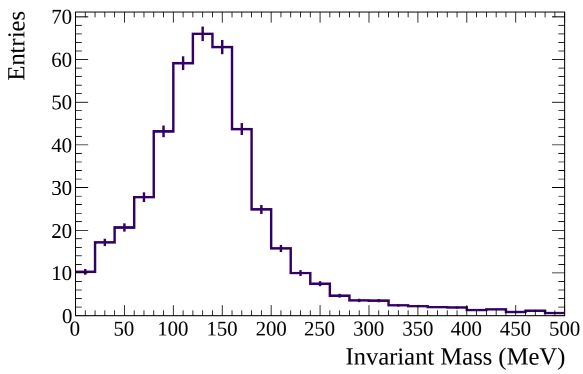

(a) Signal PDF of Selected Events.

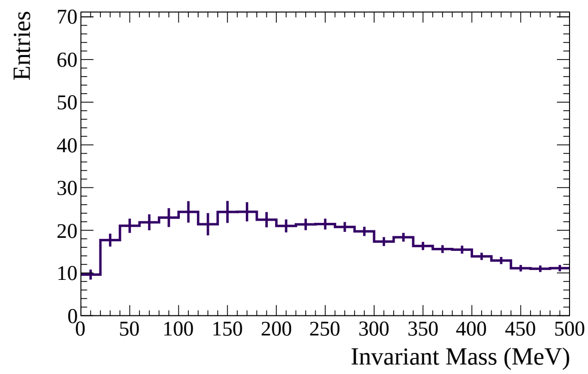

(b) Background PDF of Selected Events.

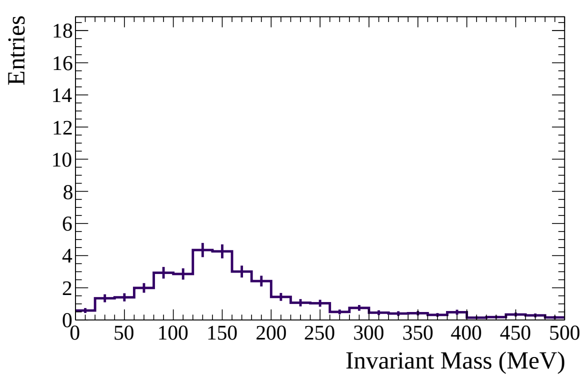

(c) Signal PDF of Sideband Events.

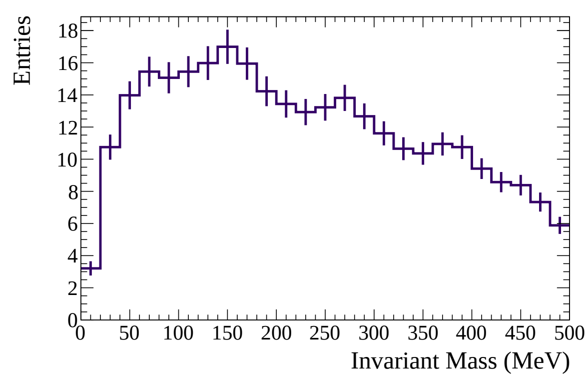

(d) Background PDF of Sideband Events.

Figure 4.34: The input PDFs for the P∅D water-in configuration. Shown are the signal and sideband events. These PDFs are normalized to one to be used in the extended maximum likelihood.

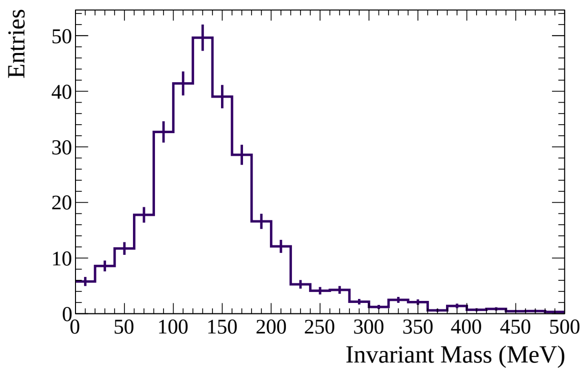

(a) Signal PDF of Selected Events.

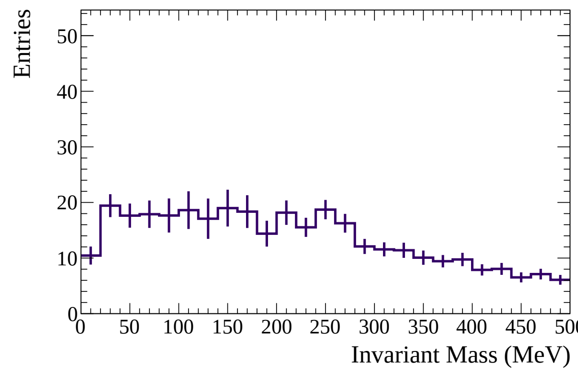

(b) Background PDF of Selected Events.

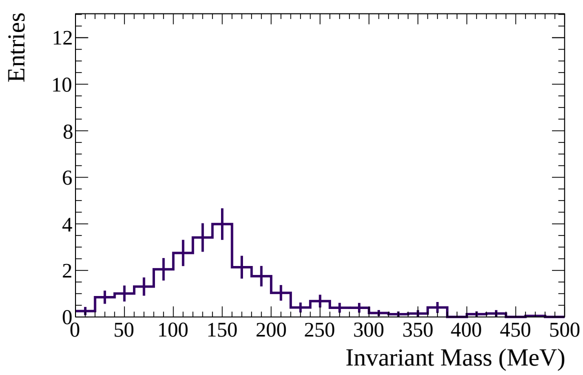

(c) Signal PDF of Sideband Events.

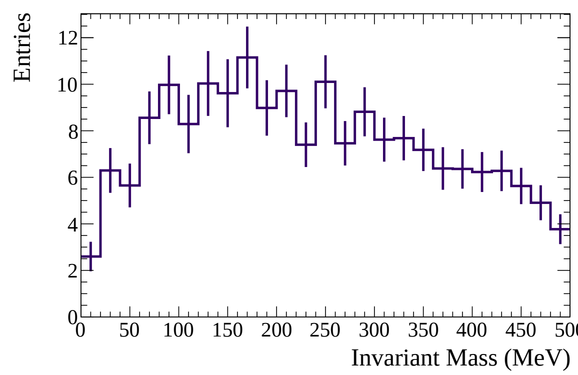

(d) Background PDF of Sideband Events.

Figure 4.35: The input PDFs for the P∅D water-out configuration. Shown are the signal and sideband events. The plots use the flux-weighted NEUT Monte Carlo as their normalization. These PDFs are normalized to one to be used in the extended maximum likelihood.

The last piece of the likelihood comes from constraints on the parameters on the fit. To that end, a covariance matrix, $\mathbb{C}$, was constructed to attempt to minimize the correlations between the individual values. The vector $\Delta\mathbf{X}$ represents the deviation from the nominal values. These constraints are added to the likelihood through

$$\mathcal{L}(N_{\text{Sig}}^{\text{Selected}}, N_{\text{Bkg}}^{\text{Selected}}, N_{\text{Sig}}^{\text{Sideband}}, N_{\text{Bkg}}^{\text{Sideband}}) \sim \exp\left(-\frac{1}{2}\Delta\mathbf{X}^{\text{T}}\mathbb{C}^{-1}\Delta\mathbf{X}\right), \tag{4.14}$$

with

$$\mathbf{X} = \begin{pmatrix} \frac{N_{\text{Sig}}^{\text{Sideband}}}{N_{\text{Sig}}^{\text{Selected}}} & \frac{N_{\text{Bkg}}^{\text{Sideband}}}{N_{\text{Bkg}}^{\text{Selected}}} \end{pmatrix}. \tag{4.15}$$

The constraint placed on the ratio of the sideband signal to the selected signal comes from the difference in data and Monte Carlo of the fake rate of muon decay cluster reconstruction which is detailed in the Subsection 5.7.3. The constraint placed on the ratio of the sideband background to the selected background comes from the difference in data and Monte Carlo muon decay cluster reconstruction efficiency also detailed in the Subsection 5.7.3.

Removing Model Dependencies

As an auxiliary analysis, an attempt at removing the dependency on the NEUT model background was made. This was performed by an addition of a shape affecting term, g. The least well known part of the background pdf occurs underneath the π^0 invariant mass peak. In order to compensate for this region, an extra shape moderated by g is added into the fit. Although any normalizable shape can be applied, the worst case scenario is that the background appears as a peak in the selected region, or reproduces the selected signal shape. If the background had the same appearance as the signal, the measurement could be a drastic overestimate or underestimate of the signal. The total number of selected events is equal to the sum of the bins in the selected signal and selected background histogram as

$$N_{\gamma\gamma}^{\text{Selected}} = \sum_{i}^{bins} \rho_{\text{Sig}}^{\text{Selected}}(i) + \sum_{i}^{bins} \rho_{\text{Bkg}}^{\text{Selected}}(i) \tag{4.16a}$$

$$\sum_{i}^{bins} \rho_{\text{Sig}}^{\text{Selected}}(i) = N_{\text{Sig}}^{\text{Selected}} + g \cdot N_{\text{Bkg}}^{\text{Selected}} \tag{4.16b}$$

$$\sum_{i}^{bins} \rho_{\text{Bkg}}^{\text{Selected}}(i) = N_{\text{Bkg}}^{\text{Selected}} - g \cdot N_{\text{Bkg}}^{\text{Selected}}. \tag{4.16c}$$

The normalization of the selected signal histogram is the number of signal plus the g factor times the number of background. It is here that the background is varied by the shape of the selected signal histogram, with a normalization of $g \cdot N_{\text{Bkg}}^{\text{Selected}}$. The background histogram contribution to the total number of selected events needs to then be modified by this g factor to retain the overall normalization. In the sideband set of equations,

$$N_{\gamma\gamma}^{\text{Sideband}} = \sum_i^{bins} \rho_{\text{Sig}}^{\text{Sideband}}(i) + \sum_i^{bins} \rho_{\text{Sig}}^{\text{Selected}}(i) + \sum_i^{bins} \rho_{\text{Bkg}}^{\text{Sideband}}(i) \tag{4.17a}$$

$$\sum_i^{bins} \rho_{\text{Sig}}^{\text{Sideband}}(i) = \alpha \cdot N_{\text{Sig}}^{\text{Selected}} \tag{4.17b}$$

$$\sum_i^{bins} \rho_{\text{Sig}}^{\text{Selected}}(i) = \beta \cdot g \cdot N_{\text{Bkg}}^{\text{Selected}} \tag{4.17c}$$

$$\sum_i^{bins} \rho_{\text{Bkg}}^{\text{Sideband}}(i) = \beta \cdot N_{\text{Bkg}}^{\text{Selected}} - \beta \cdot g \cdot N_{\text{Bkg}}^{\text{Selected}}, \tag{4.17d}$$

the application of the shape variation is more apparent. The number of sideband events is equal to the sum of the normalization of three histograms: the sideband signal histogram, the shape variation histogram, and the sideband background histogram.

The variable g allows the fit to be flexible in the peak area. The g factor is allowed to be positive or negative, which means that the shape histogram could have add or subtract from the total shape whilst retaining the overall normalization. Adding the g factor turns the overall likelihood into

$$\mathcal{L}_{\text{Signal}} = \mathcal{L}(N_{\text{Sig}}^{\text{Selected}}, N_{\text{Bkg}}^{\text{Selected}})_{\text{Norm}} \times \mathcal{L}(e, g, N_{\text{Sig}}^{\text{Selected}}, N_{\text{Bkg}}^{\text{Selected}})_{\text{Shape}} \tag{4.18a}$$

$$\mathcal{L}_{\text{Sideband}} = \mathcal{L}(N_{\text{Sig}}^{\text{Sideband}}, N_{\text{Bkg}}^{\text{Sideband}})_{\text{Norm}} \times \mathcal{L}(e, g, N_{\text{Sig}}^{\text{Sideband}}, N_{\text{Bkg}}^{\text{Sideband}})_{\text{Shape}} \tag{4.18b}$$

$$\mathcal{L}_{\text{Total}} = \mathcal{L}_{\text{Signal}} \times \mathcal{L}_{\text{Sideband}} \times \mathcal{L}_{\text{Sys}}(e, g, N_{\text{Sig}}^{\text{Selected}}, N_{\text{Bkg}}^{\text{Selected}}, N_{\text{Sig}}^{\text{Sideband}}, N_{\text{Bkg}}^{\text{Sideband}}). \tag{4.18c}$$

The normalization terms for the selected region and the sideband region are not affected by this additional shape term. Neither is the constraint term, since g is allowed to float freely.

The likelihood of the shape of the distributions, $\mathcal{L}(e, g, N_{\text{Sig}}^{\text{Selected}}, N_{\text{Bkg}}^{\text{Selected}})_{\text{Shape}}$ and $\mathcal{L}(e, g, N_{\text{Sig}}^{\text{Sideband}}, N_{\text{Bkg}}^{\text{Sideband}})_{\text{Shape}}$ must be adjusted for the g factor. For the selected region, the signal PDF is used for the signal prediction. However, the signal PDF is used again in conjunction with the background PDF to predict the overall shape of the background. This is where the power of the g factor comes in, it allows the background PDF to be varied in a predictable way underneath the signal peak. For the sideband region, the sideband signal PDF is used for the signal prediction, but the selected signal PDF is used as a variation on the sideband background. In this way, the shape of the sideband constrains the possibilities for the g factor which then effects the background shape in the selected region. The shape likelihood becomes

Table 4.18: The results of running the fit for both the PØD water-in and PØD water-out configurations.

	$N_{\text{Sig}}^{\text{Selected}}$	$N_{\text{Bkg}}^{\text{Selected}}$	$N_{\text{Sig}}^{\text{Sideband}}$	$N_{\text{Bkg}}^{\text{Sideband}}$	e (%)
Water-In	341.6 ± 32.6	388.1 ± 25.5	26.9 ± 2.6	245.4 ± 14.9	89.45 ± 3.44
Water-Out	246.5 ± 26.0	270.6 ± 21.7	20.4 ± 2.2	140.6 ± 10.7	96.71 ± 0.62

Table 4.19: The Monte Carlo prediction for the PØD water-in and PØD water-out configurations adjusted by the fitted energy scale.

	$N_{\text{Sig}}^{\text{Selected}}$	$N_{\text{Bkg}}^{\text{Selected}}$	$N_{\text{Sig}}^{\text{Sideband}}$	$N_{\text{Bkg}}^{\text{Sideband}}$
Water-In	432.6 ± 4.3	428.6 ± 4.3	32.6 ± 1.2	278.4 ± 3.4
Water-Out	290.1 ± 5.4	334.9 ± 5.9	23.5 ± 1.6	184.3 ± 4.3

$$\begin{aligned}\mathcal{L}(e, g, N_{\text{Sig}}^{\text{Selected}}, N_{\text{Bkg}}^{\text{Selected}})_{\text{Shape}} \sim \prod_i e \cdot \Bigg(& \frac{N_{\text{Sig}}^{\text{Selected}}}{N_{\text{Sig}}^{\text{Selected}} + N_{\text{Bkg}}^{\text{Selected}}} \cdot \rho_{\text{Sig}}^{\text{Selected}}(e \cdot m_i) \\ & + \frac{N_{\text{Bkg}}^{\text{Selected}}}{N_{\text{Sig}}^{\text{Selected}} + N_{\text{Bkg}}^{\text{Selected}}} \cdot g \cdot \rho_{\text{Sig}}^{\text{Selected}}(e \cdot m_i) \\ & + \frac{N_{\text{Bkg}}^{\text{Selected}}}{N_{\text{Sig}}^{\text{Selected}} + N_{\text{Bkg}}^{\text{Selected}}} \cdot (1-g) \cdot \rho_{\text{Bkg}}^{\text{Selected}}(e \cdot m_i) \Bigg)\end{aligned} \tag{4.19}$$

$$\begin{aligned}\mathcal{L}(e, g, N_{\text{Sig}}^{\text{Sideband}}, N_{\text{Bkg}}^{\text{Sideband}})_{\text{Shape}} \sim \prod_i e \cdot \Bigg(& \frac{N_{\text{Sig}}^{\text{Sideband}}}{N_{\text{Sig}}^{\text{Sideband}} + N_{\text{Bkg}}^{\text{Sideband}}} \cdot \rho_{\text{Sig}}^{\text{Sideband}}(e \cdot m_i) \\ & + \frac{N_{\text{Bkg}}^{\text{Sideband}}}{N_{\text{Sig}}^{\text{Sideband}} + N_{\text{Bkg}}^{\text{Sideband}}} \cdot g \cdot \rho_{\text{Sig}}^{\text{Selected}}(e \cdot m_i) \\ & + \frac{N_{\text{Bkg}}^{\text{Sideband}}}{N_{\text{Sig}}^{\text{Sideband}} + N_{\text{Bkg}}^{\text{Sideband}}} \cdot (1-g) \cdot \rho_{\text{Bkg}}^{\text{Sideband}}(e \cdot m_i) \Bigg).\end{aligned} \tag{4.20}$$

Table 4.20: The number of signal events found in the fit for both the water-in and water-out configurations. The errors listed come from the fit and are statistical.

	Observed	Expected	Ratio
Water-In	341.6 ± 32.6	432.6 ± 4.3	0.790 ± 0.076
Water-Out	246.5 ± 26.0	290.1 ± 5.4	0.850 ± 0.091

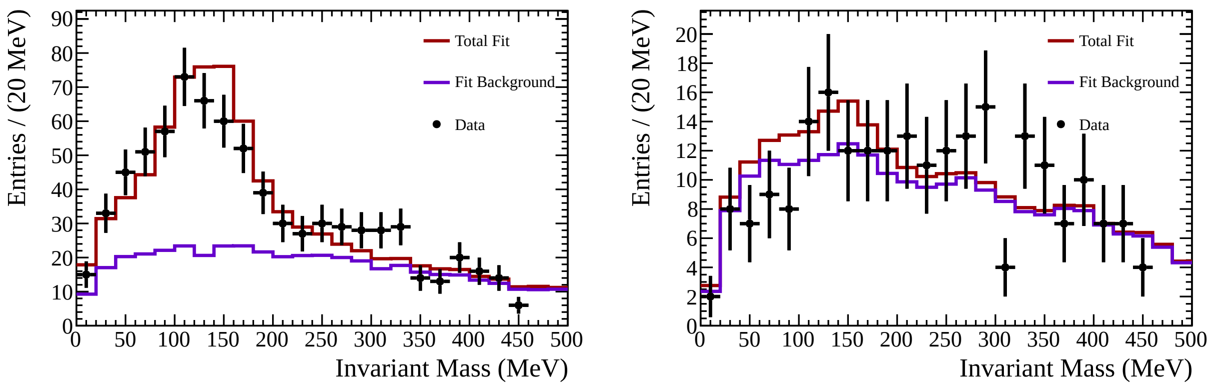

(a) Water-in Configuration

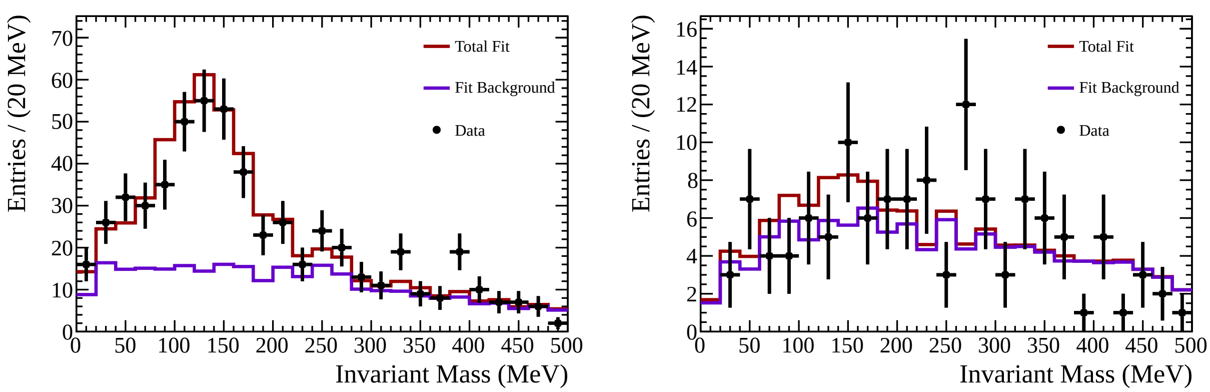

(b) Water-out Configuration

Figure 4.36: The P∅D water-in and water-out configuration simultaneous invariant mass fit.

Table 4.21: The results of running the fit for both the PØD water-in and PØD water-out configurations with an unconstrained g factor.

	$N^{\text{Selected}}_{\text{Sig}}$	$N^{\text{Selected}}_{\text{Bkg}}$	$N^{\text{Sideband}}_{\text{Sig}}$	$N^{\text{Sideband}}_{\text{Bkg}}$	e (%)	g
Water-In	408.7 ± 32.9	341.2 ± 23.6	32.2 ± 2.7	220.1 ± 14.5	91.15 ± 0.74	-0.27 ± 0.07
Water-Out	321.0 ± 28.6	214.3 ± 20.6	26.6 ± 2.4	116.1 ± 10.7	98.00 ± 0.61	-0.39 ± 0.09

Table 4.22: The Monte Carlo prediction for the PØD water-in and PØD water-out configurations adjusted by the fitted energy scale.

	$N^{\text{Selected}}_{\text{Sig}}$	$N^{\text{Selected}}_{\text{Bkg}}$	$N^{\text{Sideband}}_{\text{Sig}}$	$N^{\text{Sideband}}_{\text{Bkg}}$
Water-In	432.8 ± 4.3	433.5 ± 4.3	32.7 ± 1.2	282.3 ± 3.5
Water-Out	290.2 ± 5.4	336.3 ± 5.9	23.5 ± 1.6	185.6 ± 4.3

4.4.3 Fit Results

Figure 4.36 show the results of the simultaneous unbinned extended maximum likelihood fit. The first 22 bins of each region are used to calculate the χ^2. The last three bins are removed because they can potentially be affected by the energy scale. There are five parameters in the fit leading to a 39 degrees of freedom. The χ^2 value for the PØD water-in configuration is 40.4 for 39 degrees of freedom, leading to a p-value of 0.41. The χ^2 value for the PØD water-out configuration is 53.5 for 39 degrees of freedom, leading to a p-value of 0.06. The results of fitting the invariant mass spectrum are listed in Table 4.18. The energy scale adjusted Monte Carlo prediction is listed in Table 4.19. In order to calculate a systematic from this, first the data to Monte Carlo ratio of the number of signal events must be calculated. Table 4.20 summarizes the data to Monte Carlo ratios with statistical errors. To see the negative log likelihood curves from the fits, please look in Appendix A.

Removing Model Dependencies

The result of fitting the data with this method is shown in Figure 4.37. The first 22 bins of each region are used to calculate the χ^2. The last three bins are removed because they can potentially be affected by the energy scale. There are six parameters in the fit leading to a 38 degrees of freedom. The χ^2 value for the PØD water-in configuration is 47.5 for 38 degrees of freedom, leading to a p-value of 0.14. The χ^2 value for the PØD water-out configuration

Table 4.23: The number of signal events found in the fit for both the water-in and water-out configurations with an unconstrained g factor. The errors listed come from the fit and are statistical.

	Observed	Expected	Ratio
Water-In	408.7 ± 32.5	432.8 ± 4.3	0.944 ± 0.076
Water-Out	321.0 ± 28.6	290.2 ± 5.4	1.107 ± 0.100

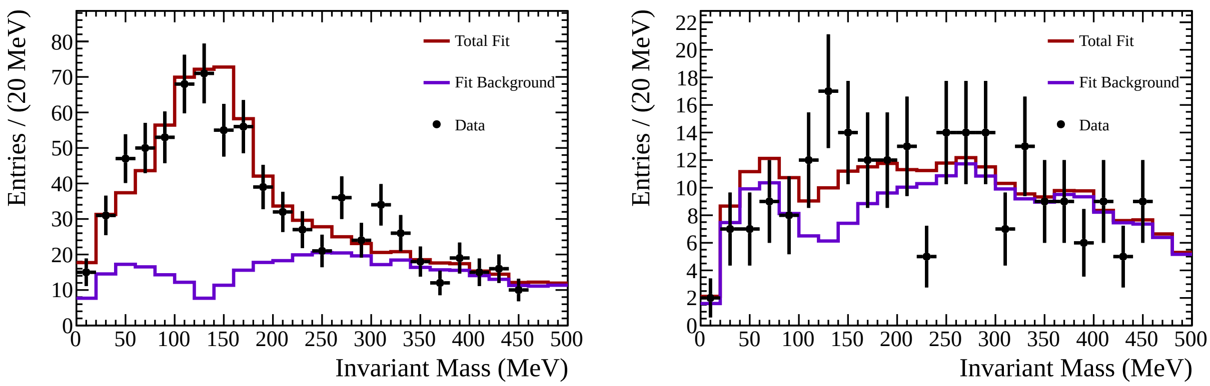

(a) Water-in Configuration

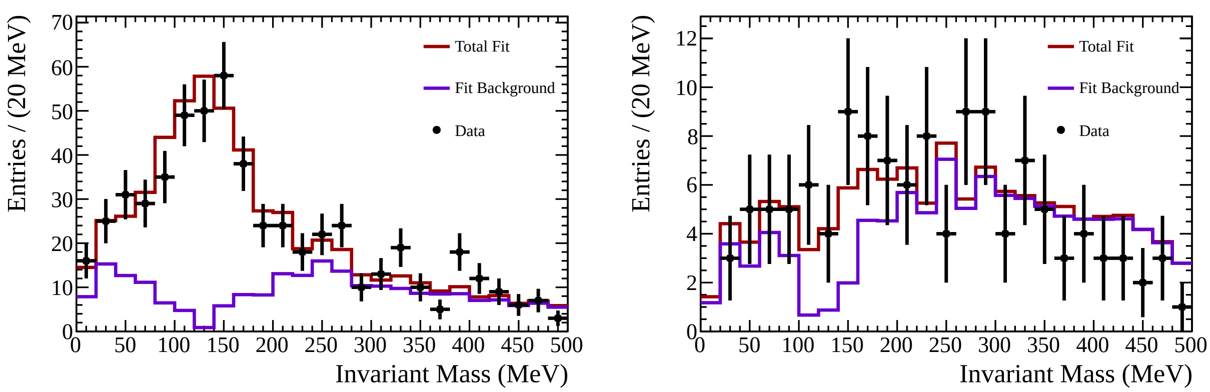

(b) Water-out Configuration

Figure 4.37: The P∅D water-in and water-out configuration simultaneous invariant mass fit with an unconstrained g factor.

Table 4.24: Listed are the efficiencies (ϵ) and the purity (π) of the selection. The total efficiencies are shown as well as the specific on-water and not-water efficiencies. Note that the P∅D water-out configuration has an effective on-water efficiency of 0.0 since there is no water in the P∅D.

	ϵ_{ff}	ϵ_A	π
Water-In			
Total	6.097 ± 0.014	12.419 ± 0.038	48.69 ± 0.17
On-Water	6.205 ± 0.024	12.663 ± 0.064	56.16 ± 0.30
Not-Water	6.037 ± 0.017	12.284 ± 0.047	45.28 ± 0.21
Water-Out			
Total	4.790 ± 0.019	10.996 ± 0.061	46.12 ± 0.32

Table 4.25: The number of Monte Carlo predicted signal NC1π^0 events for each run with a true vertex on water. Note that the entirety of Run 3 was in the P∅D water-out configuration, so it would have no on-water vertices.

Run 1	Run 2	Run 4	Total
18.3 ± 0.8	41.4 ± 1.6	97.5 ± 1.9	157.2 ± 2.5

is 38.7 for 38 degrees of freedom, leading to a p-value of 0.44.

There is a very large distortion present in the shape of the background under the peak. Although this may initially cause some concern, the distortion is accounted for in the systematics. In addition, the normalization is the information extracted, not the shape information, to perform the ratio calculations. For the data to Monte Carlo ratios of the P∅D water-in and water-out configurations, the fractional difference between the $g \neq 0$ and $g = 0$ is added in quadrature with the rest of the systematics. Tables 4.21 and 4.22 show the breakdown of the numbers of expected and observed events in both the signal region and in the sideband region. Table 4.23 lists the number of signal events expected and observed and the data to Monte Carlo ratio with statistical errors. The P∅D water-in configuration data to Monte Carlo ratio of NC1π^0 events with systematics is $0.944 \pm 0.076(\text{stat}) \pm 0.231(\text{sys})$. For the P∅D water-out configuration data to Monte Carlo ratio is $1.107 \pm 0.101(\text{stat}) \pm 0.316(\text{sys})$. To see the negative log likelihood curves from the fits, please look in Appendix A.

4.4.4 On-Water Calculation

Six numbers are necessary for the on-water calculation described in Equation 4.5, the POT, efficiency and the observed signal in the signal region for both the water-in and water-out configurations. As a sanity check, the calculation of Equation 4.5 was done with the Monte Carlo using the number of expected events. The Monte Carlo predictions for the efficiencies, broken down into on-water and not-water events, are summarized in Table 4.24. The not-water efficiency must be used due to the construction of the subtraction. A count of the Monte Carlo NC1π^0 events on water was done by checking if the location of each true vertex was in a water target, the results are shown in Table 4.25. This Monte Carlo count predicts 157.2 ± 2.5 signal events to be on-water. If the subtraction is performed on the Monte Carlo expectations of the number of water-in and water-out signal events, the prediction becomes 157.9 ± 6.8(stat). This is a discrepancy of 0.7 events which within statistical errors is consistent with zero. For the data to Monte Carlo comparison of on-water events, the number of directly counted events is used because the difference is negligible and it has a smaller statistical error. Using the subtraction method as described in Equation 4.5 on the data, 106.4 ± 41.0(stat) $\pm$ 72.6(sys) (106.4 ± 41.0(stat) $\pm$ 71.9(sys)) events were calculated, with pre-(post-)BANFF fit systematic errors. The final ratio of data to NEUT Monte Carlo of the on-water NC1π^0 is calculated as 0.677 ± 0.261(stat)$\pm$0.462(sys), with pre-BANFF fit systematic errors. The final ratio of data to NEUT Monte Carlo of the on-water NC1π^0 is calculated as 0.677 ± 0.261(stat) $\pm$ 0.457(sys), with post-BANFF fit systematic errors. A detailed discussion of the systematic error is in Section 5.

Removing Model Dependencies

This secondary analysis uses an unconstrained g shape variation factor, which has been presented in this section in detail. This result allows the background to be modified within a variation allowed by the muon decay sideband and provides a less model dependent value. Using the subtraction method as described in Equation 4.5 on the data, 102.4 ± 42.5(stat) $\pm$ 90.4(sys) (102.4 ± 42.5(stat) $\pm$ 89.3(sys)) events were calculated, with pre-(post-)BANFF fit systematic errors. The calculated number of events on-water using the shape variation is very close to the default method. The final ratio of data to NEUT Monte Carlo of the on-water NC1π^0 is calculated as 0.652 ± 0.270(stat)$\pm$0.576(sys), with pre-BANFF fit systematic errors. The final ratio of data to NEUT Monte Carlo of the on-water NC1π^0 is calculated as 0.652 ± 0.270(stat) $\pm$ 0.569(sys), with post-BANFF fit systematic errors. Further discussion of the systematic error applied to the result is in Section 5.

4.5 T2KReWeight

Although the analysis has been in comparison to the NEUT Monte Carlo, T2K has an additional tool that can be used to reweight the Monte Carlo given global and ND280 fits constructed by the Beam and Neutrino Flux Task Force (BANFF), an internal working group at T2K. This reweighting can provide different central values for the PDFs that have been constructed. The central values of the pre-BANFF fits are based on other cross section measurements, such as those done by MiniBooNE and other flux measurements, such as those done by NA61. These external restrictions provide a different central value than the nominal flux-weighted NEUT Monte Carlo initially provides. There are additionally different central values from the post-BANFF fits that incorporate ND280 analyses into the constraints. The invariant mass shape prediction differs between the flux-weighted NEUT, the pre-BANFF fit and post-BANFF fit Monte Carlos. This can be seen in Figures 4.38 and 4.39. Additionally, Figures 4.40 and 4.41 show the extent of the variance from the central values over 1000 throws of T2KReWeight.

Tweaking the cross section and flux dials will change the total number of expected events

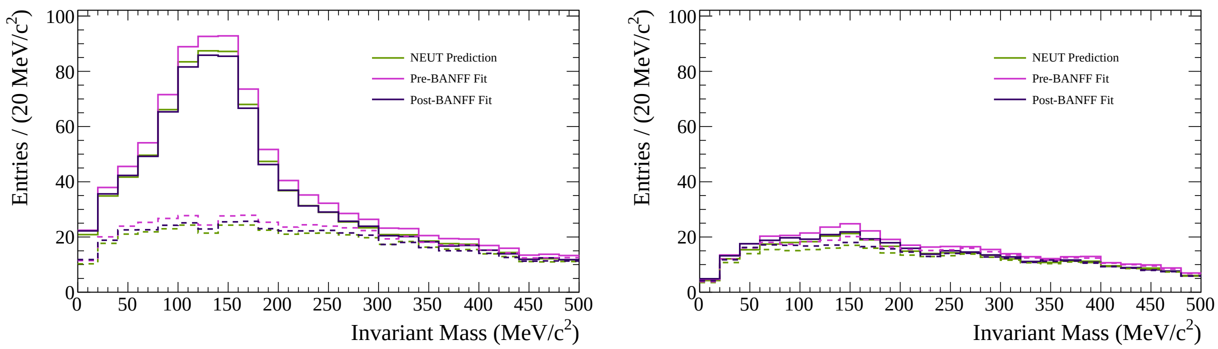

(a) Selected Region (b) Sideband Region

Figure 4.38: For the P∅D water-in configuration, the variation between the central values of the flux-weighted NEUT prediction, the pre-BANFF fit prediction and the post-BANFF fit prediction. The solid lines show the prediction of the shape of the invariant mass for all events. The dashed lines are the prediction of the background shape.

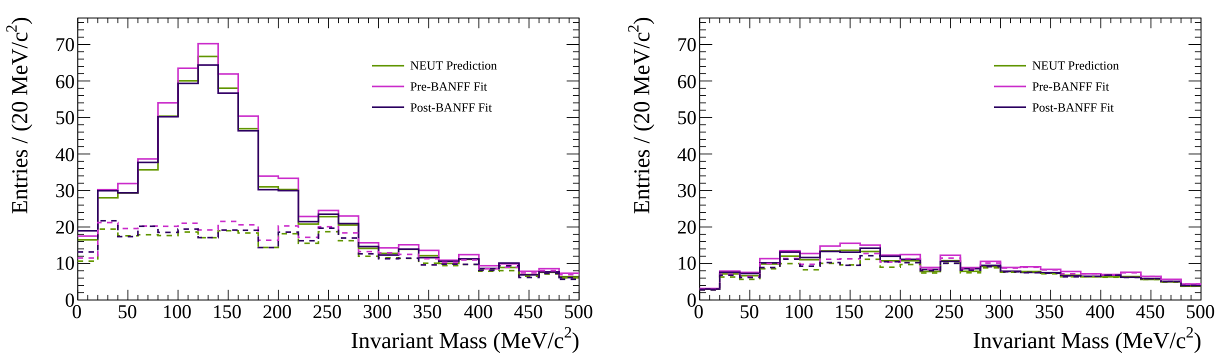

(a) Selected Region (b) Sideband Region

Figure 4.39: For the P∅D water-out configuration, the variation between the central values of the flux-weighted NEUT prediction, the pre-BANFF fit prediction and the post-BANFF fit prediction. The solid lines show the prediction of the shape of the invariant mass for all events. The dashed lines are the prediction of the background shape.

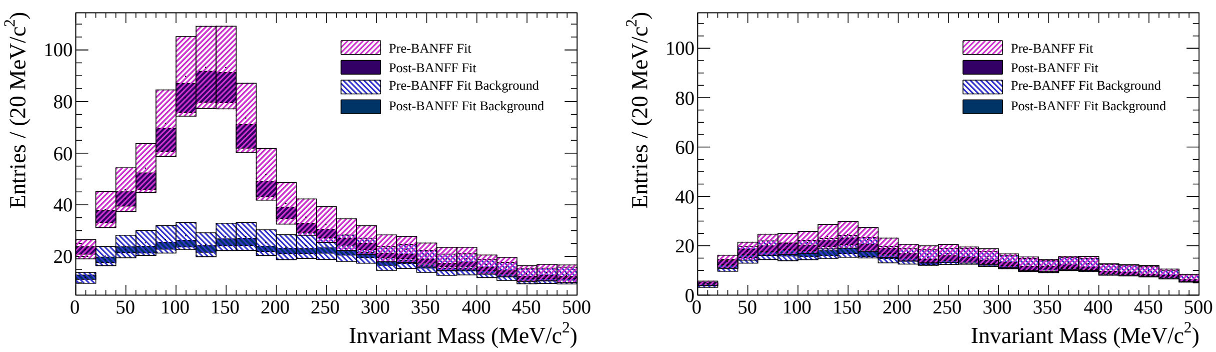

(a) Selected Region (b) Sideband Region

Figure 4.40: For the P∅D water-in configuration, the spread of the errors on the pre-BANFF fit prediction and the post-BANFF fit prediction. The length of the boxes represent the variance from the mean of the repeated throws of T2KReWeight. Both the variance for the total Monte Carlo and for the background Monte Carlo are shown.

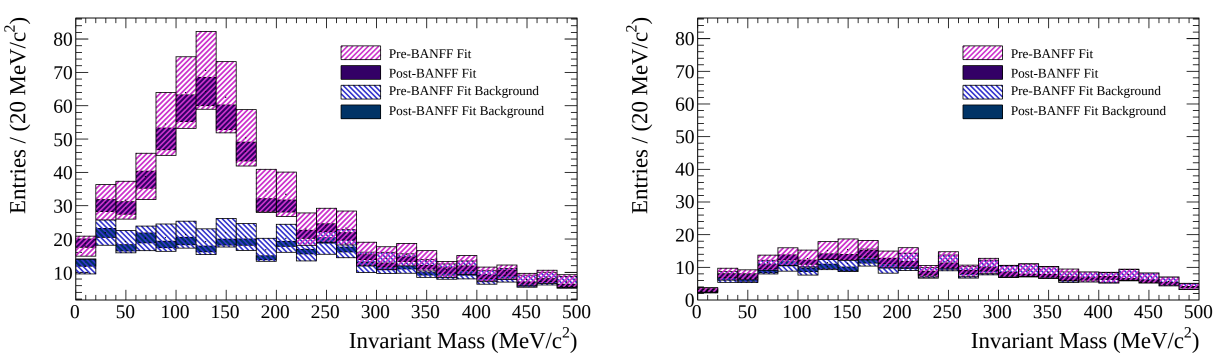

(a) Selected Region (b) Sideband Region

Figure 4.41: For the P∅D water-out configuration, the spread of the errors on the pre-BANFF fit prediction and the post-BANFF fit prediction. The length of the boxes represent the variance from the mean of the repeated throws of T2KReWeight. Both the variance for the total Monte Carlo and for the background Monte Carlo are shown.

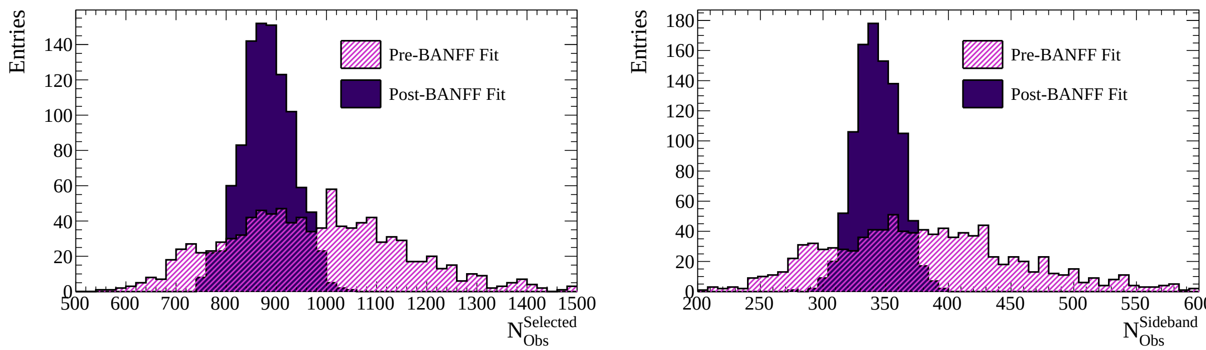

(a) Selected Region (b) Selected Region

Figure 4.42: For the PØD water-in configuration, the spread of the expectation of the number of observed events in the selected and sideband regions pulled from throws of the pre- and post-BANFF fit T2KReWeight.

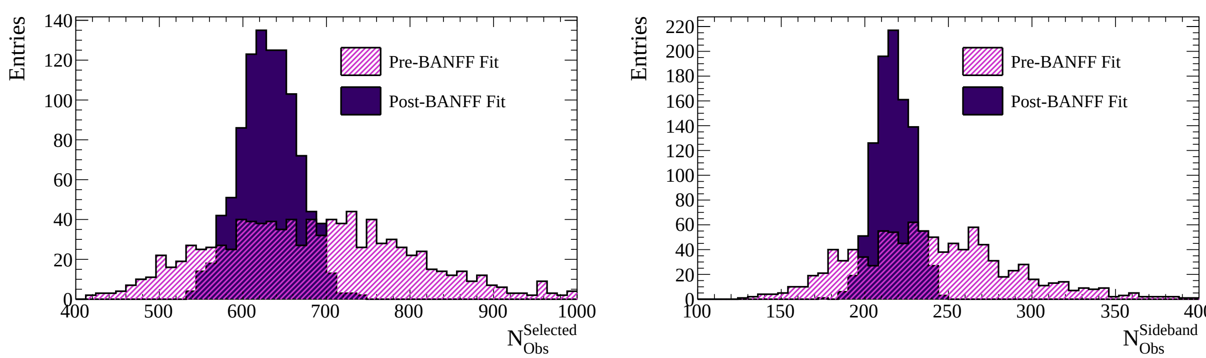

(a) Selected Region (b) Selected Region

Figure 4.43: For the PØD water-out configuration, the spread of the expectation of the number of observed events in the selected and sideband regions pulled from throws of the pre- and post-BANFF fit T2KReWeight.

Table 4.26: The results of running the fit for both the PØD water-in and PØD water-out configurations with the T2KReWeight pre-BANFF fit central values.

	$N_{\text{Sig}}^{\text{Selected}}$	$N_{\text{Bkg}}^{\text{Selected}}$	$N_{\text{Sig}}^{\text{Sideband}}$	$N_{\text{Bkg}}^{\text{Sideband}}$	e
Water-In	352.6 ± 30.2	376.8 ± 23.6	29.2 ± 2.5	243.5 ± 14.3	87.79 ± 1.11
Water-Out	249.5 ± 24.3	266.3 ± 23.6	21.5 ± 2.1	140.7 ± 11.1	96.74 ± 0.90

Table 4.27: The expected number of events from the pre-BANFF fit central values for both the PØD water-in and PØD water-out configurations.

	$N_{\text{Sig}}^{\text{Selected}}$	$N_{\text{Bkg}}^{\text{Selected}}$	$N_{\text{Sig}}^{\text{Sideband}}$	$N_{\text{Bkg}}^{\text{Sideband}}$
Water-In	452.7 ± 4.5	479.2 ± 4.8	35.8 ± 1.3	318.6 ± 4.0
Water-Out	302.3 ± 5.6	373.7 ± 6.6	25.5 ± 1.7	210.9 ± 4.9

as well. To get an idea of this variation, Figures 4.42 and 4.43 show the spread in the expected number of selected and sideband events. As is evident, the pre-BANFF fit throws show a wide range of possible expectations and the post-BANFF fit values show a more constrained expectation. However, as is explained in Subsection 5.6, the spread of the expectation is simply a normalization effect that is mostly removed by the fit.

4.5.1 Fit Results

Given that T2KReWeight changes the PDFs that enter into the simultaneous unbinned maximum likelihood fit, the fit is run with both post-BANFF and pre-BANFF values. Tables 4.26 and 4.28 describe the fit parameter results from running the fit with the pre- and post-BANFF central value PDFs. Tables 4.27 and 4.29 describe the expected reweighted Monte Carlo events from pre- and post-BANFF central value PDFs. Figures 4.44 and 4.45 show the results of the fit on the PØD water-in and water-out configurations with both the pre- and post-BANFF fit central values. Given the results of the fit and assuming the same systematic errors as listed in Table 5.24, the PØD water-in configuration ratio becomes $0.779 \pm 0.067(\text{stat}) \pm 0.141(\text{sys})$ ($0.837 \pm 0.073(\text{stat}) \pm 0.151(\text{sys})$) for the pre-(post-)BANFF fit reweighted NEUT Monte Carlo. For the PØD water-out configuration ratio, $0.825 \pm 0.082(\text{stat}) \pm 0.133(\text{sys})$ ($0.893 \pm 0.091(\text{stat}) \pm 0.141(\text{sys})$) is found. Counting the number of reweighted expected on-water events, there are 164.4 ± 2.7 (149.3 ± 2.4) NC1π^0 events are expected. Using the fit results, the on-water value is calculated. For the pre-BANFF fit,

Table 4.28: The results of running the fit for both the PØD water-in and PØD water-out configurations with the T2KReWeight post-BANFF fit central values.

	$N_{\text{Sig}}^{\text{Selected}}$	$N_{\text{Bkg}}^{\text{Selected}}$	$N_{\text{Sig}}^{\text{Sideband}}$	$N_{\text{Bkg}}^{\text{Sideband}}$	e
Water-In	342.6 ± 29.5	385.5 ± 23.3	25.9 ± 2.3	248.1 ± 14.1	87.52 ± 0.70
Water-Out	249.7 ± 25.0	268.6 ± 21.1	19.3 ± 2.0	140.5 ± 10.4	96.71 ± 0.51

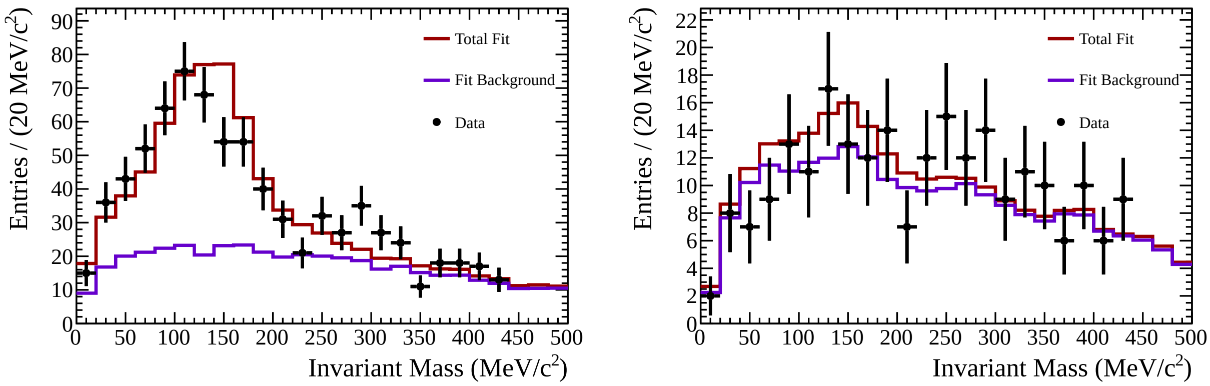

(a) Pre-BANFF Fit

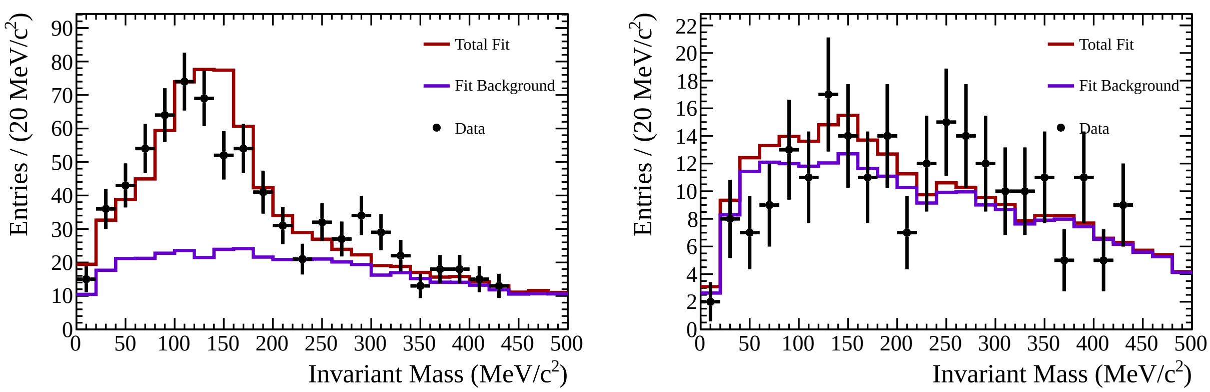

(b) Post-BANFF Fit

Figure 4.44: For the P∅D water-in configuration, the result after fitting the data to the pre- and post-BANFF fit adjusted Monte Carlo. The pre-BANFF fit result has a total χ^2 of 45.1 with 39 degrees of freedom. This leads to a probability of 0.232. The post-BANFF fit result has a total χ^2 of 49.2 with 39 degrees of freedom and a 0.127 probability.

Table 4.29: The expected number of events from the post-BANFF fit central values for both the P∅D water-in and P∅D water-out configurations.

	$N_{\text{Sig}}^{\text{Selected}}$	$N_{\text{Bkg}}^{\text{Selected}}$	$N_{\text{Sig}}^{\text{Sideband}}$	$N_{\text{Bkg}}^{\text{Sideband}}$
Water-In	409.5 ± 4.0	438.1 ± 4.4	29.5 ± 1.1	291.7 ± 3.6
Water-Out	279.6 ± 5.2	348.9 ± 6.1	21.2 ± 1.4	193.5 ± 4.5

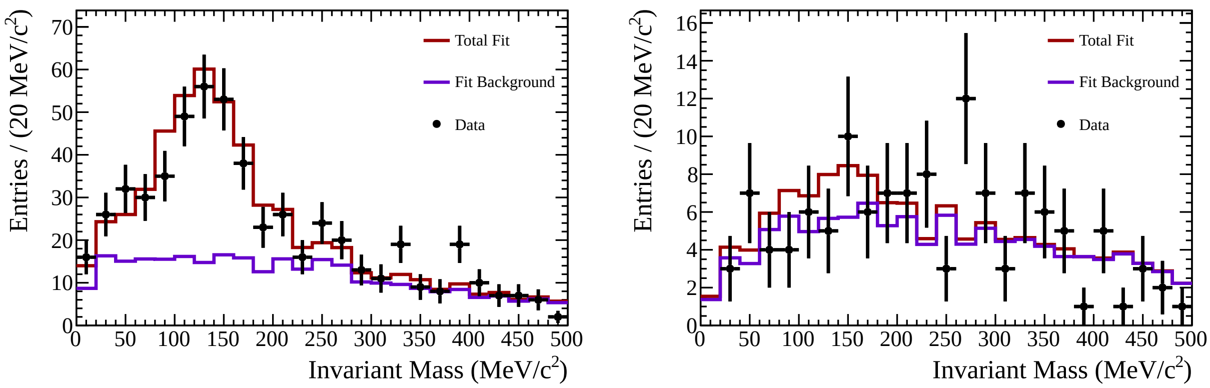

(a) Pre-BANFF Fit

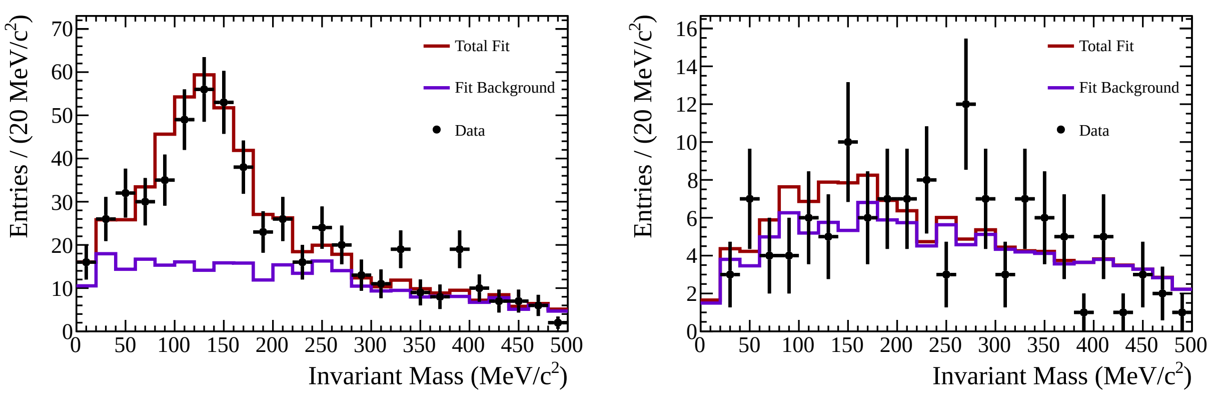

(b) Post-BANFF Fit

Figure 4.45: For the P∅D water-out configuration, the result after fitting the data to the pre- and post-BANFF fit adjusted Monte Carlo. The pre-BANFF fit result has a total χ^2 of 54.7 with 39 degrees of freedom. This leads to a probability of 0.049. The post-BANFF fit result has a total χ^2 of 53.6 with 39 degrees of freedom and a 0.060 probability.

Table 4.30: The results of running the fit for both the P∅D water-in and water-out configurations with the T2KReWeight pre-BANFF fit central values with an unconstrained g factor.

	$N_{\text{Sig}}^{\text{Selected}}$	$N_{\text{Bkg}}^{\text{Selected}}$	$N_{\text{Sig}}^{\text{Sideband}}$	$N_{\text{Bkg}}^{\text{Sideband}}$	e	g
Water-In	419.9 ± 32.2	329.9 ± 23.5	34.8 ± 2.9	217.4 ± 14.6	90.25 ± 0.64	-0.30 ± 0.08
Water-Out	326.4 ± 29.9	208.4 ± 21.7	28.2 ± 2.7	115.0 ± 11.4	98.45 ± 0.72	-0.42 ± 0.11

Table 4.31: The expected number of events from the pre-BANFF fit central values for both the P∅D water-in and water-out configurations with an unconstrained g factor.

	$N_{\text{Sig}}^{\text{Selected}}$	$N_{\text{Bkg}}^{\text{Selected}}$	$N_{\text{Sig}}^{\text{Sideband}}$	$N_{\text{Bkg}}^{\text{Sideband}}$
Water-In	453.3 ± 4.5	485.9 ± 4.8	35.9 ± 1.3	324.7 ± 4.0
Water-Out	302.4 ± 5.6	375.9 ± 6.6	25.5 ± 1.7	212.6 ± 5.0

the on-water rate is $114.6 \pm 38.1(\text{stat}) \pm 74.6(\text{sys})$ leading to a ratio of $0.697 \pm 0.232(\text{stat}) \pm 0.454(\text{sys})$. For the post-BANFF fit, the on-water rate is $104.4 \pm 40.0(\text{stat}) \pm 72.3(\text{sys})$ leading to a ratio of $0.699 \pm 0.254(\text{stat}) \pm 0.484(\text{sys})$.

Removing Model Dependencies

This section describes the results when the g factor is unconstrained. Tables 4.30 and 4.32 describe the fit parameter results from running the fit with the pre- and post-BANFF central value PDFs. Tables 4.31 and 4.33 describe the expected reweighted Monte Carlo events from pre- and post-BANFF central value PDFs. Figures 4.46 and 4.47 show the results of the fit on the P∅D water-in and water-out configurations with both the pre- and post-BANFF fit central values. Given the results of the fit and assuming the same systematic errors as listed in Table 5.26, the P∅D water-in configuration ratio becomes $0.926 \pm 0.072(\text{stat}) \pm 0.227(\text{sys})$ ($0.992 \pm 0.081(\text{stat}) \pm 0.242(\text{sys})$) for the pre-(post-)BANFF fit reweighted NEUT Monte Carlo. For the P∅D water-out configuration ratio, $1.079 \pm 0.101(\text{stat}) \pm 0.308(\text{sys})$ ($1.152 \pm 0.106(\text{stat}) \pm 0.327(\text{sys})$) is found. Counting the number of reweighted expected on-water events, there are 164.4 ± 2.7 (149.3 ± 2.4) NC1π^0 events are expected. Using the fit results, the on-water value is calculated. For the pre-BANFF fit, the on-water rate is $108.5 \pm 43.0(\text{stat}) \pm 92.5(\text{sys})$ leading to a ratio of $0.660 \pm 0.262(\text{stat}) \pm 0.566(\text{sys})$. For

Table 4.32: The results of running the fit for both the P∅D water-in and water-out configurations with the T2KReWeight post-BANFF fit central values with an unconstrained g factor.

	$N_{\text{Sig}}^{\text{Selected}}$	$N_{\text{Bkg}}^{\text{Selected}}$	$N_{\text{Sig}}^{\text{Sideband}}$	$N_{\text{Bkg}}^{\text{Sideband}}$	e	g
Water-In	406.8 ± 32.9	340.8 ± 23.7	30.8 ± 2.5	223.7 ± 14.7	90.09 ± 1.24	-0.28 ± 0.07
Water-Out	322.1 ± 29.1	214.2 ± 21.9	24.9 ± 2.3	116.8 ± 11.2	97.58 ± 0.59	-0.38 ± 0.10

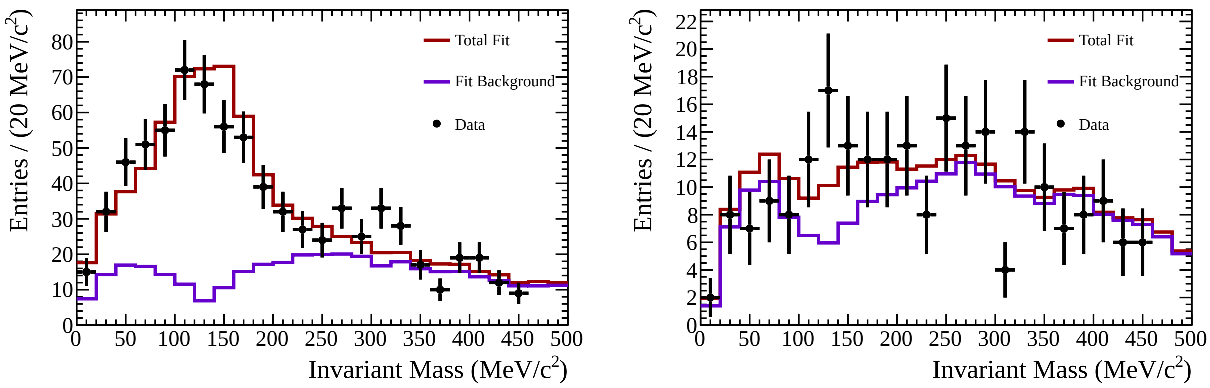

(a) Pre-BANFF Fit

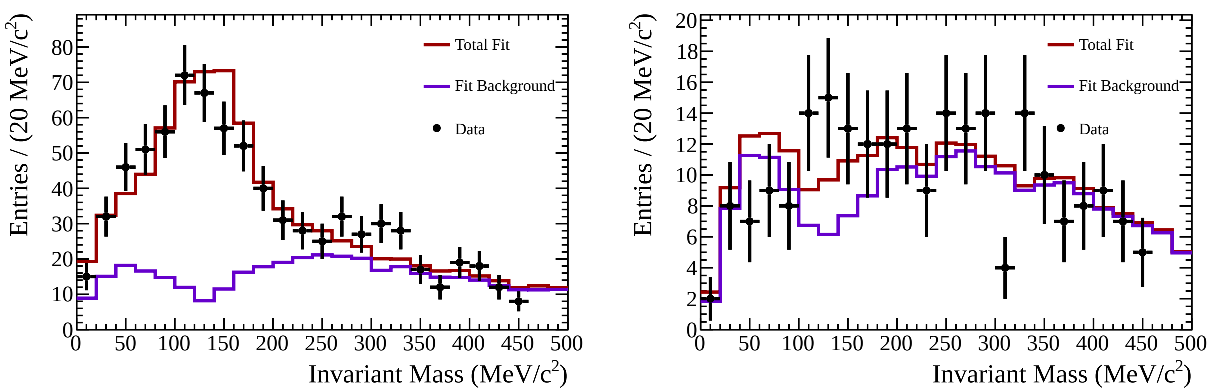

(b) Post-BANFF Fit

Figure 4.46: For the P∅D water-in configuration, the result after fitting the data to the pre- and post-BANFF fit adjusted Monte Carlo. These fits are performed with an unconstrained g factor. The pre-BANFF fit result has a total χ^2 of 46.3 with 38 degrees of freedom. This leads to a probability of 0.167. The post-BANFF fit result has a total χ^2 of 42.2 with 38 degrees of freedom and a 0.294 probability.

Table 4.33: The expected number of events from the post-BANFF fit central values for both the P∅D water-in and water-out configurations with an unconstrained g factor.

	$N_{\text{Sig}}^{\text{Selected}}$	$N_{\text{Bkg}}^{\text{Selected}}$	$N_{\text{Sig}}^{\text{Sideband}}$	$N_{\text{Bkg}}^{\text{Sideband}}$
Water-In	409.9 ± 4.0	444.8 ± 4.4	29.6 ± 1.1	297.0 ± 3.7
Water-Out	279.6 ± 5.2	349.8 ± 6.1	21.2 ± 1.4	194.6 ± 4.5

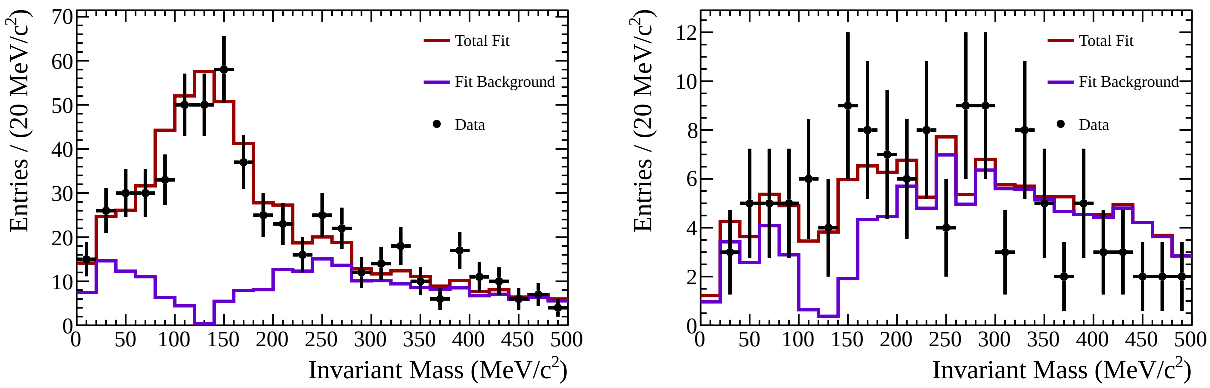

(a) Pre-BANFF Fit

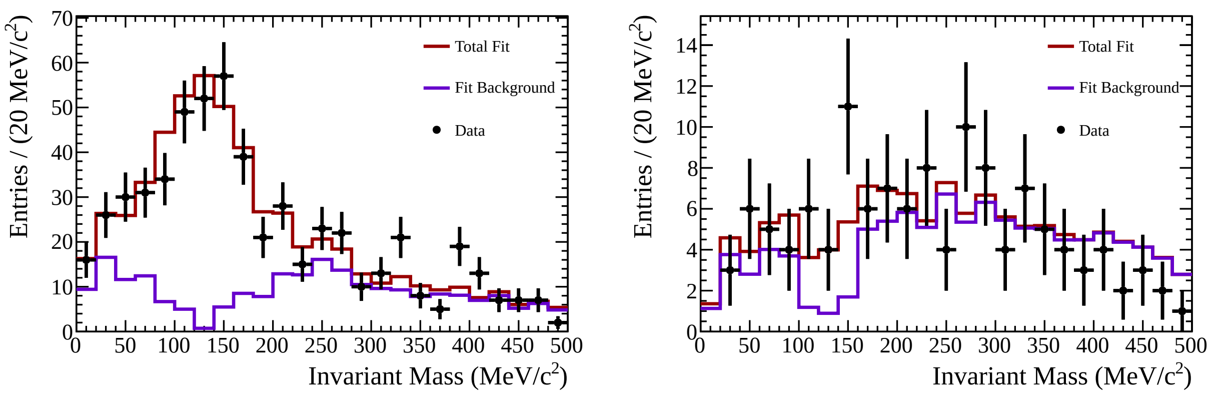

(b) Post-BANFF Fit

Figure 4.47: For the P∅D water-out configuration, the result after fitting the data to the pre- and post-BANFF fit adjusted Monte Carlo. These fits are performed with an unconstrained g factor. The pre-BANFF fit result has a total χ^2 of 38.0 with 38 degrees of freedom. This leads to a probability of 0.469. The post-BANFF fit result has a total χ^2 of 51.2 with 38 degrees of freedom and a 0.075 probability.

Table 4.34: Summary of the P∅D water-in and water-out configuration data to Monte Carlo ratios. The ratios are based on the fits of the data to the nominal flux-weighted NEUT Monte Carlo, the pre-BANFF fit reweighted Monte Carlo and the post-BANFF fit reweighted Monte Carlo. The top half of the table summarizes the results of the default fit while the bottom half shows the results from the unconstrained g fit.

	g	Water-In	Water-Out
NEUT (Pre)	No	0.790 ± 0.076(stat) $\pm$ 0.143(sys)	0.850 ± 0.091(stat) $\pm$ 0.137(sys)
NEUT (Post)	No	0.790 ± 0.076(stat) $\pm$ 0.142(sys)	0.850 ± 0.091(stat) $\pm$ 0.134(sys)
Pre-BANFF	No	0.779 ± 0.067(stat) $\pm$ 0.141(sys)	0.825 ± 0.082(stat) $\pm$ 0.133(sys)
Post-BANFF	No	0.837 ± 0.073(stat) $\pm$ 0.151(sys)	0.893 ± 0.091(stat) $\pm$ 0.141(sys)
NEUT (Pre)	Yes	0.944 ± 0.076(stat) $\pm$ 0.231(sys)	1.107 ± 0.101(stat) $\pm$ 0.316(sys)
NEUT (Post)	Yes	0.944 ± 0.076(stat) $\pm$ 0.230(sys)	1.107 ± 0.101(stat) $\pm$ 0.314(sys)
Pre-BANFF	Yes	0.926 ± 0.072(stat) $\pm$ 0.227(sys)	1.079 ± 0.101(stat) $\pm$ 0.308(sys)
Post-BANFF	Yes	0.992 ± 0.081(stat) $\pm$ 0.242(sys)	1.152 ± 0.106(stat) $\pm$ 0.327(sys)

Table 4.35: Summary of the predictions for the number of NC1π^0 on-water vertices. The pre- and post-BANFF fit reweightings predict a slightly different number of events than the flux-weighted NEUT Monte Carlo.

NEUT	Pre-BANFF	Post-BANFF
157.2 ± 2.5	164.4 ± 2.7	149.3 ± 2.4

the post-BANFF fit, the on-water rate is 99.5 ± 43.1(stat) $\pm$ 89.1(sys) leading to a ratio of 0.697 ± 0.232(stat) $\pm$ 0.454(sys).

4.5.2 Comparing Fit Results

Table 4.34 lists the possible P∅D water-in and water-out configuration ratios for the rate of NC1π^0 interactions. Listed are both the results for the default fits and the unconstrained g factor fits. With the reweighting of the pre- and post-BANFF fit central values, the Monte Carlo prediction for the number of NC1π^0 events on-water in the P∅D will shift, this is

Table 4.36: Summary of the on-water NC1π^0 event rate calculations for the P∅D. The first column are based on the results of the unconstrained g factor fits. The second column are based on the results of the default fits.

	$g \neq 0$	$g = 0$
NEUT (Pre)	102.4 ± 42.5(stat) $\pm$ 90.4(sys)	106.4 ± 41.0(stat) $\pm$ 72.6(sys)
NEUT (Post)	102.4 ± 42.5(stat) $\pm$ 89.3(sys)	106.4 ± 41.0(stat) $\pm$ 71.9(sys)
Pre-BANFF	108.5 ± 43.0(stat) $\pm$ 92.5(sys)	114.6 ± 38.1(stat) $\pm$ 74.6(sys)
Post-BANFF	99.5 ± 43.1(stat) $\pm$ 89.1(sys)	104.4 ± 40.0(stat) $\pm$ 72.3(sys)

Table 4.37: Summary of the data to Monte Carlo ratios of the rate of NC1π^0 interactions in the P∅D. The first column are based on the results of the unconstrained g factor fits. The second column are based on the results of the default fits.

	$g \neq 0$	$g = 0$
NEUT (Pre)	0.652 ± 0.270(stat) $\pm$ 0.576(sys)	0.677 ± 0.261(stat) $\pm$ 0.462(sys)
NEUT (Post)	0.652 ± 0.270(stat) $\pm$ 0.569(sys)	0.677 ± 0.261(stat) $\pm$ 0.457(sys)
Pre-BANFF	0.660 ± 0.262(stat) $\pm$ 0.566(sys)	0.697 ± 0.232(stat) $\pm$ 0.454(sys)
Post-BANFF	0.666 ± 0.289(stat) $\pm$ 0.599(sys)	0.699 ± 0.254(stat) $\pm$ 0.484(sys)

described in Table 4.35. These values can then be compared to the air subtracted on-water values listed in Table 4.36 in order to calculate the final data to Monte Carlo ratios shown in Table 4.37. Curiously, even though the P∅D water-in and water-out configuration ratios of data to Monte Carlo show a large discrepancy between the default fits and unconstrained g factor fits, the final on-water ratio is not greatly affected.

Chapter 5

Systematics

The following chapter describes the systematic uncertainties as they will be applied to the water-in and water-out NC1π^0 ratios. The first section covers the effect of the energy scale on the analysis, including effects from the geometry differences, the Monte Carlo and data photoelectron peak discrepancies, and the error on the number of signal due to the fitted energy scale. The next section describes the variation in P∅D response over time. Following that are the errors that come from the uncertainty in the knowledge of the mass and alignment. Next the fiducial volume uncertainties are explained. There are two uncertainties, one dealing with how the result will change if Monte Carlo and data are scaled together and one dealing with what happens when there is a systematic shift between data and Monte Carlo. After that, the systematic uncertainties that arise using T2KReWeight on the flux and cross sections are explained. The reconstruction uncertainties are then examined. First, a look at the systematic shift between data and Monte Carlo of the Track PID reconstruction is taken. Then, the optimized cuts are studied for any data to Monte Carlo shifts. Lastly, a description of the the muon decay fake identification rate and the efficiency for finding a muon decay is taken and used as a constraint in the constraint matrix of the simultaneous extended maximum likelihood fit. The last section deals with the systematic on the background shape, which is done by examining the result of fixing the g factor to zero. This systematic is only dealt with in the case of an unconstrained g factor.

5.1 Energy Scale

There are a few ways the energy scale can be affected. The first relies on any density differences in the detector in the as-built and Monte Carlo geometries. This can affect the efficiency of the detector. Next, an issue was found with low charge deposit between data and Monte Carlo. There was a large difference in the appearance of the photoelectric (PE) peaks expected by the MPPCs. Lastly, the error on the energy scale result of the fit needs to be accounted for and applied to the error on the number of signal events fit.

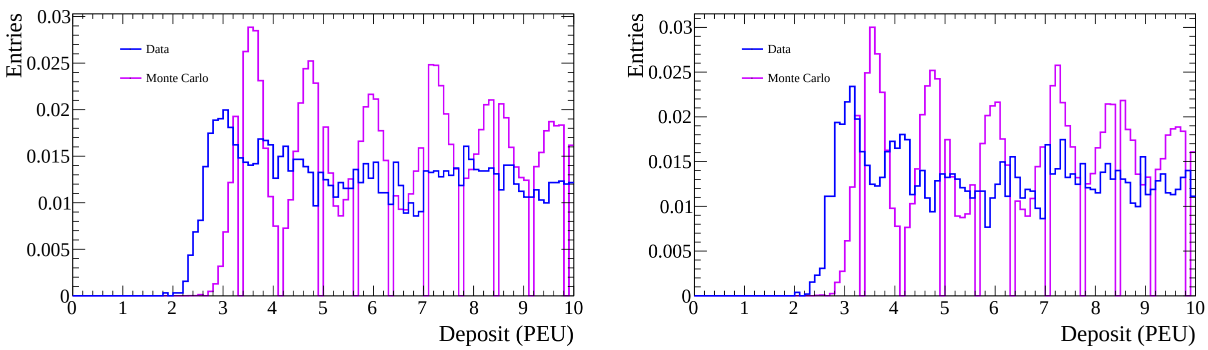

(a) Water-In Configuration

(b) Water-Out Configuration

Figure 5.1: The distributions of the charge of hits that contribute to the selected sample. The Monte Carlo shows some digitization (where the plot goes to zero) as expected from the electronics simulation.

5.1.1 Geometry Differences

In order to see how changing the detector density changes the efficiency, the P∅D water-in and water-out configuration's efficiency and mass can be used as an approximation. Using the efficiencies listed in Table 4.17, the percent change in efficiency from the P∅D water-out configuration to the P∅D water-in configuration is 127.3 ± 2.7(stat)%. Using the values of the water mass listed in Table 3.4, there is a mass of 1924.08 ± 0.11 kg in the Monte Carlo and 1902 ± 16 kg in the as-built approximation. Combining the systematic difference between the Monte Carlo and as-built masses (22.08 ± 16 kg) with its statistical uncertainty gives a conservative estimate of the total error on the difference between the P∅D water-in and water-out configurations. This total error is calculated to be 27.3 kg. Given that the dry mass of the P∅D is completely correlated between the water-in and water-out configurations, the percent change in the mass is 155.5 ± 0.03(stat) ± 0.79(sys)%. Next the fractional systematic error of the mass, which is 0.51%, is applied to the efficiency. This makes the percent change in efficiency from the P∅D water-out to P∅D water-in configuration 127.3 ± 2.7(stat) $\pm$ 0.65(sys)%. Adding the statistical and systematic errors in quadrature gives 2.8% which is then used as a conservative estimate of the systematic due to any geometric differences or density fluctuations.

5.1.2 PE Peak Uncertainty

In Production 5, the Monte Carlo incorrectly modeled the photo-electron (PE) peaks expected. There were several implementation issues found, the PE peak values, the spread of the peaks etc. This issue appears in both the P∅D water-in and water-out configurations, as seen in Figure 5.1. For a 3D shower to be reconstructed, the minimum requirement for hits is that there be at least one hit in each projection and that there be at least 5 hits in either projection. An example of this is seen in Figure 5.2. In order to estimate the effect this has on the NC1π^0 analysis, the final sample of selected events is studied. A cut is placed

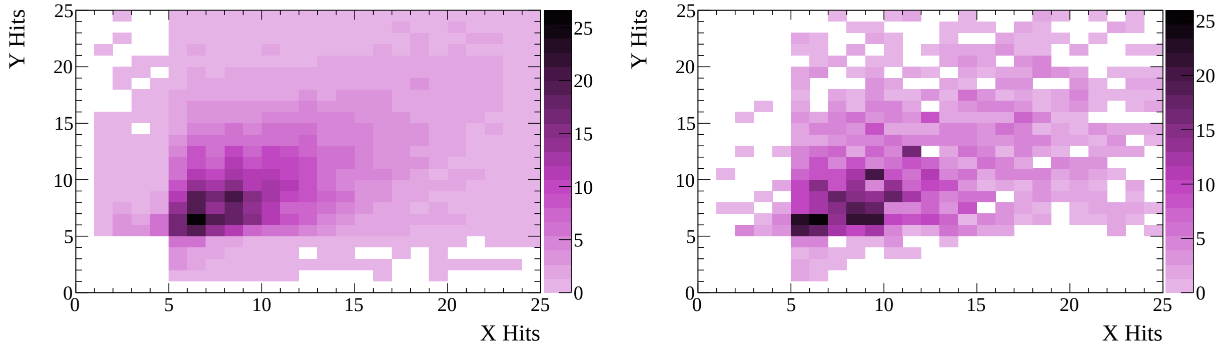

(a) Monte Carlo (b) Data

Figure 5.2: These plots demonstrate the unmodified number of hits in the X-Z and Y-Z projections for the P$\emptyset$D water-in configuration.

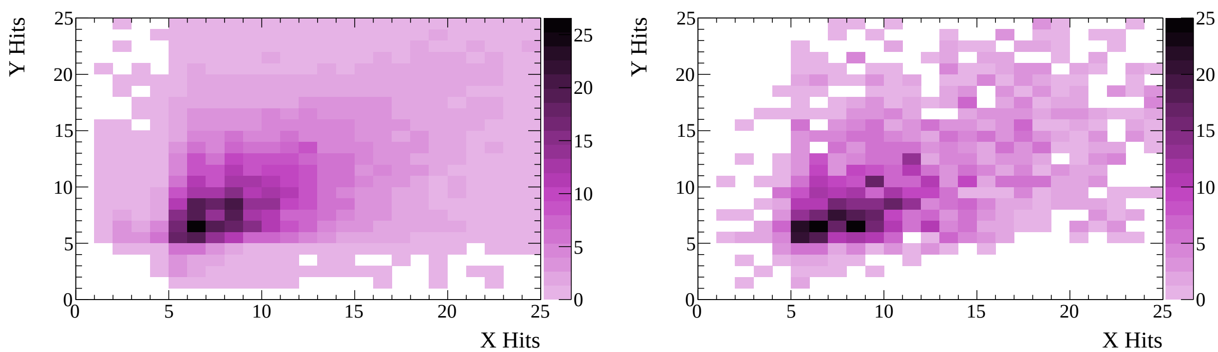

(a) Monte Carlo (b) Data

Figure 5.3: These plots demonstrate the number of hits in the X-Z and Y-Z projections for the P$\emptyset$D water-in configuration after a cut has been applied at 3.5 PEU.

Table 5.1: A summary of the loss in events for various charge deposit cuts for the PØD water-in configuration. The first column lists the charge deposit cut used. The next two columns list the number of events passing the two shower requirement for both data and Monte Carlo. The two columns after that list the percentage of the total events that are lost due to the charge deposit cut. The last column lists the difference between the percent lost of the data and Monte Carlo.

Cut	MC	Data	MC Lost (%)	Data Lost (%)	Difference (%)
0.0	893.0	775	0.0	0.0	0.0
3.0	892.8	770	0.03	0.65	0.62
3.5	891.3	768	0.20	0.90	0.71
4.0	888.0	766	0.57	1.16	0.59
4.5	886.7	765	0.71	1.29	0.58
5.0	884.5	764	0.96	1.42	0.46
5.5	882.8	763	1.15	1.55	0.40
6.0	881.0	760	1.34	1.94	0.59
10.0	860.0	743	3.63	4.13	0.50

Table 5.2: A summary of the loss in events for various charge deposit cuts for the PØD water-out configuration. The first column lists the charge deposit cut used. The next two columns list the number of events passing the two shower requirement for both data and Monte Carlo. The two columns after that list the percentage of the total events that are lost due to the charge deposit cut. The last column lists the difference between the percent lost of the data and Monte Carlo.

Cut	MC	Data	MC Lost (%)	Data Lost (%)	Difference (%)
0.0	629.4	555	0.0	0.0	0.0
3.0	629.4	555	0.0	0.0	0.0
3.5	628.5	552	0.14	0.54	0.40
4.0	626.5	552	0.46	0.54	0.08
4.5	626.2	549	0.51	1.08	0.57
5.0	623.6	548	0.93	1.26	0.34
5.5	622.7	546	1.07	1.62	0.56
6.0	620.9	545	1.35	1.80	0.45
10.0	607.4	538	3.51	3.06	0.45

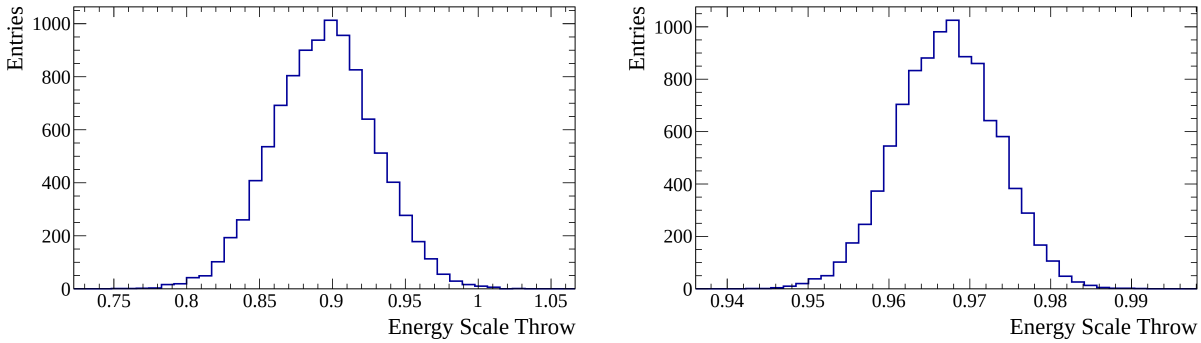

(a) Water-In Configuration

(b) Water-Out Configuration

Figure 5.4: The distribution of the throws of the energy scale values. The mean and sigma of the distributions come from the analysis fits.

Table 5.3: The systematic result from the error on the energy scale output from the fit. The first column is the number of Monte Carlo predicted events. The next two columns describe the distribution after throwing the energy scale. The last three columns are the result of calculated the fractional shift from nominal, the fractional RMS of the distribution and the final systematic error.

	Signal	Mean	RMS	Shift (%)	Shift Error (%)	Total Error (%)
Water-In	434.9	411.4	8.6	-5.4	2.1	5.8
Water-Out	290.3	287.8	0.4	-0.9	0.1	0.9

on the charge deposit and the hits are counted. An example of the effect of the charge cut set at 3.5 PEU for the P∅D water-in configuration is shown in Figure 5.3 where a migration to the lower left corner is seen. If the shower fails the requirement for five hits in one projection and some hits in both, the event is failed. The percentage of failed data events is compared to the percentage of failed Monte Carlo events in order to extract a systematic error. The effect of various charge deposit cuts is listed in Tables 5.1 and 5.2. There is a small turn on effect of the cut, so in order to get a systematic, the average of the data to Monte Carlo difference is taken for all cuts above 3.5 PEU. This gives a final systematic of 0.6% for the P∅D water-in configuration and a 0.4% systematic for the P∅D water-out configuration.

5.1.3 Energy Scale

After the fit has been completed, the energy scale was modeled as a Gaussian using the value and error from the fit as the mean and sigma. The goal is to turn this error on the energy scale and map it to an error on the number of selected signal events. The effect of this scale and its error need to be quantified on the final event rate. Then the NC1π^0 efficiency curve, ϵ, as a function of momentum, $\vec{p}$, was calculated, see Figure 4.24. In order

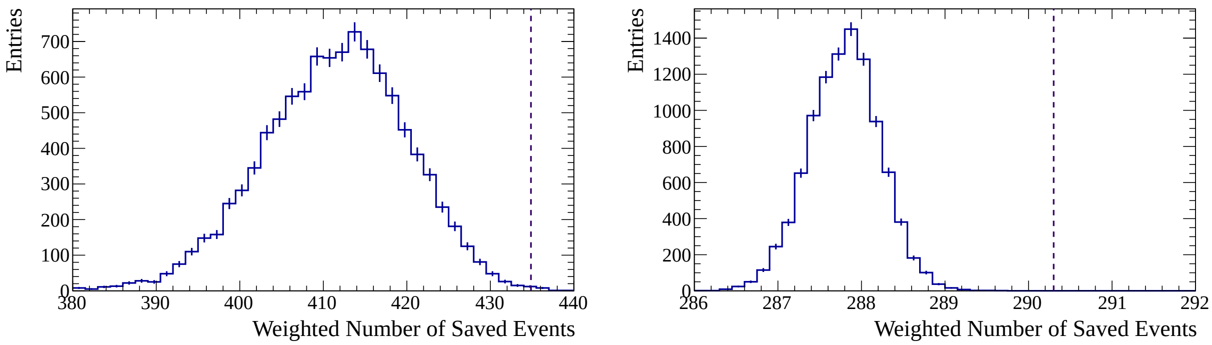

(a) Water-In Configuration (b) Water-Out Configuration

Figure 5.5: The distribution of the weighted signal events from throws of the energy scale values. The vertical dashed line represents the nominal number of Monte Carlo signal weighted events.

Table 5.4: The systematic result from the error on the energy scale output from the fit with an unconstrained g factor. The first column is the number of Monte Carlo predicted events. The next two columns describe the distribution after throwing the energy scale. The last three columns are the result of calculated the fractional shift from nominal, the fractional RMS of the distribution and the final systematic error.

	Signal	Fit Mean	Fit Sigma	Shift (%)	Shift Error (%)	Total Error (%)
Water-In	434.9	415.9	1.8	-4.4	0.4	4.4
Water-Out	290.3	288.7	0.5	-0.5	0.2	0.6

to understand this systematic, the efficiency curve was shifted by a random throw of the energy scale, e, i.e. $\epsilon(|\vec{p}|) \rightarrow \epsilon(|\vec{p}| \cdot e)$. Taking the ratio of the shifted efficiency curve to the nominal efficiency curve results in a new event weighting. Using this new weighting, the number of saved signal events in the Monte Carlo is calculated for each of many throws of the energy scale and stored in a histogram. The mean and RMS of the distribution is extracted to be used as a systematic error. The shift from the nominal number of Monte Carlo NC1π^0 saved events and the fractional size of the RMS are components of the final systematic error. The shift and the error are added in quadrature to extract the systematic value. The distribution of the ten thousand throws of the energy scale are shown in Figure 5.4. The effect of the energy scale on the weighted sum is shown in Figure 5.5 and listed in Table 5.3. The P∅D water-in and water-out configurations are expected to have different resolutions, which is reflected by the difference in the values of the systematic errors, due to a different fraction of active material.

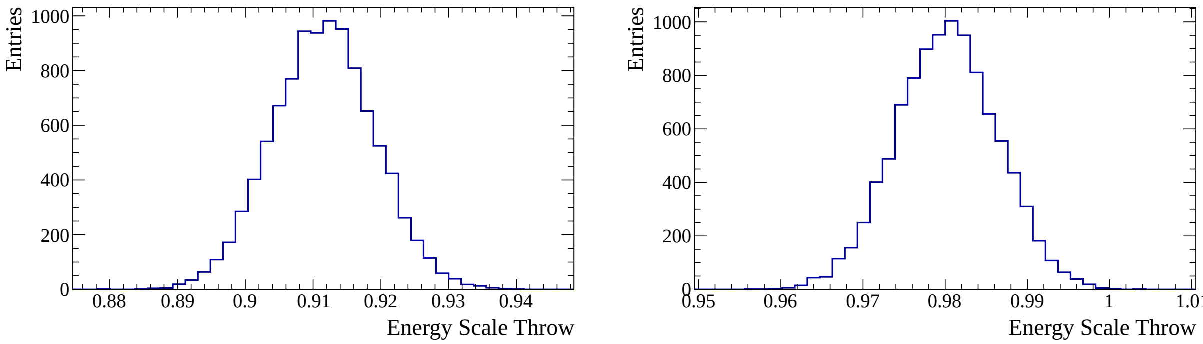

(a) Water-In Configuration

(b) Water-Out Configuration

Figure 5.6: The distribution of the throws of the energy scale values from the unconstrained g factor fit. The mean and sigma of the distributions come from the analysis fits.

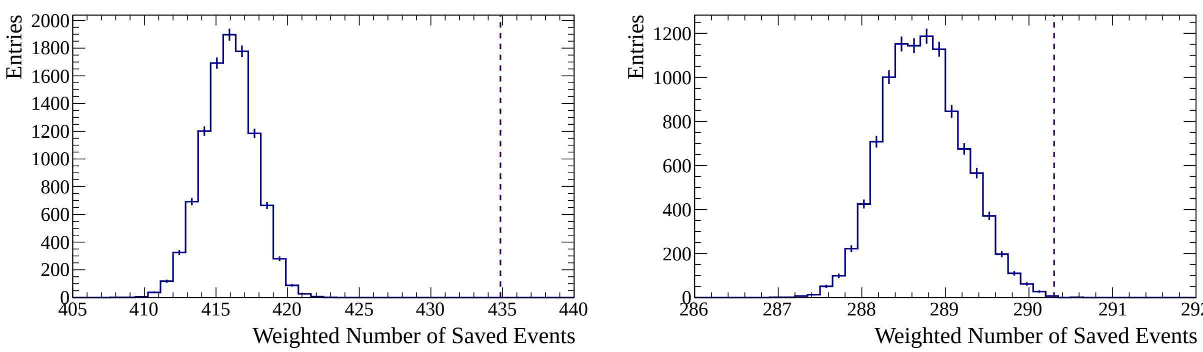

(a) Water-In Configuration

(b) Water-Out Configuration

Figure 5.7: The distribution of the weighted signal events from throws of the energy scale values from the unconstrained g factor fit. The vertical dashed line represents the nominal number of Monte Carlo signal weighted events.

Removing Model Dependencies

The energy scale for the unconstrained g factor fit differs from that in the default fit, therefore, this systematic needs to be dealt with separately. The distribution of the ten thousand throws of the energy scale are shown in Figure 5.6. The effect of the energy scale on the weighted sum is shown in Figure 5.7 and listed in Table 5.4.

5.2 Detector Variations

In Production 4, an extensive study of the channel-to-channel variations was performed. The end result was that this provided a negligible effect to the overall systematics ($< 1\%$) [27]. Additionally, a study smearing the Monte Carlo deposit by 15%, this value was chosen in a data comparison study, was performed. After the smearing, the energy scale was found to be effected by 0.1% which is negligible compared to the other systematics.

Variation in P∅D Response Over Time

The P∅D charge deposit response varies over time. Most of the variation is removed at the calibration stage. However, the remaining, small, variations lead to this systematic which are studied by a subsample of the data containing through-going muons. The Monte Carlo fixes the MIP peak at 37 which the data MIP peaks need to be corrected to match. The MIP peak is extracted by plotting the charge deposit for each hit from events with a single track that crosses the P∅D. The distributions are then fit to Landau Gaussian convolutions.

For good fits, selected with a reduced $\chi^2 < 25$, the most probable values are saved. Runs 1-3 are processed with all appropriate calibration (RDP- real data processing) and therefore get an average correction to 37 by run. Run 4 the calibration has not been fully processed (FPP- first pass processing) and each week gets a separate calibration constant.

The systematic uncertainty assigned to this correction, which is also applied in the NC1π^0 analysis, is calculated from the mean and RMS or the spread of the post-correction peak values. This is shown in Figure 5.8 and is summarized in Table 5.5. Two errors are considered, one uses the RMS of the distribution, the other uses the more conservative value of the total spread of the distribution. This analysis will use the conservative error of 1.8%.

Table 5.5: A summary of the post-correction data. The mean and RMS are from the distributions in Figure 5.8. The width is the width of the distributions disregarding outliers.

	Mean (PEU)	RMS (PEU)	Width (PEU)	Error (%)	Conservative Error (%)
X Layers	37.00	0.15	0.55	0.40	1.49
Y Layers	36.97	0.21	0.65	0.58	1.76
Combined	36.99	0.18	0.65	0.48	1.76

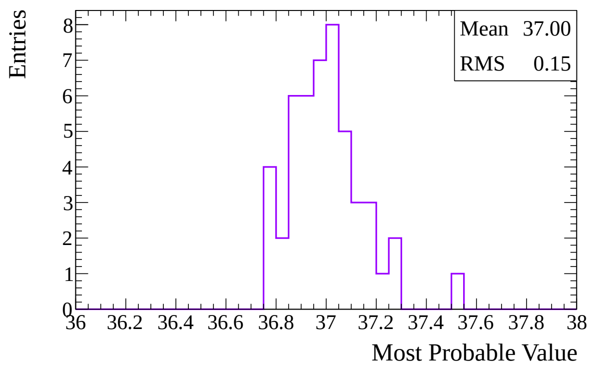

(a) X Layers

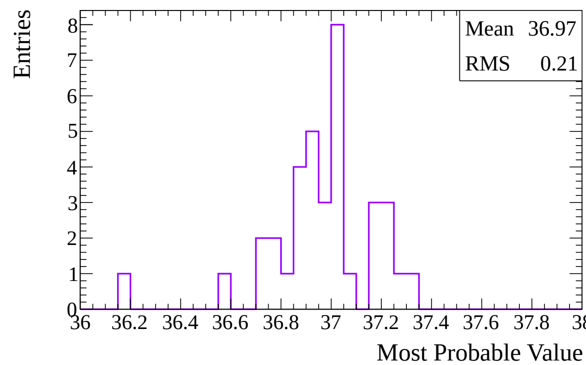

(b) Y Layers

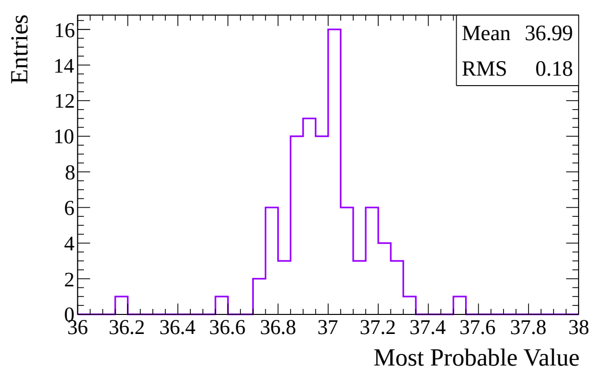

(c) X and Y Layers Combined

Figure 5.8: The MIP peak values after correction. Each entry in the histograms represent one continuous week of data. There are outliers due to low statistic weeks, but these are not considered when calculating the systematic error.

5.3 Mass Uncertainty

A detailed mass calculation was done for the as-built mass as well as the mass in the Monte Carlo in Section 3.1. At the time of writing, an analysis of the fiducial mass of the water for Run 4 was unavailable, so this analysis is applying the previously calculated information from Run 2. A summary of the pertinent masses is in Table 3.4.

Two corrections are applied depending where the true vertex is located. If the true vertex is not on-water, it gets weighted by the averaged dry mass. If the true vertex is on-water, and the P∅D is in the water-in configuration, then the vertex is weighted by the water mass.

However some added complexity falls into the P∅D dry mass correction. Between Runs 1 and 2, the entire water sensor system was replaced leading to a slight difference in the fiducial mass, which is handled by Run. It should be noted, most of the Monte Carlo to as-built difference stems from the water target dead material not being modeled in the Monte Carlo. In order to understand the systematic error that arises from the mass, 10,000 Gaussian throws are done of the mass correction factors. The Gaussian distribution for the throws have the mean and sigma pulled from the values in Table 5.6. An example of a series of throws done for the P∅D water-in fit is shown in Figure 5.9. The fit is rerun with these different correction factors applied to Monte Carlo. Since the energy scale is handled separately, the energy scale is fixed to the nominal fit value, all other variables are allowed to float freely. The fitted data to Monte Carlo ratio is then fit to a Gaussian distribution, see Figure 5.10. The results of the fits are described in Table 5.7. The systematic errors are the taken as the sigmas of the fitted distributions. The P∅D water-in configuration has a systematic error of 0.5% and the P∅D water-out configuration has a systematic of 0.9%.

Removing Model Dependencies

As the output of this systematic depends on the results of the fit, the systematic is calculated again for the unconstrained g factor fit. The fitted data to Monte Carlo ratio is then fit to a Gaussian distribution, see Figure 5.11. The results of the fits are described in Table 5.8. The P∅D water-in configuration has a systematic error of 0.4% and the P∅D water-out configuration has a systematic of 0.6%.

Table 5.6: The correction factor of the mass for the running period for both the on-water and off-water components.

Run Period	On-Water (%)	Off-Water (%)
Run 1	98.9 ± 0.8	102.6 ± 1.0
Run 2+	98.9 ± 0.8	103.1 ± 1.0

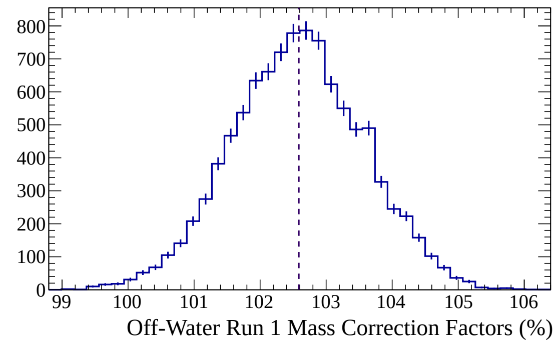

(a) Run 1 Dry Mass

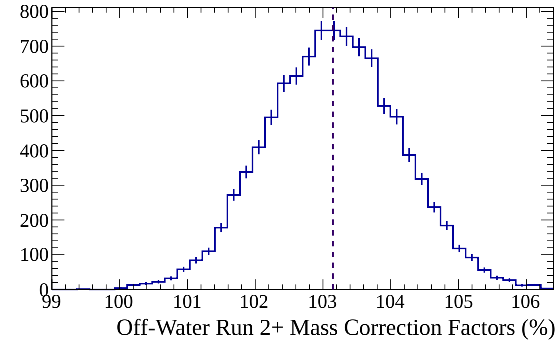

(b) Run 2+ Dry Mass

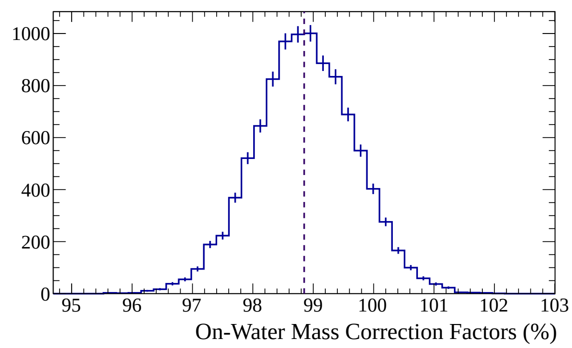

(c) Water Mass

Figure 5.9: An example of the throws of the mass corrections. These were used to reweight the Monte Carlo events before fitting to the data. The vertical line marks the central values given in Table 5.6.

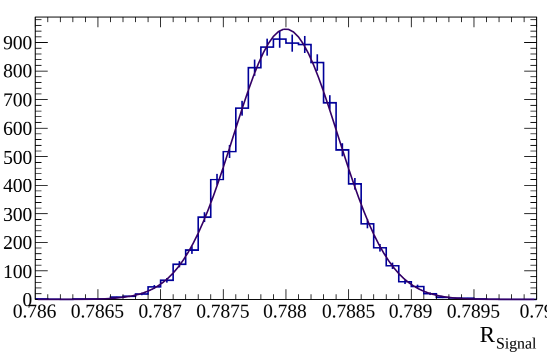

(a) Water-in configuration.

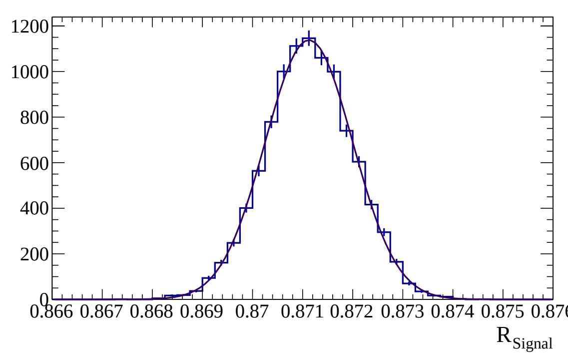

(b) Water-in configuration.

Figure 5.10: The data to Monte Carlo ratios of the fitted signal after 10,000 throws of the mass corrections. Shown are the distributions for both the P∅D water-in and P∅D water-out configurations.

Table 5.7: The summary of the Gaussian fits in Figure 5.10. Listed are the fitted values, for the data to Monte Carlo ratio of the number of signal events in the P∅D water-in and P∅D water-out configuration. The mean is the ratio and the sigma is taken as the systematic error.

	Constant	Mean (%)	Sigma (%)
Water-In	1222.9 ± 15.0	77.4 ± 0.0	0.41 ± 0.00
Water-Out	1264.8 ± 15.5	84.2 ± 0.0	0.63 ± 0.00

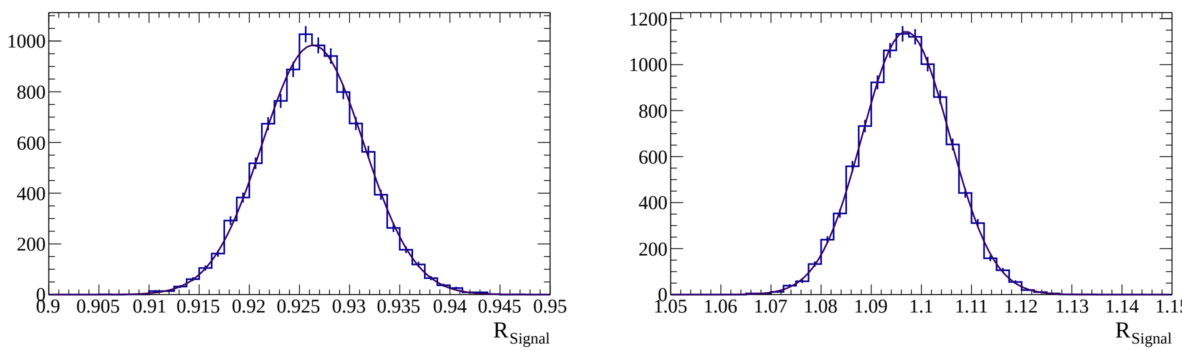

(a) Water-in configuration.

(b) Water-out configuration.

Figure 5.11: The data to Monte Carlo ratios of the fitted signal after 10,000 throws of the mass corrections. Shown are the distributions for both the P∅D water-in and P∅D water-out configurations.

Table 5.8: The summary of the Gaussian fits in Figure 5.11. Listed are the fitted values for the data to Monte Carlo ratio of the number of signal events in the P∅D water-in and P∅D water-out configuration. The mean is the ratio and the sigma is taken as the systematic error.

	Constant	Mean (%)	Sigma (%)
Water-In	983.8 ± 12.1	92.6 ± 0.0	0.51 ± 0.00
Water-Out	1143.9 ± 14.0	109.7 ± 0.0	0.87 ± 0.01

5.4 Alignment

The shifts on the alignment are less than 2 mm, as reported in Section 3.6. The approximate resolution of the detector in X and Y is 2.5 mm. Due to the construction of the fiducial volume, the Z boundaries of the volume occur in the middle of a P∅Dule, so alignment shifts in Z will have little to no effect on this analysis. If the fiducial volume is scaled by the resolution in X and Y, there is a 0.31% change in the fiducial volume. If instead, the fiducial volume is scaled by the maximum alignment parameter, a 0.24% change is found. Of primary concern is the change due to alignment, so the difference is considered as the systematic, 0.07%.

5.5 Fiducial Volume

Two concerns were addressed when examining the fiducial volume. The first was how data and Monte Carlo scaled together. The second was how the data can shift or scale separately from the Monte Carlo fiducial volume.

5.5.1 Fiducial Volume Scaling

The vertex resolutions discussed in Section 4.1 are used as the step size to expand and contract the fiducial volume. The concern for this systematic is the migration of selected events into and out of the fiducial volume if the volume definition changes. First, the number of events in data and Monte Carlo are counted for varying sizes of the fiducial volume. The fiducial volume is varied in the X, Y, Z Downstream, and Z Upstream independently and the results are combined for the final systematic error. The Z upstream and Z downstream refer to the edges of the fiducial volume that are perpendicular to the Z axis. The upstream and downstream edges are considered separately because a large difference in the statistics of the vertices that make it to the final sample at each edge is expected. A vertex that is created at the upstream edge is more likely to make it to the final sample than one at the downstream edge due to the containment cut. The nominal volume is considered as the reference point, so the ratio of data to Monte Carlo events is set to 1.0 with an error of 0.0. For the $\pm 1\sigma$ and $\pm 2\sigma$ steps, the number of events added or subtracted from the previous step (either nominal for 1σ or 1σ values for 2σ) is calculated. The ratio of this excess or deficiency is calculate and appropriate Poisson errors are assigned. A linear fit is performed on this set of five points, see Figures 5.12 and 5.13. The fit parameters and their errors are accessed. At 1σ from the nominal fiducial volume, the change in the data to Monte

Table 5.9: Summary of the fiducial scaling systematic errors.

Coordinate	X (%)	Y (%)	Z-Upstream (%)	Z-Downstream (%)
Water-In	0.54	0.80	0.73	1.02
Water-Out	1.17	0.51	1.13	0.00

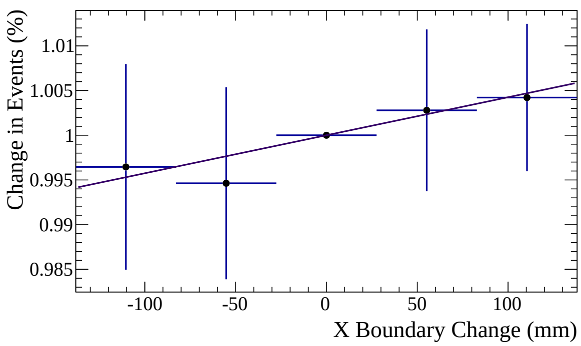

(a) X Fiducial Boundary

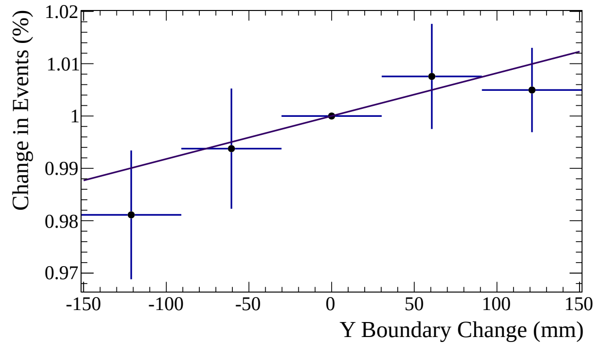

(b) Y Fiducial Boundary

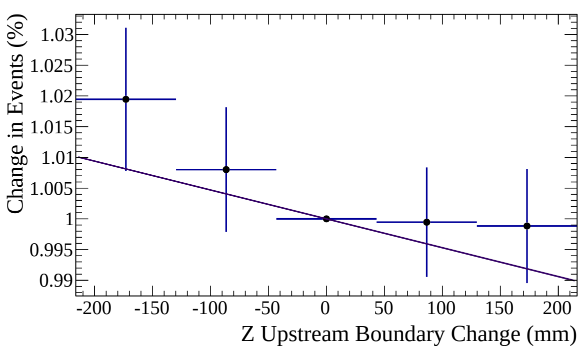

(c) Z Upstream Fiducial Boundary

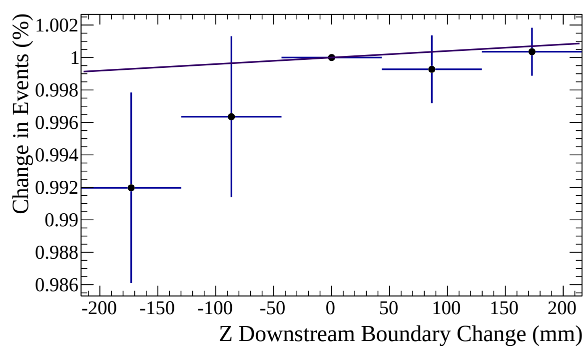

(d) Z Downstream Fiducial Boundary

Figure 5.12: The ratios of data to Monte Carlo candidate events at the edge of the fiducial volume for the water-in configuration.

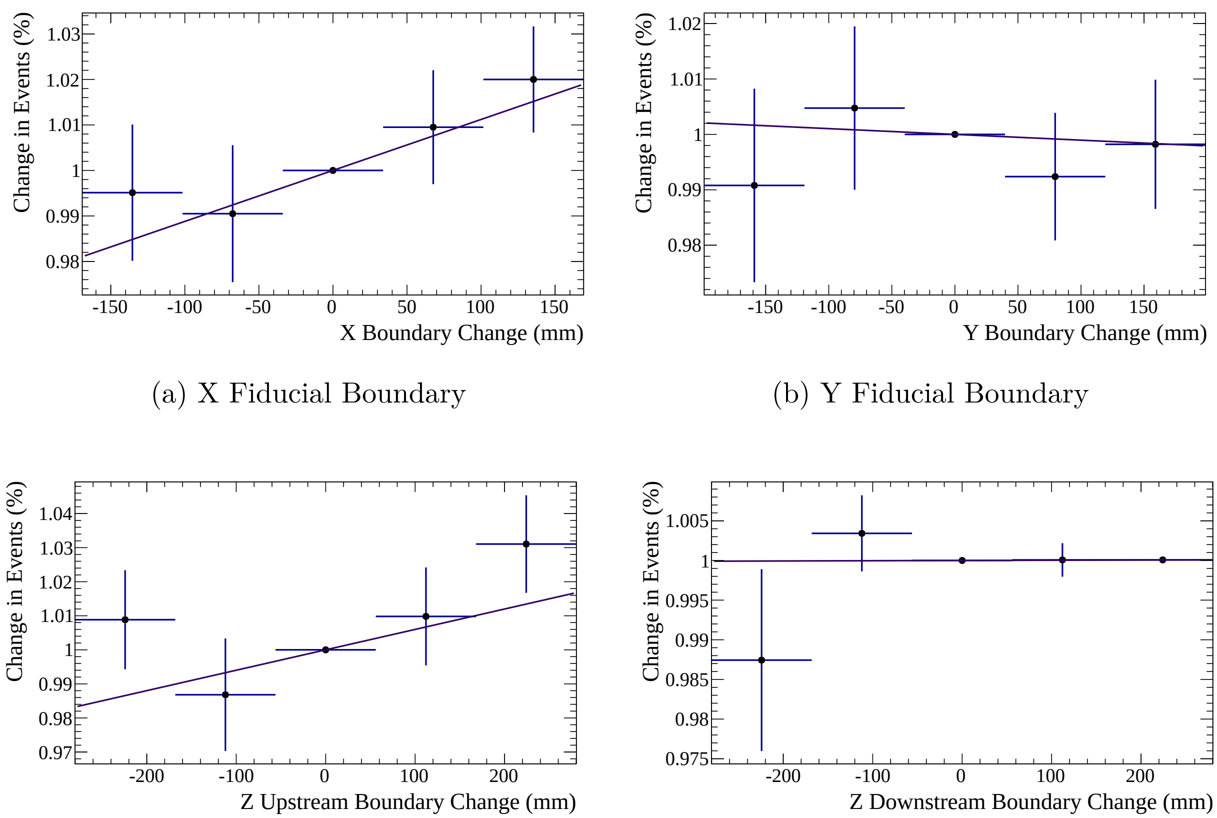

(a) X Fiducial Boundary

(b) Y Fiducial Boundary

(c) Z Upstream Fiducial Boundary

(d) Z Downstream Fiducial Boundary

Figure 5.13: The ratios of data to Monte Carlo candidate events at the edge of the fiducial volume for the water-out configuration.

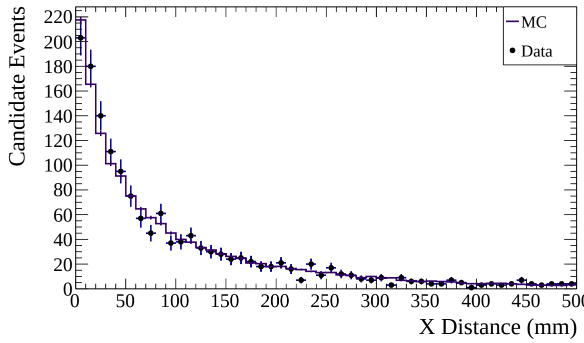

(a) X Direction

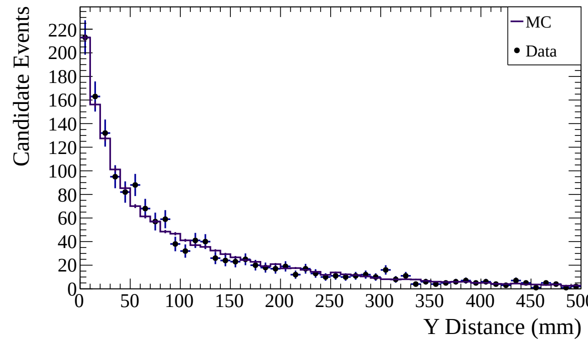

(b) Y Direction

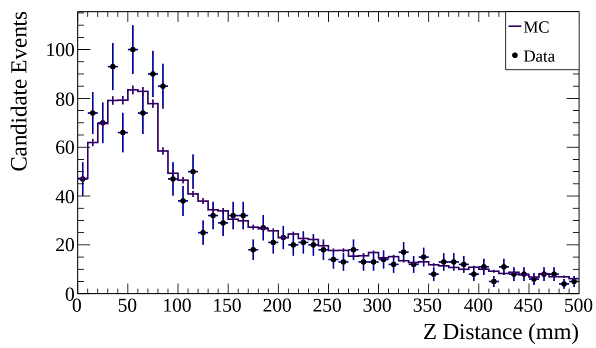

(c) Z Direction

Figure 5.14: The bias between data and Monte Carlo is judged by the difference in the average distance from the π^0 vertex and the reconstructed photon vertices. These plots show the distributions for the P∅D water-in configuration.

Carlo ratio is calculated. The error on the change in the data to Monte Carlo is calculated using the errors extracted from the fit. The slope and additional error are added together to be utilized as the systematic error. The X and Y fiducial systematics are added linearly then combined with the rest of the errors in quadrature. The result is a systematic error of 1.5% from fiducial volume scaling for the P∅D water-in configuration and 2.0% for the P∅D water-out configuration.

5.5.2 Fiducial Volume Shift

The previous systematic dealt with data and Monte Carlo scaling together. This systematic addresses the case where the Monte Carlo scales different from the data (or vise versa). In order to understand if the reconstruction is biased between the data and Monte Carlo, the distance between the reconstructed π^0 vertex and the decay photons were measured in X, Y and Z, shown in Figures 5.14 and 5.15. A summary of the bias values is in Table 5.10. If these are compared to the vertex resolution in Tables 4.1 and 4.2, these biases are found

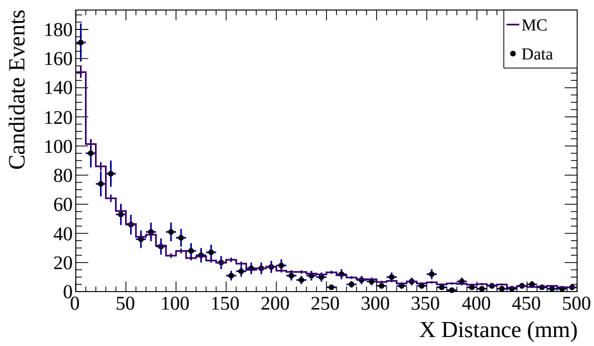

(a) X Direction

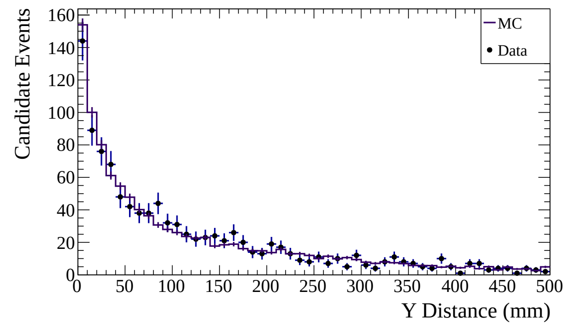

(b) Y Direction

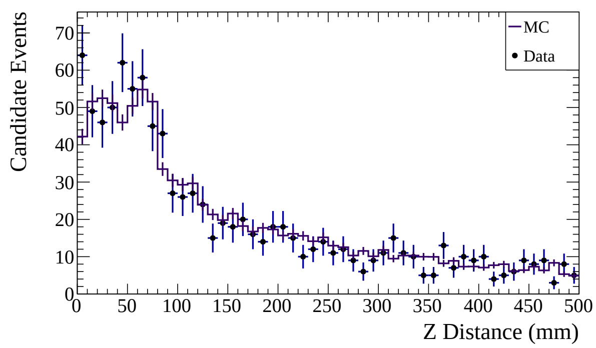

(c) Z Direction

Figure 5.15: The bias between data and Monte Carlo is judged by the difference in the average distance from the π^0 vertex and the reconstructed photon vertices. These plots show the distributions for the P∅D water-out configuration.

Table 5.10: Summary of the bias between data and Monte Carlo as measured by the distance between reconstructed vertex and the reconstruction photons.

	X (mm)	Y (mm)	Z (mm)
Water-In	1.5 ± 2.8	2.3 ± 2.8	6.3 ± 3.3
Water-Out	9.3 ± 3.6	1.0 ± 3.8	5.6 ± 4.4

to be relatively small. The difference in the means of the distributions is taken as the bias between data and Monte Carlo. The number of selected events is assumed to scale linearly with the target area. The volume is recalculated scaling all three lengths up and down by the bias and its error. The fractional change in the volume from the nominal fiducial volume is calculated and the larger fluctuation is used as the systematic error. For the PØD water-in configuration, the systematic error is 1.1% and for the PØD water-out configuration, the error is 1.7%.

5.6 Flux and Event Generator Uncertainties

The information from T2KReWeight is accessed in two ways. The first way provides constraints for the covariance matrix in the fit. The second uses the reweighted Monte Carlo invariant mass spectrum to rerun the fit multiple times in order to get a systematic error for flux and cross section on the final fit result.

The flux parameters and their errors are listed in Table 5.11. This analysis ignores the Super Kamiokande related flux errors, so there are only 25 parameters of interest. The energy binning of the flux errors is described in Table 5.12. The cross section parameters and their errors are listed in Table 5.13. The energy binning of the binned cross section errors is shown in Table 5.14. There are 21 input parameters defined by the BANFF matrix. A small subsample of cross section parameter contains an energy binning and that binning is described in Table 5.13. These parameters were used in the 2013a oscillation analyses [20]. The errors on all 46 parameters can be seen visually in Figure 5.17. There is a clear improvement on the understanding of the parameter errors after the BANFF fit has been performed. The correlations between the parameters are shown in Figure 5.16.

After fixing the MC sample of selected events, the RooTracker Vertices for those events are found and saved in a tree. Using those skimmed vertices, the selected events are passed into T2KReWeight. The parameters described above are then tweaked and new weights are created for every event.

The majority of the T2KReWeight parameters are normalization factors. In order to understand the sensitivity of the fit to T2KReWeight, the input PDFs are reweighted with the tweaked values in each throw. After reweighting the PDFs, the fit is rerun. There were 1000 throws of the parameters. Each reweighted fit result is compared to the T2KReWeight nominal Monte Carlo prediction, post- or pre-BANFF fit. The nominal T2KReWeight values are discussed in Section 4.5. Figures 5.18 and 5.19 show the spread of the results after running the fit. The distributions are summarized in Table 5.15. Taking the sum in quadrature of the sigma and its error of the output fit gives the final systematic error. For the pre-BANFF fit, the error is 2.9% and 3.7% for the PØD water-in and water-out configurations respectively. For the post-BANFF fit, the error is 1.5% and 1.9% respectively. The size of these errors indicate that the fit is relatively independent of the cross section normalizations.

Removing Model Dependencies

As the systematic depends on the output of the fit, to calculate the systematic for the shape varying fit, the procedure is run again, freeing the g factor. Figures 5.20 and 5.21 show

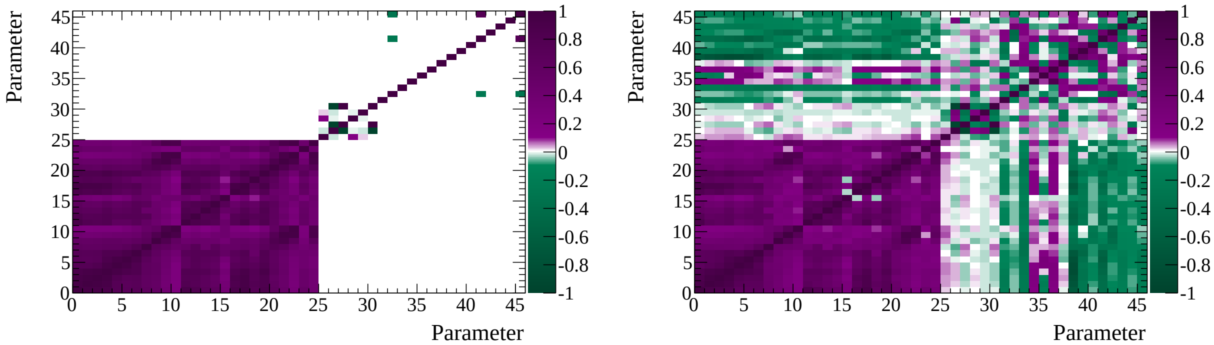

(a) Pre-Fit Correlation Matrix (b) Post-Fit Correlation Matrix

Figure 5.16: The input BANFF correlation matrices for the beam flux (parameters 0-24) and cross section (parameters 25-45) for the 2013 T2K oscillation analyses. Shown are the correlation matrices before and after the BANFF fit.

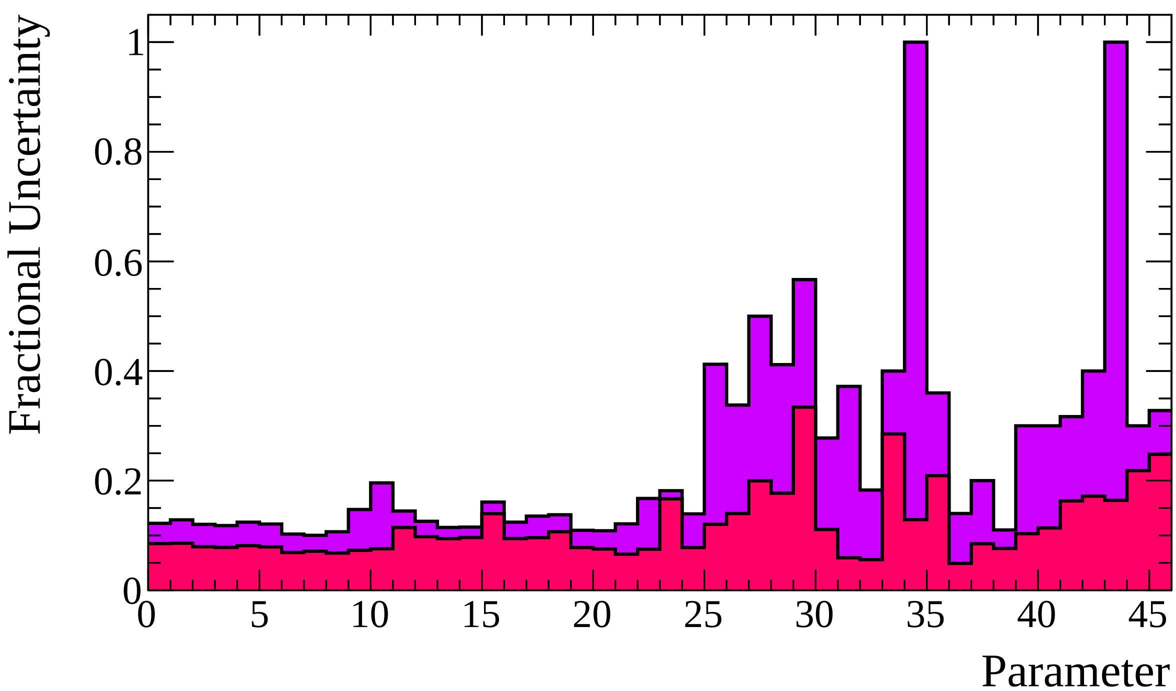

Figure 5.17: The input errors for the beam flux (parameters 0-24) and cross section (parameters 25-45) for the 2013 T2K oscillation analyses. The larger violet histogram shows the errors on the pre-BANFF fit parameters. The red overlay shows the errors on the post-BANFF fit parameters. Shown are the covariance matrices before and after the BANFF fit.

Table 5.11: Summary of beam flux systematic errors used in T2K Reweight in the 2013 T2K oscillation analyses.

Parameter	Index	BANFF Pre-Fit	BANFF Post-Fit
ν_μ flux E0	0	1.000 ± 0.122	1.027 ± 0.085
ν_μ flux E1	1	1.000 ± 0.128	1.012 ± 0.086
ν_μ flux E2	2	1.000 ± 0.120	0.994 ± 0.079
ν_μ flux E3	3	1.000 ± 0.118	0.965 ± 0.078
ν_μ flux E4	4	1.000 ± 0.124	0.934 ± 0.081
ν_μ flux E5	5	1.000 ± 0.121	0.972 ± 0.079
ν_μ flux E6	6	1.000 ± 0.102	1.027 ± 0.069
ν_μ flux E7	7	1.000 ± 0.100	1.059 ± 0.071
ν_μ flux E8	8	1.000 ± 0.107	1.039 ± 0.068
ν_μ flux E9	9	1.000 ± 0.147	0.980 ± 0.073
ν_μ flux E10	10	1.000 ± 0.196	0.960 ± 0.076
$\overline{\nu}_\mu$ flux E0	11	1.000 ± 0.145	1.030 ± 0.114
$\overline{\nu}_\mu$ flux E1	12	1.000 ± 0.126	1.010 ± 0.098
$\overline{\nu}_\mu$ flux E2	13	1.000 ± 0.115	0.997 ± 0.094
$\overline{\nu}_\mu$ flux E3	14	1.000 ± 0.115	1.015 ± 0.096
$\overline{\nu}_\mu$ flux E4	15	1.000 ± 0.161	1.039 ± 0.140
ν_e flux E0	16	1.000 ± 0.124	1.024 ± 0.094
ν_e flux E1	17	1.000 ± 0.135	1.020 ± 0.096
ν_e flux E2	18	1.000 ± 0.138	0.988 ± 0.107
ν_e flux E3	19	1.000 ± 0.109	0.995 ± 0.078
ν_e flux E4	20	1.000 ± 0.109	1.015 ± 0.075
ν_e flux E5	21	1.000 ± 0.121	0.997 ± 0.066
ν_e flux E6	22	1.000 ± 0.167	0.947 ± 0.075
$\overline{\nu}_e$ flux E0	23	1.000 ± 0.182	1.014 ± 0.167
$\overline{\nu}_e$ flux E1	24	1.000 ± 0.139	0.953 ± 0.078

Table 5.12: The bin divisions in true neutrino energy for the binned beam flux parameters in the 2013 T2K oscillation analyses.

Parameter	Bins	True Neutrino Energy Bin Divisions (GeV)
ν_μ	11	0.0 - 0.4 - 0.5 - 0.6 - 0.7 - 1.0 - 1.5 - 2.5 - 3.5 - 5.0 - 7.0 - 30.0
$\overline{\nu}_\mu$	5	0.0 - 0.7 - 1.0 - 1.5 - 2.5 - 30.0
ν_e	7	0.0 - 0.5 - 0.7 - 0.8 - 1.5 - 2.5 - 4.0 - 30.0
$\overline{\nu}_e$	2	0.0 - 2.5 - 30.0

Table 5.13: Summary of event generator systematic errors used in T2K Reweight in the 2013 T2K oscillation analyses.

Parameter	Index	BANFF Pre-Fit	BANFF Post-Fit
FSI inelastic low	25	0.000 ± 0.412	0.118 ± 0.120
FSI inelastic high	26	0.000 ± 0.338	0.445 ± 0.140
FSI π production	27	0.000 ± 0.500	-0.685 ± 0.200
FSI π absorption	28	0.000 ± 0.412	-0.270 ± 0.177
FSI charge exchange low	29	0.000 ± 0.567	0.360 ± 0.334
FSI charge exchange high	30	0.000 ± 0.278	-0.381 ± 0.111
M_a^{QE}	31	1.000 ± 0.372	1.025 ± 0.059
M_a^{RES}	32	1.163 ± 0.183	0.797 ± 0.056
DIS/Multi-π Shape	33	0.000 ± 0.400	0.225 ± 0.285
Spectral Function	34	0.000 ± 1.000	0.240 ± 0.129
E_b	35	1.000 ± 0.360	1.236 ± 0.209
p_F	36	1.000 ± 0.140	1.227 ± 0.049
π-less Δ decay	37	0.000 ± 0.200	0.006 ± 0.085
CCQE E0	38	1.000 ± 0.110	0.966 ± 0.076
CCQE E1	39	1.000 ± 0.300	0.931 ± 0.103
CCQE E2	40	1.000 ± 0.300	0.852 ± 0.114
CC1π E0	41	1.154 ± 0.317	1.265 ± 0.163
CC1π E1	42	1.000 ± 0.400	1.122 ± 0.172
CC Coherent	43	1.000 ± 1.000	0.449 ± 0.164
NC Other	44	1.000 ± 0.300	1.410 ± 0.218
NC1π^0	45	0.963 ± 0.328	1.135 ± 0.248

Table 5.14: The bin divisions in true neutrino energy for the binned cross section parameters in the 2013 T2K oscillation analyses.

Parameter	Bins	True Neutrino Energy Bin Divisions (GeV)
CCQE	3	0.0 - 1.5 - 3.5 - 30.0
CC1π	2	0.0 - 2.5 - 30.0

Table 5.15: The Gaussian fit results of Figures 5.18 and 5.19. The systematic error is taken from the spread of the distribution.

		Constant	Mean	Sigma
Water-In	Pre-BANFF	129.3 ± 5.6	74.2 ± 0.1	2.48 ± 0.07
Water-In	Post-BANFF	315.8 ± 12.6	80.1 ± 0.0	1.08 ± 0.03
Water-Out	Pre-BANFF	115.2 ± 4.7	81.5 ± 0.1	3.27 ± 0.08
Water-Out	Post-BANFF	260.7 ± 10.3	88.5 ± 0.0	1.49 ± 0.03

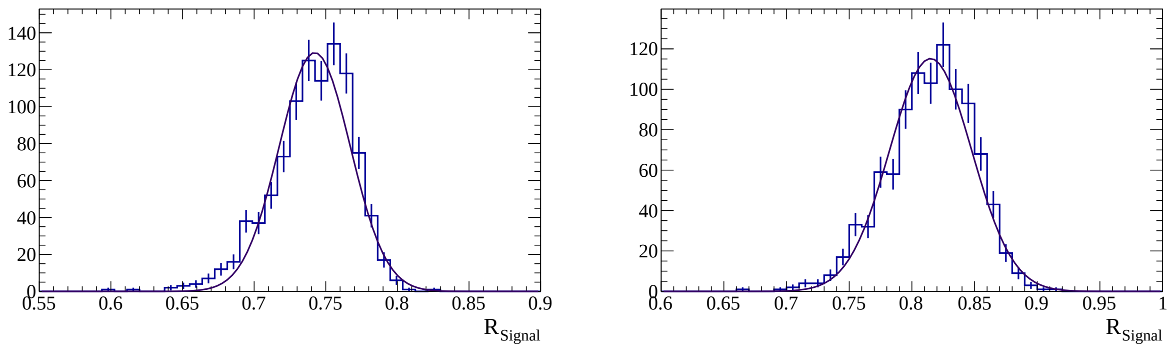

(a) Water-in Configuration. (b) Water-out Configuration.

Figure 5.18: The distribution of the ratio of signal in the selected region based on multiple fits using the T2KReWeight pre-BANFF fit throws. The P∅D water-in configuration had a 98.0% convergence rate and the P∅D water-out configuration had a 97.8% convergence rate.

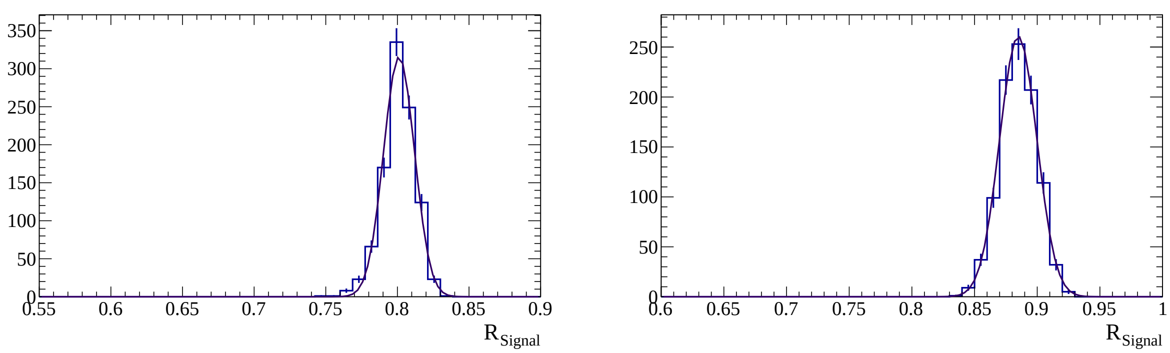

(a) Water-in Configuration. (b) Water-out Configuration.

Figure 5.19: The distribution of the ratio of signal in the selected region based on multiple fits using the T2KReWeight post-BANFF fit throws. The P∅D water-in configuration had a 100.0% convergence rate and the P∅D water-out configuration had a 97.3% convergence rate.

Table 5.16: The Gaussian fit results of Figures 5.20 and 5.21 with unconstrained g factors. The systematic error is taken from the spread of the distribution.

		Constant	Mean	Sigma
Water-In	Pre-BANFF	126.7 ± 5.4	89.5 ± 0.1	2.94 ± 0.08
Water-In	Post-BANFF	267.8 ± 11.2	97.0 ± 0.0	1.46 ± 0.04
Water-Out	Pre-BANFF	101.0 ± 4.4	106.3 ± 0.1	3.71 ± 0.11
Water-Out	Post-BANFF	201.1 ± 8.1	114.1 ± 0.1	1.91 ± 0.05

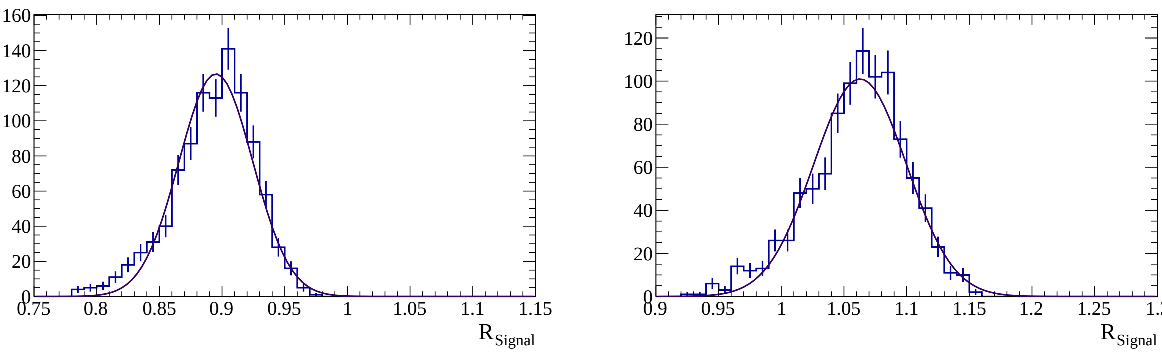

(a) Water-in Configuration (b) Water-out Configuration

Figure 5.20: The distribution of the ratio of signal in the selected region based on multiple fits using the T2KReWeight pre-BANFF fit throws with an unconstrained g factor. The P∅D water-in configuration had a 98.3% convergence rate and the P∅D water-out configuration had a 97.5% convergence rate.

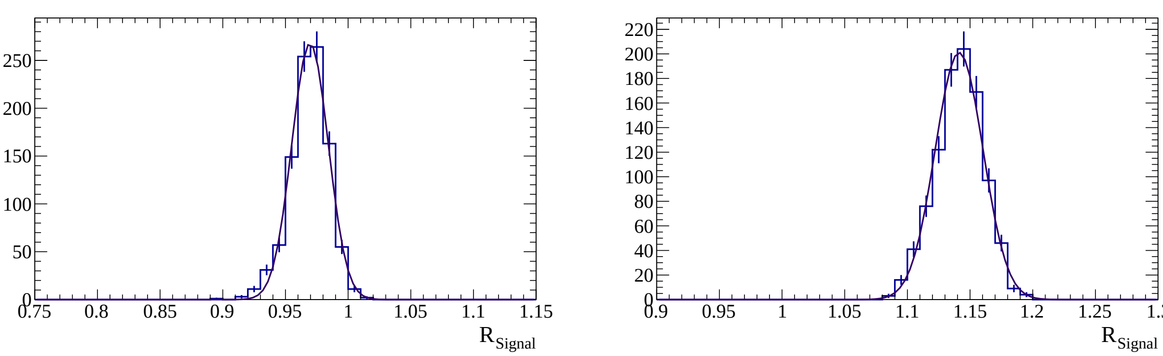

(a) Water-in Configuration. (b) Water-out Configuration.

Figure 5.21: The distribution of the ratio of signal in the selected region based on multiple fits using the T2KReWeight post-BANFF fit throws with an unconstrained g factor. The P∅D water-in configuration had a 100.0% convergence rate and the P∅D water-out configuration had a 97.3% convergence rate.

the spread of the results after running the fit. The distributions are summarized in Table 5.16. Taking the sum in quadrature of the sigma and its error of the output fit gives the final systematic error. For the pre-BANFF fit, the error is 2.5% and 3.3% for the P∅D water-in and water-out configurations respectively. For the post-BANFF fit, the error is 1.1% and 1.5% respectively. Again, the size of these errors indicate that the fit is relatively independent of the cross section normalizations.

5.7 Reconstruction Uncertainties

There are three types of reconstruction uncertainties of concern. The first issue is the efficiency of an event getting to the shower reconstruction, where most of the selection cuts are geared toward. The second is the data to Monte Carlo discrepancy in the cuts depending on the reconstruction, such as the PID weight, the charge in the showers and the shower separation. The third issue, has two parts: how well the Monte Carlo predicts muon decay and how accurate that reconstruction is.

5.7.1 Track PID Efficiency

The analysis for this systematic is detailed in Section 3.4. There is a 5.4% inefficiency difference of muons being misidentified as EM for the water-in configuration and a 5.1% inefficiency for the water-out configuration.

5.7.2 Continuous Distribution Cuts

There are three optimized cuts: Charge in Shower, Shower Separation and PID Weight Difference. In order to study the systematic effect of these continuous cuts, double sideband plots are examined. For example, to look at Shower Separation, events that fail the Charge in Shower and PID Weight Difference, but pass all other cuts. This way the events come from a low purity sample and are not effected by any data to Monte Carlo signal difference. The purities of the samples are summarized in Table 5.19. The percent of saved events for varying cuts is shown in Figures 5.22 and 5.23 and the values are interpolated from the histograms. The systematic error extracted is the difference of the percent of saved events in data and Monte Carlo divided by the Monte Carlo value at the cut. This systematic error has an intrinsic statistical error from the binomial error on the interpolated values. Assuming the statistical errors on the percent of saved events are Gaussian, the statistical error can be propagated through to apply to the systematic. At this point, the systematic and statistical errors are added in quadrature and the final systematic error is extracted. A summary of these systematic errors are shown in Tables 5.17 and 5.18. After adding the continuous cut systematics in quadrature, the systematic error on the efficiency due to the continuous cuts is 13.0% for the P∅D water-in configuration and 12.3% for the P∅D water-out configuration.

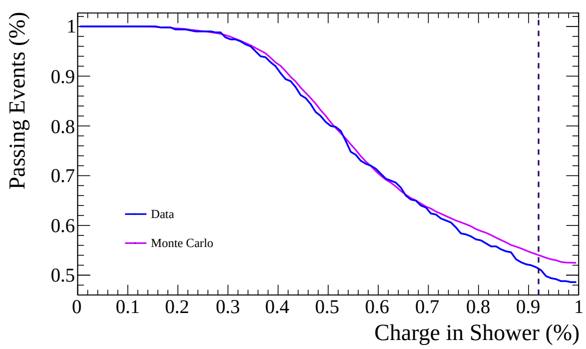

(a) Charge in Shower

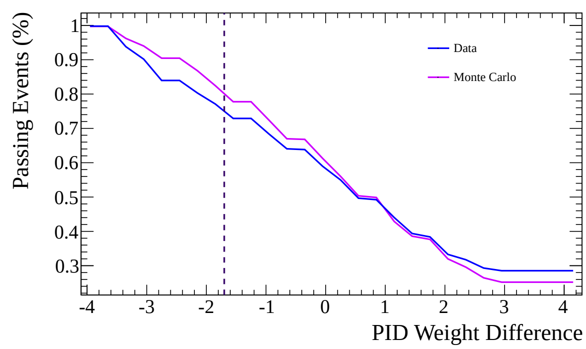

(b) PID Weight

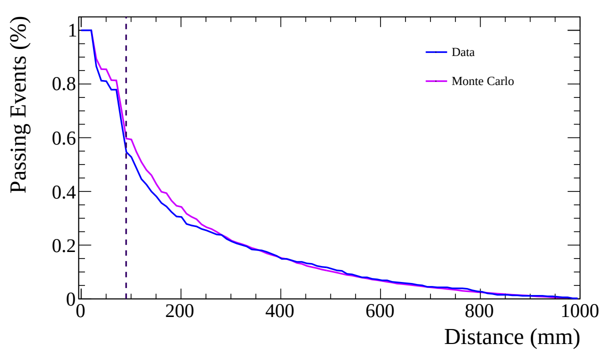

(c) Nearest Shower

Figure 5.22: Percent of events passing continuous cuts. These distributions show the difference between data and Monte Carlo in the N-2 sidebands for the P∅D water-in configuration.

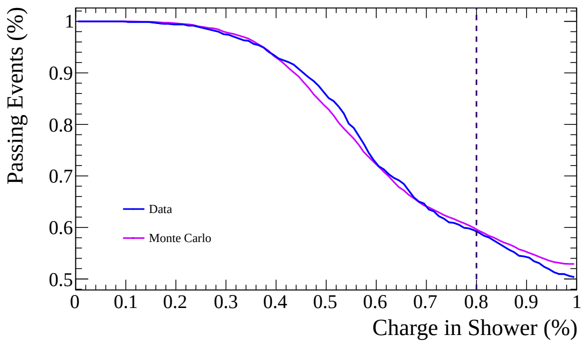

(a) Charge in Shower

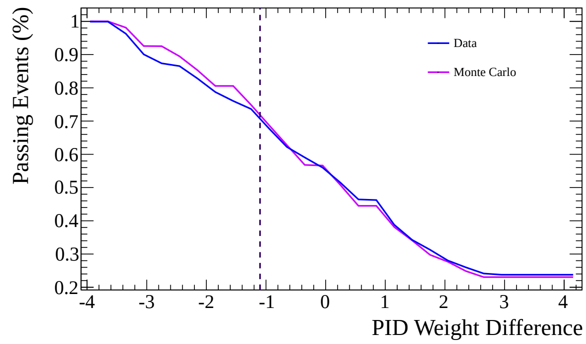

(b) PID Weight

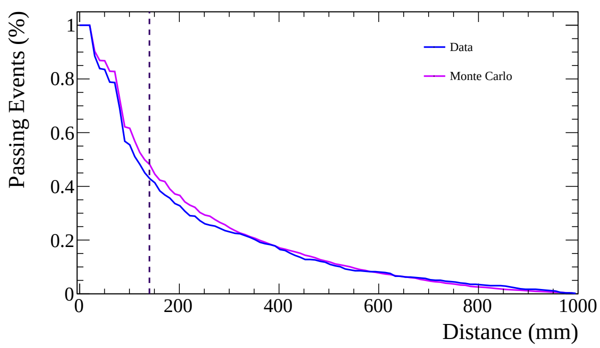

(c) Nearest Shower

Figure 5.23: Percent of events passing continuous cuts. These distributions show the difference between data and Monte Carlo in the N-2 sidebands for the P∅D water-out configuration.

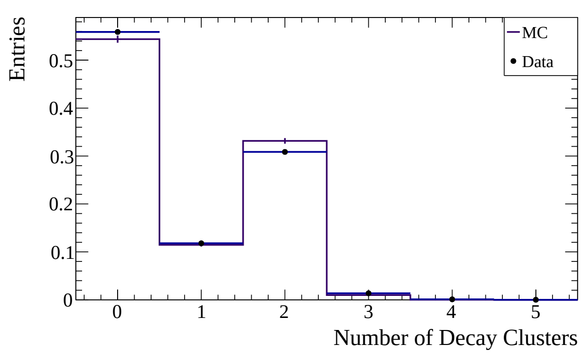

(a) Water-In Configuration

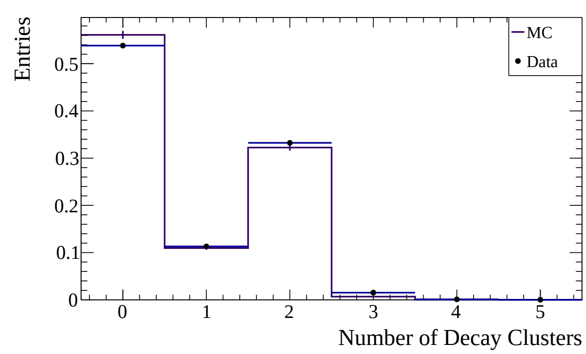

(b) Water-Out Configuration

Figure 5.24: For the stopping muon sample, the number of muon decay clusters reconstructed. Data and Monte Carlo histograms are shown normalized to one.

Table 5.17: The summary of the systematic error on the optimizable cuts for the PØD water-in configuration. The columns divide the three continuous cuts of interest. The first two rows summarize the interpolated values of the efficiencies at the cut value. The next row contains the systematic difference between the data and Monte Carlo efficiencies. The next two rows summarize the statistical error of the data and Monte Carlo efficiency values. The penultimate row describes the statistical error on the systematic difference between data and Monte Carlo. The last row shows the combined systematic shift and statistical error, which is used as the total systematic error for the cuts.

	Charge in Shower	Shower Separation	PID Weight
Monte Carlo Cut Efficiency	54.0	60.2	80.1
Data Cut Efficiency	51.3	55.18	75.0
Systematic Error	5.1	8.3	6.4
Monte Carlo Statistical Error	0.5	0.5	0.3
Data Statistical Error	2.2	2.1	1.4
Statistical Error	4.2	3.6	1.8
Total Systematic Error	6.6	9.1	6.6

Table 5.18: The summary of the systematic error on the optimizable cuts for the PØD water-out configuration. The columns divide the three continuous cuts of interest. The first two rows summarize the interpolated values of the efficiencies at the cut value. The next row contains the systematic difference between the data and Monte Carlo efficiencies. The next two rows summarize the statistical error of the data and Monte Carlo efficiency values. The penultimate row describes the statistical error on the systematic difference between data and Monte Carlo. The last row shows the combined systematic shift and statistical error, which is used as the total systematic error for the cuts.

	Charge in Shower	Shower Separation	PID Weight
Monte Carlo Cut Efficiency	59.6	48.2	71.8
Data Cut Efficiency	59.2	43.0	70.7
Systematic Error	0.7	10.8	1.6
Monte Carlo Statistical Error	0.6	0.7	0.5
Data Statistical Error	1.7	2.0	1.4
Statistical Error	3.0	4.3	2.0
Total Systematic Error	3.1	11.6	2.6

Table 5.19: A summary of the purities predicted in the double sidebands for the PØD water-in and water-out configurations.

	Charge in Shower	Shower Separation	PID Weight
Water-In	9.7 ± 0.3	6.7 ± 0.3	7.1 ± 0.2
Water-Out	7.7 ± 0.3	4.3 ± 0.3	5.9 ± 0.3

Table 5.20: The efficiency of finding a muon decay for a reconstructed muon in a stopping muon sample. The first column describes the PØD water status. The second and third column list the efficiency of finding any muon decay cluster in both the Monte Carlo stopping muon particle gun and in the data. The final column describes the fractional difference between data and Monte Carlo. This is used as the constraint on the ratio of background events in the sideband region to background events in the selected region. All numbers are listed in percentage.

Configuration	ϵ_{MC}	ϵ_{Data}	$(\epsilon_{Data} - \epsilon_{MC})/\epsilon_{MC}$
Water-In	45.6 ± 0.5	44.1± 0.5	3.3 ± 0.7
Water-Out	43.9 ± 0.6	46.2 ± 0.6	5.2 ± 0.8

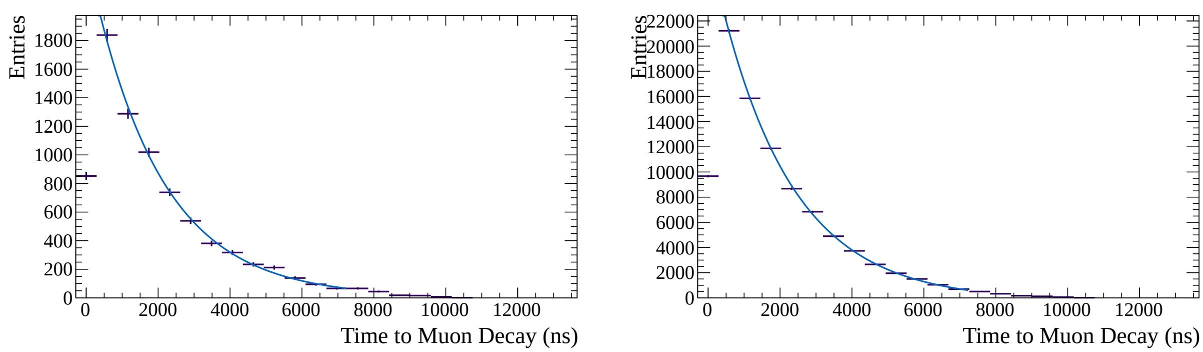

(a) Monte Carlo (b) Data

Figure 5.25: For the stopping muon sample, the time difference between the neutrino interaction and the muon decay clusters for the PØD water-in configuration

Table 5.21: The result of the fit to Equation 5.1 to the muon decay time curve in Figure 5.25 for the PØD water-in configuration stopping muons.

Parameter	Monte Carlo	Data
a	2405.7 ± 56.4	28368.3 ± 28368.3
b	1.96 ± 0.07 μs	2.05 ± 0.02 μs
c	6.6 ± 11.9	-224.6 ± 42.5

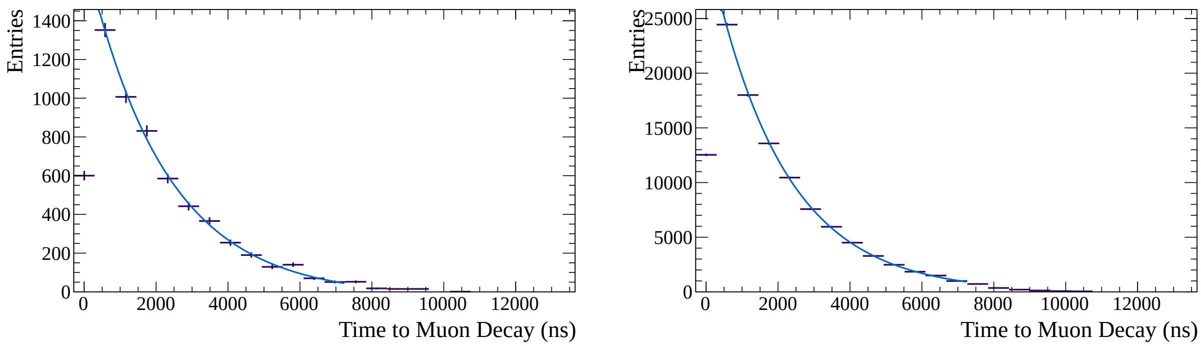

(a) Monte Carlo (b) Data

Figure 5.26: For the stopping muon sample, the time difference between the neutrino interaction and the muon decay clusters for the P∅D water-in configuration

Table 5.22: The result of the fit to Equation 5.1 to the muon decay time curve in Figure 5.26 for the P∅D water-out configuration stopping muons.

Parameter	Monte Carlo	Data
a	1783.8 $\pm$ 43.3	32150.8 $\pm$ 32150.8
b	2.21 $\pm$ 0.09 μs	2.05 $\pm$ 0.02 μs
c	-23.7 $\pm$ 12.9	-24.4 $\pm$ 48.7

5.7.3 Muon Decay Systematic

The behavior of the muon decay finding is used in two different ways as input constraints to the fit. The probability of an event with a muon (a background event) entering the selected region rather than the sideband region is determined by the efficiency of detecting a muon decay. The probability of a neutral current event (a signal event) entering the sideband region is determined by the false rate of finding muon decay clusters. For both studies a sample of stopping muons was used. The same sample used for the Track PID efficiency study, described in 3.4 was repurposed for these studies.

For the ratio of the backgrounds, the efficiency of finding a muon decay was examined. For all tracks satisfying the requirement for a stopping muon, the number of muon decay clusters that occur after the neutrino interaction are counted. In Figure 5.24, the number of muon decay clusters found is shown. The data and Monte Carlo histograms are area normalized to one. The efficiency of the reconstruction is calculated from the number of events that have any muon decay clusters and the total number events. The fractional difference between data and Monte Carlo is added in quadrature to its statistical error and used as the constraint on the ratio. This constraint is 3.4% for the PØD water-in configuration and 5.2% for the PØD water-out configuration. A summary of the efficiencies is in Table 5.20.

For a constraint on the ratio of the signal in the selected and sideband regions, the rate of fake muon decay clusters is considered. The fake muon decay clusters occur when there are decay clusters reconstructed when there isn't a precursor muon. Figures 5.25 and 5.26 show the time difference between all muon decay clusters and their associated neutrino vertex interaction. The histograms are binned in units of the cycle length. There is a clear exponential decay representing the correctly reconstructed muon decays. The range of interest is from a one cycle difference to a twelve cycle difference. Although there are twenty-three cycles, the beam spill only occurs between cycles four and eleven. If an interaction occurred in cycle 11, there are 12 succeeding cycles in which is it possible to reconstruct a muon decay cluster. If the range above a difference of twelve is examined, then there would be an additional loss of reconstructed muon decays due to late cycle interactions. This is clearly shown when Figures 5.25 and 5.26 are plotted on a log scale. In addition, there is an issue with looking at the number of same cycle events. For these reasons, the exponential decay function,

$$y = ae^{-\frac{1}{b}x} + c, \tag{5.1}$$

is fit to the subrange of time difference from one cycle to twelve. Equation 5.1 has two parts. The first half of the equation describes a simple decay with a normalization of a and a muon decay lifetime of b. The parameter c describes an additional offset due to a possible fake muon decay rate. The results of the fits are listed in Tables 5.21 and 5.22. As verification, one can see that the muon decay lifetime represented by parameter b approaches $2.2\mu s$. Parameter c, normalized by parameter a, is used to extract the fake rate. Then the absolute value of that difference between data and Monte Carlo is used to quantify the constraint. For the PØD water-in configuration there is a $1.1 \pm 0.5\%$ difference which sums in quadrature to a 1.6% constraint. For the PØD water-out configuration there is a $1.3 \pm 0.7\%$ difference which sums in quadrature to a 2.0% constraint.

A summary of the constraints the muon decay efficiency and fake reconstruction rate is present in Table 5.25. These describe the input constraints on the fit performed in the Analysis section.

5.8 g Factor

There are two parts to this systematic. One is the statistical error on g as the output to the fit, the other is the systematic difference due to the inclusion of the g factor in the fit. There appears to be a correlation between using the g and not using it in the on-water subtraction. As such, the systematic difference is only used as a systematic error on the individual PØD water-in and PØD water-out configuration ratios. The statistical error gets passed through the subtraction to be applied to the on-water result.

5.8.1 Statistical g Contribution

The calculation of the statistical contribution to the number of signal events is approached in much the same way as the energy scale error was evaluated. After constructing the fit, the resulting value of g and its error are used to pull 10,000 times from a Gaussian distribution, see Figure 5.27. Using the pulls, the number of signal events was recalculated, shown in Figure 5.28. The mean and RMS of the resulting distribution are used to calculate the effect of the statistical error on g on the final number of selected signal events. The results of the statistical effect is summarized in Table 5.23.

5.8.2 Systematic g Contribution

In order to try to understand the effect of the g factor on the simultaneous fit, a comparison was made between the default fit and the unconstrained g factor fit. Section 4.4.3 describes the results of both fits. The error is the fractional difference between the $g = 0$ and $g \neq 0$ which is 16.4% for the PØD water-in configuration and 23.2% for the PØD water-out configuration.

This systematic is not propagated through the on-water subtraction due to a correlation between the PØD water-in and water-out configurations with and without the g factor. The on-water calculation without using the g factor gives $106.4 \pm 41.0(\text{stat}) \pm 72.6(\text{sys})$

Table 5.23: The systematic result from the error on the g factor output from the fit. The first column is the number of Monte Carlo predicted events. The next two columns describe the distribution after throwing the g factor. The last three columns are the result of calculated the fractional shift from nominal, the fractional RMS of the distribution and the final systematic error.

	Signal	Mean	RMS	Shift (%)	Shift Error (%)	Total Error (%)
Water-In	532.3	531.0	19.9	-0.2	3.8	3.8
Water-Out	385.5	384.7	16.1	-0.2	4.2	4.2

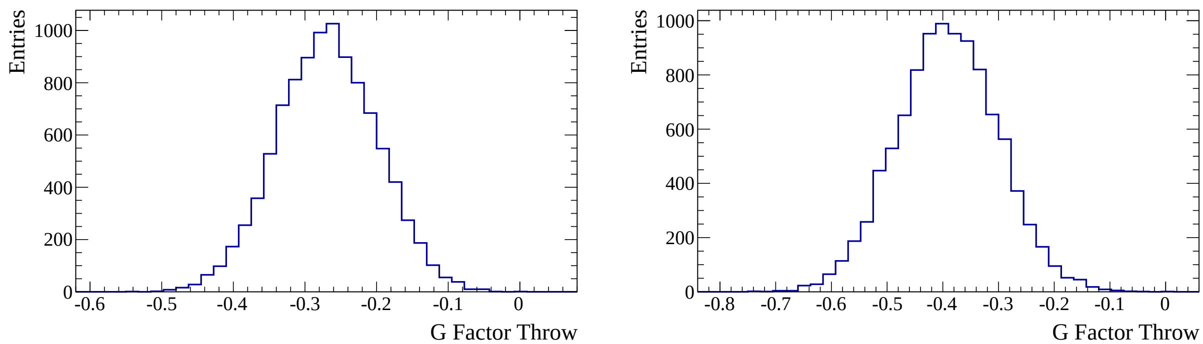

(a) Water-in Configuration (b) Water-out Configuration

Figure 5.27: The distribution of the throws of the g factor. The mean and sigma of the base distribution come from the fit results.

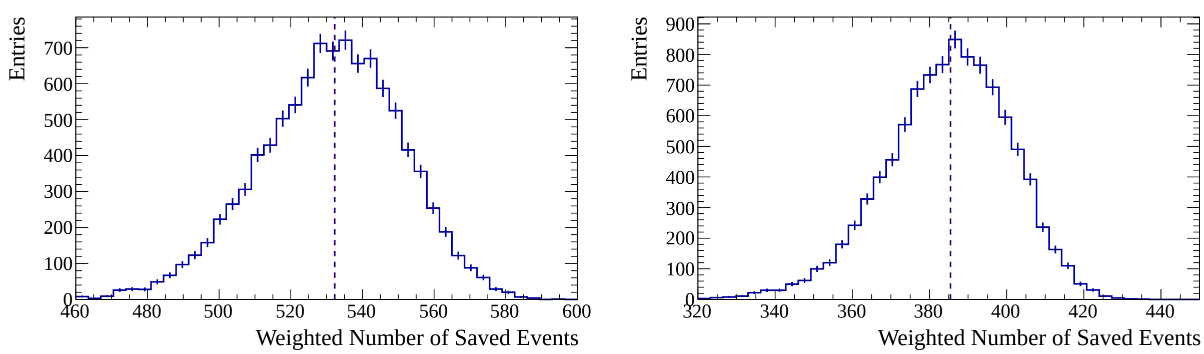

(a) Water-in Configuration (b) Water-out Configuration

Figure 5.28: The distribution of the weighted signal events using the g factor throws. The vertical dashed line represents the nominal number of Monte Carlo signal weighted events.

events where processing the fit with g gives $102.4 \pm 42.5(\text{stat}) \pm 90.4(\text{sys})$. Propagating this information through implies a fractional systematic error of 3.9% on the on-water result. This is added in quadrature to the other systematic errors after calculating the on-water data to Monte Carlo ratio.

5.9 Summary of Systematic Errors

The systematic errors are summarized in Table 5.24. The muon decay cluster reconstruction systematics that are used as constraints on the fit are listed in Table 5.25. For more details on how the muon decay cluster reconstruction contributes to the constraints on the fit, please see Subsection 5.7.3.

Removing Model Dependencies

The g factor systematic error is applied directly to the data to Monte Carlo ratio for the PØD water-in and water-out configurations. It is not propagated with the remaining systematic errors through to the on-water result. Instead, the fractional difference between the $g = 0$ and $g \neq 0$ on-water data to Monte Carlo ratio is taken as the systematic error due to g on the final number. The error is passed through the subtraction as an error on the number of reconstructed data events.

Table 5.24: Summary of Systematic errors.

Parameter	Uncertainty	
	Water-In	Water-Out
Geometry Differences	2.8%	2.8%
PE Peak Discrepancy	0.6%	0.4%
Energy Scale	5.8%	0.9%
Detector Variations	$< 0.1\%$	$< 0.1\%$
P∅D Response	1.8%	1.8%
Mass Uncertainty	0.5%	0.9%
Alignment	$< 0.1\%$	$< 0.1\%$
Fiducial Volume Scaling	1.5%	2.0%
Fiducial Volume Shift	1.1%	1.7%
Flux and Event Generator	2.9%(1.5%)	3.7%(1.9%)
Track PID Efficiency	5.4%	5.1%
Shower Separation	10.9%	13.5%
PID Weight	8.1%	3.4%
Charge In Shower	7.8%	3.0%
Total Systematic	18.1%(18.0%)	16.1%(15.8%)

Table 5.25: Summary of the constraints to be applied in the fit. The first column describes the source of the constraint. The second column lists the parameter that the constraint is used for. The last two columns list the constraints used for the P∅D water-in and water-out configurations.

Error	Parameter	Parameter Value	
		Water-In	Water-Out
Muon Decay Fake Rate	$N_{\text{Sig}}^{\text{Sideband}}/N_{\text{Sig}}^{\text{Selected}}$	1.6%	2.0%
Muon Decay Efficiency	$N_{\text{Bkg}}^{\text{Sideband}}/N_{\text{Bkg}}^{\text{Selected}}$	3.4%	5.2%

Table 5.26: Summary of Systematic errors with an unconstrained g factor. There are two values listed for the Flux and Event Generator errors. The first are the pre-BANFF fit systematic errors, the latter are the post-BANFF fit systematic errors. The penultimate line is the sum in quadrature of all previous systematics. The g factor systematic is listed separately as it will be handled separately in the analysis.

Parameter	Uncertainty	
	Water-In	Water-Out
Geometry Differences	2.8%	2.8%
PE Peak Discrepancy	0.6%	0.4%
Energy Scale	4.4%	0.6%
Detector Variations	$< 0.1\%$	$< 0.1\%$
P∅D Response	1.8%	1.8%
Mass Uncertainty	0.4%	0.6%
Alignment	$< 0.1\%$	$< 0.1\%$
Fiducial Volume Scaling	1.5%	2.0%
Fiducial Volume Shift	1.1%	1.7%
Flux and Event Generator	2.5% (1.1%)	3.3% (1.5%)
Track PID Efficiency	5.4%	5.1%
Shower Separation	10.9%	13.5%
PID Weight	8.1%	3.4%
Charge In Shower	7.8%	3.0%
g Factor (statistical)	3.8%	4.2%
Total Systematic	18.2%(18.0%)	16.7%(16.4%)
g Factor (systematic)	16.4%	23.2%

Chapter 6

Conclusion

An on-water NC1π^0 rate analysis has been performed using T2K Run 1, Run 2 and Run 4 water-in data with 2.64×10^{20} POT and Run 2, Run 3, and Run 4 water-out data with 3.49×10^{20} POT. An enriched sample of NC1π^0 events was selected with an efficiency of $6.01 \pm 0.01\%(4.79 \pm 0.02\%)$ and a purity of $48.7 \pm 0.17\%(46.1 \pm 0.3\%)$ for the water-in (water-out) sample. The Monte Carlo expects 432.8 ± 4.3 signal events for the water-in configuration and 290.2 ± 5.4 signal events for the water-out configuration. An extended maximum likelihood fit was performed, using Minuit, on each sample with the invariant mass window limited to 0-500 MeV. There were two versions of the analysis conducted.

In order to directly compare the result to the NEUT Monte Carlo, the background shape is not allowed to vary. This background shape fixed analysis found 341.6 ± 32.6 observed signal events on P∅D water-in data and 246.5 ± 26.0 observed signal events on P∅D water-out data. Using the T2KReWeight pre-BANFF fit correlation matrix, the flux and cross section systematic errors are estimated in conjunction with detector systematic errors. The resulting data to Monte Carlo ratios are $0.790 \pm 0.076(\text{stat}) \pm 0.143(\text{sys})$ for water-in and $0.850 \pm 0.091(\text{stat}) \pm 0.137(\text{sys})$ for water-out. The NEUT Monte Carlo predicts 157.2 ± 2.5 signal events. Using the ratio of the water-in and water-out POT and efficiencies, there were $106.4 \pm 41.0(\text{stat}) \pm 72.6(\text{sys})$ signal on-water events observed. This leads to an on-water production rate ratio of $0.677 \pm 0.261(\text{stat}) \pm 0.462(\text{sys})$ in the P∅D.

The secondary analysis allows the shape to be constrained and modified by the muon decay sideband. This background shape varying analysis found 408.7 ± 32.5 observed signal events on P∅D water-in data and 324.1 ± 28.6 observed signal events on P∅D water-out data. Using the T2KReWeight pre-BANFF fit correlation matrix, the flux and cross section systematic errors are estimated in conjunction with detector systematic errors. The resulting data to Monte Carlo ratios are $0.944 \pm 0.076(\text{stat}) \pm 0.231(\text{sys})$ for water-in and $1.107 \pm 0.101(\text{stat}) \pm 0.316(\text{sys})$ for water-out. Using the ratio of the water-in and water-out POT and efficiencies, there were $102.4 \pm 42.5(\text{stat}) \pm 90.4(\text{sys})$ signal on-water events observed. This leads to an on-water production rate ratio of $0.652 \pm 0.270(\text{stat}) \pm 0.576(\text{sys})$ in the P∅D.

Although there is a large difference between the default analysis and the model independent analysis, the on-water result seems to be relatively unaffected with a difference between the data and Monte Carlo ratios at 0.025 which is a tenth of the statistical error.

6.1 Future Improvements

There are many ways to improve this analysis, which is the first of its kind. Due to the subtraction method, the errors on the water-in and water-out measurements combine to become quite large on the on-water calculation. As of now, T2K has received only 8% of the total expected POT. With more data, the statistical errors will be reduced. In particular, the muon decay sideband sample will gain more statistical power and, therefore, will have more strength to regulate the background shape.

A concerted effort must be undertaken to reduce the systematic errors on the measurements. In Table 5.24, the largest errors come from the optimized cut errors (shower separation, PID weight, and charge in shower). When the cuts were optimized, the potential systematic errors introduced were not considered. However, the cut values can be reevaluated and reduced by considering the size of these errors. Additionally, improvements have been made on the reconstruction for Production 6, the next version of the ND280 software. Among those, are improvements in the shower PID of which Production 5 contained a beta version. The improvements would also reflect on the track PID, another high systematic error. However, more improvements can be made to the reconstruction by trying to extract a clean sample of reconstructed electrons and photons to compare between data and Monte Carlo. Up to now, the driving force behind the PID and reconstruction came from the stopping and through-going muon samples.

Another change that could be made to the analysis, is the definition of the shower separation cut. As it is written now, it is susceptible to noise in the detector. A more robust definition, perhaps comparing the second or third nearest hit, should be employed. Or even a distance between the ellipsoid surface of the three dimensional clusters in the shower.

Further studies can be made on the shape independent fit. Although this analysis chose the selected signal shape as a shape variation, there are many other choices. One shape of interest is a linearly adjusted muon decay background shape which would allow for the suppression of the low energy background but leave the high tail unaffected. By looking at a collection of different shapes, a better understanding of the effect of the shape and the ability to remove the NEUT model shape dependency is possible.

Overall, the errors considered were evaluated on the conservative side to provide an upper limit on the possible values for the rate of the NC1π^0 interaction. Future analyses will be able to reduce and improve the systematic error on the water-in and water-out measurements, thereby increasing the power of the final on-water measurement.

Bibliography

[1] Particle Data Group. The Review of Particle Physics. http://pdg.lbl.gov/index.html, May 2014.

[2] K. Zuber. *Neutrino physics*. CRC Press, 2011.

[3] W. Pauli. Excerpt from a Letter. http://www.physics.ucdavis.edu/~svoboda/doublechooz/bkg/pauli.html, June 2006.

[4] F. Wilson. Fermi's theory of beta decay. *American Journal of Physics*, 36(12):1150–1160, 1968.

[5] G. Rodeback and J. Allen. Neutrino Recoils Following the Capture of Orbital Electrons in A 37. *Physical Review*, 86(4):446, 1952.

[6] M. Goldhaber, L. Grodzins, and A. Sunyar. Helicity of neutrinos. *Physical review*, 109(3):1015, 1958.

[7] F. Reines and C. Cowan Jr. Free antineutrino absorption cross section. I. Measurement of the free antineutrino absorption cross section by protons. *Physical Review*, 113(1):273, 1959.

[8] G. Danby et al. Observation of high-energy neutrino reactions and the existence of two kinds of neutrinos. *Physical Review Letters*, 9(1):36–44, 1962.

[9] K. Kodama et al. Observation of tau neutrino interactions. *Physics Letters B*, 504(3):218–224, 2001.

[10] SLD Electroweak, LEP Electroweak Working Group, et al. Precision electroweak measurements on the Z resonance. *Physics Reports*, 427:257, 2006.

[11] R. Davis Jr. Attempt to Detect the Antineutrinos from a Nuclear Reactor by the Cl 37 ($\bar{\nu}$, e^-) A 37 Reaction. *Physical Review*, 97(3):766, 1955.

[12] J. Bahcall. Solar Neutrinos. I. Theoretical. *Phys. Rev. Lett.*, 12:300–302, Mar 1964.

[13] R. Davis. Solar Neutrinos. II. Experimental. *Phys. Rev. Lett.*, 12:303–305, Mar 1964.

[14] R. Davis Jr, D. Harmer, and K. Hoffman. Search for neutrinos from the sun. *Physical Review Letters*, 20(21):1205, 1968.

[15] J. Bahcall, N. Bahcall, and G. Shaviv. Present Status of the Theoretical Predictions for the Cl^{37} Solar-Neutrino Experiment. *Physical Review Letters*, 20(21):1209–1212, 1968.

[16] K. Hirata et al. Observation in the Kamiokande-II detector of the neutrino burst from supernova SN1987A. *Physical Review D*, 38(2):448, 1988.

[17] Y. Fukuda et al. Evidence for oscillation of atmospheric neutrinos. *Physical Review Letters*, 81(8):1562, 1998.

[18] Q. Ahmad et al. Measurement of the Rate of $\nu_e + d \to p + p + e^-$ Interactions Produced by B 8 Solar Neutrinos at the Sudbury Neutrino Observatory. *Physical Review Letters*, 87(7):071301, 2001.

[19] Q. Ahmad et al. Direct evidence for neutrino flavor transformation from neutral-current interactions in the Sudbury Neutrino Observatory. *Physical Review Letters*, 89(1):011301, 2002.

[20] K. Abe et al. Observation of Electron Neutrino Appearance in a Muon Neutrino Beam. *Phys. Rev. Lett.*, 112:061802, Feb 2014.

[21] E. Worcester. Observation of electron antineutrino disapperance by the Daya Bay Reactor Neutrino Experiment. In *Proceedings of the DPF 2013 Meeting of the American Physical Society Division of Particles and Fields, Santa Cruz, California, August 13-17, 2013*, Oct 2013.

[22] S. Nakayama et al. Measurement of single production π^0 in neutral current neutrino interactions with water by a 1.3 gev wide band muon neutrino beam. *Physics Letters B*, 619(3âĂŞ4):255 – 262, 2005.

[23] T2K collaboration. Tokai-to-Kamiokande (T2K) Long Baseline Neutrino Oscillation Experiment Proposal, 2006.

[24] K. Abe et al. T2K neutrino flux prediction. *Physical Review D*, 87(1):012001, 2013.

[25] K. Abe et al. The T2K experiment. *Nuclear Instruments and Methods in Physics Research Section A: Accelerators, Spectrometers, Detectors and Associated Equipment*, 659(1):106–135, 2011.

[26] S. Assylbekov et al. The T2K ND280 off-axis π^0 detector. *Nuclear Instruments and Methods in Physics Research Section A: Accelerators, Spectrometers, Detectors and Associated Equipment*, 686:48–63, 2012.

[27] Glenn Lopez. *Measurement of the Single Neutral Pion Production Cross Section in Neutral-Current Neutrino Interactions in the T2K Pi-zero Detector*. PhD thesis, Stony Brook University, Stony Brook, NY, 2012.

[28] Phoc Trung Le. *Event reconstruction and energy calibration using cosmic muons for the T2K π^0 detector*. PhD thesis, Stony Brook University, Stony Brook, NY, 2009.

Appendix A

Supporting Plots for Fit Result

The following plots show the supporting information for the default fit result. There are the negative log likelihood curves for the five parameters that are fit as well as the two dimensional likelihood contours of the number of signal and background in both the selected and sideband regions. The one-dimensional negative log likelihood curves are shown as well as the two dimensional comparison between the number of signal and the number of background events in the selected and sideband regions. The two-dimensional contours give a visual sense of the correlation between the normalization of the signal and the background.

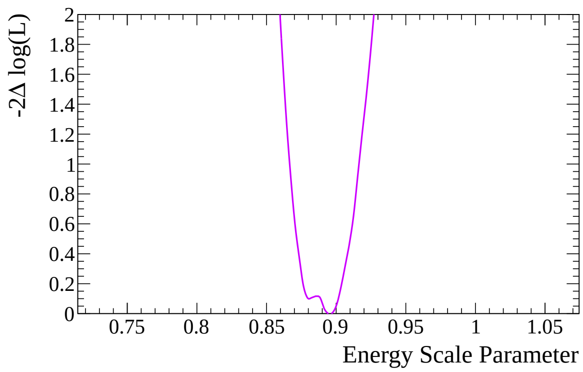

(a) Water-in Configuration

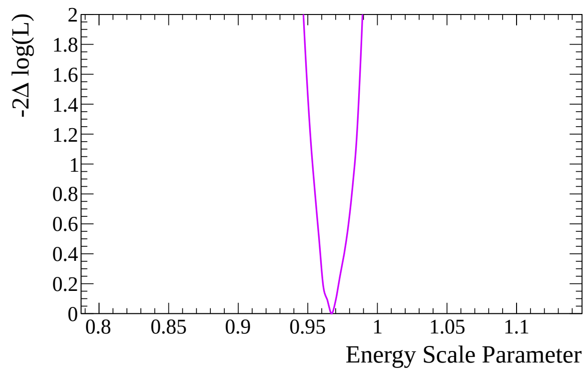

(b) Water-out Configuration

Figure A.1: The negative log likelihood curves for the energy scale parameter for both the PØD water-in and water-out configurations.

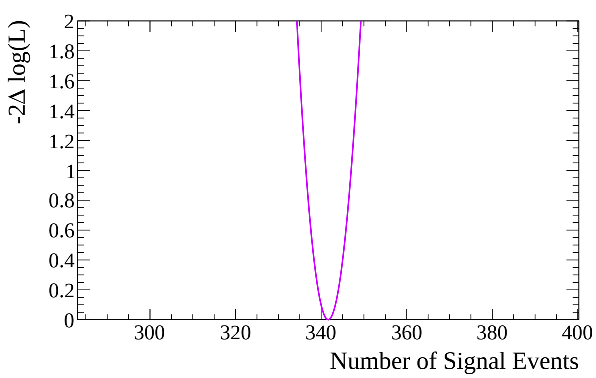

(a) Water-in Configuration

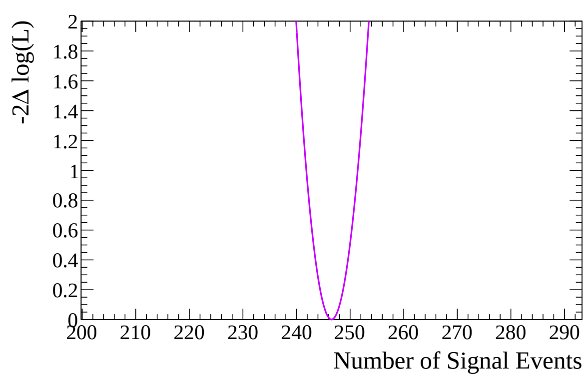

(b) Water-out Configuration

Figure A.2: The negative log likelihood curves for the number of signal events in the selected region for both the PØD water-in and water-out configurations.

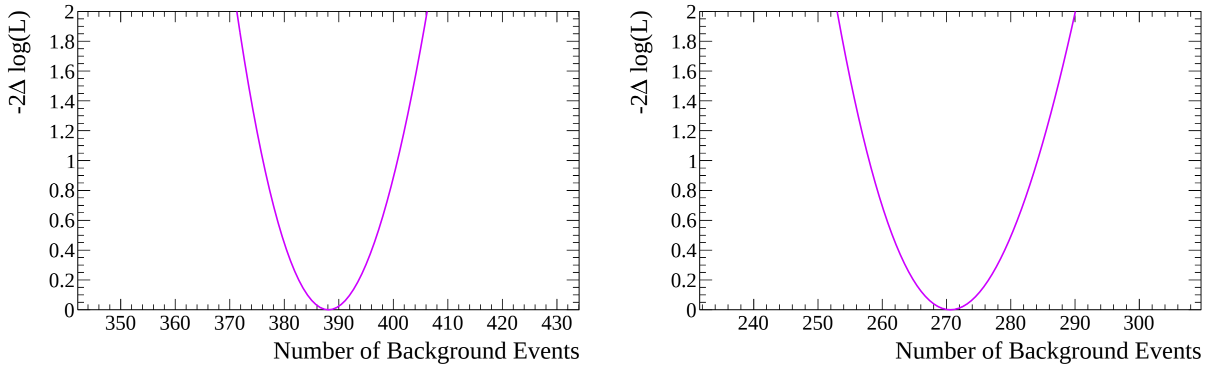

(a) Water-in Configuration

(b) Water-out Configuration

Figure A.3: The negative log likelihood curves for the number of background events in the selected region for both the PØD water-in and water-out configurations.

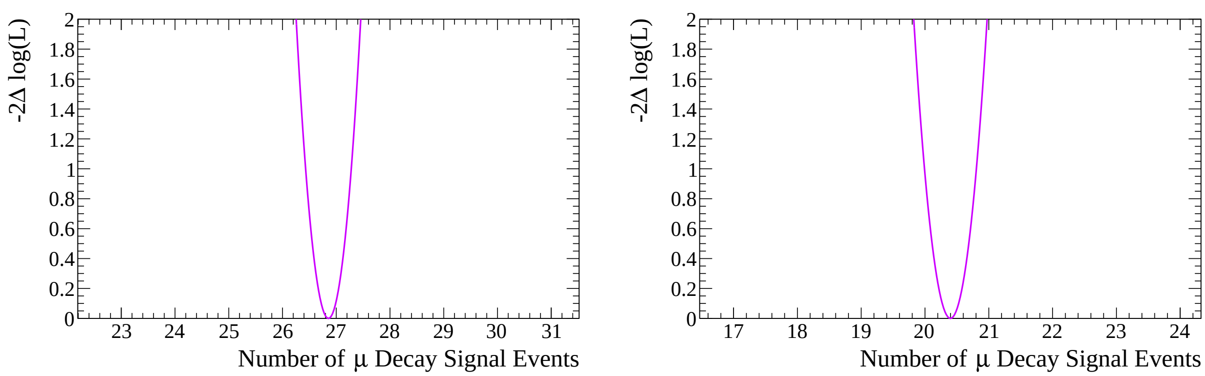

(a) Water-in Configuration

(b) Water-out Configuration

Figure A.4: The negative log likelihood curves for the number of signal events in the sideband region for both the PØD water-in and water-out configurations.

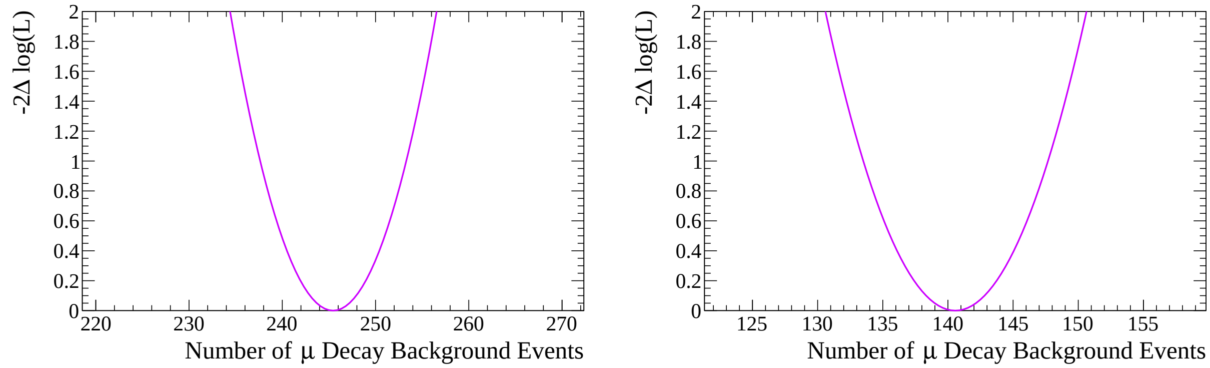

(a) Water-in Configuration (b) Water-out Configuration

Figure A.5: The negative log likelihood curves for the number of background events in the sideband region for both the P∅D water-in and water-out configurations.

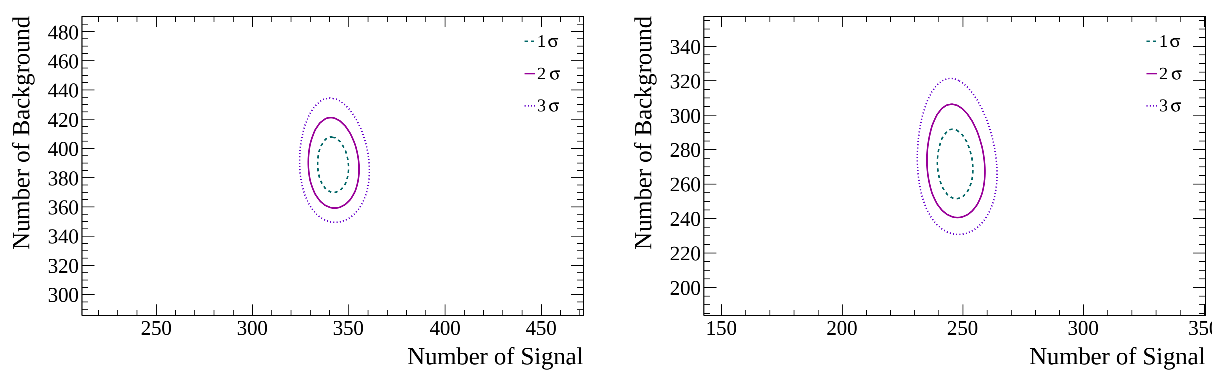

(a) Water-in Configuration (b) Water-out Configuration

Figure A.6: The negative log likelihood curves for the number of signal events in the sideband region for both the P∅D water-in and water-out configurations.

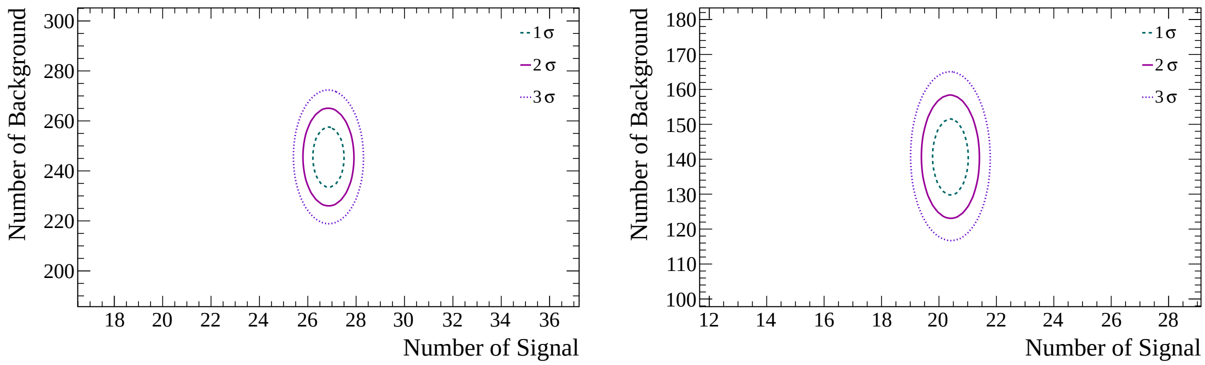

(a) Water-in Configuration

(b) Water-out Configuration

Figure A.7: The negative log likelihood curves for the number of background events in the sideband region for both the P∅D water-in and water-out configurations.

A.1 Unconstrained g Fit

The following series of plots show the negative log likelihood curves for the extended maximum likelihood fit without a constraint on g. The one-dimensional negative log likelihood curves are shown as well as the two dimensional comparison between the number of signal and the number of background events in the selected and sideband regions. The two-dimensional contours give a visual sense of the correlation between the normalization of the signal and the background.

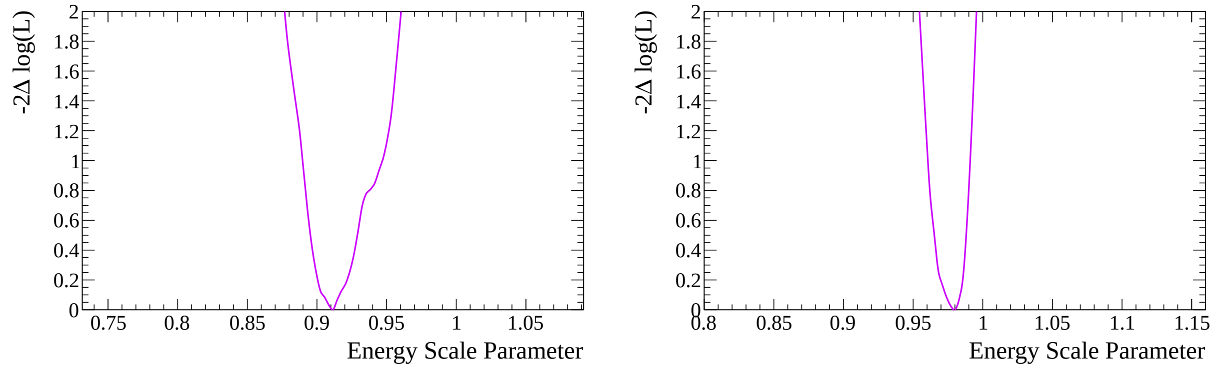

(a) Water-in Configuration

(b) Water-out Configuration

Figure A.8: The negative log likelihood curves for the energy scale parameter for both the P∅D water-in and water-out configurations.

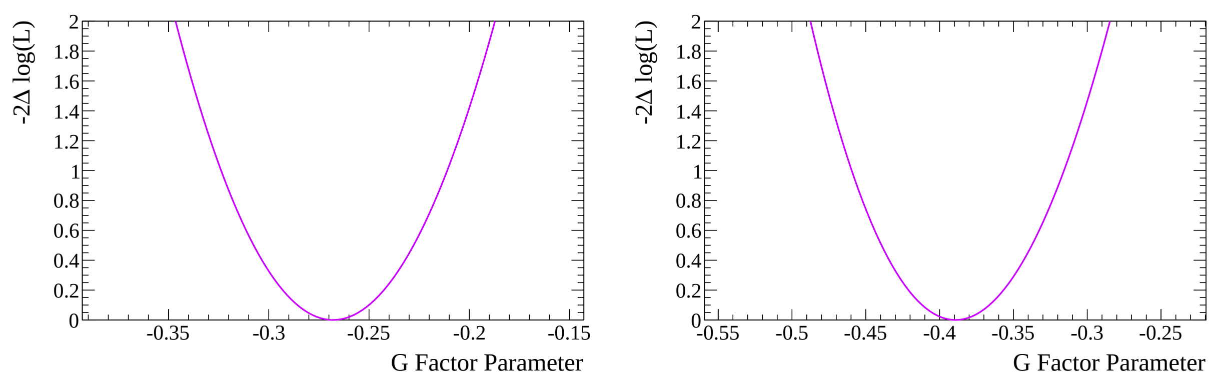

(a) Water-in Configuration

(b) Water-out Configuration

Figure A.9: The negative log likelihood curves for the g factor parameter for both the P∅D water-in and water-out configurations.

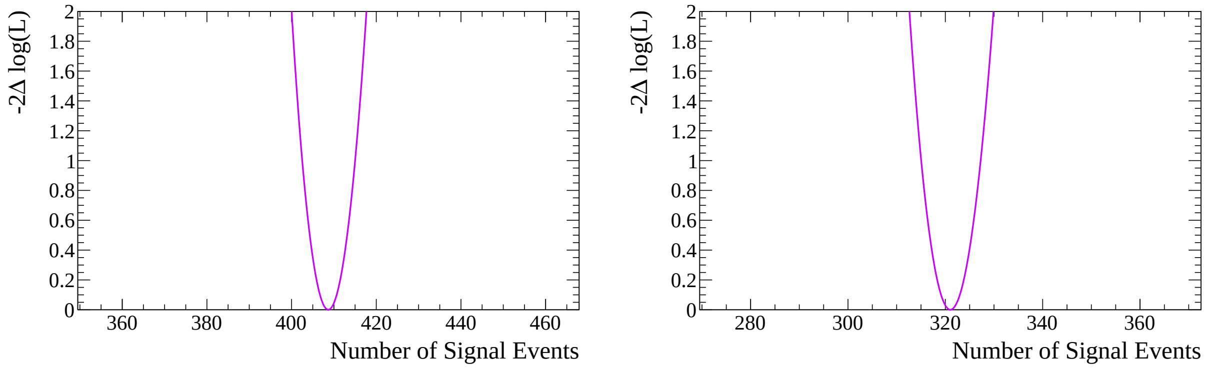

(a) Water-in Configuration (b) Water-out Configuration

Figure A.10: The negative log likelihood curves for the number of signal events in the selected region for both the P∅D water-in and water-out configurations.

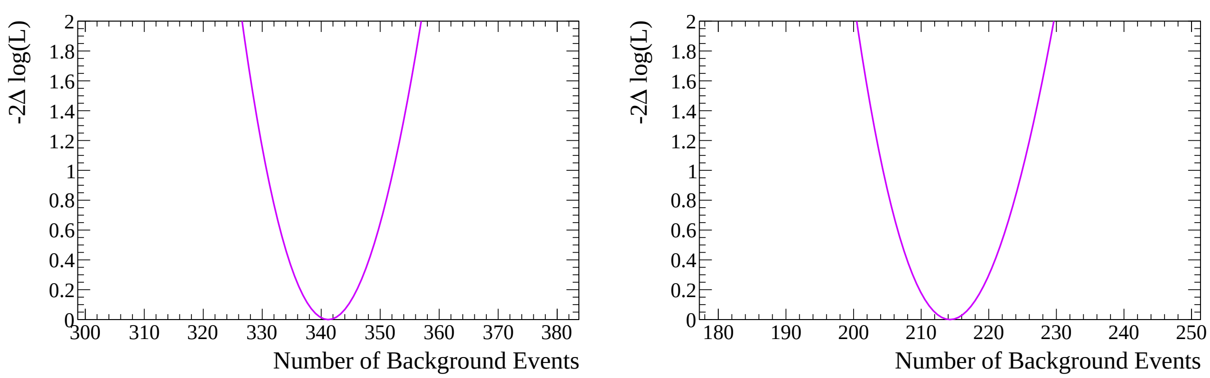

(a) Water-in Configuration (b) Water-out Configuration

Figure A.11: The negative log likelihood curves for the number of background events in the selected region for both the P∅D water-in and water-out configurations.

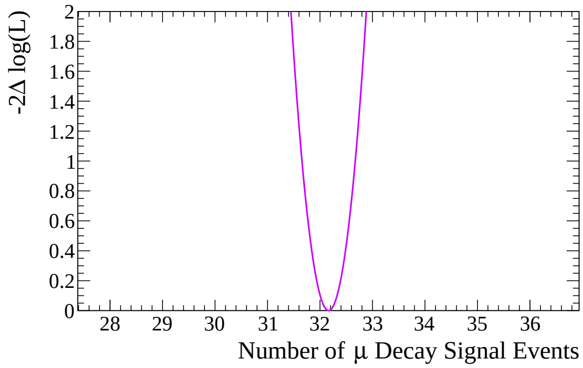

(a) Water-in Configuration

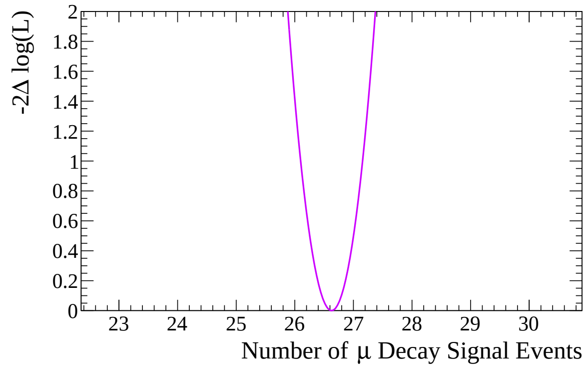

(b) Water-out Configuration

Figure A.12: The negative log likelihood curves for the number of signal events in the sideband region for both the P∅D water-in and water-out configurations.

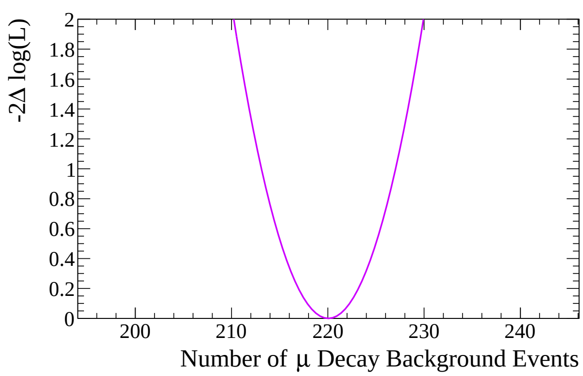

(a) Water-in Configuration

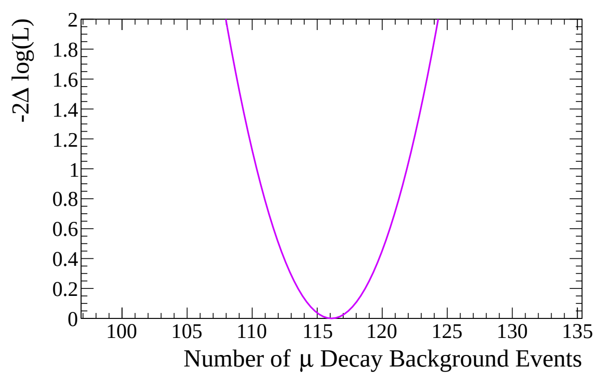

(b) Water-out Configuration

Figure A.13: The negative log likelihood curves for the number of background events in the sideband region for both the P∅D water-in and water-out configurations.

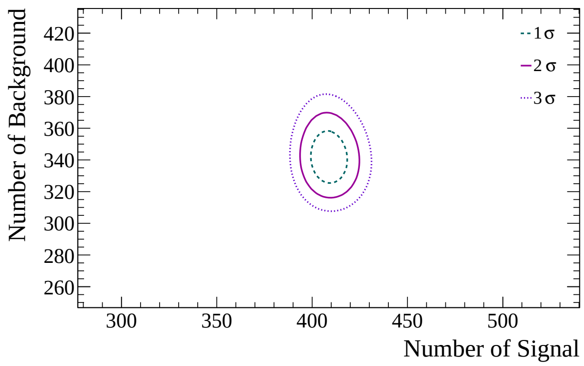

(a) Water-in Configuration

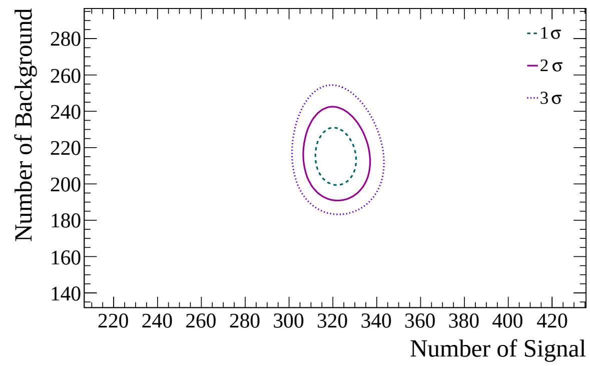

(b) Water-out Configuration

Figure A.14: The negative log likelihood curves for the number of signal events in the sideband region for both the P∅D water-in and water-out configurations.

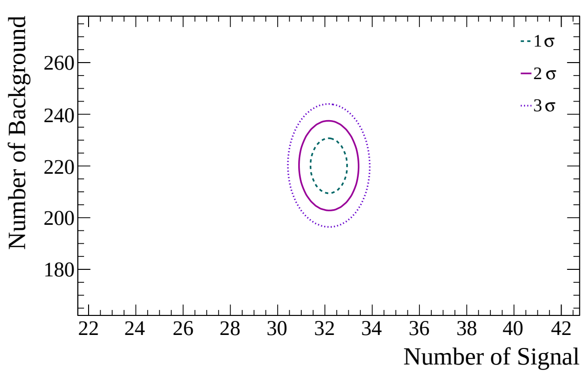

(a) Water-in Configuration

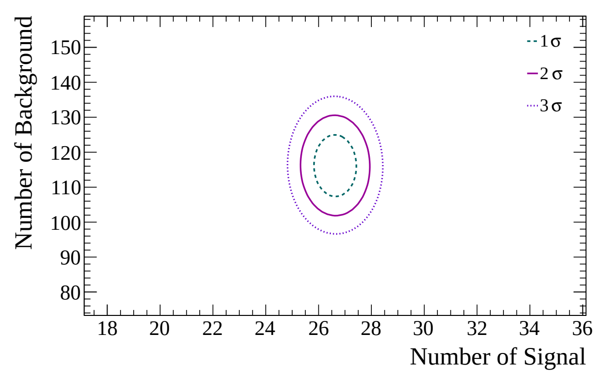

(b) Water-out Configuration

Figure A.15: The negative log likelihood curves for the number of background events in the sideband region for both the P∅D water-in and water-out configurations.